

MODELING, ANALYSIS, AND CONTROL OF A RADIAL ELECTRODYNAMIC
WHEEL VEHICLE AND ANALYSIS OF AN AXIAL ELECTRODYNAMIC WHEEL

by

Jason Douglas Wright

A dissertation submitted to the faculty of
The University of North Carolina at Charlotte
in partial fulfillment of the requirements
for the degree of Doctor of Philosophy in
Electrical Engineering

Charlotte

2019

Approved by:

Dr. Yogendra Kakad

Dr. Jonathan Bird

Dr. Sukumar Kamalasadan

Dr. Christopher Vermillion

©2019
Jason Douglas Wright
ALL RIGHTS RESERVED

ABSTRACT

JASON DOUGLAS WRIGHT. Modeling, analysis, and control of a radial electrodynamic wheel vehicle and analysis of an axial electrodynamic wheel. (Under the direction of DR. JONATHAN Z. BIRD)

Maglev, the concept of using magnetic forces to levitate a vehicle above a guideway for frictionless motion, has received renewed interest as of late due to several high profile projects, including the proposed next-generation transit system Hyperloop, and imaginative gadgets such as the Lexus Slide and Hendo Hoverboard, both of which allow the user to levitate off of a surface using magnetic fields. One emerging technology, the Electrodynamic Wheel (EDW) offers the integration of lift, thrust, and braking which can all be generated from a single device. This is accomplished by rotating a magnetic rotor above a passive conductive surface (typically referred to as the “track”). The time-varying field intercepting the track induces eddy currents in the conductive material, causing the track to generate its own magnetic fields which interact with the rotor’s field. Depending on the motion of the rotor, this can generate the aforementioned lift, thrust, and/or braking forces.

This dissertation focuses on applying a computationally efficient analytic solution for calculating the forces from an EDW to build and simulate multi-EDW vehicle models. The force model allows for the quick calculation of each EDW’s stiffness and damping coefficients. These terms are analyzed from a vehicle dynamics perspective by identifying which values carry the potential to destabilize the system, and how various motions of the vehicle could drive these terms towards increasing instability. The terms are then used to develop a 4 degrees of freedom (DOF) model of a 4-rotor/EDW prototype vehicle that has

also been replicated experimentally. Using reasonable assumptions about the vehicle's run-time parameters, the differential equations are simplified and decoupled into a simple state-space system. Various controls are applied to the 4-DOF system, emphasizing that the analytical force model's stiffness and damping terms have now greatly reduced the complexity required to control an EDW vehicle system, and the rapid re-calculation time of these terms even allows the controller's estimation of the system to be updated at run-time. An alternate topology of rotor called an axial EDW is also explored using finite element models, an analytic model, and an experimental prototype.

DEDICATION

I dedicate this dissertation to my family and friends for their unending support throughout this process.

ACKNOWLEDGMENTS

I am most sincerely grateful to my doctoral advisor, Dr. Jonathan Z. Bird (Portland State University), for his support, guidance, and patience throughout my graduate career. Despite moving to another institution, he graciously agreed to continue his role as my advisor and has provided a great amount of help to this dissertation. I would also like to thank Dr. Yogendra Kakad, Dr. Sukumar Kamalasadan, and Dr. Chris Vermillion (North Carolina State University) for taking the time to be on my doctoral committee and providing me with their valued input. Gratitude is also extended to Dr. Kakad for taking on the additional responsibility of being my advisor at UNCC following Dr. Bird's departure.

I would like to offer my appreciation to the Graduate School for providing financial assistance. I am also grateful to Dr. Bird and Dr. Wesley Williams for providing financial support through Research Assistantships. Thanks are also given to JMAG Corporation for providing access to their finite-element analysis software.

Finally, I would like to extend gratitude to the students whose works are the building blocks for this dissertation: Dr. Jonathan Bird, Nirmal Paudel, Walter Bomela, and Subhra Paul.

TABLE OF CONTENTS

| | |
|---|------|
| LIST OF TABLES | ix |
| LIST OF FIGURES | xi |
| LIST OF ABBREVIATIONS | xxiv |
| LIST OF SYMBOLS | xxvi |
| CHAPTER 1: INTRODUCTION AND LITERATURE REVIEW | 1 |
| 1.1 INTRODUCTION | 1 |
| 1.2 SUSPENSION TECHNOLOGIES | 2 |
| 1.3 ELECTRODYNAMIC SUSPENSION MODELING | 9 |
| 1.3.1 DYNAMIC CONTROL OF MAGLEV SYSTEMS | 16 |
| 1.3.2 INDUCTRACK DYNAMICS AND CONTROL | 28 |
| 1.4 ELECTRODYNAMIC WHEEL | 35 |
| 1.5 CONCLUSION | 39 |
| CHAPTER 2: ELECTRODYNAMIC WHEEL VEHICLE | 40 |
| 2.1 VEHICLE DEFINITIONS | 40 |
| 2.2 DAMPING AND STIFFNESS TERM DEFINITIONS | 45 |
| 2.3 DAMPING AND STIFFNESS RELATIONSHIPS | 53 |
| 2.3.1 TRANSLATIONAL THRUST STIFFNESS | 55 |
| 2.3.2 TRANSLATIONAL HEAVE STIFFNESS | 62 |
| 2.3.3 VERTICAL HEAVE STIFFNESS | 67 |
| 2.3.4 TRANSVERSE STIFFNESS | 72 |
| 2.3.5 TRANSVERSE THRUST STIFFNESS | 75 |
| 2.3.6 TRANSVERSE HEAVE STIFFNESS | 77 |
| 2.3.7 THRUST TRANSLATIONAL DAMPING | 79 |
| 2.3.8 TRANSLATIONAL HEAVE DAMPING | 84 |
| 2.4 CONCLUSION | 88 |

| | |
|---|-----|
| CHAPTER 3: MAGLEV VEHICLE DYNAMIC MODEL..... | 92 |
| 3.1 AXIS MOTION DEFINITIONS | 92 |
| 3.2 FOUR DEGREES OF FREEDOM MODEL..... | 96 |
| 3.3 HEAVE DYNAMIC EQUATIONS | 106 |
| 3.4 ROLL DYNAMIC EQUATIONS | 109 |
| 3.5 PITCH DYNAMIC EQUATIONS | 112 |
| 3.6 YAW DYNAMIC EQUATIONS..... | 116 |
| 3.7 CONCLUSION..... | 119 |
| CHAPTER 4: FULL SYSTEM MODEL | 120 |
| 4.1 FULL SYSTEM MODEL EQUATIONS..... | 120 |
| 4.2 CONVERSION OF X-AXIS MOVEMENTS TO ANGLES | 124 |
| 4.3 4-DOF STATE SPACE MODEL | 126 |
| 4.4 DECOUPLING OUTPUTS..... | 130 |
| 4.5 INCLUSION OF MOTOR DYNAMICS | 141 |
| 4.6 MODEL VALIDATION | 147 |
| 4.7 CONCLUSION..... | 153 |
| CHAPTER 5: CONTROL OF PROTOTYPE 4-DOF SYSTEM | 154 |
| 5.1 TRANSFER FUNCTIONS..... | 154 |
| 5.2 LINEAR CONTROL OF SYSTEM DYNAMICS BLOCKS | 162 |
| 5.3 SETPOINT TRACKING | 175 |
| 5.3.1 LINEAR QUADRATIC REGULATOR WITH PRE-COMPENSATED REFERENCE . | 175 |
| 5.3.2 LINEAR QUADRATIC INTEGRAL CONTROL..... | 177 |
| 5.4 OBSERVER-BASED CONTROL | 186 |
| 5.4.1 STATE OBSERVER DERIVATION..... | 186 |
| 5.4.2 REDUCED ORDER OBSERVER METHODS | 190 |
| 5.4.3 OBSERVER EXAMPLES AND SIMULATIONS | 197 |
| 5.5 NONLINEAR OBSERVER CONTROL | 219 |

| | | |
|---|---|-----|
| 5.5.1 | LINEAR QUADRATIC GAUSSIAN INTEGRAL CONTROL | 219 |
| 5.5.2 | NONLINEAR QUADRATIC GAUSSIAN INTEGRAL CONTROL | 236 |
| 5.6 | CONCLUSION..... | 256 |
| CHAPTER 6: AXIAL ELECTRODYNAMIC WHEEL..... | | 257 |
| 6.1 | INTRODUCTION | 257 |
| 6.2 | FINITE ELEMENT ANALYSIS MODEL | 259 |
| 6.3 | ANALYTIC SOURCE FIELD VERIFICATION | 261 |
| 6.4 | VALIDATION OF ANALYTIC FIELD MODEL..... | 270 |
| 6.4.1 | VERIFICATION OF FIELD USING LI'S ROTOR DIMENSIONS | 270 |
| 6.4.2 | VALIDATION OF ANALYTIC FIELD SOLUTION FOR PROTOTYPE ROTOR | 274 |
| 6.5 | AXIAL ELECTRODYNAMIC WHEEL SOVP MODEL..... | 287 |
| 6.5.1 | REVIEW OF PREVIOUS SOURCE FIELD..... | 287 |
| 6.5.2 | FORCE CALCULATION TIME..... | 288 |
| 6.5.3 | SOVP RESULTS..... | 289 |
| 6.6 | AXIAL ELECTRODYNAMIC WHEEL EXPERIMENTAL RESULTS | 296 |
| 6.7 | CONCLUSION..... | 306 |
| CHAPTER 7: CONCLUSION AND FUTURE WORKS..... | | 307 |
| 7.1 | INTRODUCTION | 307 |
| 7.2 | RESEARCH CONCLUSION..... | 307 |
| 7.3 | RESEARCH CONTRIBUTIONS | 309 |
| 7.3.1 | MAJOR CONTRIBUTIONS | 309 |
| 7.3.2 | MINOR TECHNICAL CONTRIBUTIONS..... | 311 |
| 7.4 | FUTURE WORK..... | 311 |
| CHAPTER 8: REFERENCES..... | | 313 |

LIST OF TABLES

| | |
|---|-----|
| Table 1: Rotor, guideway, and vehicle parameters for the radial experimental setup | 43 |
| Table 2: Stability of damping and stiffness terms when $s = 0$, $v_y = 0$, and v_x varies | 89 |
| Table 3: Stability of damping and stiffness terms when $s = 0$, $v_x = 0$, and v_y varies | 90 |
| Table 4: Stability of damping and stiffness terms when $v_y = 0$, $v_x = 0$, and s varies | 90 |
| Table 5: Radial EDW vehicle state-space simulation parameters | 148 |
| Table 6: Radial EDW vehicle simulation damping and stiffness terms | 156 |
| Table 7: Radial EDW vehicle simulation step disturbance | 165 |
| Table 8: Radial EDW vehicle simulation position command (reference signals) | 180 |
| Table 9: Cross-comparison of full-order and reduced order observer expressions [77] | 192 |
| Table 10: Height observer system initial conditions | 202 |
| Table 11: Roll observer system initial conditions | 206 |
| Table 12: Pitch observer system initial conditions | 210 |
| Table 13: Yaw observer system initial conditions | 214 |
| Table 14: LQGI observer system initial conditions | 225 |
| Table 15: Nonlinear radial EDW vehicle simulation parameters | 242 |
| Table 16: Standard axial Halbach rotor field simulation parameters | 259 |
| Table 17: Li's axial Halbach rotor dimensions | 270 |
| Table 18: Comparison of FEA and analytic field results for Li's axial Halbach rotor | 273 |
| Table 19: 8 Segment-per-pole prototype axial Halbach rotor dimensions | 274 |
| Table 20: Comparison of FEA and analytic field results | 278 |
| Table 21: 4 Segment-per-pole prototype axial Halbach rotor dimensions | 283 |

| | |
|---|-----|
| Table 22: Comparison of FEA and analytic field results for 4-segment prototype axial Halbach rotor | 286 |
| Table 23: Summary of axial Halbach field computation time vs. accuracy of field model | 289 |
| Table 24: Track parameters for axial EDW SOVP simulation | 290 |
| Table 25: Experimental axial Halbach rotor parameters | 296 |

LIST OF FIGURES

| | |
|---|----|
| Fig. 1: (a) EMS maglev system uses magnetic attraction to provide lift (b) EMS system used on Transrapid train to provide lift, thrust, and guidance [8] | 2 |
| Fig. 2: (a) Superconducting (SC) Maglev uses a “Figure 8 Loop” on the side of the guideway for lateral stability and another “Figure 8 (null-flux) Loop” on the bottom of the guideway for levitation and vertical stability as it interacts with the superconducting magnets on the carriage. [10] | 4 |
| Fig. 3: Inductrack principle, showing Halbach arrays’ interaction with passive copper coils [14] | 5 |
| Fig. 4: Ideal Halbach array magnet orientation [39] | 6 |
| Fig. 5: Practical Halbach array magnet orientation [39] | 6 |
| Fig. 6: Inductrack levitation model showing levitation and guidance arrays [14] | 6 |
| Fig. 7: Plot of levitation and drag forces for an EDS system using 3-D analytical solution [16][17] | 6 |
| Fig. 8: Finite element model of single radial electrodynamic wheel, where v_x is the translational velocity of the EDW and v_r is the surface velocity of the wheel with respect the track [30] | 8 |
| Fig. 9: Axial EDW topology used by Fujii <i>et al.</i> [53] | 8 |
| Fig. 10: Levitation coils described by Davey [12] | 10 |
| Fig. 11: Davey’s simulation results using Runge Kutta technique for EDS system [10] (a) Coil Current (b) Lift mass [12] | 11 |
| Fig. 12: Layout of magnet passing over null-flux coil [13] | 12 |
| Fig. 13: De Boeij null-flux coil experimental setup sketch [13] | 12 |
| Fig. 14: De Boeij experimental results compared to models [15] | 13 |
| Fig. 15: Diagram of EDS bearings and forces (a) EDS bearing with internal rotor (b) EDS bearing with external rotor [19] | 14 |
| Fig. 16: System identification technique used to identify General Atomics Urban Maglev System [41] | 15 |
| Fig. 17: Single degree-of-freedom maglev model, where i is coil current, R is coil resistance, L is coil inductance, m is the sprung mass, k is the spring | |

- constant, c is the damper constant, l_o is the airgap, y is vertical displacement (for this example only), and f_{em} is the levitation force [62] 16
- Fig. 18: Tracking of reference trajectory, y^* , with noise contamination and actuator saturation for Beltran-Carbajal's model and feedback controller [62] 17
- Fig. 19: Block diagram for feedback linearization, where the nonlinear model is described by \dot{x} , f is a function describing the system response to the states, g is a function describing the plant response to the input, the output is described by y , which is a function, h , of the states, u is the plant input, α is the plant feedback, v is the system input, and β is the input transformation function [81] 18
- Fig. 20: Pradhan's comparison between feedback linearization control (NLC), and PID control [72] 19
- Fig. 21: Model reference controller, where Y_m is the reference model output, Y_s is the plant output, e is the error signal, and r is the input [18] 20
- Fig. 22: Vehicle-track model [18], $f_e(t)$ is the electromagnetic force, m_1 and m_2 are the masses of the vehicle carriage and electromagnets, respectively, k_3 is the secondary suspension stiffness, c_3 is the secondary suspension damping, x is the vehicle lateral displacement, L is the tracks' lateral length, $z_1(t)$ is the distance from the reference frame to the vehicle's suspension, $z_2(t)$ is the distance from the reference frame to the vehicle body, $d(t)$ is the airgap, and $h(x, t)$ is the vertical displacement of the track. 20
- Fig. 23: Songqi's simulation results showing vehicle displacement at a constant speed of v_0 [18] 21
- Fig. 24: Dimensional definitions for De Boeij's 5-DOF system, where solid black squares represent permanent magnets [14] 22
- Fig. 25: Six magnet and ten coil EDS system, where z -axis is through the page and y -axis is perpendicular to x -axis parallel to page [14] 22
- Fig. 26: De Boeij's sliding mode controller performance results [15] 23
- Fig. 27: Bächle's Nonlinear MPC transition simulation under the effect of model error and measurement noise [66] 25
- Fig. 28: Qin's comparison between a PID controller, MPC using the ARX model, and MPC using the RBF-ARX model, for a 2.2mm jump command [68] 27
- Fig. 29: Cross-section of maglev carriage studied at Lawrence Livermore National Laboratory, where y is the vertical vehicle displacement, z is the

| | |
|---|----|
| lateral vehicle displacement, x is the vehicle's longitudinal position on the track, and θ is the vehicle roll angle about the x -axis [45] | 28 |
| Fig. 30: General Atomics full scale maglev test track [47] | 29 |
| Fig. 31: Simulation showing Halbach array's magnetic field [9] | 29 |
| Fig. 32: Definition of Halbach geometry wavelength, λ_e | 31 |
| Fig. 33: Ko's results: (a) Uncontrolled vehicle height vs time (b) LQR controlled vehicle height vs. time [11] | 34 |
| Fig. 34: Drawing of Halbach rotor [21] | 35 |
| Fig. 35: Bird's calculated lift force vs. slip and translational velocity using 2D steady-state current model [21][22] | 37 |
| Fig. 36: Bird's calculated thrust force vs. slip and translational velocity using 2D steady-state current model [21][22] | 37 |
| Fig. 37: Prototype electrodynamic wheel consisting of an axial Halbach rotor and an aluminum track | 40 |
| Fig. 38: Experimental EDW Maglev vehicle rendering and axis definitions | 41 |
| Fig. 39: Guideway wheel setup with an in-line gear reducer and DC braking motor [22] | 42 |
| Fig. 40: EDW vehicle setup consisting of 4 EDWs and brushless DC drive motors. Four laser displacement sensors were used to accurately measure air-gap dynamics | 42 |
| Fig. 41: 2-D sketch of vehicle pitch forces (x - y plane) | 43 |
| Fig. 42: 2-D sketch of vehicle roll forces (y - z plane) | 44 |
| Fig. 43: 2-D sketch of pitch x -axis force induced pitching moment (x - y plane) | 44 |
| Fig. 44: 2-D sketch of yawed vehicle from above (x - z plane) | 44 |
| Fig. 45: Approximate vehicle operating regions | 55 |
| Fig. 46: Thrust/translational force, F_x , vs. slip for various values of translational velocity, v_x , $y = 10\text{mm}$ and all other positions and velocities zero | 56 |
| Fig. 47: Surface plot of k_{xx} vs. slip vs. v_x , ($v_y = 0$), $y = 10\text{mm}$, and all other positions and velocities zero | 57 |

| | |
|---|----|
| Fig. 48: Contour plot of k_{xx} vs. slip vs. v_x , ($v_y = 0$), $y = 10\text{mm}$, and all other positions and velocities zero | 58 |
| Fig. 49: Plot of k_{xx} and F_x vs. v_x when $(v_y, v_r) = (0, 10)$ m/s, $y = 10\text{mm}$ and all other positions and velocities zero | 58 |
| Fig. 50: Trust/translational force, F_x vs. slip for various values of v_y , $y = 10\text{mm}$ and all other positions and velocities zero | 59 |
| Fig. 51: Surface plot of k_{xx} vs. slip vs. v_y , $y = 10\text{mm}$, and all other positions and velocities zero (note $v_x = 0$, so slip is analogous to ω_m) | 60 |
| Fig. 52: Contour plot of k_{xx} vs. slip vs. v_y , $y = 10\text{mm}$, and all other positions and velocities zero (note $v_x = 0$, so slip is analogous to ω_m) | 61 |
| Fig. 53: Plot of k_{xx} and F_x vs. v_y when $(v_x, v_r) = (0, 10)$ m/s, $y = 10\text{mm}$ and all other positions and velocities zero | 61 |
| Fig. 54: Surface plot of k_{xy} vs. slip vs. v_x , ($v_y = 0$), $y = 10\text{mm}$, and all other positions and velocities zero | 63 |
| Fig. 55: Contour plot of k_{xy} vs. slip vs. v_x , ($v_y = 0$), $y = 10\text{mm}$, and all other positions and velocities zero | 63 |
| Fig. 56: Plot of k_{xy} and F_x vs. v_x when $(v_y, v_r) = (0, 10)$ m/s, $y = 10\text{mm}$ and all other positions and velocities zero | 64 |
| Fig. 57: Surface plot of k_{xy} vs. slip vs. v_y , $y = 10\text{mm}$, and all other positions and velocities zero (note $v_x = 0$, so slip is analogous to ω_m) | 65 |
| Fig. 58: Contour plot of k_{xy} vs. slip vs. v_y , $y = 10\text{mm}$, and all other positions and velocities zero (note $v_x = 0$, so slip is analogous to ω_m) | 66 |
| Fig. 59: Plot of k_{xy} and F_x vs. v_y when $(v_x, v_r) = (0, 10)$ m/s, $y = 10\text{mm}$ and all other positions and velocities zero | 66 |
| Fig. 60: F_y vs. slip for various values of v_x , $y = 10\text{mm}$, and all other positions and velocities zero | 67 |
| Fig. 61: Surface plot of k_{yy} vs. slip vs. v_x , ($v_y = 0$), $y = 10\text{mm}$, and all other positions and velocities zero | 68 |
| Fig. 62: Contour plot of k_{yy} vs. slip vs. v_x , ($v_y = 0$), $y = 10\text{mm}$, and all other positions and velocities zero | 69 |
| Fig. 63: Plot of k_{yy} and F_x vs. v_x when $(v_y, v_r) = (0, 10)$ m/s, $y = 10\text{mm}$ and all other positions and velocities zero | 69 |

| | |
|--|----|
| Fig. 64: F_y vs. slip for various values of v_y , $y = 10\text{mm}$, and all other positions and velocities zero | 70 |
| Fig. 65: Surface plot of k_{yy} vs. slip vs. v_y , $y = 10\text{mm}$, and all other positions and velocities zero (note $v_x = 0$, so slip is analogous to ω_m) | 71 |
| Fig. 66: Contour of k_{yy} vs. slip vs. v_y , $y = 10\text{mm}$, and all other positions and velocities zero (note $v_x = 0$, so slip is analogous to ω_m) | 71 |
| Fig. 67: Plot of k_{yy} and F_x vs. v_y when $(v_x, v_r) = (0, 10)$ m/s, $y = 10\text{mm}$ and all other positions and velocities zero | 72 |
| Fig. 68: Surface plot of the transverse stiffness, k_{zz} , as a function of slip, s , and translational velocity when $(x, y, z) = (0, 10, 0)$ mm and $(v_y, v_z) = (0, 0)$ m/s | 73 |
| Fig. 69: Contour plot of the transverse stiffness, k_{zz} , as a function of slip, s , and translational velocity when $(x, y, z) = (0, 10, 0)$ mm and $(v_y, v_z) = (0, 0)$ m/s | 74 |
| Fig. 70: Surface plot of the transverse stiffness k_{zz} vs. slip and heave, v_y when $(x, y, z) = (0, 10, 0)$ mm and $(v_x, v_z) = (0, 0)$ m/s | 74 |
| Fig. 71: Contour plot of the transverse stiffness k_{zz} vs. slip and heave, v_y when $(x, y, z) = (0, 10, 0)$ mm and $(v_x, v_z) = (0, 0)$ m/s | 75 |
| Fig. 72: Surface plot of the transverse thrust stiffness k_{zx} vs. slip and translational velocity, v_x when $(x, y, z) = (0, 10, 5)$ mm and $(v_y, v_z) = (0, 5)$ m/s | 76 |
| Fig. 73: Contour plot of the transverse thrust stiffness k_{zx} vs. slip and translational velocity, v_x when $(x, y, z) = (0, 10, 5)$ mm and $(v_y, v_z) = (0, 5)$ m/s | 77 |
| Fig. 74: Surface plot of the transverse heave stiffness k_{zy} vs. slip and translational velocity, v_x when $v_y = 0$, $v_z = 5$ m/s and $(x, y, z) = (0, 10, 5)$ mm and $(v_y, v_z) = (0, 5)$ m/s | 78 |
| Fig. 75: Contour plot of the transverse heave stiffness k_{zy} vs. slip and translational velocity, v_x when $v_y = 0$, $v_z = 5$ m/s and $(x, y, z) = (0, 10, 5)$ mm and $(v_y, v_z) = (0, 5)$ m/s | 79 |
| Fig. 76: Surface plot of d_{xx} vs. slip vs. v_x , ($v_y = 0$), all other positions and velocities zero | 80 |
| Fig. 77: Contour plot of d_{xx} vs. slip vs. v_x , ($v_y = 0$), all other positions and velocities zero | 81 |
| Fig. 78: Plot of d_{xx} and F_x vs. v_x when $(v_y, v_r) = (0, 10)$ m/s, all other positions and velocities zero | 81 |

| | |
|---|-----|
| Fig. 79: Surface plot of d_{xx} vs. slip vs. v_y , all other positions and velocities zero (note $v_x = 0$, so slip is analogous to ω_m) | 82 |
| Fig. 80: Contour plot of d_{xx} vs. slip vs. v_y , all other positions and velocities zero (note $v_x = 0$, so slip is analogous to ω_m) | 83 |
| Fig. 81: Plots of d_{xx} and F_x vs. v_y when $(v_x, v_r) = (0,10)$ m/s, all other positions and velocities zero | 83 |
| Fig. 82: Surface plot of d_{xy} vs. slip vs. v_x , ($v_y = 0$), all other positions and velocities zero | 85 |
| Fig. 83: Contour plot of d_{xy} vs. slip vs. v_x , ($v_y = 0$), all other positions and velocities zero | 85 |
| Fig. 84: Plot of d_{xy} and F_x vs. v_x when $(v_y, v_r) = (0,10)$ m/s, all other positions and velocities zero | 86 |
| Fig. 85: Surface plot of d_{xy} vs. slip vs. v_y , all other positions and velocities zero (note $v_x = 0$, so slip is analogous to ω_m) | 87 |
| Fig. 86: Contour plot of d_{xy} vs. slip vs. v_y , all other positions and velocities zero (note $v_x = 0$, so slip is analogous to ω_m) | 87 |
| Fig. 87: Plot of d_{xy} and F_x vs. slip vs. v_y when $(v_x, v_r) = (0,10)$ m/s, all other positions and velocities zero | 88 |
| Fig. 88: 4-DOF radial EDW vehicle system decoupled state flow diagram | 131 |
| Fig. 89: State flow diagram of input decoupling block | 137 |
| Fig. 90: Separated dynamics systems of prototype radial EDW vehicle linearized model | 138 |
| Fig. 91: Decoupled system state flow diagram | 139 |
| Fig. 92: Vehicle average height vs. time using Table 5 and $\delta V_n=12V$ | 148 |
| Fig. 93: Zoomed-in view of height vs. time using Table 5 and $\delta V_n=12V$ | 149 |
| Fig. 94: Vehicle roll angle vs. time using Table 5 and $\delta V_n=12V$ | 149 |
| Fig. 95: Vehicle pitch angle vs. time using Table 5 and $\delta V_n=12V$ | 150 |
| Fig. 96: Air-gap height of rotor 3 vs. time using Table 5 and $\delta V_n=12V$ | 151 |
| Fig. 97: Zoomed-in view of air-gap height of rotor 3 vs. time using Table 5 and $\delta V_n=12V$ | 151 |

| | |
|---|-----|
| Fig. 98. Height irregularities in the left and right side of the guideway track | 152 |
| Fig. 99: Height system open-loop Bode plot, using parameters from Table 6 | 156 |
| Fig. 100: Roll system open-loop Bode plot, using parameters from Table 6 | 158 |
| Fig. 101: Pitch system open-loop Bode plot, using parameters from Table 6 | 159 |
| Fig. 102: Yaw system open-loop Bode plot, using parameters from Table 6 | 160 |
| Fig. 103: Block diagram of dynamic system with LQR control | 164 |
| Fig. 104: Height dynamics open loop vs LQR control (parameters from Table 1, Table 6, and Table 7) | 166 |
| Fig. 105: Heave dynamics open loop vs LQR control (parameters from Table 1, Table 6, and Table 7) | 166 |
| Fig. 106: Roll dynamics: open loop vs LQR control (parameters from Table 1, Table 6, and Table 7) | 167 |
| Fig. 107: Roll Velocity dynamics: open loop vs LQR control (parameters from Table 1, Table 6, and Table 7) | 167 |
| Fig. 108: Pitch dynamics: open loop vs LQR control (parameters from Table 1, Table 6, and Table 7) | 168 |
| Fig. 109: Pitch velocity dynamics: open loop vs LQR control (parameters from Table 1, Table 6, and Table 7) | 168 |
| Fig. 110: Yaw dynamics: open loop vs LQR control (parameters from Table 1, Table 6, and Table 7) | 169 |
| Fig. 111: Yaw velocity dynamics: open loop vs LQR control (parameters from Table 1, Table 6, and Table 7) | 169 |
| Fig. 112: Individual rotor rotational velocities for open loop system simulation (parameters from Table 1, Table 6, and Table 7) | 171 |
| Fig. 113: Individual rotor torque and force plots for open loop system simulation (parameters from Table 1, Table 6, and Table 7) | 172 |
| Fig. 114: Individual rotor rotational velocities for closed loop LQR system simulation (parameters from Table 1, Table 6, and Table 7) | 173 |
| Fig. 115: Individual rotor torque and force plots for closed loop LQR system simulation (parameters from Table 1, Table 6, and Table 7) | 174 |

| | |
|--|-----|
| Fig. 116: Generalized LQR controller with pre-compensator to achieve steady-state tracking | 175 |
| Fig. 117: Height dynamics simulation with LQR and pre-compensation controller (parameters from Table 1, Table 6, and Table 7) | 177 |
| Fig. 118: Generalized block diagram of LQI controller, where e_d is the error signal, x_{di} is the integrator state, K_d is the LQR (feedback) gain matrix, and K_{di} is the integrator gain | 177 |
| Fig. 119: Vertical displacement simulation with LQI control (parameters from Table 1, Table 6, and Table 8) | 182 |
| Fig. 120: Roll simulation with LQI control (parameters from Table 1, Table 6, and Table 8) | 182 |
| Fig. 121: Pitch simulation with LQI control (parameters from Table 1, Table 6, and Table 8) | 183 |
| Fig. 122: Yaw simulation with LQI control (parameters from Table 1, Table 6, and Table 8) | 183 |
| Fig. 123: Individual rotor rotational velocity plots for closed loop LQI system simulation (parameters from Table 1, Table 6, and Table 8) | 184 |
| Fig. 124: Individual rotor torque and force plots for closed loop LQI system simulation (parameters from Table 1, Table 6, and Table 8) | 185 |
| Fig. 125: General block diagram of system control using state observer, $D_d = []$ | 187 |
| Fig. 126: Reduced-order observer general block diagram | 194 |
| Fig. 127: Height dynamics observer simulation (parameters from Table 1, Table 6, Table 7, Table 10) | 203 |
| Fig. 128: Roll dynamics observer simulation (parameters from Table 1, Table 6, Table 7, Table 11) | 207 |
| Fig. 129: Pitch dynamics observer simulation (parameters from Table 1, Table 6, Table 7, Table 12) | 211 |
| Fig. 130: Yaw dynamics observer simulation (parameters from Table 1, Table 6, Table 7, Table 13) | 215 |
| Fig. 131: First moments of yaw dynamics observer simulation (parameters from Table 1, Table 6, Table 7, Table 13) | 216 |
| Fig. 132: Individual rotor rotational velocity during simulations from Fig. 127 to Fig. 131 | 217 |

| | |
|---|-----|
| Fig. 133: Individual rotor torque and vertical force during simulations from Fig. 127 to Fig. 131 | 218 |
| Fig. 134: LQG block diagram, where K_{dc} is the LQR controller gain and G_d defines how the noise is distributed across the states | 221 |
| Fig. 135: Height dynamics LQGI simulation for initial conditions $(y, \hat{y}) = (9.29, 8.79)$ mm, $(v_y, \hat{v}_y) = (0, -0.1)$ m/s, and $r_y = 10.29$ mm, (parameters from Table 1, Table 6, Table 7, Table 14) | 227 |
| Fig. 136: Roll dynamics LQGI simulation for initial conditions $(\theta_x, \theta_x) = (0, 0.02)$ rad, $(\omega_x, \omega_x) = (0, -0.1)$ rad/s, and $r_y = 0.00698$ rad, (parameters from Table 1, Table 6, Table 7, Table 14) | 228 |
| Fig. 137: Pitch dynamics LQGI simulation for initial conditions $(\theta_z, \theta_z) = (0, 0.01)$ rad, $(\omega_z, \omega_z) = (0, -0.7)$ rad/s, and $r_z = -0.00524$ rad, (parameters from Table 1, Table 6, Table 7, Table 14) | 230 |
| Fig. 138: Yaw dynamics LQGI simulation for initial conditions $(\theta_y, \theta_y) = (0, -0.05)$ rad, $(\omega_y, \omega_y) = (0, 0.05)$ rad/s, and $r_{\theta y} = 0.0349$ rad, (parameters from Table 1, Table 6, Table 7, Table 14) | 231 |
| Fig. 139: Comparison of height dynamics using simple Observer control and LQGI (parameters from Table 1, Table 6, Table 7, Table 14) | 232 |
| Fig. 140: Zoomed view of Observer vs. LQGI control of height system for (a) Observer, (b) LQGI | 233 |
| Fig. 141: Individual rotor rotational velocity during simulations from Fig. 135 to Fig. 138 | 234 |
| Fig. 142: Individual rotor torque and vertical force during simulations from Fig. 135 to Fig. 138 | 235 |
| Fig. 143: Generalized nonlinear system model incorporating regulator and Kalman estimator | 236 |
| Fig. 144: Probability distribution of time require to calculate SOVP damping and stiffness terms for 2 nd order LTI systems (rotor parameters from Table 1) using Intel E5620 running at 2.4GHz | 241 |
| Fig. 145: NQGI vs. LQGI height dynamic system simulation (parameters from Table 1, and Table 15) | 244 |
| Fig. 146: NQGI gain variation for height dynamic system (parameters from Table 1, and Table 15) | 244 |

| | |
|--|-----|
| Fig. 147: NQGI vs. LQGI roll dynamic system simulation (parameters from Table 1, and Table 15) | 246 |
| Fig. 148: NQGI gain variation for roll dynamic system (parameters from Table 1, and Table 15) | 246 |
| Fig. 149: NQGI vs. LQGI pitch dynamic system simulation (parameters from Table 1, and Table 15) | 248 |
| Fig. 150: NQGI gain variation for pitch dynamic system (parameters from Table 1, and Table 15) | 248 |
| Fig. 151: NQGI vs. LQGI yaw dynamic system simulation (parameters from Table 1, and Table 15) | 249 |
| Fig. 152: NQGI gain variation for yaw dynamic system (parameters from Table 1, and Table 15) | 250 |
| Fig. 153: Individual rotor rotational velocities for simulations from Fig. 145 - Fig. 152 | 252 |
| Fig. 154: Individual rotor torque and vertical force for simulations from Fig. 145 - Fig. 152 | 253 |
| Fig. 155: Simulation comparing height system stability for NQGI and LQGI system (parameters from Table 1, and Table 15, using cost weights from (5.259) - (5.262)) | 254 |
| Fig. 156: Gain variation between stable NQGI and unstable LQGI height systems (parameters from Table 1, and Table 15, using cost weights from (5.259) - (5.262)) | 255 |
| Fig. 157: An axial Halbach rotor, where r_i is the inner radius, r_o is the outer radius, d is the rotor thickness [71] | 258 |
| Fig. 158: Axial EDW FEA model (4 pole, 4 segment-per-pole) | 258 |
| Fig. 159: Axial EDW Cartesian coordinate axis definitions | 259 |
| Fig. 160: Prototype axial EDW FEA calculated field at $r = 50\text{mm}$ and $y = 10\text{mm}$ (rotor parameters from Table 16) | 260 |
| Fig. 161: Axial magnetic flux density simulation at a $r = 50\text{mm}$ when using (6.1) (rotor parameters from Table 16) | 263 |
| Fig. 162: 3-D axial magnetic flux density using equation (6.1) (rotor parameters from Table 16) | 263 |

| | |
|--|-----|
| Fig. 163: (a) Real y field using polar equation (6.1) and Table 16 at $r = 50\text{mm}$ (b) Real y field using Cartesian equation (6.7) and Table 16 at $r = 50\text{mm}$ (rotor parameters from Table 16) | 266 |
| Fig. 164: (a) Real y field using polar equation (6.1) and Table 16 at $z = 0\text{mm}$ (b) Real y field using Cartesian equation (6.7) and Table 16 at $z = 0\text{mm}$ (rotor parameters from Table 16) | 267 |
| Fig. 165: a) Real y field using polar equation (6.1) and Table 16 at $z = 30\text{mm}$ (b) Real y field using Cartesian equation (6.7) and Table 16 at $z = 30\text{mm}$ (rotor parameters from Table 16) | 267 |
| Fig. 166: Comparison of real and imaginary normal field from axial EDW rotor using (6.7) at $r = 50\text{mm}$ (rotor parameters from Table 16) | 268 |
| Fig. 167: Comparison of real and imaginary 3-D field using (6.7) (rotor parameters from Table 16) | 269 |
| Fig. 168: Field comparison at $r = 90\text{mm}$, airgap $y = 12\text{mm}$, for Li's rotor defined by Table 17 | 271 |
| Fig. 169: Field comparison at $r = 98\text{mm}$, airgap $y = 8\text{mm}$, for Li's rotor defined by Table 17, including a reconstructed JMAG field using only the fundamental of the FFT | 271 |
| Fig. 170: Field comparison at $r = 94\text{mm}$, airgap $y = 3\text{mm}$, for Li's rotor defined by Table 17, including a reconstructed JMAG field using only the fundamental of the FFT | 272 |
| Fig. 171: Field comparison at $r = 96\text{mm}$, airgap $y = 1\text{mm}$, for Li's rotor defined by Table 17, including a reconstructed JMAG field using only the fundamental of the FFT | 272 |
| Fig. 172: Field comparison at $r = 35\text{mm}$, airgap $y = 12\text{mm}$, for prototype rotor defined by Table 19 | 275 |
| Fig. 173: Field comparison at $r = 50\text{mm}$, airgap $y = 12\text{mm}$, for prototype rotor defined by Table 19 | 276 |
| Fig. 174: Field comparison at $r = 65\text{mm}$, airgap $y = 12\text{mm}$, for prototype rotor defined by Table 19 | 276 |
| Fig. 175: Field comparison at $r = 50\text{mm}$, airgap $y = 3\text{mm}$, for prototype rotor defined by Table 19, including a reconstructed JMAG field using only the fundamental of the FFT | 277 |

| | |
|--|-----|
| Fig. 176: Field comparison at $r = 50\text{mm}$, airgap $y = 1\text{mm}$, for prototype rotor defined by Table 19, including a reconstructed JMAG field using only the fundamental of the FFT | 277 |
| Fig. 177: Magnitude of M_y vs. angular position for 4 segment-per-pole rotor | 280 |
| Fig. 178: Magnitude of M_θ vs. angular position for 4 segment-per-pole rotor | 280 |
| Fig. 179: Field comparison at $r = 50\text{mm}$, airgap $y = 12\text{mm}$, for 4-segment prototype rotor defined by Table 21 | 284 |
| Fig. 180: Field comparison at $r = 65\text{mm}$, airgap $y = 3\text{mm}$, for 4-segment prototype rotor defined by Table 21, including a reconstructed FEA field using only the fundamental of the DFT | 284 |
| Fig. 181: Field comparison at $r = 35\text{mm}$, airgap $y = 1\text{mm}$, for 4-segment prototype rotor defined by Table 21, including a reconstructed FEA field using only the fundamental of the DFT | 285 |
| Fig. 182: Original y -axis source field from radial Halbach rotor used in SOVP model (rotor parameters from Table 1 and above) | 287 |
| Fig. 183: Axial Halbach source field for use in SOVP model (rotor parameters from Table 16) | 289 |
| Fig. 184: Comparison of vertical force results from analytic solution and FEA when ω_m varies and $v_y = v_x = 0$ | 291 |
| Fig. 185: Comparison of translational force results from analytic and FEA solution when ω_m varies and $v_y = v_x = 0$ | 292 |
| Fig. 186: Comparison of power loss results from analytic and FEA solution when ω_m varies and $v_y = v_x = 0$ | 292 |
| Fig. 187: Comparison of translationally induced lift force predicted by analytic and FEA models when v_x varies and $v_y = \omega_m = 0$ | 294 |
| Fig. 188: Comparison of translationally induced thrust force predicted by analytic and FEA models when v_x varies and $v_y = \omega_m = 0$ | 294 |
| Fig. 189: Comparison of translationally induced power loss predicted by analytic and FEA models when v_x varies and $v_y = \omega_m = 0$ | 295 |
| Fig. 190: Axial EDW at various stages of assembly (a) Bare rotor with assembly fixture bolted in place | 298 |
| Fig. 191: Experimental axial EDW rotating assembly | 299 |
| Fig. 192: Experimental axial EDW mounted to test bench | 300 |

| | |
|---|-----|
| Fig. 193: Prototype axial EDW field measurements at airgap = 5.7mm (parameters from Table 25) | 301 |
| Fig. 194: Comparison of simulated analytic field and experimental field when $y = 5.7\text{mm}$ and $r = 32.94\text{mm}$, (parameters from Table 25) | 301 |
| Fig. 195: Comparison of simulated analytic field and experimental field when $y = 5.7\text{mm}$ and $r = 50\text{mm}$, (parameters from Table 25) | 302 |
| Fig. 196: Comparison of simulated analytic field and experimental field when $y = 5.7\text{mm}$ and $r = 62.71\text{mm}$, (parameters from Table 25) | 303 |
| Fig. 197: Prototype axial EDW experimental torque results at airgap of $y = 14.7\text{mm}$ (parameters from Table 25) | 304 |
| Fig. 198: Prototype axial EDW experimental torque results at airgap of $y = 8.87\text{mm}$ (parameters from Table 25) | 305 |

LIST OF ABBREVIATIONS

| | |
|--------|---------------------------------------|
| BLDC | brushless DC |
| DOF | degrees of freedom |
| DP | dynamic programming |
| DFT | discrete Fourier transform |
| EDS | electrodynamic suspension |
| EDW | electrodynamic wheel |
| EMF | electromotive force |
| EMS | electromagnetic suspension |
| EWV | electrodynamic wheel vehicle |
| FEA | finite element analysis |
| FEM | finite element modeling |
| LQI | linear quadratic integral |
| LQG | linear quadratic Gaussian |
| LQGI | linear quadratic Gaussian integral |
| NQGI | nonlinear quadratic Gaussian integral |
| LQR | linear quadratic regulator |
| LSM | linear synchronous motor |
| Maglev | magnetic levitation |
| MPC | model predictive control |
| NeFeB | neodymium iron boron |
| NMPC | nonlinear model predictive control |
| QP | quadratic programming |

| | |
|------|----------------------------------|
| SC | superconducting |
| SOVP | second order vector potential |
| SQP | sequential quadratic programming |

LIST OF SYMBOLS

| | |
|--------------|--|
| x | position along the track's longitudinal axial (used to indicate forward/backward motion) |
| y | position along track's vertical axis |
| z | position along track's transverse axis (used to indicate sideways motion) |
| θ_x | roll angle \rightarrow rotational position about the x -axis |
| θ_y | yaw angle \rightarrow rotational position about the y -axis |
| θ_z | pitch angle \rightarrow rotational position about the z -axis |
| v_x | translational velocity |
| v_y | vertical (heave) velocity |
| v_z | transverse (strafe) velocity |
| v_r | surface velocity of radial rotor |
| ω_x | roll velocity |
| ω_y | yaw velocity |
| ω_z | pitch velocity |
| s | slip speed |
| t | time |
| \hat{x} | unit vector in x -axis |
| \hat{y} | unit vector in y -axis |
| \hat{z} | unit vector in z -axis |
| ω_m | mechanical rotational velocity |
| ω_e | electrical rotational velocity |
| \mathbf{F} | force vector |

| | |
|----------------|---|
| F_x | thrust force |
| F_y | lift force |
| F_z | lateral force |
| T_{em} | electromagnetic torque |
| P_{loss}/P_l | power loss |
| ϕ | magnetic scalar potential |
| μ_r | relative magnetic permeability |
| μ_o | permeability of free space $\rightarrow 4\pi \times 10^{-7}$ |
| ρ_m | magnetic charge density |
| σ | conductivity |
| B | magnetic flux density |
| B_{rem} | residual flux density |
| M | magnetization vector |
| M | magnetization magnitude |
| c_{fh} | fundamental magnetizing constant |
| U_m | energy from surface charge distribution and reflected field interaction |
| ρ_{ms} | Fourier components of charge density |
| S | density of power flow |
| r_i | rotor inner radius |
| r_o | rotor outer radius |
| w_r | rotor width |
| P | number of magnetic pole-pairs |
| $2l$ | length of vehicle (in x-direction) |

| | |
|------------------|--|
| $2w$ | width of vehicle (in z -direction) |
| m | mass of vehicle |
| r_g | circular track outer radius |
| w_g | circular track width |
| h | conductive surface (track) thickness |
| l_p | length of track |
| w_p | width of track |
| I_{xx} | rotational inertia about the x body axis |
| I_{yy} | rotational inertia about the y body axis |
| I_{zz} | rotational inertia about the z body axis |
| K_t | motor torque constant |
| δ | Dirac delta function |
| $\text{Re}\{ \}$ | real part of complex number |
| $\text{Im}\{ \}$ | imaginary part of complex number |
| K_T | controller (variable T denotes subtype/subsystem) gain |
| L_T | observer/estimator (variable T denotes subtype/subsystem) gain |
| $k_{a_1 a_2}$ | stiffness in a_1 axis with respect to motion in a_2 axis |
| $d_{a_1 a_2}$ | damping in a_1 axis with respect to motion in a_2 axis |
| c_f | general purpose scaling factor |

CHAPTER 1: INTRODUCTION AND LITERATURE REVIEW

This chapter serves to provide a review of relevant literature in magnetic levitation and magnetic levitation controls, as well as background knowledge pertaining to magnetic levitation and magnetic linear propulsion.

1.1 INTRODUCTION

Magnetic Levitation, or Maglev, is a mode of transportation whereby a vehicle is suspended above or below a track using the interaction of magnetic fields to achieve attraction and/or repulsion for both lift and thrust. This accomplishes reduced friction for the potential of increased efficiency, lower noise, vibration, and harshness (NVH). Maglev offers the potential for higher speeds than conventional rail and reduced wear and maintenance items due to a lack on contact between the vehicle and the track [8]. The primary disadvantages of maglev systems are their significantly higher initial capital cost and increased guideway complexity compared to conventional iron-rail systems. Despite drawbacks, it remains a candidate for future generations of environmentally conscious, low maintenance, reliable, fast, and safe mass transportation.

In section 1.2, different maglev suspension technologies are reviewed. In section 1.3, a review of electrodynamic suspension dynamic modeling techniques are discussed. Common controller designs and implementations are also covered in 1.3. Finally, in section 1.4, the main levitation technology explored by this dissertation, electrodynamic wheel maglev, is reviewed.

1.2 SUSPENSION TECHNOLOGIES

Electromagnetic Suspension (EMS) systems make use of a set of electromagnetic coils along the length of the vehicle which are attracted to a flat iron track and are actively controlled in order to maintain an airgap between the track and carriage. This concept is shown in Fig. 1.

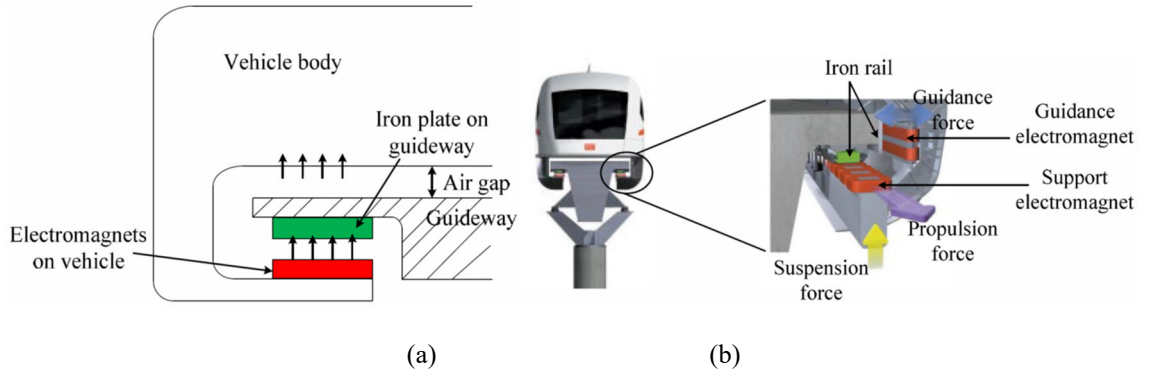


Fig. 1: (a) EMS maglev system uses magnetic attraction to provide lift (b) EMS system used on Transrapid train to provide lift, thrust, and guidance [8]

An inherent problem with EMS systems is that there is reduced lift performance at higher speeds when using a solid iron/steel guideway [17]. The inherent instability makes it difficult to maintain a precise and uniform airgap at higher speeds [55]. In addition, the cost and added complexity of using laminated steel for the entire length of the guideway must be considered when attempting to increase high speed performance.

Du and Ohsaki explored the effects of higher speeds on attractive levitation EMS systems that use solid steel guideways rather than laminations [17]. As the electromagnetic levitation coils travel over a solid iron guideway at higher speeds, eddy currents flow within

the iron which produce a magnetic field that disrupts low-speed model calculations. Du *et al.* also found that while the location of the eddy current peak does not change with velocity, the eddy current density does increase with velocity. This causes the distribution of airgap flux density to be distorted, with higher velocity leading to a smaller average airgap flux density, in turn causing reduced levitation force [17]. Therefore, for speeds above 200 km/h, a laminated track is required.

High speed EMS systems have been marketed and built (Transrapid), but are very expensive due to the cost of installing a linear synchronous motor in the guideway. In general, the cost of the guideway/track makes up the bulk of the initial expense [43].

While EMS uses attraction forces, Electrodynamic Suspension (EDS) systems utilize repulsive forces for levitation. Either superconducting or neodymium iron boron (NdFeB) magnets on a carriage induce currents in the conductive coils or conductive plates along the track as the vehicle travels. A model of the superconducting null-flux coil design proposed by Powell and Danby [23] and used by Post *et al.* is shown in Fig. 2 [10]. The translational motion of the superconducting vehicle coils relative to stationary guideway coils induces currents in the null-flux coils. This allows the coils' magnetic fields to levitate the vehicle as they interact with the superconducting coils on the carriage. Depending on configuration, some degrees of freedom, such as the lift axis, are inherently stable [55].

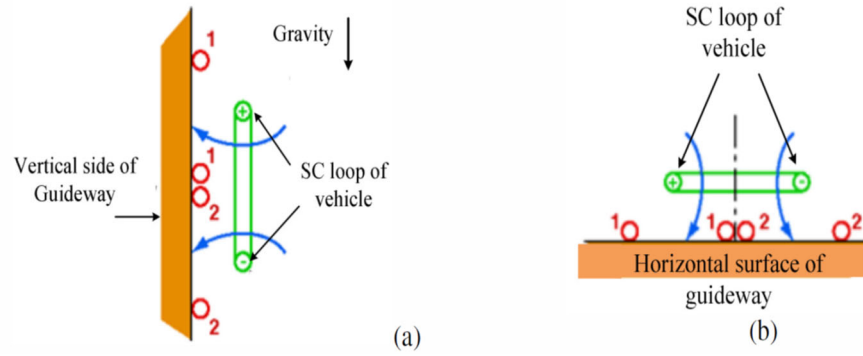


Fig. 2: (a) Superconducting (SC) Maglev uses a “Figure 8 Loop” on the side of the guideway for lateral stability and another “Figure 8 (null-flux) Loop” on the bottom of the guideway for levitation and vertical stability as it interacts with the superconducting magnets on the carriage. [10]

The superconducting null-flux type maglev system can operate with a large airgap and can operate with a relatively large lift-to-drag ratio during high speed operation [18], however it also suffers from high initial capital cost due to the guideway null-flux coils needed for lift and the linear synchronous motor (LSM) required for propulsion [20], as well as the cost of the superconducting magnets or coils.

An example of an EDS levitation setup that uses NdFeB magnets is shown in Fig. 3. This EDS system is called Inductrack. It uses a passive track for levitation and an LSM for propulsion, with the passive track being composed of either copper coils or sheets of aluminum and copper. The underside of the carriage has a Halbach array of magnets which induces eddy currents in the stationary guideway coils as the carriage moves over the track. As with the superconducting EDS system, the induced eddy currents in the passive track produce their own magnetic field which levitates the carriage. The Halbach array is a configuration of magnets which focuses virtually all of the magnetic field sinusoidally on one side thereby effectively eliminating the field from the opposite side.

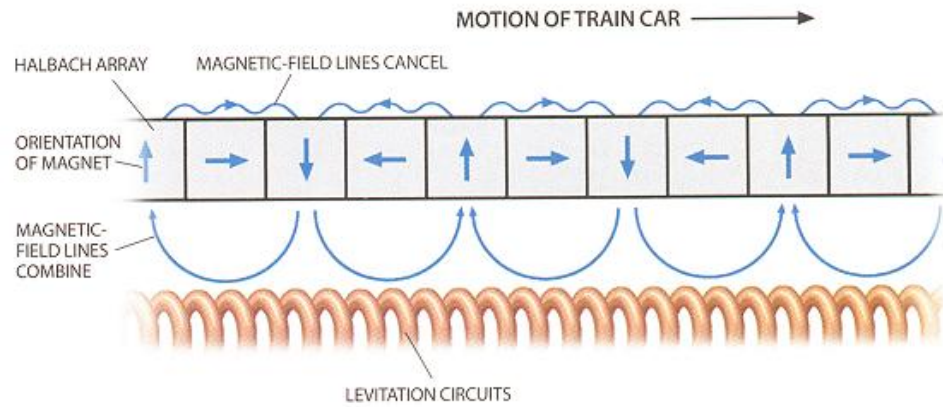


Fig. 3: Inductrack principle, showing Halbach arrays' interaction with passive copper coils [14]

Ideally, the Halbach array would consist of magnets whose field varies continuously along its length, as shown in Fig. 4. Practically, this is difficult to produce, so arrays are constructed according to Fig. 3 and Fig. 5. Han, *et al.*, used the non-ideal magnet array's harmonics and developed a strategy to optimize the arrays' geometry in order to maximize the square of the flux per unit weight of magnet material for use in a maglev system [39][40]. A layout of the magnets on a carriage is shown in Fig. 6. Unfortunately, despite the advantage of an inherently Lyapunov stable levitation geometries [15][65], a byproduct of lift is a drag force [17] that must be overcome with additional energy input from the linear motor which provides thrust. The relationship between lift and drag force was explored by Chen, Zhang, Bird, Paul, and Zhang when they derived a 3-D analytical solution of a null-flux electrodynamic system. This relationship is shown in Fig. 7.



Fig. 4: Ideal Halbach array magnet orientation [39]

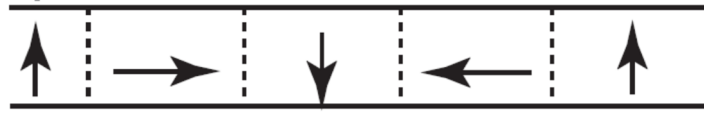


Fig. 5: Practical Halbach array magnet orientation [39]

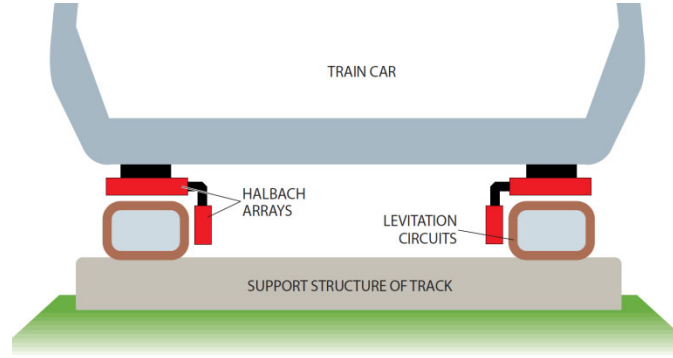


Fig. 6: Inductrack levitation model showing levitation and guidance arrays [14]

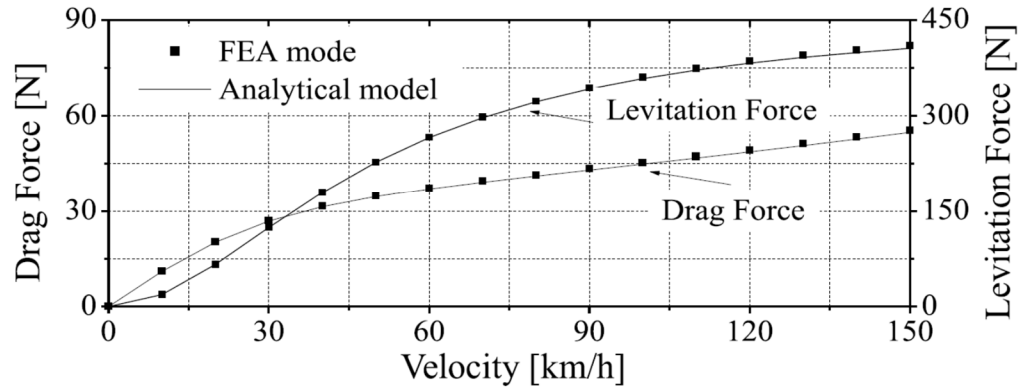


Fig. 7: Plot of levitation and drag forces for an EDS system using 3-D analytical solution [16][17]

Lee *et al.* made comparisons between EMS, EDS, and conventional iron wheel-on-rail systems [55]. According to Lee, some notable advantages of maglev over conventional

rail systems are better weight-load distribution on the guideway, leading to reduced construction costs, steeper achievable grades and smaller radius curves, faster acceleration and deceleration, reduced susceptibility to weather conditions, and elimination of gears, couplings, bearings etc. Conversely, due to increased power requirements to levitate more weight, freight duties may not be well suited to Maglev. Additionally, switching and branching of the train carriages introduces an extra level of complexity, as does the magnetic shielding required to prevent strong fields from entering the passenger compartment [55].

A newer maglev methodology which is still in a research and development phase is called electrodynamic wheel (EDW) maglev [21][22][24][30][31][34][35]. The EDW produces a lift force similar to EDS, whereby currents are induced in a conductive track to form an opposing magnetic field for levitation [21]. However, since magnets are wrapped around a rotor, the magnets are able to rotate above the surface of the track without the vehicle moving. In addition, while the vehicle is underway, the rotors can rotate so that the rotor surface velocity is greater than the train speed. Thus, the typical drag force associated with EDS can then be used instead as thrust. A radial EDW topology is shown in Fig. 8, and an axial topology, shown in Fig. 9, has also been studied by Fujii *et al.* [51][52][53], and is the source of levitation in the Arx Pax Hendo hoverboard [44]. The axial topology, while being able to produce lift with no translational speed, cannot be used for thrust if the rotor's axis is orthogonal to the track.

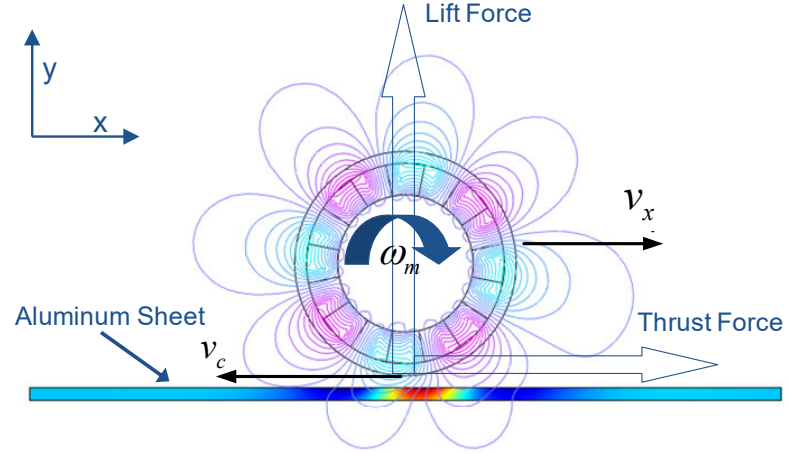


Fig. 8: Finite element model of single radial electrodynamic wheel, where v_x is the translational velocity of the EDW and v_r is the surface velocity of the wheel with respect the track [30]

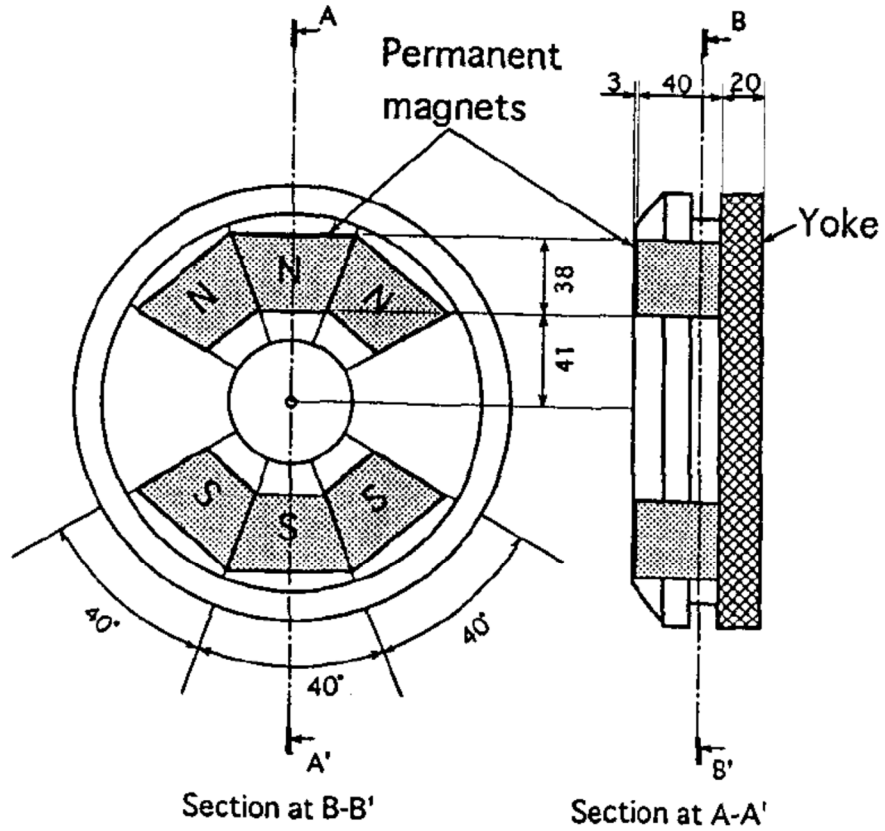


Fig. 9: Axial EDW topology used by Fujii *et al.* [53]

1.3 ELECTRODYNAMIC SUSPENSION MODELING

The dynamic motion of mechanical devices subjected to 3-D eddy current forces can be difficult to model, particularly when there is more than one mechanical degree of freedom. Experimental pendulum-type eddy current setups have been shown to be particularly useful when trying to understand the complex electromechanical dynamic interactions associated with eddy current forces with a varying airgap. Yamada studied eddy current dynamics by utilizing an experimental pendulum setup comprising of a magnet array supported by a string that was free to oscillate next to an aluminum sheet guideway wheel [25]. Moon, Chen and Zhu studied eddy current damping by affixing magnets to cantilever beams and then measuring the resultant oscillations when a rotating aluminum sheet wheel was placed below the magnets [26][27][28][38]. Although these experimental models were extremely useful for understanding damping and stiffness characteristics (the change of force with respect to position and velocity, respectively), the authors did not accurately compare the dynamic experimental results with calculations.

Davey [12], Post [8][10], and Boeij [13][14][15] used coupled lumped parameter circuit modeling techniques to model the voltage and currents in an EDS maglev vehicle system that used a track consisting of conductive wires. They used the models to arrive at a set of algebraic equations that model the forces without using finite element model (FEM) methods, which are compute-intensive. Since no numerical solution is required, these equations can be used in real-time control of an EDS system [14][15].

Davey describes the core principle of maglev suspension used by the Japanese superconducting maglev systems at Yamanashi [12]. The electromagnetic coil designs are shown in Fig. 2 and Fig. 10.

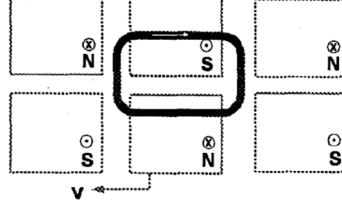


Fig. 10: Levitation coils described by Davey [12]

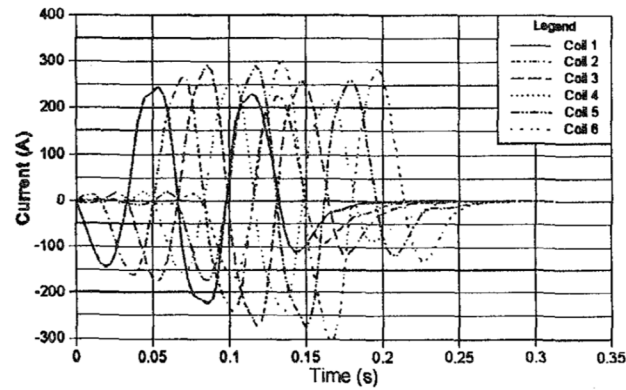
The voltages and currents induced in the coils can be approximately modelled by representing the magnets using equivalent surface currents [42]. The lift force can be calculated based on the derivative of the co-energy of the coil system:

$$\mathbf{F}^a = \sum_{k=1}^m \sum_{j=1}^n \mathbf{I}_j^a \mathbf{I}_k^a \nabla \mathbf{M}_{kj}^a \quad (1.1)$$

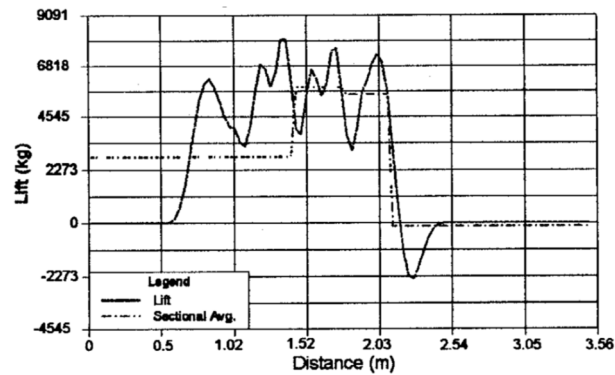
where bold signifies a matrix, such that \mathbf{M}_{kj}^a is m coils by n magnets matrix of the mutual coupling of the j^{th} magnet to the k^{th} coil, \mathbf{I}_j^a is the surface current of the j^{th} magnet, and \mathbf{I}_k^a is the k^{th} coil current. Note that the “a” superscript is used to signify variables that apply only to this equation, so that other definitions of F , I , and M can be used later.

This lumped parameter approach neglects the skin effect. Using this type of lumped parameter equivalent circuit based approach cannot be used when using conductive sheets [12]. Equivalent magnetic circuit models are also frequently used to roughly model the forces in a maglev system, but these methods yield only an approximation and often lead

to poor matchup between FEA, analytical models, and experimental models [48]. A simulation example by Davey showing the lift mass and currents generated when 6 coils move over the a set of magnets is shown in Fig. 11.



(a)



(b)

Fig. 11: Davey's simulation results using Runge Kutta technique for EDS system [10] (a) Coil Current (b) Lift mass [12]

Post and Ryutov also describe the Inductrack EDS system dynamics using a very basic lumped parameter circuit theory approach [10]. The null-flux coil system used by J. de Boeij, *et al.* [13], is shown in Fig. 12.

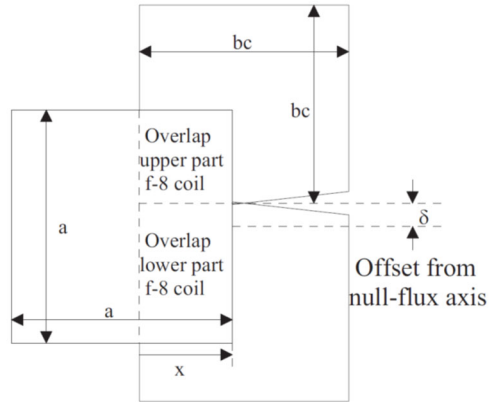


Fig. 12: Layout of magnet passing over null-flux coil [13]

The flux linking the upper and lower portion of the figure-8 coil (null flux coil), can be defined as the area that the magnet and coil overlap multiplied by a constant magnetic field density. Then, by subtracting the flux linking the lower portion of the coil from the flux linking the upper portion of the coil, the net flux linking the coil can be calculated [13]-[15]. A sketch of the experimental setup used by De Boeij to validate his model is shown in Fig. 13.

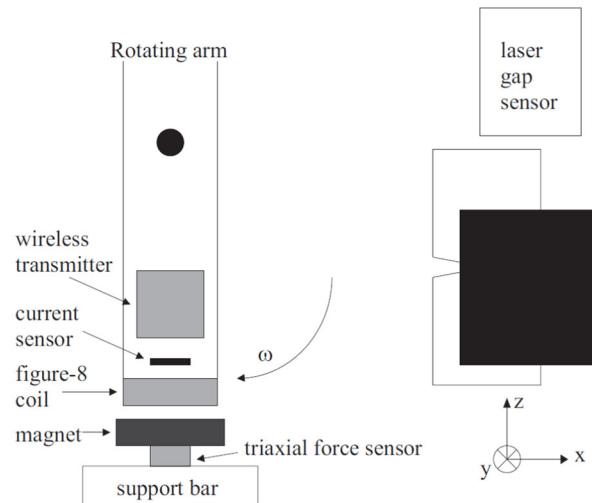


Fig. 13: De Boeij null-flux coil experimental setup sketch [13]

Results of the forces modeled by de Boeij, *et al.*, are shown in Fig. 14, showing that the analytical techniques roughly match the experimental results.

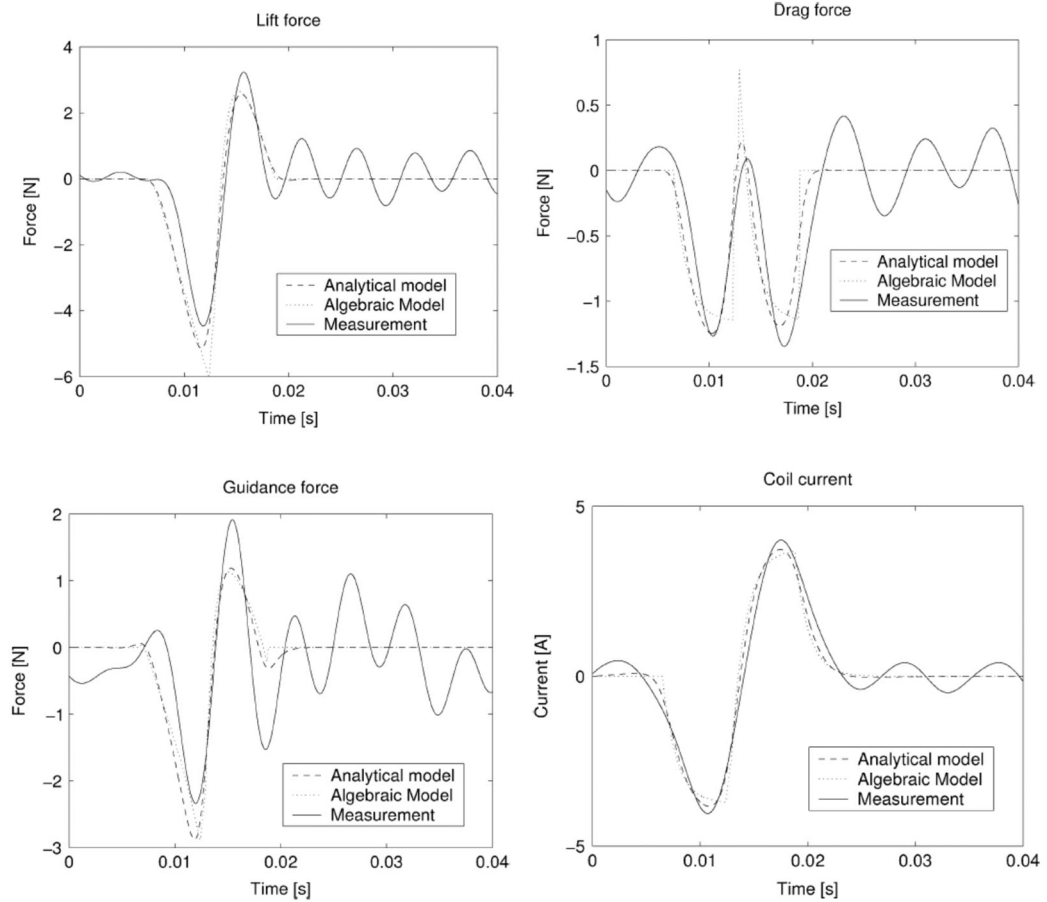


Fig. 14: De Boeij experimental results compared to models [15]

Dumont *et al.* showed another use for maglev technology in a new type of electrodynamic contactless centering bearing based on interactions between a short circuited winding in which currents are induced, and permanent magnets which are used to generate excitation, similar in principle to EDS maglev vehicle levitation [19]. The general construction of such a bearing is shown in Fig. 15. When the rotor is centered, the

magnetic field has no homopolar component and there is no electromotive force (EMF). However, an induced EMF is produced when the rotor is off-center because a time-dependent magnetic flux is being intercepted by the rotor. This creates a centering Lorentz force between the permanent magnet field and the winding. Through analysis of the magnetic flux, Dumont devised a set of guidelines for designing a null-flux electrodynamic bearing [19].

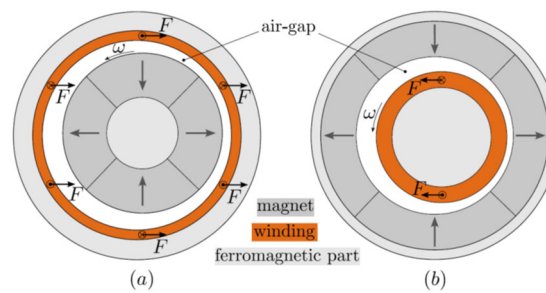


Fig. 15: Diagram of EDS bearings and forces (a) EDS bearing with internal rotor (b) EDS bearing with external rotor [19]

Borowy and Kang studied the General Atomics Urban Maglev design to come up with a system model using the system identification technique [41]. They used an iterative process using experimental data to arrive at a linear discrete time-invariant system for a six degree-of-freedom maglev system. Their method to formulate and validate the model is shown in Fig. 16.

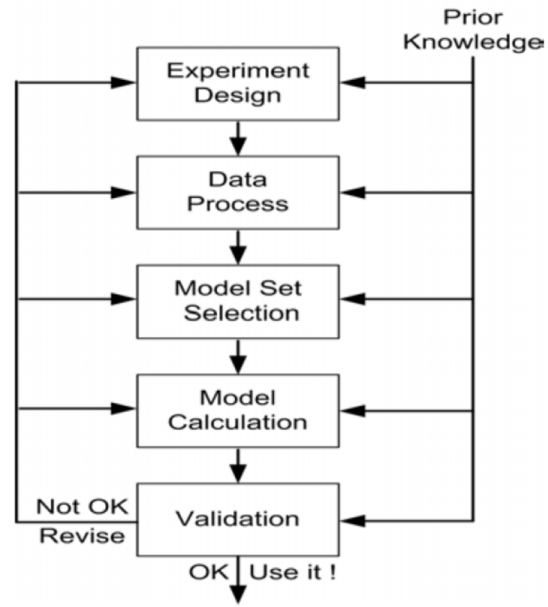


Fig. 16: System identification technique used to identify General Atomics Urban Maglev System [41]

1.3.1 DYNAMIC CONTROL OF MAGLEV SYSTEMS

In this section, a sampling of different control methodologies commonly used for maglev are discussed. These concepts will be built upon in later chapters to develop more advanced controllers for a 4 rotor EDW maglev vehicle.

Beltran-Carbajal *et al.* showed that a simplified 1 degree of freedom EMS maglev system could be adequately controlled using feedback control to track a reference signal [62]. This was based on the fact that the system exhibited the principle of differential flatness, so that a set of independent outputs completely parameterizes every state variable and control input [61]. The model used by Beltran-Carbajal is shown in Fig. 17, and a resulting simulation of the control technique is shown in Fig. 18.

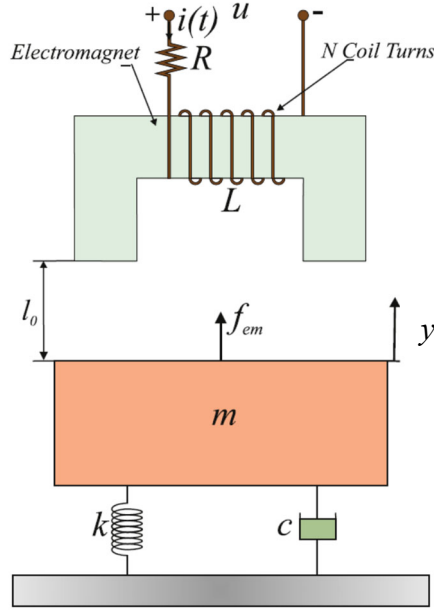


Fig. 17: Single degree-of-freedom maglev model, where i is coil current, R is coil resistance, L is coil inductance, m is the sprung mass, k is the spring constant, c is the damper constant, l_0 is the airgap, y is vertical displacement (for this example only), and f_{em} is the levitation force [62]

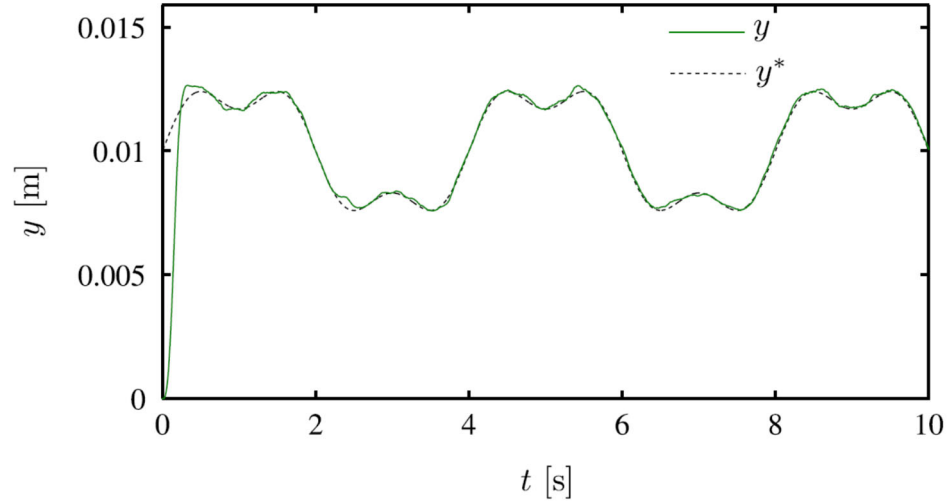


Fig. 18: Tracking of reference trajectory, y^* , with noise contamination and actuator saturation for Beltran-Carbajal's model and feedback controller [62]

Pradhan *et al.* and El Hajjaji *et al.* used an input-output feedback linearization approach to stabilize a ferrous ball suspended below an actively controlled coil [64][72]. Feedback linearization is an approach that uses a change of variables and special control input to transform a nonlinear system into linear system. This can be accomplished when the system is well understood and modeled [63]. A block diagram of feedback linearization system is shown in Fig. 19. El Hajjaji makes an important note that while maglev systems are highly nonlinear, most researchers tend to use linear techniques and/or linear approximations that are only accurate within a small operating region [64].

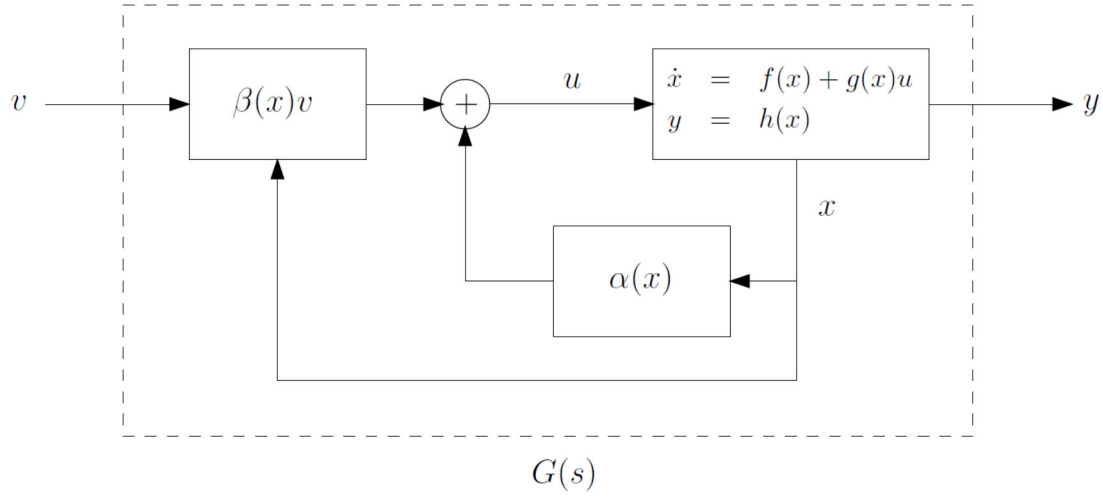


Fig. 19: Block diagram for feedback linearization, where the nonlinear model is described by \dot{x} , f is a function describing the system response to the states, g is a function describing the plant response to the input, the output is described by y , which is a function, h , of the states, u is the plant input, α is the plant feedback, v is the system input, and β is the input transformation function [81]

A comparison between classical proportional integral differential (PID) control and feedback linearization, denoted by “NLC” (nonlinear control), is shown in Fig. 20. The poor tracking and steady-state error of the PID control technique highlight the drawback of requiring a linear model that accurately describes a nonlinear system, which is not always possible, while feedback linearization proved to be more robust for this simulation [72].

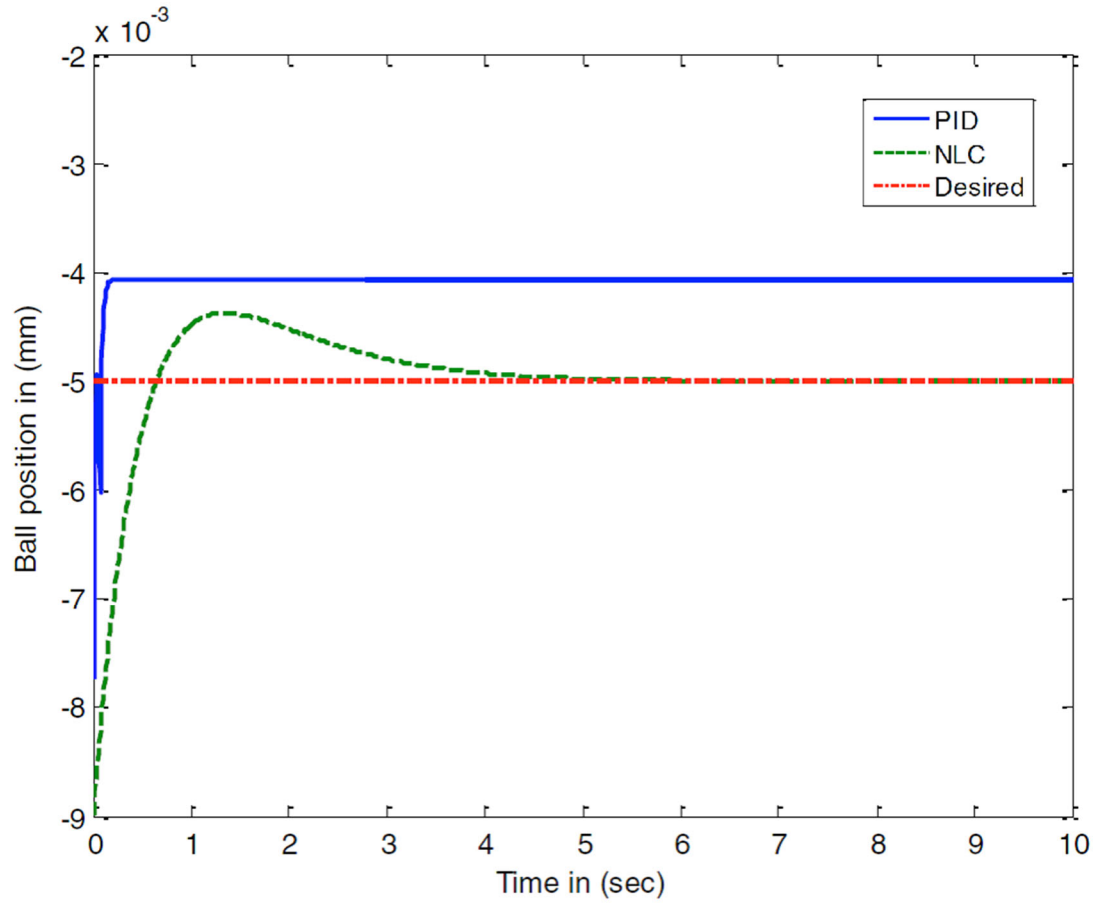


Fig. 20: Pradhan's comparison between feedback linearization control (NLC), and PID control [72]

Songqi *et al.* used an adaptive model reference control method for controlling an EMS system [18]. A model reference controller uses the output of a reference model designed to meet performance requirements to drive an error signal that is passed to the controller, as shown in Fig. 21. The controller is designed to stabilize the EMS system when the track has varying height according to the model in Fig. 22.

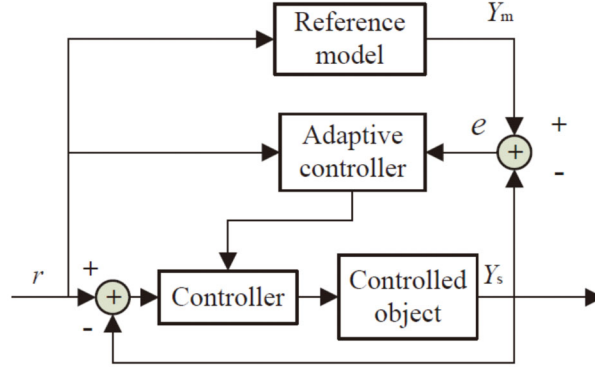


Fig. 21: Model reference controller, where Y_m is the reference model output, Y_s is the plant output, e is the error signal, and r is the input [18]

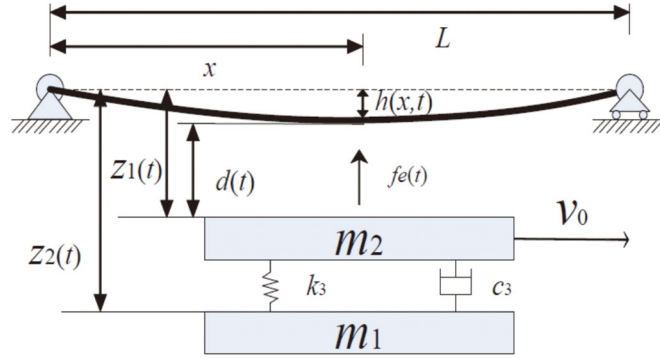


Fig. 22: Vehicle-track model [18], $f_e(t)$ is the electromagnetic force, m_1 and m_2 are the masses of the vehicle carriage and electromagnets, respectively, k_3 is the secondary suspension stiffness, c_3 is the secondary suspension damping, x is the vehicle lateral displacement, L is the tracks' lateral length, $z_1(t)$ is the distance from the reference frame to the vehicle's suspension, $z_2(t)$ is the distance from the reference frame to the vehicle body, $d(t)$ is the airgap, and $h(x,t)$ is the vertical displacement of the track.

Without being able to measure the time and displacement dependent term $h(x,t)$ directly, it has the effect of an external disturbance on the vehicle. An adaptive controller using both feedforward and feedback was used to obtain stable dynamics when the track was vibrated. This is shown in Fig. 23.

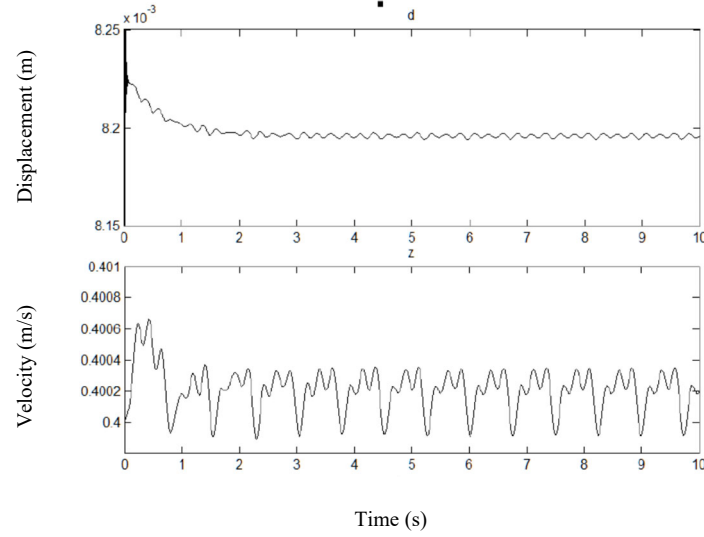


Fig. 23: Songqi's simulation results showing vehicle displacement at a constant speed of v_0 [18]

De Boeij *et al.* used a lumped parameter force model to create a state-space model of an EDS sled on a passive track, and applied sliding mode feedback control to the system [15], in which a discontinuous control signal causes the system to move towards the desired state until the state is passed, at which point the control signal switches to return the system back towards the desired state. This type of control is characterized by feedback control laws and a decision rule, implemented as a switching function [60]. While the dynamic behavior of the system can be directly tailored by the switching function for desired performance, the switching frequency must necessarily be infinite to achieve uncertainty rejection [60]. Fig. 24 and Fig. 25 show the system layout used by De Boeij with 6 magnets and 10 coils.

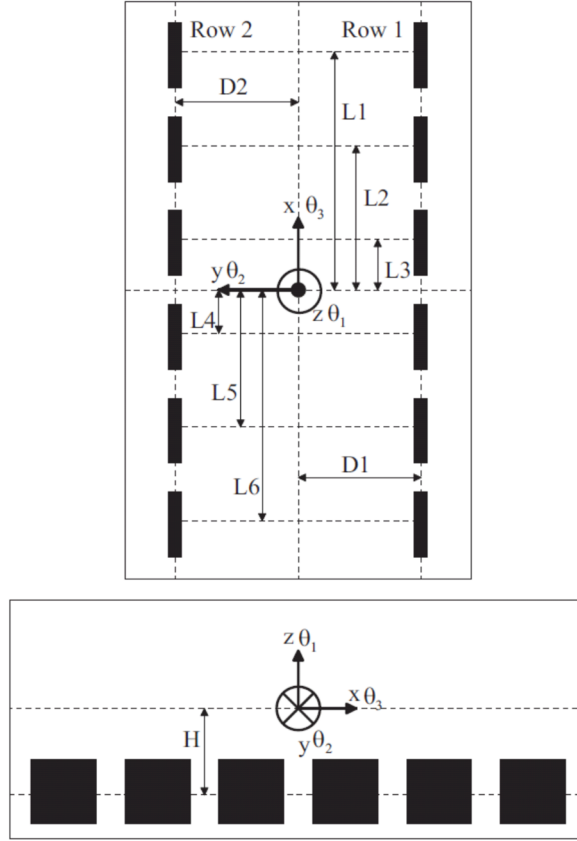


Fig. 24: Dimensional definitions for De Boeij's 5-DOF system, where solid black squares represent permanent magnets [14]

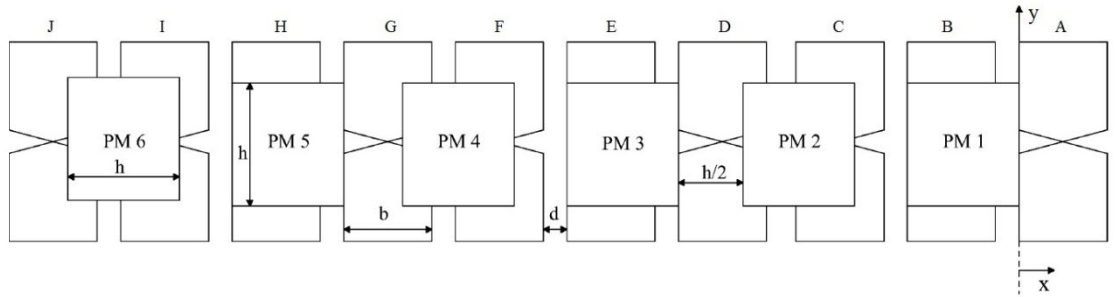


Fig. 25: Six magnet and ten coil EDS system, where z -axis is through the page and y -axis is perpendicular to x -axis parallel to page [14]

The first order sliding mode controller successfully tracks all three degrees of freedom and guarantees global asymptotic stability. Simulation results are shown in Fig. 26 [15].

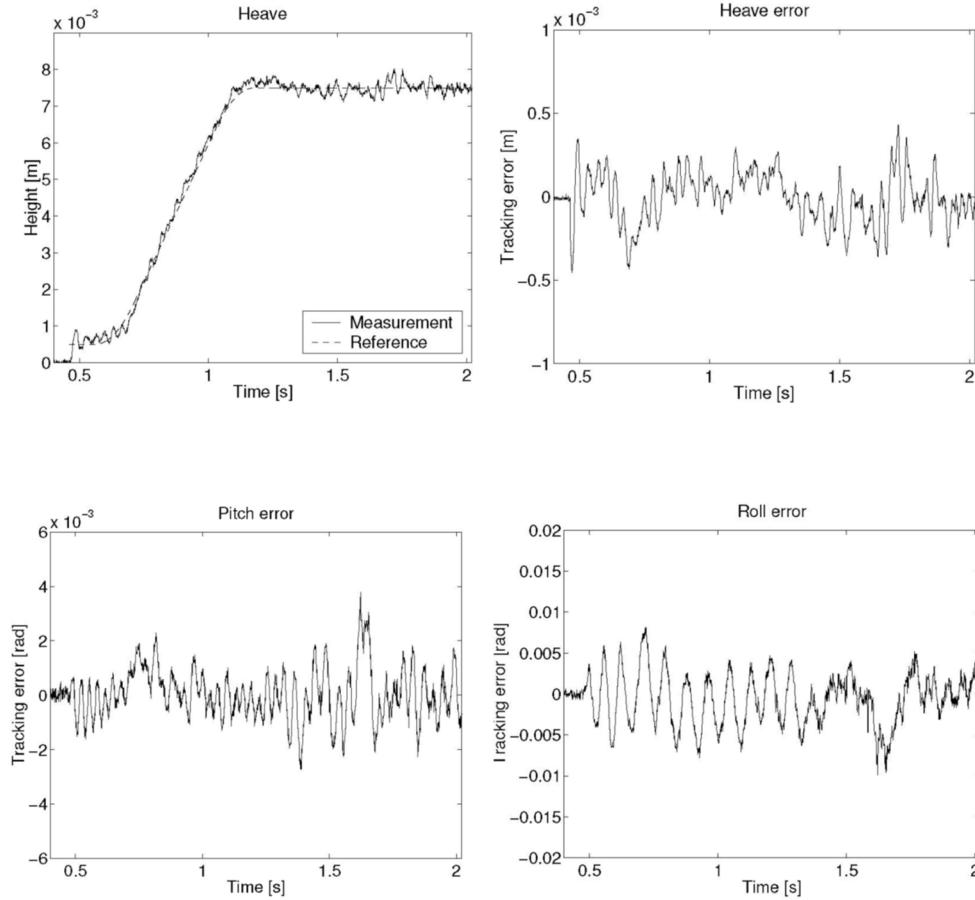


Fig. 26: De Boeij's sliding mode controller performance results [15]

Model predictive control (MPC) works on the basis of applying an optimal control trajectory for a finite receding horizon in discrete-time. MPC allows the use of various optimal control techniques on linear and non-linear systems, while also enforcing constraints, or a set of maximum and minimum allowable values for the control and state variables of a system. At each time step, the optimal control sequence is computed, then the first step of the control trajectory is implemented. This process is repeated at each time step, thereby achieving closed loop behavior [56].

If the model is linear, the cost is described by a quadratic function, and there are no constraints, then a simpler approach such as a linear quadratic regulator (LQR) as described by Kirk is appropriate [58]. If the dynamics are linear, the cost is quadratic, and the system must operate within an affine constraint set, then linear MPC (LMPC) using quadratic programming (QP) to calculate the optimal control trajectory is appropriate. QP problems can be solved using a variety of methods including interior point methods, active set methods, and the simplex algorithm, covered in detail by Papalambros *et al.* [57].

For more complex problems involving nonlinear model dynamics, a non-quadratic cost function, and/or nonlinear constraints, nonlinear MPC (NMPC) is suitable [56]. The control sequence for NMPC is often calculated using either sequential quadratic programming (SQP) or dynamic programming (DP). SQP is a generalization of Newton's method that divides the problem into QP sub-problems where the quadratic model of the problem is minimized for each step. SQP is robust and can be used for a large variety of problems, but only guarantees optimal trajectory to a local minimum or maximum [57]. Dynamic programming (DP) can guarantee convergence to a global minimum/maximum, but requires quantization of all of the states and control variables, leading to the potential for quantization errors. DP relies on calculating all of the stage costs of going from each state to the next, and calculating the minimum of the sum of the stage costs for each sequence, according to Bellman's principle of optimality [58].

Similar to El Hajjaji, Bächle *et al.* claims that linear approximations and control strategies are only suitable for small operating regions for electromagnetic levitation

systems [66]. Conversely, while MPC is well suited for maglev control, it is often too slow to be used for on-line applications unless approximations are made to reduce computational load. Bächle used a gradient descent method to obtain the optimal input [66]. A polynomial fit of 3 gradient iteration points is used to approximate the solution of step size, significantly speeding up the MPC algorithm. It was shown that linear MPC could lead to poor performance and instability, while non-linear MPC using the step size approximation converged towards the desired set-point [66]. A simulation of the controller performance is shown in Fig. 27.

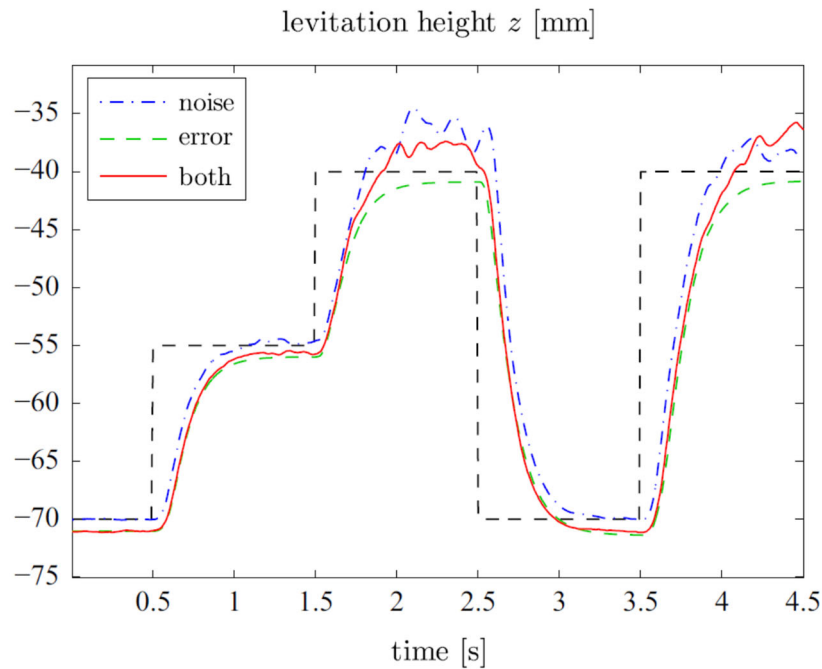


Fig. 27: Bächle's Nonlinear MPC transition simulation under the effect of model error and measurement noise [66]

Periyasamy *et al.* developed an MPC model for a 1-DOF maglev system using a neural network to develop a plant model and a particle storm optimization for calculate the optimal trajectory [67]. The plant and neural plant model were fed identical inputs and the

difference between the two models' outputs is analyzed by a learning algorithm to adjust the weights of the network. The particle swarm optimization iteratively moved candidate solution "particles" within the search-space to find the best solution. Rather than using the gradient, the particles moved according to their own best known position and the other particles' (swarm's) best known position, thereby providing the advantage of not requiring the optimization problem to be differentiable.

Qin *et al.*, claimed that capturing the non-linearities of a maglev system is an obstacle, and used a State-dependent AutoRegressive with eXogenous input (SD-ARX) model to represent the dynamic behavior between coil current and the position of a levitated ferrous ball [68]. The coefficients of the model were approximated by a Gaussian radial basis function (RBF) neural network to further refine the behavior [68]. The plant model could therefore be generated without relying on a physical or electrodynamic model. A comparison of PID and MPC control for the model is shown in Fig. 28.

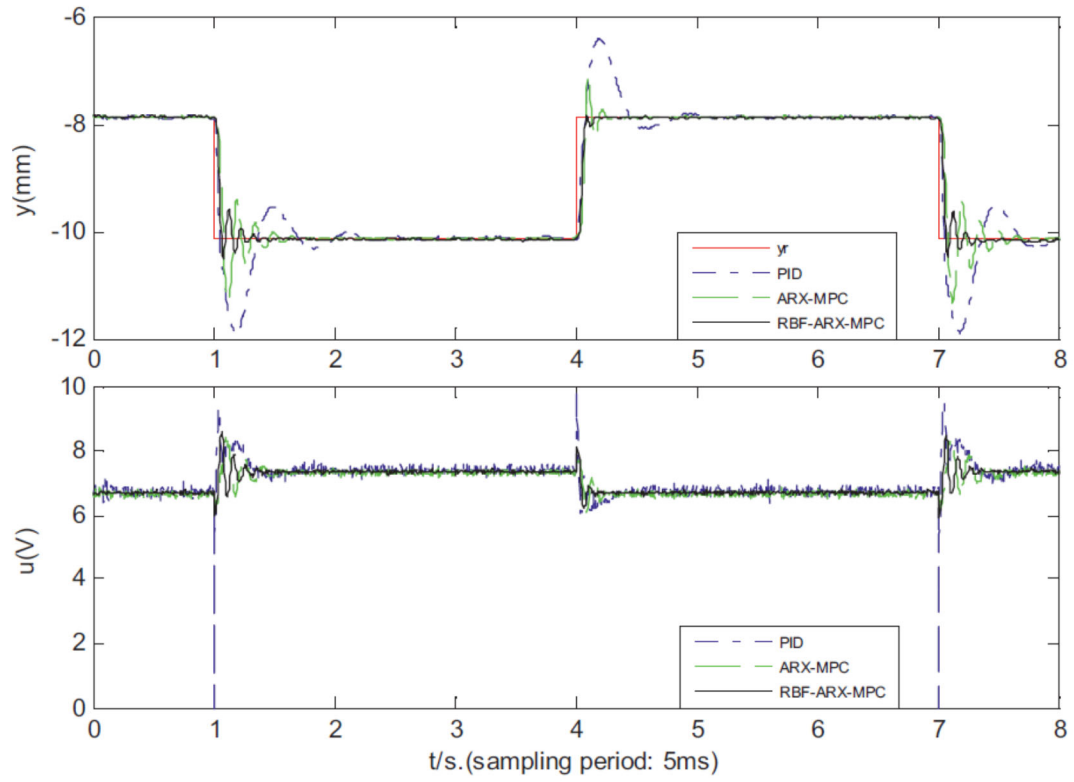


Fig. 28: Qin's comparison between a PID controller, MPC using the ARX model, and MPC using the RBF-ARX model, for a 2.2mm jump command [68]

1.3.2 INDUCTRACK DYNAMICS AND CONTROL

Kim, *et al.* studied the dynamics of the Inductrack proof-of-concept vehicle studied at Lawrence Livermore National Laboratory [45]. They first used a lumped parameter approach to numerically simulate only the lift force, then expanded the system to include 2-DOF, height and longitudinal position, and finally a 4-DOF system which included lateral motion and roll [45]. A cross section of the vehicle is shown in Fig. 29.

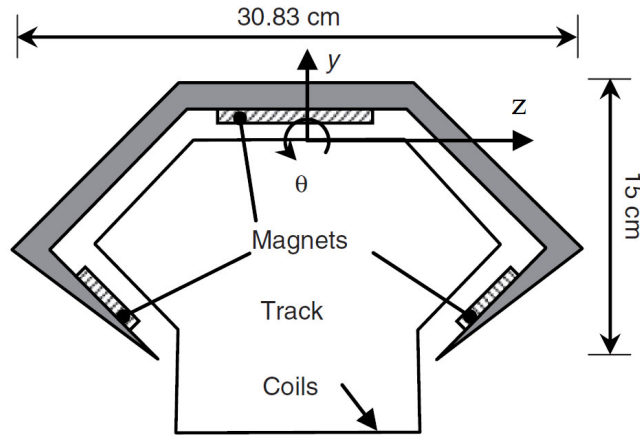


Fig. 29: Cross-section of maglev carriage studied at Lawrence Livermore National Laboratory, where y is the vertical vehicle displacement, z is the lateral vehicle displacement, x is the vehicle's longitudinal position on the track, and θ is the vehicle roll angle about the x -axis [45]

Sepe, *et al.*, taking into account the General Atomics current control architecture, developed a novel position sensing approach which does not use mechanical or optical measuring devices. The method is similar to existing quadrature based approaches, but uses a dual-phase demodulator and mechanical observer to determine speed [46].

Gurol, *et al.*, described the status of the General Atomics Urban Maglev prototype vehicle with 120m of track and a 25mm airgap [47], as shown in Fig. 30.



Fig. 30: General Atomics full scale maglev test track [47]

Ko, *et al.* developed a set of dynamic equations that describe an Inductrack vehicle and a controller for the vehicle [11][37]. We will go into some detail since the linearization and modelling concepts will be useful in other sections of this document. A simulation showing the field from a Halbach array is shown in Fig. 31.

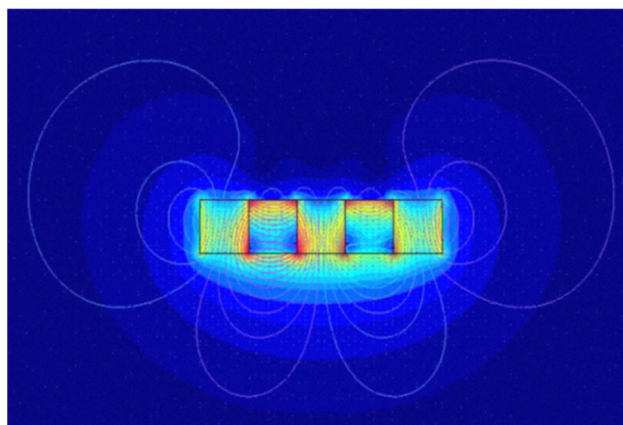


Fig. 31: Simulation showing Halbach array's magnetic field [9]

The force equations that were derived by Post and Ryutov were expanded in a Taylor series to account for small perturbations in displacement variables [10]:

$$F_y(y) = F_y(y_o) + \left. \frac{\partial F_y}{\partial y} \right|_{y=y_o} (y - y_o) \quad (1.2)$$

where

$$F_y(y_o) = m^i g \quad (1.3)$$

is an equilibrium point, $F_y(y)$ is the force in the y direction (lift), m^i is the mass of the vehicle, and g is the acceleration due to Earth's gravitational field, and y is the airgap between the vehicle and the track. Note that the i superscript in the equations in this section are used simply to differentiate this set of equations from those from other sections.

Ko linearized (1.2) to arrive at [11]:

$$F(y) = F(y_o)(1 - 2k^i \delta y) \quad (1.4)$$

where δy is the change in y position,

$$\delta y = y - y_o \quad (1.5)$$

and

$$k^i = 2\pi / \lambda^i \quad (1.6)$$

where λ^i is the geometric wavelength of the Halbach array, shown in Fig. 32.

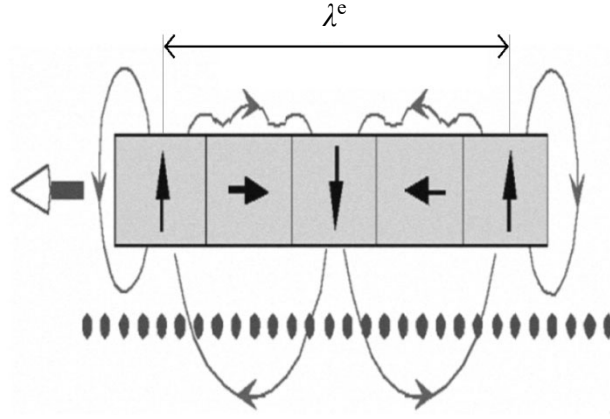


Fig. 32: Definition of Halbach geometry wavelength, λ_e

From the 2nd law of motion:

$$m^i \delta \ddot{y} = -F(y_0) 2k^i \delta y \quad (1.7)$$

Substituting (1.3) into (1.7) gives:

$$m^i \delta \ddot{y} = -m^i g 2k^i \delta y \quad (1.8)$$

A similar process was applied to the lateral dynamics [11]. The forces for a set of Halbach arrays (both levitation and guidance arrays) are summed in the body reference frame to arrive at a set of equations for the forces and moments in 5-DOF. The simplified vehicle dynamics are described by:

$$\mathbf{M}_{RB} \ddot{\mathbf{a}}_0^i = \overline{\boldsymbol{\tau}}_{RB} \quad (1.9)$$

where,

$$\mathbf{M}_{RB} = \begin{bmatrix} m^i & 0 & 0 & 0 & 0 \\ 0 & m^i & 0 & 0 & 0 \\ 0 & 0 & I_{xx}^i & 0 & 0 \\ 0 & 0 & 0 & I_{yy}^i & 0 \\ 0 & 0 & 0 & 0 & I_{zz}^i \end{bmatrix} \quad (1.10)$$

$$\mathbf{a}_0^i = [\delta z \quad \delta y \quad \theta_x \quad \theta_y \quad \theta_z]^T \quad (1.11)$$

$$\bar{\tau}_{RB} = \begin{bmatrix} F_z & F_y & M_K & M_M & M_N \end{bmatrix}^T \quad (1.12)$$

Note that δy is the vehicle displacement from equilibrium in the levitation direction and δz is the vehicle displacement from equilibrium in the lateral direction, F_y is the force in the y direction, F_z is the force in the z direction, I_{xx} , I_{yy} , and I_{zz} are the moment of inertia in the x , y , and z axes, respectively, and M_K , M_M , M_N are the moments in the x , y , and z axes, respectively.

With this system, two control methodologies were explored by Ko *et al.* [11]. The first is simple damping control whereby the Lagrange multiplier optimization method was used to solve for a set of damping control factors. Improved stability and performance were observed using damping control, but further improvement was made using a Linear Quadratic Regulator (LQR) controller. Note the general form for a state space system:

$$\dot{\mathbf{x}} = \mathbf{A}\mathbf{x} + \mathbf{B}\mathbf{u} \quad (1.13)$$

$$\mathbf{y} = \mathbf{C}\mathbf{x} + \mathbf{D}\mathbf{u} \quad (1.14)$$

As to not confuse this system with later systems, unique notation is given:

$$\dot{\mathbf{x}}^i = \mathbf{A}^i \mathbf{x}^i + \mathbf{B}^i \mathbf{u}^i \quad (1.15)$$

and a performance index defined by [9]:

$$J^i = \int_0^\infty (\mathbf{x}^i \mathbf{Q}^i \mathbf{x}^i + \mathbf{u}^i \mathbf{R}^i \mathbf{u}^i) dt \quad (1.16)$$

where $\bar{\mathbf{x}}^i$ represents the systems' states, $\bar{\mathbf{u}}^i$ represents the input, \mathbf{A}^i is the system matrix, \mathbf{B}^i is the input matrix, \mathbf{Q}^i is the cost weighting matrix, \mathbf{R}^i is a positive scalar that weights the inputs. When the time horizon is infinite, the control input can obey a simple feedback law with a constant gain matrix [58], \mathbf{K}^i , so that the control input vector is:

$$\mathbf{u}^i(t) = -\mathbf{K}^i \mathbf{x}^i(t) \quad (1.17)$$

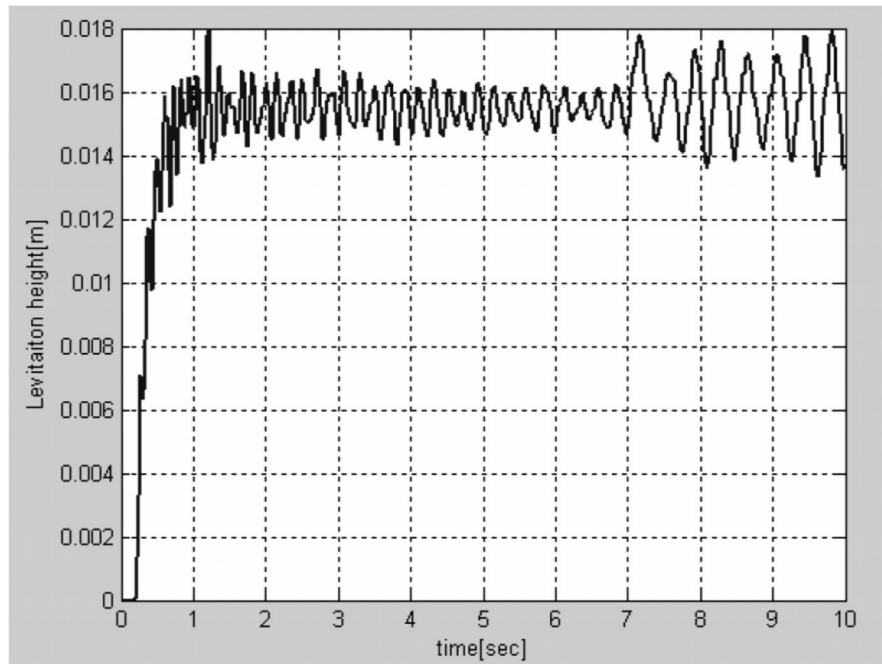
Solving for the positive definite solution, $\mathbf{P}_i = \mathbf{P}_i^T$, of the algebraic Riccati equation [9]:

$$\mathbf{A}^i \mathbf{P}_i + \mathbf{P}_i \mathbf{A}^i - \mathbf{P}_i \mathbf{B}^i \mathbf{P}_i^{-1} \mathbf{B}^i \mathbf{P}_i + \mathbf{Q}^i = 0 \quad (1.18)$$

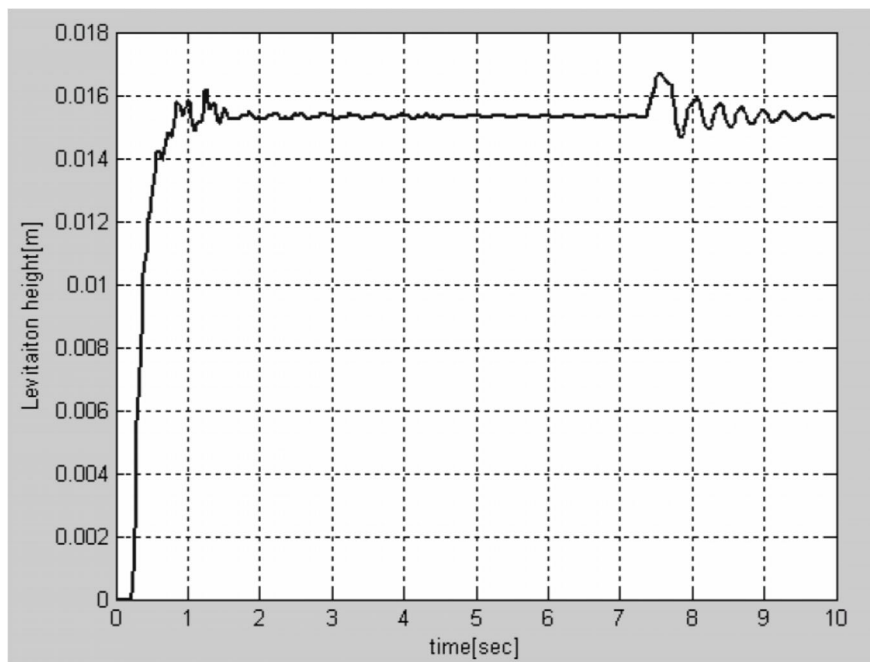
The control gains can then be found:

$$\mathbf{K}^i = (\mathbf{R}^i)^{-1} \mathbf{B}^i \mathbf{P}_i \quad (1.19)$$

The LQR controlled system used by Ko showed better tracking and disturbance rejection than open loop, as shown in Fig. 33.



(a)



(b)

Fig. 33: Ko's results: (a) Uncontrolled vehicle height vs time (b) LQR controlled vehicle height vs. time [11]

1.4 ELECTRODYNAMIC WHEEL

Another methodology of EDS is using electrodynamic wheels (EDW), as proposed by Bird *et. al* [21] and much earlier by Davis *et. al* [29]. An EDW can be thought of as a linear Halbach array that has been wrapped around into a circular shape to form a rotor, allowing the axially or radially oriented magnets to be mechanically rotated above a conductive track, as in Fig. 34. The induced currents in the track can then be used to provide simultaneous lift and thrust [21][22]. This provides many advantages, including the ability to generate lift force at zero translational velocity, therefore not necessitating low-speed mechanical drive systems, as well as eliminating and repurposing the drag forces associated with lift generation on a traditional EDS system. The cost of an EDW system could be low as the track can be a passive conductive sheet. However, an EDW maglev vehicle will need to have an on-board power source or power will need to be transferred to the vehicle.

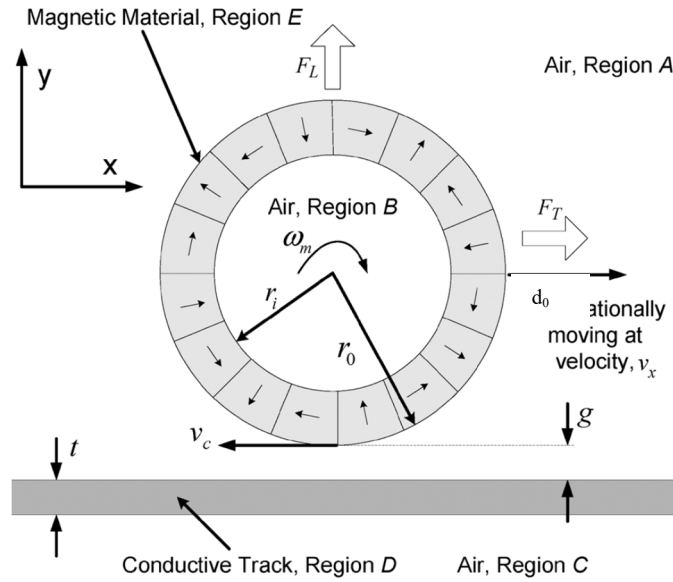


Fig. 34: Drawing of Halbach rotor [21]

Bird used FEA to compute the optimal ratio of rotor inner to outer radii that maximizes the lift to weight ratio for a Halbach rotor. For a 4 pole-pair rotor, this was calculated to be 0.68 [21]. This value was then confirmed using a 2D steady-state current sheet model [22].

The lift and thrust forces from an EDW are derived from a slip velocity, s , defined as:

$$s = v_c - v_x \quad (1.20)$$

where v_x is the translational velocity of the rotor and v_r is the circumferential velocity of the rotor:

$$v_r = \omega_m r_o \quad (1.21)$$

where ω_m is the rotor's mechanical rotational velocity, and r_o is the rotor's outer radius. A 2D steady state FEA model was used to plot the forces generated from various slip and translational velocities, as shown in Fig. 35 and Fig. 36. Later, Bird developed 3-D FEA models and experimentally validated the simulations [34].

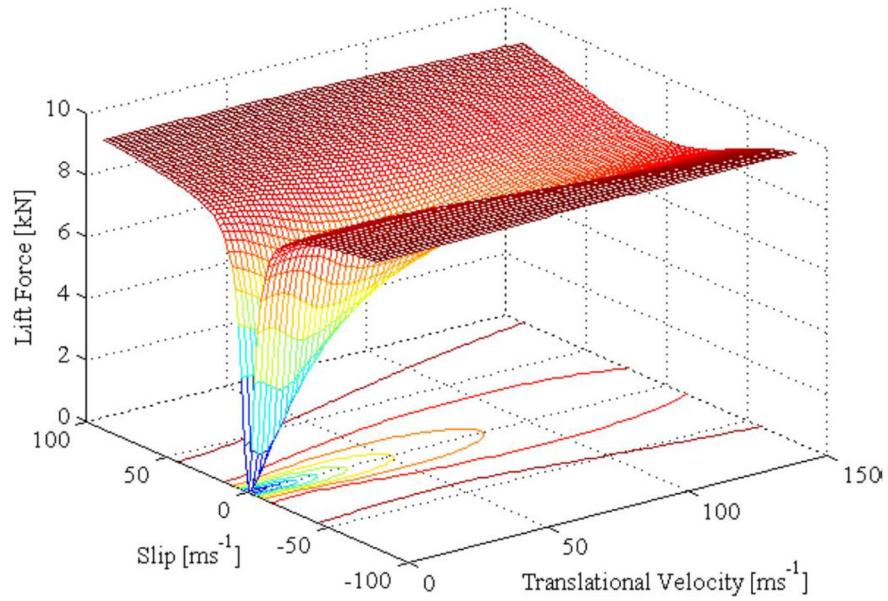


Fig. 35: Bird's calculated lift force vs. slip and translational velocity using 2D steady-state current model [21][22]

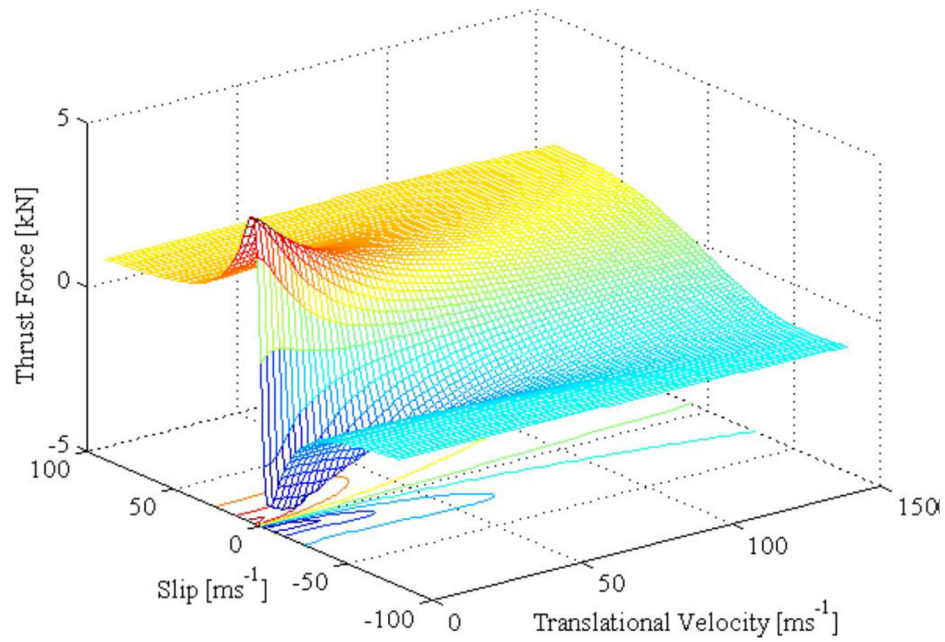


Fig. 36: Bird's calculated thrust force vs. slip and translational velocity using 2D steady-state current model [21][22]

Paudel developed a 2-D analytic model of an EDW and experimentally showed that if velocity and position changes are dynamically accounted for within the steady-state eddy

current force equations then an accurate mechanical model can be created [30][31]. Using the steady-state eddy current forces greatly reduces the complexity. More recently, Paul derived 3-D eddy current models of the EDW [31], as well as 3-D stiffness and damping eddy current terms, defined as the change in force with respect to position and velocity, respectively [35].

1.5 CONCLUSION

A number of important concepts were reviewed in this chapter which lay a foundation for the development of EDW maglev vehicle model and control, and development of an axial EDW topology which can be modeled analytically. Current models based on lumped parameters are not accurate enough to simulate multi-wheeled EDW systems and their respective controllers, which will necessitate using an SOVP approach.

CHAPTER 2: ELECTRODYNAMIC WHEEL VEHICLE

In this section, a prototype EDW vehicle is presented and the axes and motion coordinate system is defined. The 3-D eddy current damping and stiffness terms which will be used later to describe the equations of motion are also derived and explored.

2.1 VEHICLE DEFINITIONS

The exact steady-state stiffness and damping terms derived in [35] for a conductive plate guideway are incorporated into a state-space system representation in order to model the dynamics of an experimental sub-scale electrodynamic wheel vehicle (EWV) in section CHAPTER 3:. A prototype EDW is shown in Fig. 37, and a vehicle rendering is shown in Fig. 38.

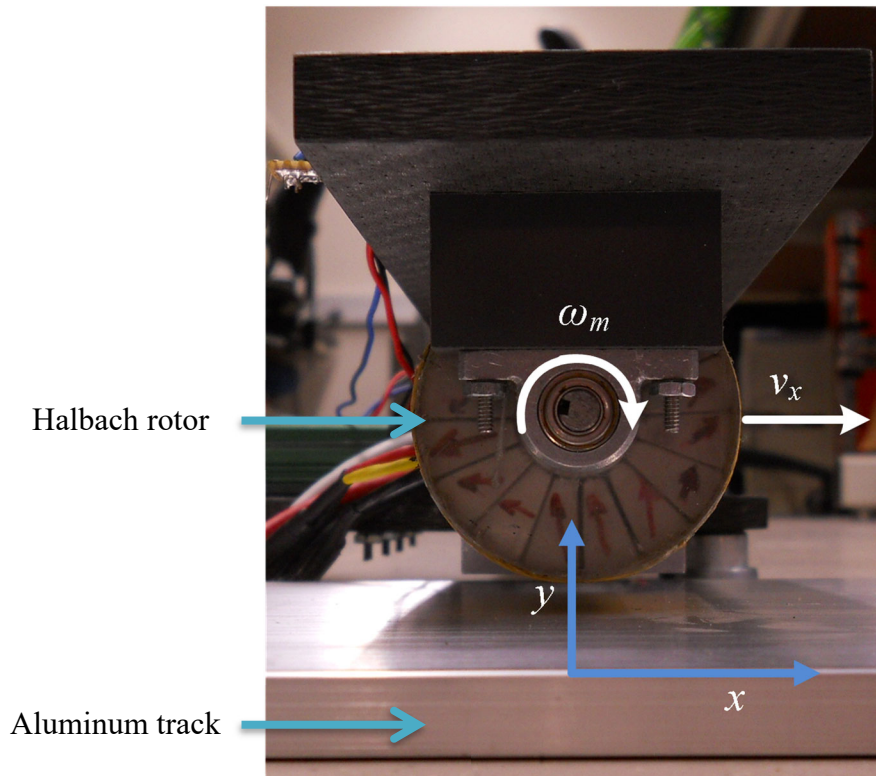


Fig. 37: Prototype electrodynamic wheel consisting of an axial Halbach rotor and an aluminum track

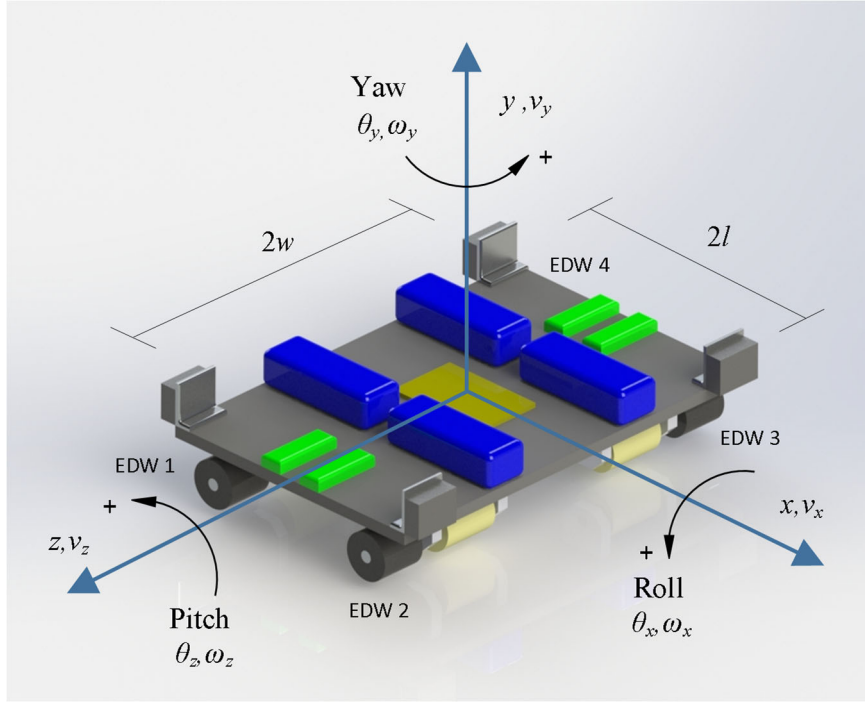


Fig. 38: Experimental EDW Maglev vehicle rendering and axis definitions

By rotating the EDWs over a conductive plate, an eddy current lift force, F_y , and thrust force, F_x , is created. The experimental setup being used in this study is shown in Fig. 39 and Fig. 40. Table 1 shows the experimental setup parameters. The aluminum guideway wheel consists of two tracks each 77mm wide 1.2m in diameter. The top of the track is visible in Fig. 40. As the radius of the guideway is large relative to the EDW radius the rotational motion of the guideway wheel is modeled as a translational velocity term, v_x . Each EDW is individually controlled by a brushless DC (BLDC) motor. Four laser displacement sensors at each corner of the vehicle are used to measure the air-gap heights y_1, y_2, y_3 and y_4 .

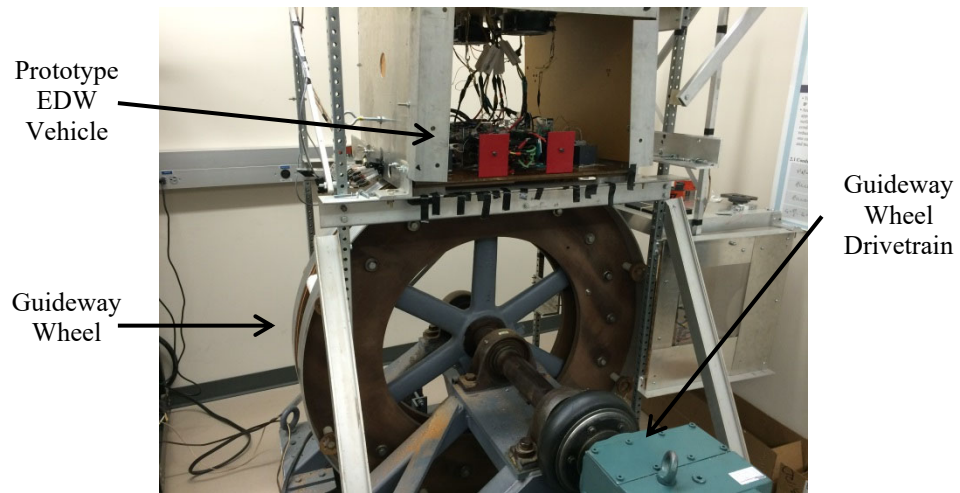


Fig. 39: Guideway wheel setup with an in-line gear reducer and DC braking motor [22]

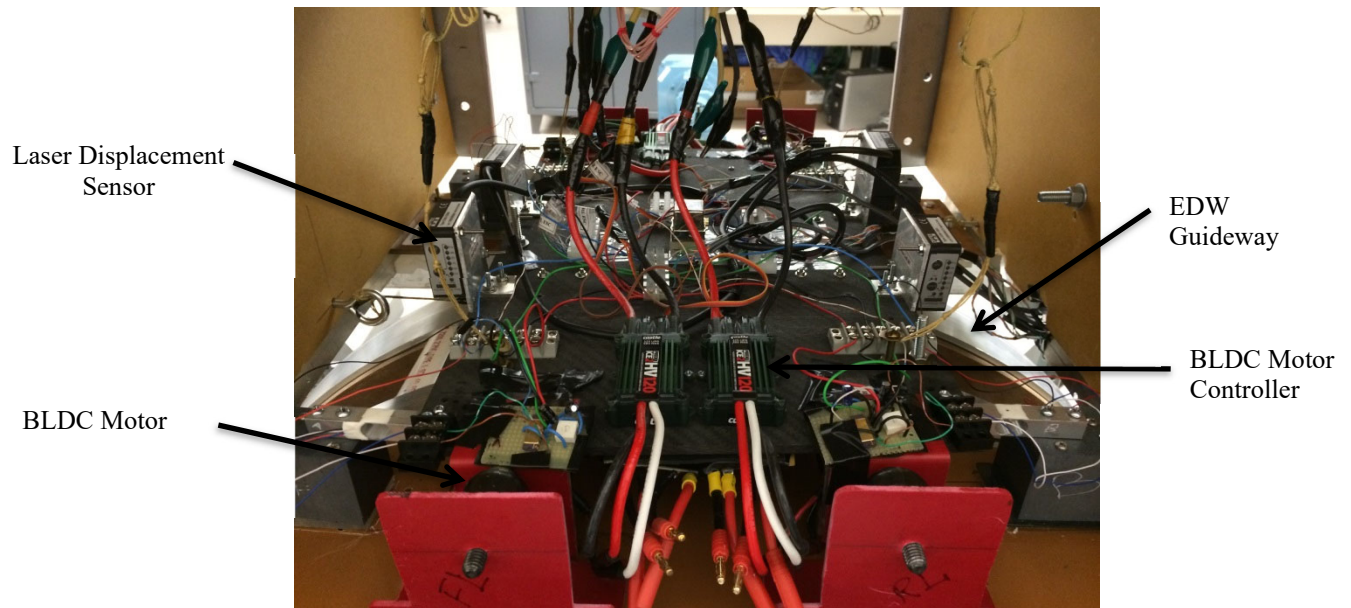


Fig. 40: EDW vehicle setup consisting of 4 EDWs and brushless DC drive motors. Four laser displacement sensors were used to accurately measure air-gap dynamics

Table 1. Rotor, guideway, and vehicle parameters for the radial experimental setup

| Parameter | | Value | Unit |
|--|---------------------------------------|------------------------|--------------------------------|
| Rotor | Outer radius, r_o | 26 ± 0.58 | mm |
| | Inner radius, r_i | 9.6 | mm |
| | Width of rotor, w_o | 52 | mm |
| | Residual flux density, B_{rem} | 1.42 | T |
| | relative permeability, μ_r | 1.108 | - |
| | Pole-pairs, P | 2 | - |
| Guideway | Outer radius, r_g | 600 ± 0.73 | mm |
| | Guideway width, w_g | 77 | mm |
| | Thickness, h | 6.3 | mm |
| | Conductivity, σ (Al, 6061-T06) | 2.459×10^{-7} | Sm^{-1} |
| Vehicle | Total mass, m | 10.315 | kg |
| | Length, $2l$ | 0.173 | m |
| | Width, $2w$ | 0.3254 | m |
| | z-axis rotational Inertia, I_{zz} | 0.08821 | kgm^2 |
| | x-axis rotational Inertia, I_{xx} | 0.1977 | kgm^2 |
| | y-axis rotational inertia, I_{yy} | 0.259 | kgm^2 |
| BLDC motors (Scorpion SII-4035-250KV)[74] | Winding inductance, L_a | 4.7×10^{-6} H | H |
| | Winding resistance, R_a | 0.037 | Ω |
| | Back-emf constant, K_e | 0.036 | Vs/rad |
| | Torque constant, K_t | 0.0295 | Nm/s |
| | rotational inertia, J | 0.00386 | kgm^2 |
| | Viscous damping coefficient, b | 2.295×10^{-6} | $\text{Nm} \cdot \text{s/rad}$ |

The definitions used for each vehicle axis and motion are shown in Fig. 41 through Fig. 44. Note that in these figures, $\omega_1 - \omega_4$ represent the rotational velocities, $F_{y1} - F_{y4}$ represent vertical forces, and $F_{x1} - F_{x4}$ represent translational forces, and $y_1 - y_4$ represent rotor heights, on rotors 1 through 4, respectively.

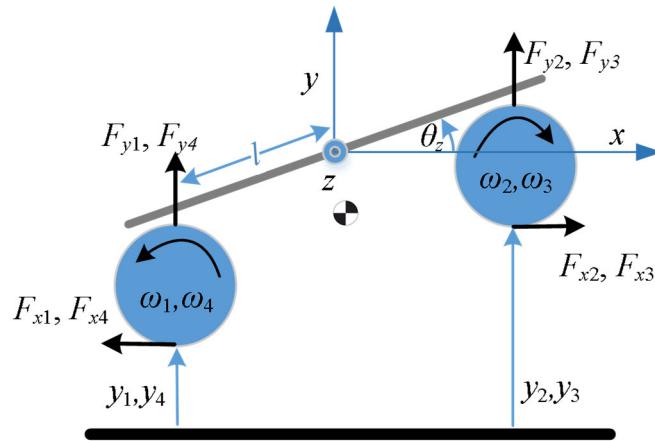


Fig. 41: 2-D sketch of vehicle pitch forces (x-y plane)

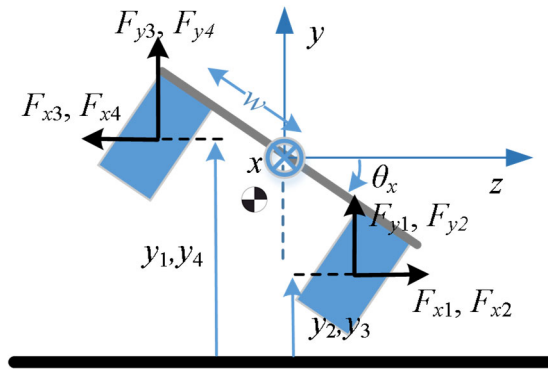


Fig. 42: 2-D sketch of vehicle roll forces (y-z plane)

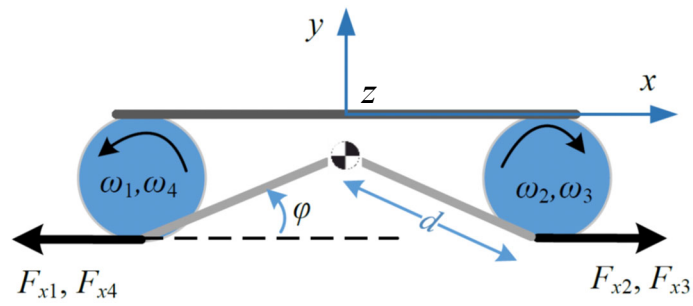


Fig. 43: 2-D sketch of pitch x-axis force induced pitching moment (x-y plane)

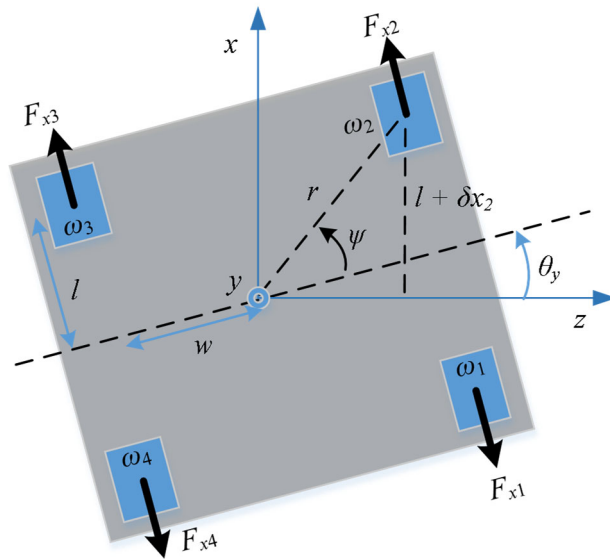


Fig. 44: 2-D sketch of yawed vehicle from above (x-z plane)

2.2 DAMPING AND STIFFNESS TERM DEFINITIONS

The source field of the EDW can be modelled using a fictitious magnetic charge distribution, ρ_{ms} , while the reflected eddy current plate field can be modeled using the magnetic scalar potential, ϕ^r [35]. The energy, U_m , associated with the interaction of the surface charge distribution with the reflected field will be [35]

$$U_m = \frac{1}{2} \int_S \rho_{ms}^* \phi^r dS \quad (2.1)$$

where the star superscript denotes complex conjugation. The force within the magnetostatic air region is defined as

$$\mathbf{F} = -\nabla U_m \big|_{p_{ms}=\text{constant}} \quad (2.2)$$

where the force vector is composed of the 3 axial components of force:

$$\mathbf{F} = F_x \hat{x} + F_y \hat{y} + F_z \hat{z} \quad (2.3)$$

Holding the surface charge distribution constant, the force in the magnetostatic region is

$$\mathbf{F} = -\frac{1}{2} \int_S \rho_{ms}^* \nabla \phi^r dS \quad (2.4)$$

Note that the magnetic scalar potential can be related to flux density by

$$\mathbf{B}^r = -\mu_o \nabla \phi^r \quad (2.5)$$

where μ_o is the vacuum permeability constant. The force can then be rewritten as [69][70]

$$\mathbf{F} = \frac{1}{2\mu_o} \int_S \rho_{ms}^* \mathbf{B}^r dS \quad (2.6)$$

The magnetic source field can be modeled using a fictitious magnetic charge sheet at a distance of y_g above the a finite thickness conductive plate [32][33]. The plate width, w_p ,

and length, l_p , are selected to be large enough that the field source and reflected eddy current field are zero at the edges. Therefore, the model requires that the plate is infinitely wide and long. The magnetic charge distribution must be related to the normal component of the source field at height y_g , according to [33]

$$\rho_{ms}(x, z) = 2B_y^s(x, y_g, z) \quad (2.7)$$

Substituting (2.7) into (2.6) produces Maxwell stress tensor force on the conductive plate [35]

$$\mathbf{F} = \frac{1}{\mu_o} \int_{-l_p/2}^{l_p/2} \int_{-w_p/2}^{w_p/2} \underbrace{B_y^s(x, y_g, z)}_{\text{Halbach source field}}^* \underbrace{\mathbf{B}^r(x, y_g, z)}_{\text{Reflected eddy current field}} dx dz \quad (2.8)$$

The force can be computed using a double Fourier approach in which case

$$\mathbf{F}(x, y_g, z) = \frac{w_p l_p}{\mu_o} \sum_{m=-\infty}^{\infty} \sum_{n=-\infty}^{\infty} B_{y,mn}^s(x, y_g, z) * B_{mn}^r(x, y_g, z) dy dx \quad (2.9)$$

The source field located at $y=y_g$ must therefore be in Fourier harmonic form in order to achieve term-by-term mode matching of the source field with the conductive plate reflected eddy current field. The Fourier harmonic field components at an airgap y is [35]

$$B_{y,mn}^s(x, y, z, t) = S_{mn} e^{j\xi_m x} e^{\kappa_{mn} y - y_g} e^{jk_n z} e^{-jP\omega_m t} \quad (2.10)$$

where

$$S_{mn} = \frac{e^{jP\omega_m t}}{l_p w_p} \int_{-w_p/2}^{w_p/2} \int_{-l_p/2}^{l_p/2} B_y^{so}(x, y, z, t) e^{-j\xi_m x} e^{-jk_n z} dx dz \quad (2.11)$$

The Halbach source term in (2.8) was modeled by Paul *et al* [33][34]. The B_y component of the source field of a Halbach rotor in 3-D is

$$B_y^{so}(x, y, z, t) = \frac{B_r r_o e^{-jP\omega_r t}}{2\pi} \int_0^{2\pi} \int_{-w_0/2}^{w_0/2} \frac{e^{jP\theta_o}}{R^3} (y - y_c - r_o \sin \theta_o) dz_o d\theta_o \quad (2.12)$$

where

$$B_r = \frac{2B_{res} P(1 + \mu_r)(r_i^{P+1} - r_o^{P+1})r_o^{2P}}{(1 + P) \left[(1 - \mu_r)^2 r_i^{2P} - (1 + \mu_r)^2 r_o^{2P} \right] r_o^{P+1}} \quad (2.13)$$

$$R = \sqrt{(x - x_c - r_o \cos \theta_o)^2 + (y - y_c - r_o \sin \theta_o)^2 + (z - z_c - z_o)^2} \quad (2.14)$$

$$\theta_m = \omega_m t \quad (2.15)$$

The steady-state reflected eddy-current field Fourier harmonic components, B_{mn}^r , created above the conductive plate is given by [31][33]

$$B_{mn}^r(x, y, z, t) = -jS_{mn} R_{mn} \left[\xi_m \hat{x} + j\kappa_{mn} \hat{y} + k_n \hat{z} \right] \left[\frac{1}{\kappa_{mn}} e^{-\kappa_{mn}(y+y_g)} e^{j\xi_m x} e^{jk_n z} e^{-jP\omega_m t} \right] \quad (2.16)$$

where the reflection coefficient, R_{mn} , is given by

$$R_{mn} = \frac{\mu_0 \sigma \tau_{mn}}{\xi_m^2 + k_n^2 + \gamma_{mn}^2 + 2\kappa_{mn} \beta_{mn} \coth(\beta_{mn} h)} \quad (2.17)$$

and where the following variable definitions apply

$$\xi_m = 2\pi m / l_p \quad (2.18)$$

$$k_n = 2\pi n / w_p \quad (2.19)$$

$$\beta_{mn}^2 = \lambda^2 + \gamma_{mn}^2 \quad (2.20)$$

$$\lambda = -0.5v_y\mu_0\sigma \quad (2.21)$$

$$\gamma_{mn}^2 = \kappa_{mn}^2 - j\mu_0\sigma(Pw_m + \xi_m v_x + k_n v_z) \quad (2.22)$$

$$\kappa_{mn}^2 = \xi_m^2 + k_n^2 \quad (2.23)$$

$$\tau_{mn} = \kappa_{mn}v_y + j(Pw_m + \xi_m v_x + k_n v_z) \quad (2.24)$$

Note that the rotor is rotating with a rotational velocity of ω_m and $(x, y, z) = (x_c, y_c, z_c)$ is the position of the center of the rotor. The steady-state field rotation of the rotor is modeled using the complex exponential term in (2.12). Table 1 provides parameter definitions required by (2.17) - (2.24) and the standard values used for simulations in this chapter, where applicable. The track length and width are modeled as $l_p = 250\text{mm}$ and $w_p = 150\text{mm}$. As the rotor diameter and width are 52mm, this ensures the field is zero at the model boundary edges.

The eddy current forces generated for an EDW rotating above a finite thickness, conductive, non-magnetic, plate of infinite extent along the x - z plane, is obtained by substituting (2.10) and (2.16) into (2.9). This yields [35]

$$\mathbf{F} = w_p l_p \text{Re} \left\{ \sum_{m=-\infty}^{\infty} \sum_{n=-\infty}^{\infty} B_{mn}^s R_{mn} \left[\frac{j\xi_m}{\kappa_{mn}} \hat{x} - \hat{y} + \frac{jk_n}{\kappa_{mn}} \hat{z} \right] \right\} \quad (2.25)$$

The S_{mn} term is defined in (2.10). By a similar process, the eddy-current torque acting on the EDW can be calculated to be [35]:

$$T_{em} = w_p l_p P \text{Re} \left\{ \sum_{m=-\infty}^{\infty} \sum_{n=-\infty}^{\infty} B_{mn}^s R_{mn} \frac{-j}{\kappa_{mn}} \right\} \quad (2.26)$$

Note that (2.26) can also be written in terms of the imaginary component of the product of the source and reflected fields:

$$T_{em} = w_p l_p P \text{Im} \left\{ \sum_{m=-\infty}^{\infty} \sum_{n=-\infty}^{\infty} \frac{B_{mn}^s R_{mn}}{\kappa_{mn}} \right\} \quad (2.27)$$

The change in eddy-current forces and torque is given by [35]:

$$[\mathbf{k}] = \begin{bmatrix} k_{xx} & k_{xy} & k_{xz} & k_{x\theta} \\ k_{xy} & k_{yy} & k_{yz} & k_{y\theta} \\ k_{zx} & k_{zy} & k_{zz} & k_{z\theta} \\ k_{x\theta} & k_{y\theta} & k_{z\theta} & k_{\theta\theta} \end{bmatrix} = \begin{bmatrix} \frac{\partial F_x}{\partial x} & \frac{\partial F_x}{\partial y} & \frac{\partial F_x}{\partial z} & \frac{\partial F_x}{\partial \theta_m} \\ \frac{\partial F_y}{\partial x} & \frac{\partial F_y}{\partial y} & \frac{\partial F_y}{\partial z} & \frac{\partial F_y}{\partial \theta_m} \\ \frac{\partial F_z}{\partial x} & \frac{\partial F_z}{\partial y} & \frac{\partial F_z}{\partial z} & \frac{\partial F_z}{\partial \theta_m} \\ \frac{\partial T_{em}}{\partial x} & \frac{\partial T_{em}}{\partial y} & \frac{\partial T_{em}}{\partial z} & \frac{\partial T_{em}}{\partial \theta_m} \end{bmatrix} \quad (2.28)$$

Note the symmetry of the eddy-current stiffness matrix. Note that the k_{ni} notation denotes the eddy current stiffness in the n axis with respect to i -axis displacement, where i can be x, y, z , or θ_m .

We can note from (2.8) that the force will depend on the product of the source and reflected field. In addition, the source field is delineated by axis components in (2.10). The change in force with respect to movement in any axis will depend on the partial derivative of (2.9). Equation (2.9) must be used to evaluate the terms in (2.28) because after multiplying the reflected and source fields the dependence on (x,y,z) is eliminated due to the conjugation of the complex exponential terms. We can view how each stiffness value will relate to (2.25) and (2.26) by taking the partial derivative of XX whilst holding the Fourier harmonic field in each axis:

$$\frac{\partial}{\partial x} = j\xi_m \quad (2.29)$$

$$\frac{\partial}{\partial y} = -\kappa_{mn} \quad (2.30)$$

$$\frac{\partial}{\partial z} = jk_n \quad (2.31)$$

$$\frac{\partial}{\partial \theta_r} = -jP \quad (2.32)$$

For the off-diagonal terms of the \mathbf{k} matrix in (2.28):

$$\frac{\partial F_x}{\partial y} = k_{xy} = w_p l_p \operatorname{Re} \left\{ \sum_{m=-\infty}^{\infty} \sum_{n=-\infty}^{\infty} j\xi_m B_{mn}^s R_{mn} \right\} \quad (2.33)$$

$$\frac{\partial F_z}{\partial y} = \frac{\partial F_y}{\partial z} = k_{yz} = k_{zy} = -w_p l_p \operatorname{Re} \left\{ \sum_{m=-\infty}^{\infty} \sum_{n=-\infty}^{\infty} jk_n B_{mn}^s R_{mn} \right\} \quad (2.34)$$

$$\frac{\partial F_x}{\partial z} = \frac{\partial F_z}{\partial x} = k_{xz} = k_{zx} = w_p l_p \operatorname{Re} \left\{ \sum_{m=-\infty}^{\infty} \sum_{n=-\infty}^{\infty} \frac{\xi_m k_n}{\kappa_{mn}} B_{mn}^s R_{mn} \right\} \quad (2.35)$$

$$\frac{\partial F_x}{\partial \theta_r} = \frac{\partial F_{\theta_r}}{\partial x} = k_{x\theta} = k_x = -w_p l_p P \operatorname{Re} \left\{ \sum_{m=-\infty}^{\infty} \sum_{n=-\infty}^{\infty} \frac{\xi_m}{\kappa_{mn}} B_{mn}^s R_{mn} \right\} \quad (2.36)$$

$$\frac{\partial F_y}{\partial \theta_r} = \frac{\partial F_{\theta_r}}{\partial y} = k_{y\theta} = k_y = w_p l_p P \operatorname{Re} \left\{ \sum_{m=-\infty}^{\infty} \sum_{n=-\infty}^{\infty} j B_{mn}^s R_{mn} \right\} \quad (2.37)$$

$$\frac{\partial F_z}{\partial \theta_r} = \frac{\partial F_{\theta_r}}{\partial z} = k_{z\theta} = k_z = -w_p l_p P \operatorname{Re} \left\{ \sum_{m=-\infty}^{\infty} \sum_{n=-\infty}^{\infty} \frac{k_n}{\kappa_{mn}} B_{mn}^s R_{mn} \right\} \quad (2.38)$$

The diagonal terms of (2.28) are:

$$\frac{\partial F_x}{\partial x} = k_{xx} = w_p l_p \operatorname{Re} \left\{ \sum_{m=-\infty}^{\infty} \sum_{n=-\infty}^{\infty} \frac{\xi_m^2}{\kappa_{mn}} B_{mn}^s R_{mn} \right\} \quad (2.39)$$

$$\frac{\partial F_y}{\partial y} = k_{yy} = w_p l_p \operatorname{Re} \left\{ \sum_{m=-\infty}^{\infty} \sum_{n=-\infty}^{\infty} \kappa_{mn} B_{mn}^s R_{mn} \right\} \quad (2.40)$$

$$\frac{\partial F_z}{\partial z} = k_{zz} = w_p l_p \operatorname{Re} \left\{ \sum_{m=-\infty}^{\infty} \sum_{n=-\infty}^{\infty} \frac{k_n^2}{\kappa_{mn}} B_{mn}^s R_{mn} \right\} \quad (2.41)$$

$$\frac{\partial T_{em}}{\partial \theta_r} = k_{\theta} = w_p l_p P^2 \operatorname{Re} \left\{ \sum_{m=-\infty}^{\infty} \sum_{n=-\infty}^{\infty} \frac{1}{\kappa_{mn}} B_{mn}^s R_{mn} \right\} \quad (2.42)$$

The eddy current damping terms can also be represented as a matrix:

$$[\mathbf{D}] = \begin{bmatrix} d_{xx} & d_{xy} & d_{xz} & d_{x\theta} \\ d_{yx} & d_{yy} & d_{yz} & d_{y\theta} \\ d_{zx} & d_{zy} & d_{zz} & d_{z\theta} \\ d_x & d_y & d_z & d_{\theta} \end{bmatrix} = \begin{bmatrix} \frac{\partial F_x}{\partial v_x} & \frac{\partial F_x}{\partial v_y} & \frac{\partial F_x}{\partial v_z} & \frac{\partial F_x}{\partial \omega_m} \\ \frac{\partial F_y}{\partial v_x} & \frac{\partial F_y}{\partial v_y} & \frac{\partial F_y}{\partial v_z} & \frac{\partial F_y}{\partial \omega_m} \\ \frac{\partial F_z}{\partial v_x} & \frac{\partial F_z}{\partial v_y} & \frac{\partial F_z}{\partial v_z} & \frac{\partial F_z}{\partial \omega_m} \\ \frac{\partial T_{em}}{\partial v_x} & \frac{\partial T_{em}}{\partial v_y} & \frac{\partial T_{em}}{\partial v_z} & \frac{\partial T_{em}}{\partial \omega_m} \end{bmatrix} \quad (2.43)$$

where d_{ni} represents the damping change in force in the n axis for a given change in the velocity of the i dimension. Again, note that some of the terms have unique notation that will be used later in the chapter. The reflection term (2.17) depends on velocity. Starting with the force/torque equations, (2.25) and (2.26)/(2.27), and multiplying by a term that accounts for the partial derivative of velocity in each axis, \mathbf{M}_{mn} , we can arrive at a succinct representation of the damping terms [35]:

$$[\mathbf{D}] = w_p l_p \operatorname{Re} \sum_{m=-\infty}^{\infty} \sum_{n=-\infty}^{\infty} \frac{B_{mn}^s}{\kappa_{mn}} [\mathbf{M}_{mn}] \quad (2.44)$$

where

$$[\mathbf{M}_{mn}] = \begin{bmatrix} -j\xi_m \\ \kappa_{mn} \\ -jk_n \\ jP \end{bmatrix} \begin{bmatrix} \frac{\partial R_{mn}}{\partial v_x} & \frac{\partial R_{mn}}{\partial v_y} & \frac{\partial R_{mn}}{\partial v_z} & \frac{\partial R_{mn}}{\partial \omega_m} \end{bmatrix} \quad (2.45)$$

The reflection coefficient derivative terms in (2.45) are

$$\frac{\partial R_{mn}}{\partial v_x} = \frac{j\xi_m [a_{mn} + \tau_{mn}(1 + \kappa_{mn}b_{mn})]}{a_{mn}^2} \quad (2.46)$$

$$\frac{\partial R_{mn}}{\partial v_y} = \frac{\kappa_{mn} [a_{mn} - 0.5v_y b_{mn} \tau_{mn}]}{a_{mn}^2} \quad (2.47)$$

$$\frac{\partial R_{mn}}{\partial v_z} = \frac{jk_n [a_{mn} + \tau_{mn}(1 + \kappa_{mn}b_{mn})]}{a_{mn}^2} \quad (2.48)$$

$$\frac{\partial R_{mn}}{\partial \omega_m} = \frac{jP [a_{mn} + \tau_{mn}(1 + \kappa_{mn}b_{mn})]}{a_{mn}^2} \quad (2.49)$$

where

$$a_{mn} = \frac{\kappa_{mn}^2 + \gamma_{mn}^2 + 2\kappa_{mn}\beta_{mn} \coth(\beta_{mn}h)}{\mu_0\sigma} \quad (2.50)$$

$$b_{mn} = \frac{\coth(\beta_{mn}h)}{\beta_{mn}} - h \operatorname{csch}^2(\beta_{mn}h) \quad (2.51)$$

2.3 DAMPING AND STIFFNESS RELATIONSHIPS

The section serves to document the behavior of the rotor forces for a reasonable subset of operating conditions. Surface and contour plots show how the stiffness and damping terms change with respect varying rotor speeds and translational movements. The simulation operating parameters are as defined in Table 1.

Note that on the 4 EDW vehicle model, the rotor angular rotational velocity directions are as shown in Fig. 38. The vehicle is assumed to be operating around a stationary operating point (v_x is zero at $t = 0$) since the rotors on the front and back of the vehicle are pulling in opposite directions. While a stationary vehicle is trivial for practical applications, it serves as good way to validate the model. Once a satisfactory model is achieved, the addition of an x -velocity is a simple modification. In fact, just applying a negative rotational velocity to one set of rotors (either front or back) will result in all rotors rotating in the same direction, applying a thrust to move the vehicle down the length of the track. For section 2.3, in order to characterize the expected forces acting on each rotor, we simply consider a single rotor with rotational velocity ω_m .

In the following sections, the stiffness and damping relationship with respect to the trust, F_x , and lift force, F_y , are investigated with respect to x , y , v_x , v_y , and ω_m changes. Slip, a variable relating ω_m and v_x can be defined:

$$s = r_c \omega_m - v_x \quad (2.52)$$

We can also express the rotor's rotational velocity as the linear surface velocity of the rotor:

$$v_r = r_c \omega_m \quad (2.53)$$

Note that for the 2-D plots, a ω_m of 3673rpm is often used because it adds a convenient 10 m/s of slip, and because this is sufficient to levitate the prototype vehicle for our low speed tests. The equivalence of 3673rpm rotor speed and 10 m/s of rotor slip is due to:

$$\omega_m = \frac{s}{r_c} = \frac{10 \text{ m/s}}{0.026 \text{ m}} = 3673 \text{ rpm} \quad (2.54)$$

The influence of F_z and v_z , and z motion is neglected because the prototype vehicle is physically constrained in the z -axis. When analyzing how the damping and stiffness terms are affected by s , v_x , and v_y , it is also beneficial to envision how the vehicle would typically operate. Starting from a standstill, $s = v_x = v_y = 0$, slip increases until the vehicle levitated. Translational speed, v_x , then begins to catch up to slip, until it reaches steady-state, at which point v_x lags behind slip by a consistent amount. Upon braking, slip lags behind v_x by an amount dependent on the amount of braking force desired. This is shown in Fig. 45, noting that this is the generalized behavior and the actual regions would vary based on operating conditions.

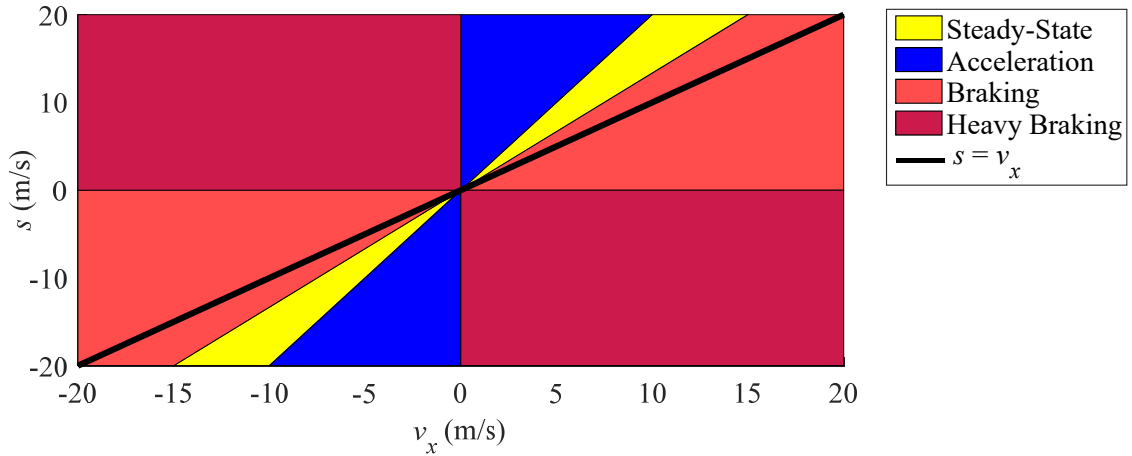


Fig. 45: Approximate vehicle operating regions

2.3.1 TRANSLATIONAL THRUST STIFFNESS

In the following section Fig. 46 shows how the translational force, F_x , varies with slip, for various values of translational velocity, v_x . Again, note that the prototype vehicle is not meant to be run at any significant translational speed, so v_x is chosen to only vary from -20 m/s to 20 m/s. Additionally, keeping the slip magnitude below 20 m/s prevents the hand-built prototype EDWs from exceeding their mechanical limitations.

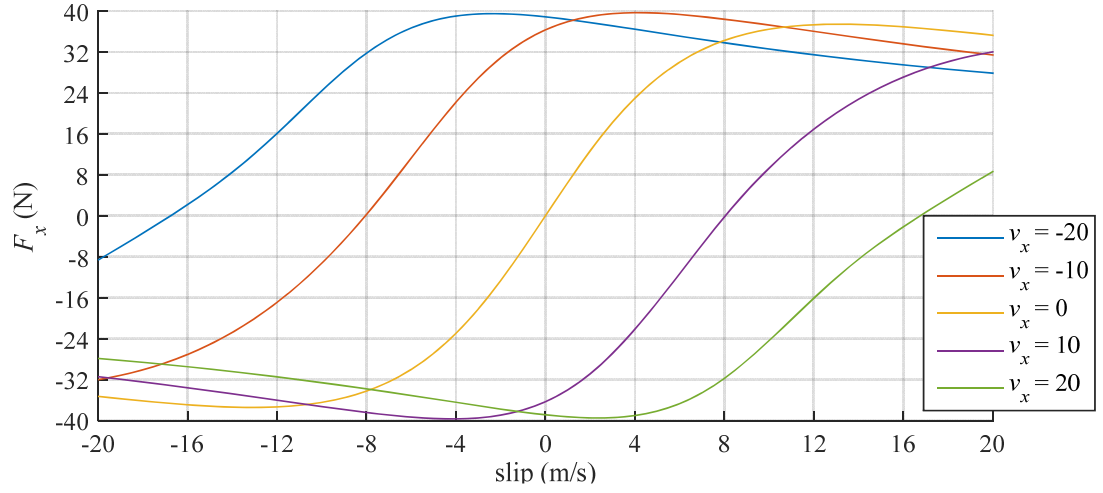


Fig. 46: Thrust/translational force, F_x , vs. slip for various values of translational velocity, v_x , $y = 10\text{mm}$ and all other positions and velocities zero

Fig. 47 and Fig. 48 show how the translational stiffness in the x -direction, k_{xx} , is affected by slip and v_x . The definition of k_{xx} is

$$k_{xx}(v_x, v_y, \omega_m) = \frac{\partial F_x}{\partial x} \quad (2.55)$$

The symmetry about the s - v_x line, despite being offset by rotor velocity, implies that the stiffness is affected similarly by both slip and x velocity. This is expected from (2.52), since slip is related to both v_x and ω_m . As k_{xx} is always less than zero under these operating conditions (note that v_y is zero here), it is a stabilizing force in the x -axis. When either v_x or slip increases in magnitude, the stabilizing force becomes greater. Fig. 49 better shows the behavior when rotor speed is held constant ($\omega_r = 3673$ rpm, or $v_r = 10$ m/s). It is clearly evident that the stiffness term decreases as the rotor moves faster relative to the track. A minimum stiffness is achieved when the x velocity is offset by the rotor velocity such that

$$v_x = r_o \omega_m \quad (2.56)$$

In steady-state operation, k_{xx} is less stabilizing, and becomes more stabilizing as the vehicle accelerates and decelerates significantly. Light braking that moves the system towards equation (2.56) can minimize the stabilization.

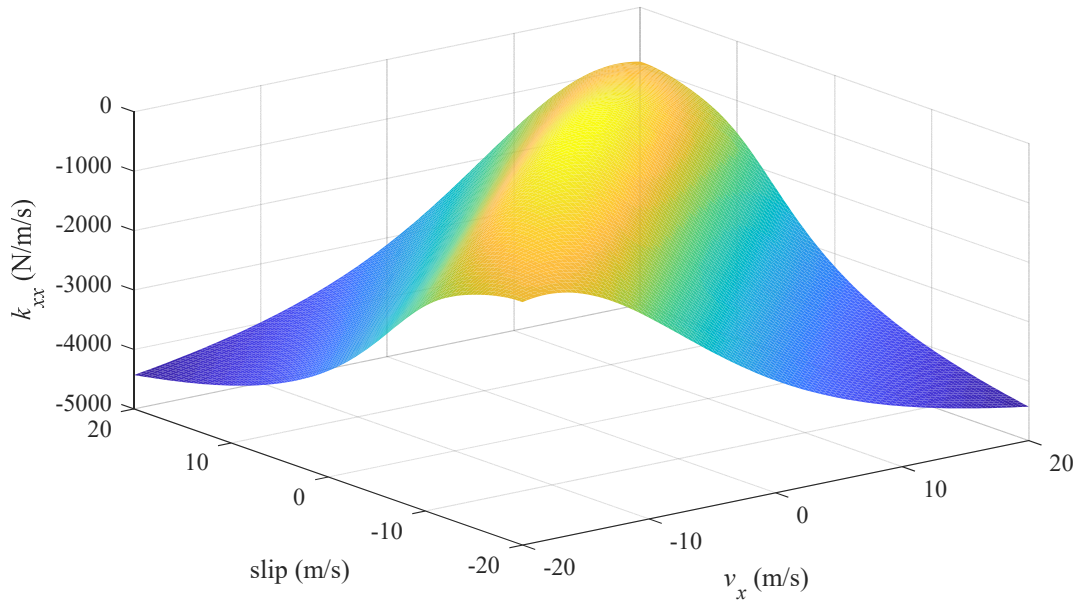


Fig. 47: Surface plot of k_{xx} vs. slip vs. v_x , ($v_y = 0$), $y = 10\text{mm}$, and all other positions and velocities zero

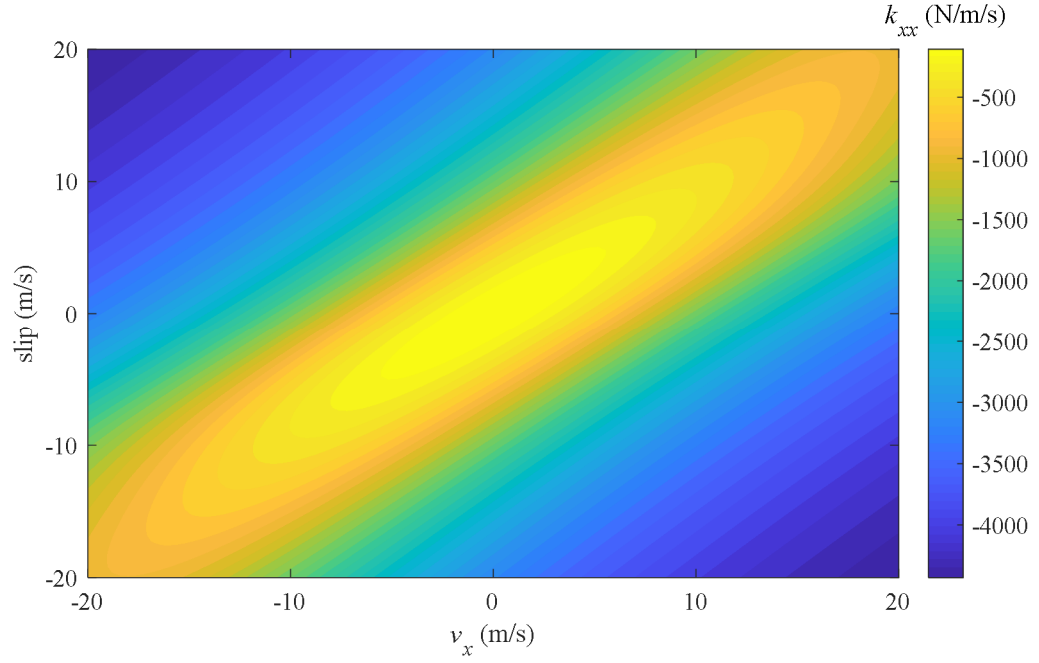


Fig. 48: Contour plot of k_{xx} vs. slip vs. v_x , ($v_y = 0$), $y = 10\text{mm}$, and all other positions and velocities zero

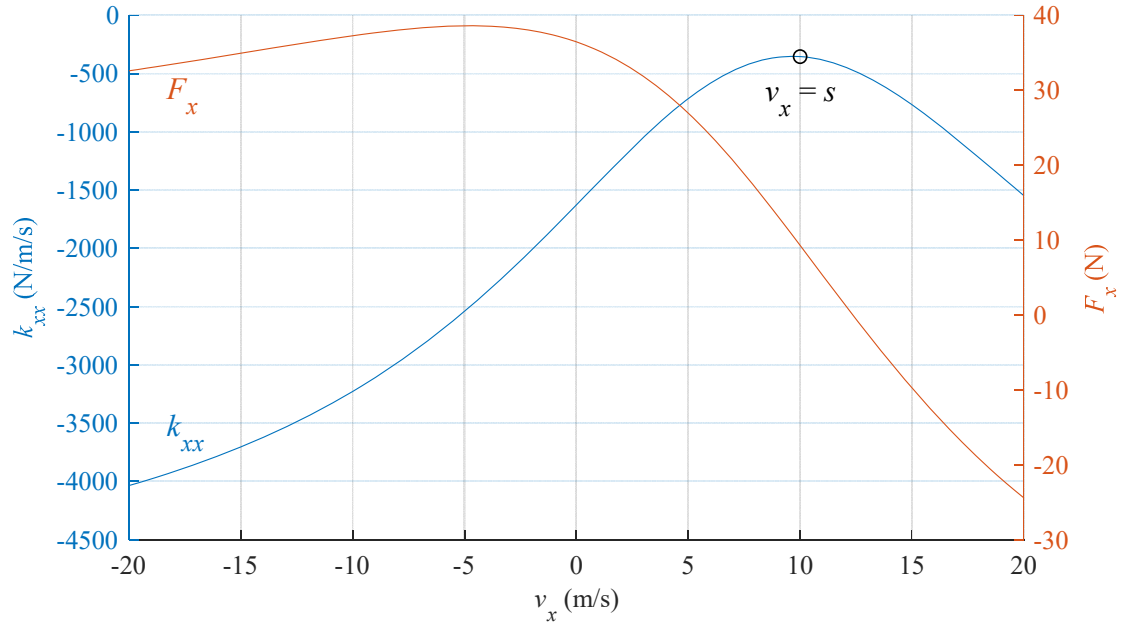


Fig. 49: Plot of k_{xx} and F_x vs. v_x when $(v_y, v_r) = (0, 10)$ m/s, $y = 10\text{mm}$ and all other positions and velocities zero

In order to evaluate how v_y affects k_{xx} , we can first observe how the force is affected by a range of expected heave values, shown in Fig. 50. Note that any non-zero heave is considered transient, and is expected to be small, so we chose to evaluate only from $v_y = 5 \text{ m/s}$ to $v_y = -5 \text{ m/s}$.

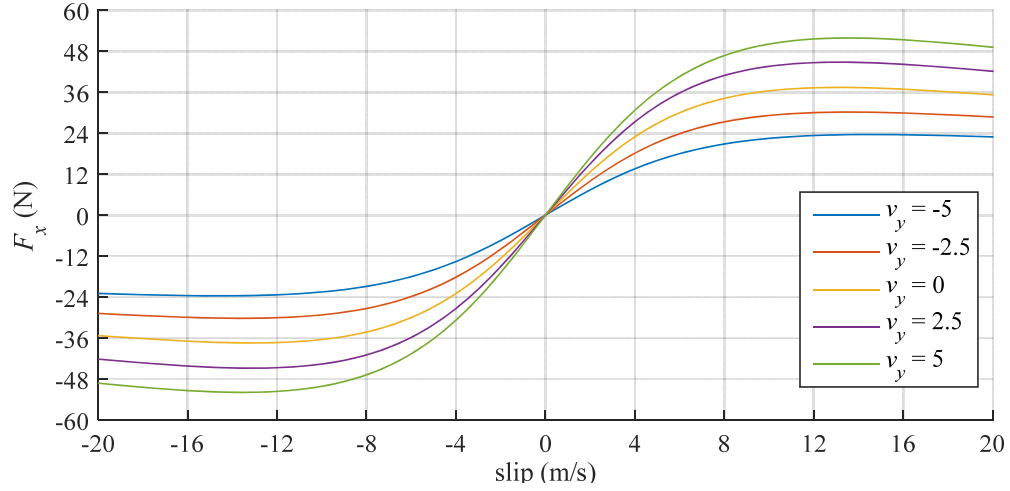


Fig. 50: Trust/translational force, F_x vs. slip for various values of v_y , $y = 10\text{mm}$ and all other positions and velocities zero

The surface and contour plots in Fig. 51 and Fig. 52 show the translational stiffness changes as slip and v_y vary when $v_x = 0 \text{ m/s}$. The plotting area was chosen to show the expected behavior in the operating region. We can see that in the expected operating region, slices of k_{xx} changes fairly linearly when slip is constant. This helps bolster the argument for linearizing this dynamic for control purposes. While k_{xx} is negative and therefore stabilizing for a majority of the operating region, k_{xx} becomes positive and therefore destabilizing when the vertical velocity is strongly positive and the slip speed is small. While this must be considered for transient behavior, during cruise, the vehicle would have significant slip and very little vertical velocity. Increasing slip magnitude, on the other hand, is a stabilizing action on k_{xx} with respect to v_y , since increasing slip

magnitude drives the stiffness down. Fig. 53 shows that when rotor speed is held constant at $(v_x, v_r) = (0, 10)$ m/s, k_{xx} increases nearly linearly with v_y . Notice that when the rotor speed is 3673 rpm, k_{xx} is negative and therefore stabilizing.

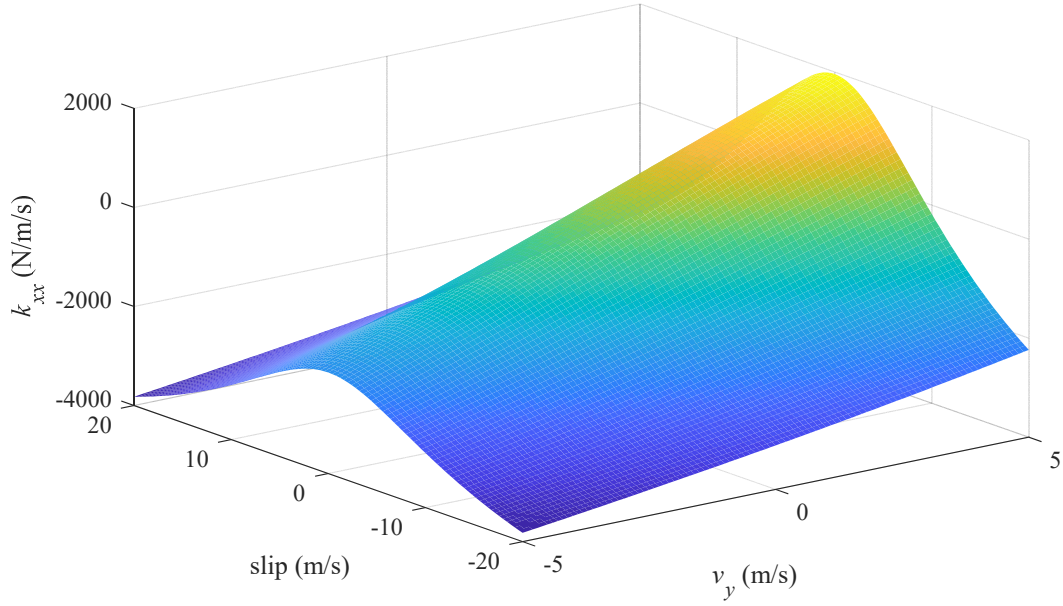


Fig. 51: Surface plot of k_{xx} vs. slip vs. v_y , $y = 10$ mm, and all other positions and velocities zero (note $v_x = 0$, so slip is analogous to ω_m)

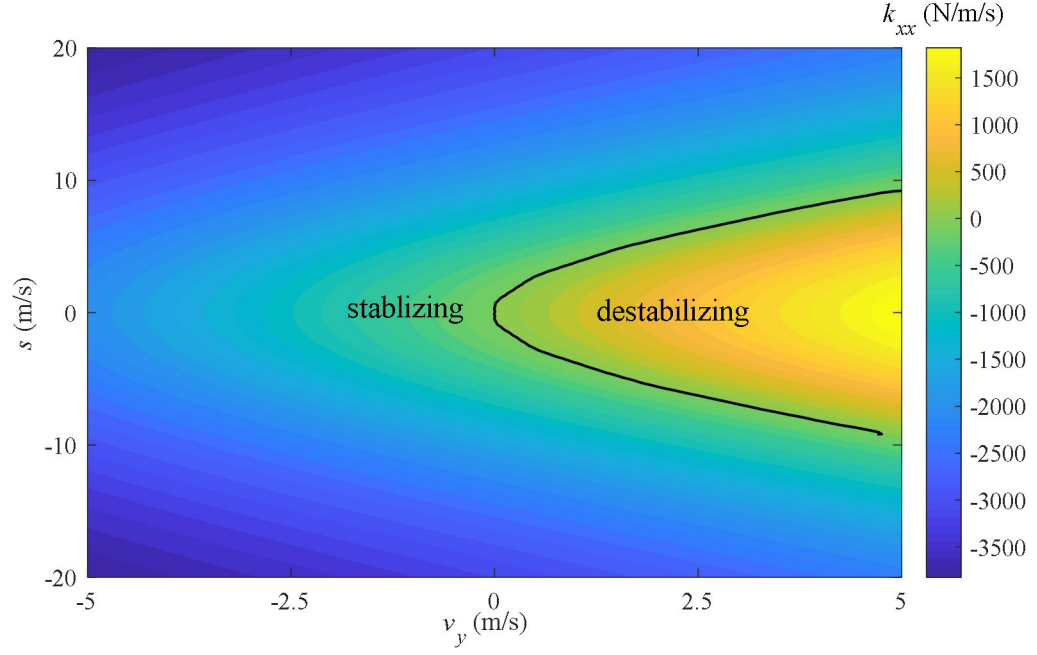


Fig. 52: Contour plot of k_{xx} vs. slip vs. v_y , $y = 10\text{mm}$, and all other positions and velocities zero (note $v_x = 0$, so slip is analogous to ω_m)

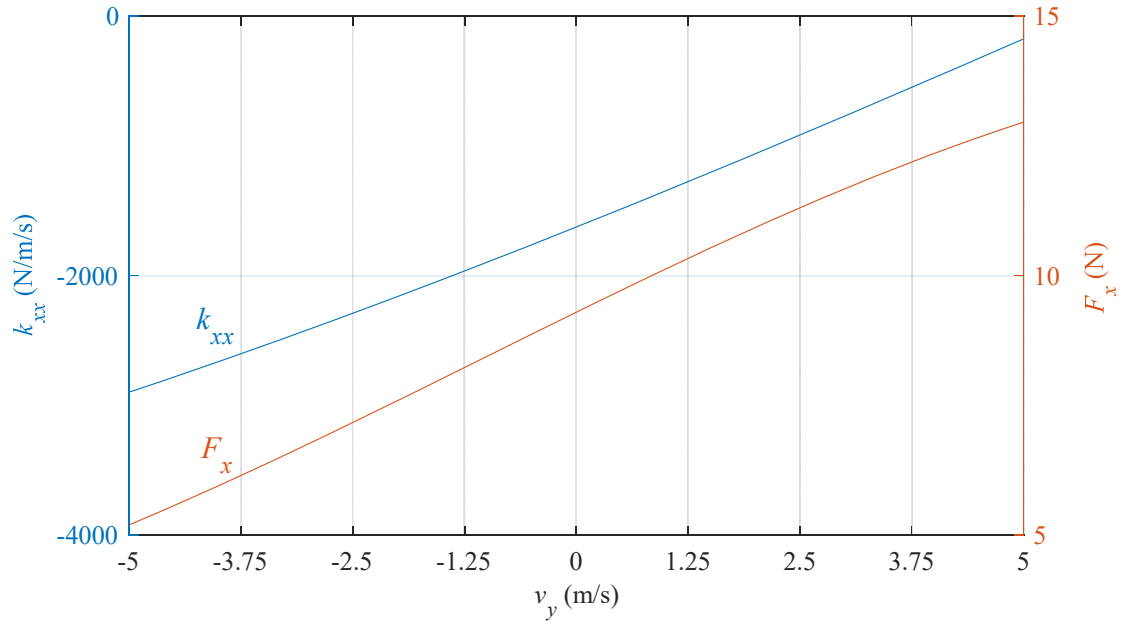


Fig. 53: Plot of k_{xx} and F_x , vs. v_y , when $(v_x, v_r) = (0,10)$ m/s, $y = 10\text{mm}$ and all other positions and velocities zero

2.3.2 TRANSLATIONAL HEAVE STIFFNESS

The definition of the heave translational force, k_{xy} , is the partial derivative of thrust force with respect to vertical position:

$$k_{xy}(v_x, v_y, \omega_m) = \frac{\partial F_x}{\partial y} \quad (2.57)$$

Note that due to symmetry of the stiffness matrix defined in equation (2.28), k_{xy} can also be defined as the partial derivative of lift force with respect to horizontal position:

$$k_{xy}(v_x, v_y, \omega_m) = \frac{\partial F_y}{\partial x} \quad (2.58)$$

Therefore, due to this off-diagonal equivalence in (2.28), the lift force will be affected by δx the same way that thrust force is affected by δy .

Fig. 54 and Fig. 55 show the relationship of k_{xy} with slip and v_x . The plots show symmetrical behavior as expected from equation (2.52). Note that despite the nonlinear behavior, there exists a general trend of a positive, destabilizing stiffness for larger slip and translational velocities, and a negative, stabilizing stiffness for smaller slip and translational velocities. The line $s = v_x$ is the cutoff between stabilizing and destabilizing k_{xy} contribution. In addition, we can observe that as slip or translational velocity become very large, k_{xy} values plateau and weakly decrease in magnitude.

From Fig. 45, we can see that this dynamic would be strongly stable during acceleration, weakly stable during steady-state operation, and less stable as more braking

force is applied. Note that stability while braking is only possible when a small braking force is applied that does not cross the $s = v_x$ threshold.

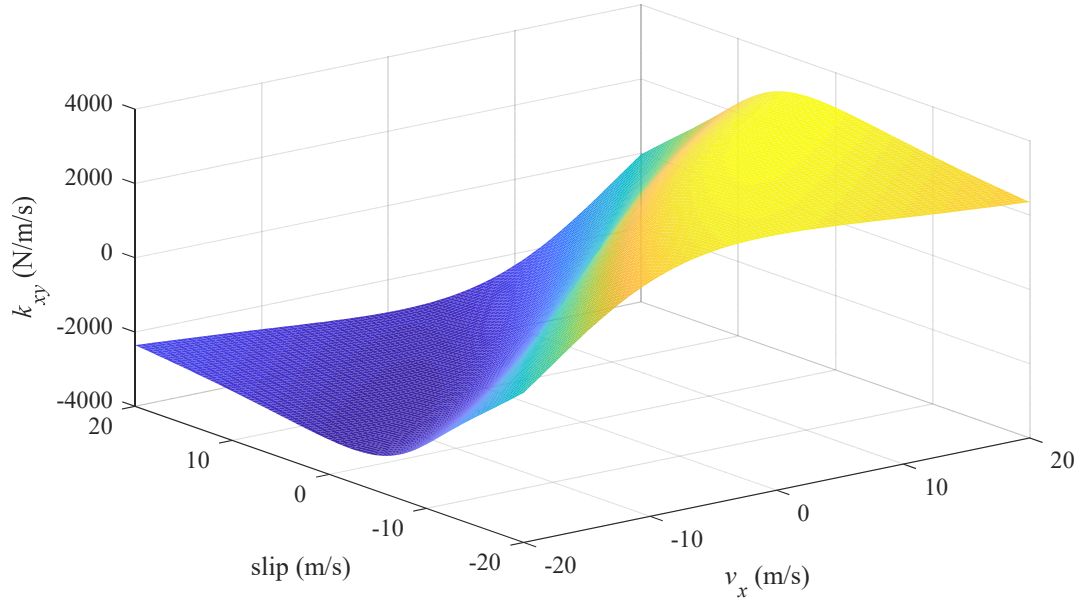


Fig. 54: Surface plot of k_{xy} vs. slip vs. v_x , ($v_y = 0$), $y = 10\text{mm}$, and all other positions and velocities zero

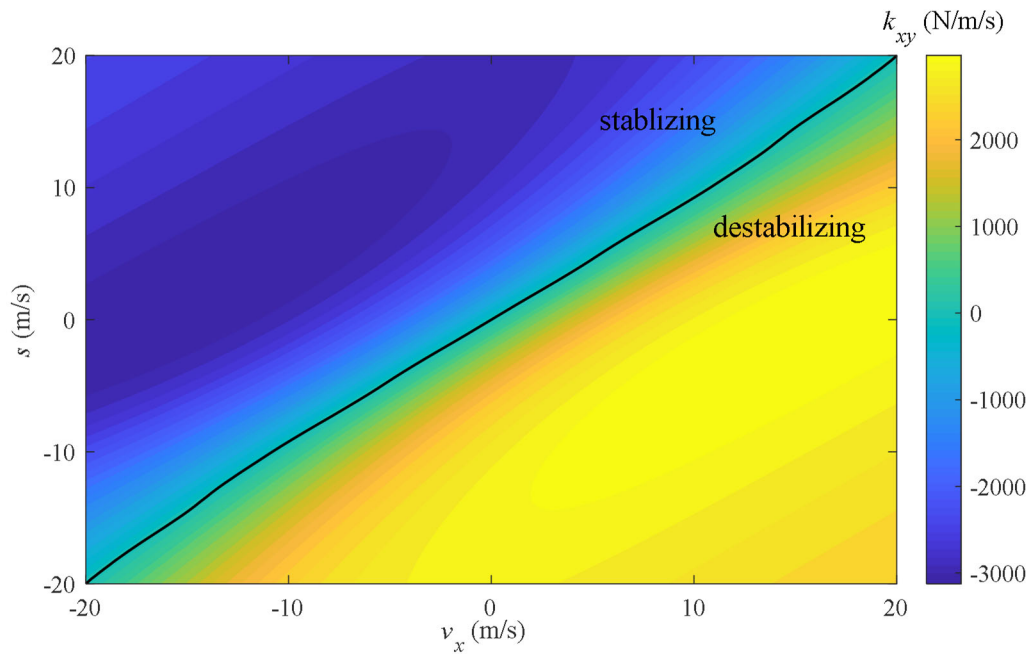


Fig. 55: Contour plot of k_{xy} vs. slip vs. v_x , ($v_y = 0$), $y = 10\text{mm}$, and all other positions and velocities zero

Fig. 56 shows how k_{xy} changes as v_x changes while $(v_y, v_r) = (0, 10)$ m/s. The non-linear, non-quadratic behavior can have an adverse impact on the application of control if we chose to use a linear system representation, necessitating updating the model during run-time to reflect the actual k_{xy} value. Large forward translational speeds (an expected operating condition) lead to instability.

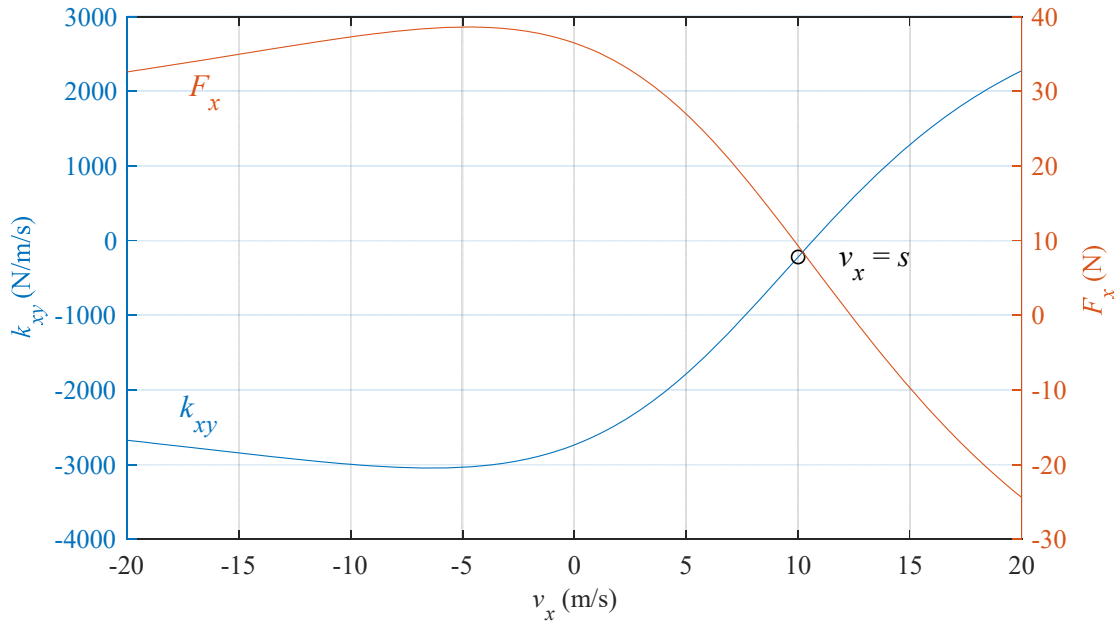


Fig. 56: Plot of k_{xy} and F_x vs. v_x when $(v_y, v_r) = (0, 10)$ m/s, $y = 10$ mm and all other positions and velocities zero

Fig. 57 and Fig. 58 show how k_{xy} varies with slip and v_y . Slices of k_{xy} vs. s when v_y is held constant show that k_{xy} becomes more stabilizing with increased slip, while slices of k_{xy} vs. v_y when s is held constant show that k_{xy} is more stabilizing with increasing vertical velocity when slip is positive and more destabilizing with increased vertical velocity when slip is negative. Due to the symmetry of the stiffness matrix from equation (2.28), \mathbf{k} , we can also infer the same stabilizing/destabilizing action in the x -axis. A slice of k_{xy} vs v_y when $(v_y, v_r) = (0, 10)$ m/s in Fig. 59 shows a strong linearity around an operating point with

constant rotor velocity, which is a reasonable assumption for a vehicle travelling at a constant velocity. This term therefore lends itself well to linear modeling in this mode.

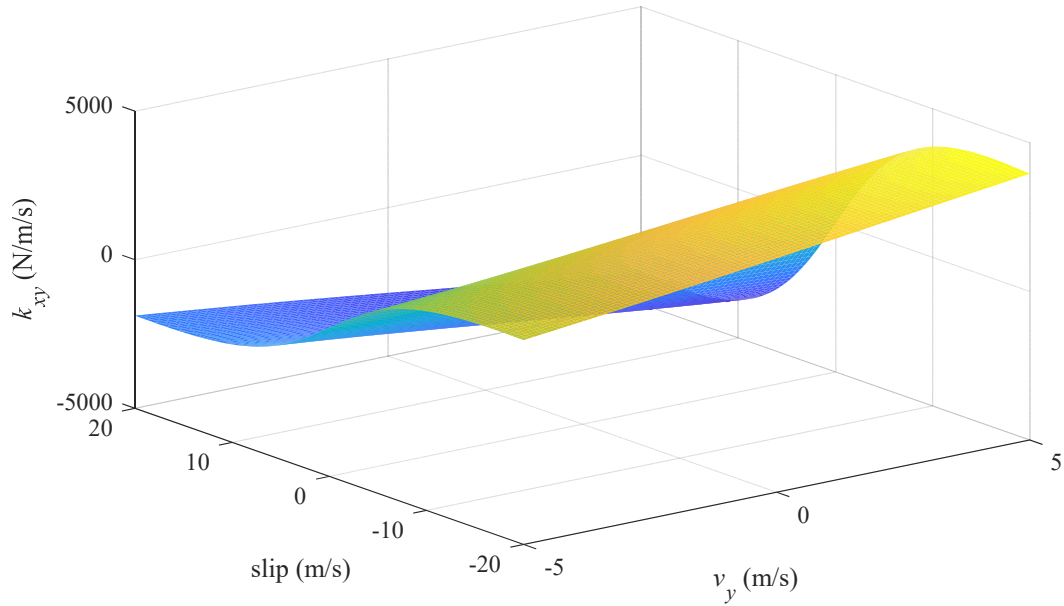


Fig. 57: Surface plot of k_{xy} vs. slip vs. v_y , $y = 10\text{mm}$, and all other positions and velocities zero (note $v_x = 0$, so slip is analogous to ω_m)

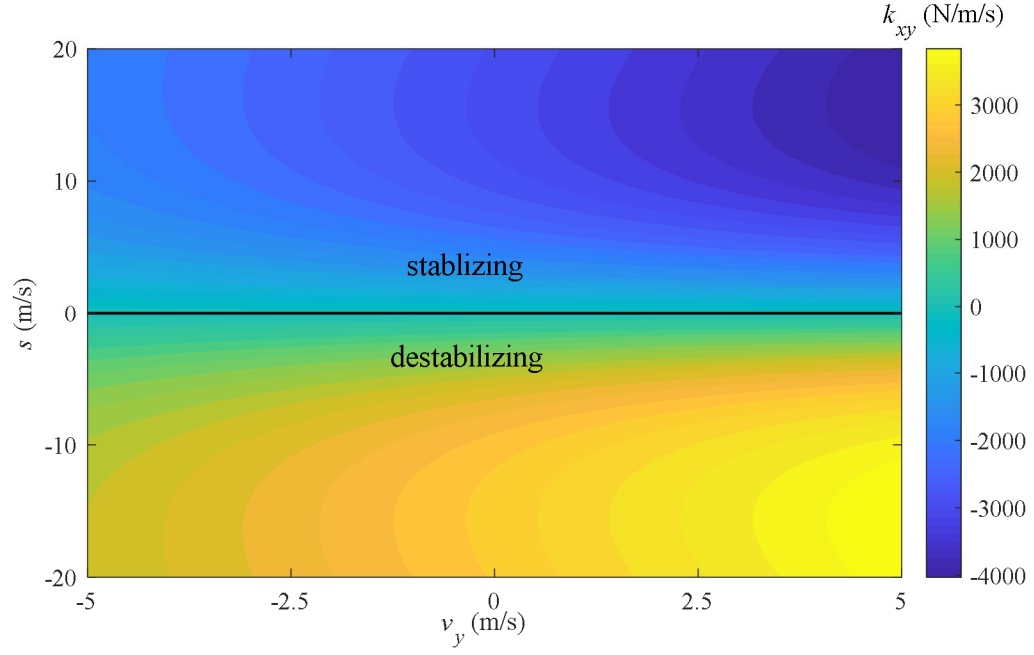


Fig. 58: Contour plot of k_{xy} vs. slip vs. v_y , $y = 10\text{mm}$, and all other positions and velocities zero (note $v_x = 0$, so slip is analogous to ω_m)

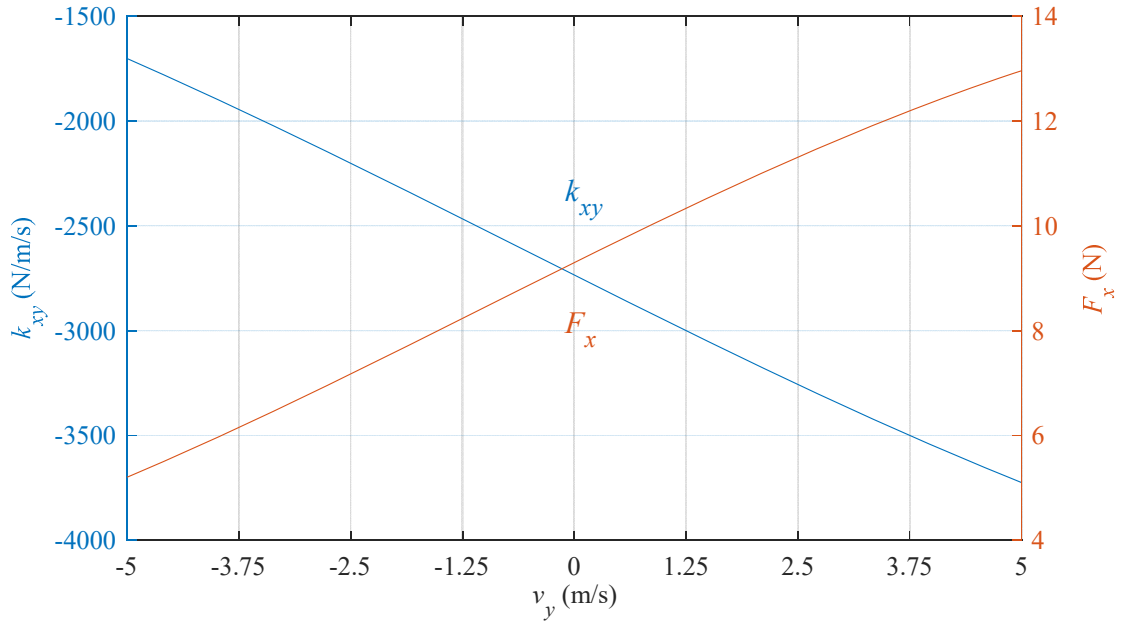


Fig. 59: Plot of k_{xy} and F_x vs. v_y when $(v_x, v_r) = (0,10)$ m/s, $y = 10\text{mm}$ and all other positions and velocities zero

Observing Fig. 54 and Fig. 57 or Fig. 55 and Fig. 58, a possible detrimental synergistic effect can be noticed. If the system is operating in an unstable braking region, then the braking force will be increased, leading to a larger change in x . This larger change in x , from (2.57), will lead to larger changes in F_y and therefore y , which, because of (2.58), will lead to larger changes in F_x and therefore x , thus indicating a positive feedback loop.

2.3.3 VERTICAL HEAVE STIFFNESS

The heave vertical stiffness, k_{yy} , is defined as the partial derivative in vertical force with respect to variations in the vertical position:

$$k_{yy}(v_x, v_y, \omega_m) = \frac{\partial F_y}{\partial y} \quad (2.59)$$

The vertical lift force, F_y , is always positive when $v_y = 0$ and generally tends to increase when the quantity $s - v_x$ increases, as shown in Fig. 60.

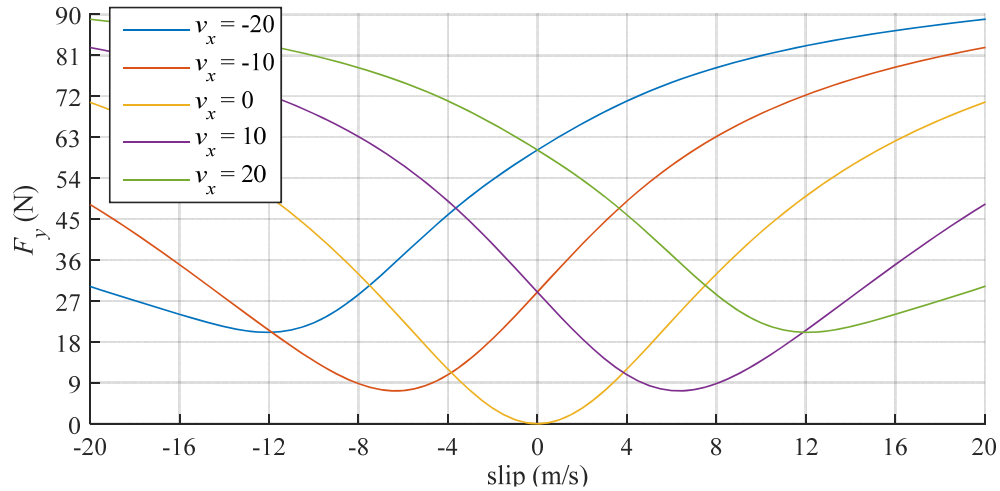


Fig. 60: F_y vs. slip for various values of v_x , $y = 10\text{mm}$, and all other positions and velocities zero

The surface and contour plots in Fig. 61 and Fig. 62 show the relationship of k_{yy} with slip and v_x . Again we obtain near symmetry about $s = v_x$ due to (2.52). The negative values suggest k_{yy} with respect to slip and v_x is always stabilizing in the y -axis under the expected operating conditions. Additionally, the magnitude gets larger for larger slip and v_x values (further from the $s - v_x$ line), applying more restorative force. The magnitude of k_{yy} at extreme slip and translational velocities is also larger than other stiffness terms, so k_{yy} has a very pronounced open loop stabilizing effect. The strongly negative k_{yy} value is why past researchers have stated that electrodynamic levitation is stable [55]. Fig. 63 shows a slice of k_{yy} vs. v_x , showing a nonlinear characteristic when $(v_y, v_r) = (0, 10)$ m/s. Note that for mild braking in the vicinity of $s = v_x$, there is a reduction in the stabilizing force, but during more pronounced transient operation (accelerating or braking), k_{yy} increases.

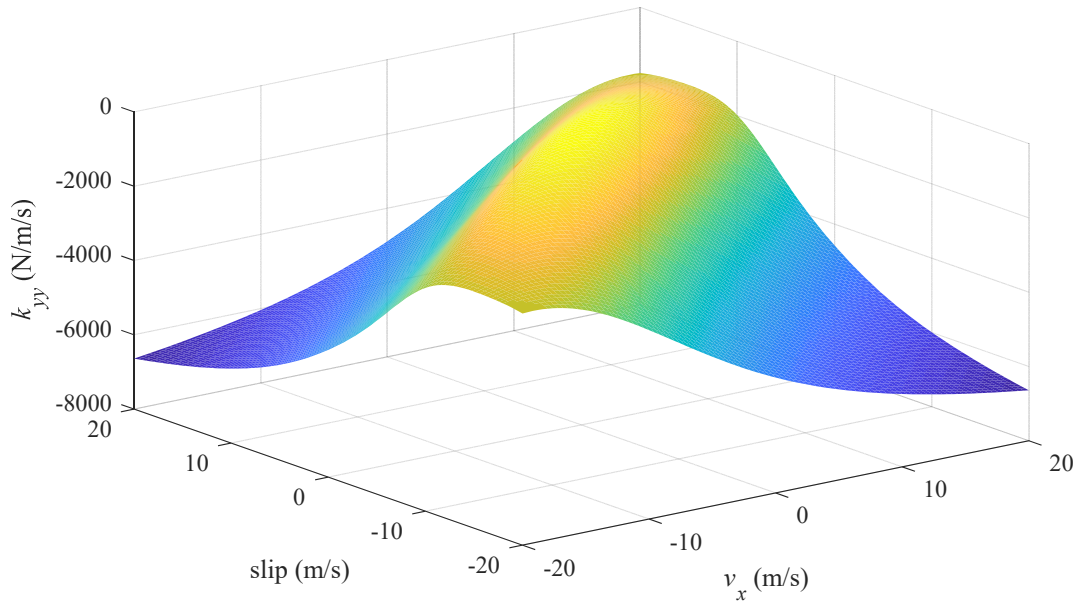


Fig. 61: Surface plot of k_{yy} vs. slip vs. v_x , ($v_y = 0$), $y = 10$ mm, and all other positions and velocities zero

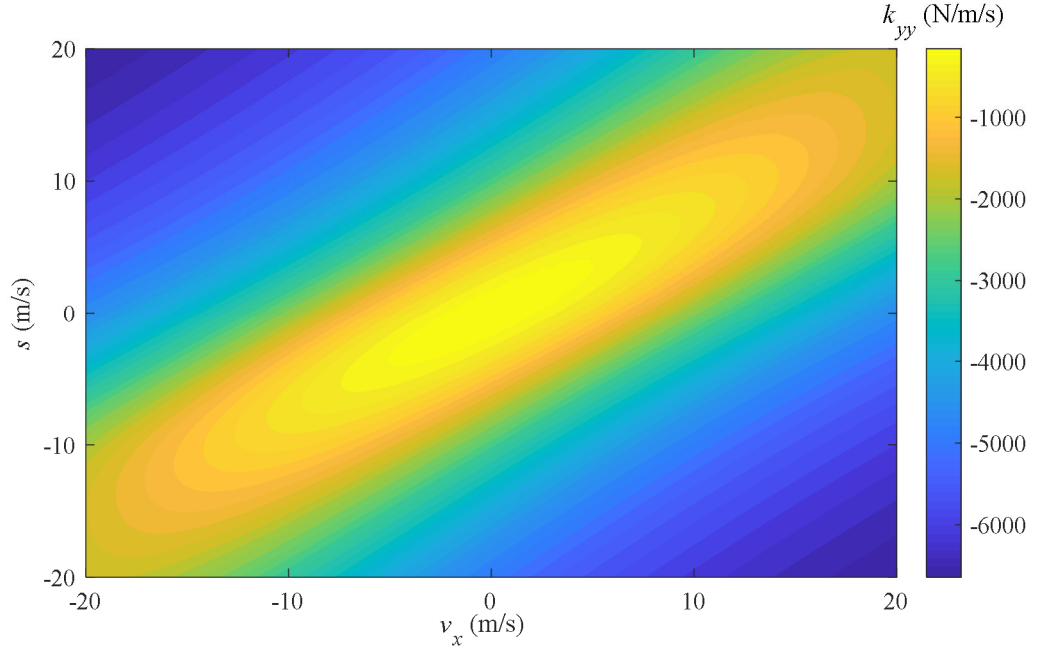


Fig. 62: Contour plot of k_{yy} vs. slip vs. v_x , ($v_y = 0$), $y = 10\text{mm}$, and all other positions and velocities zero

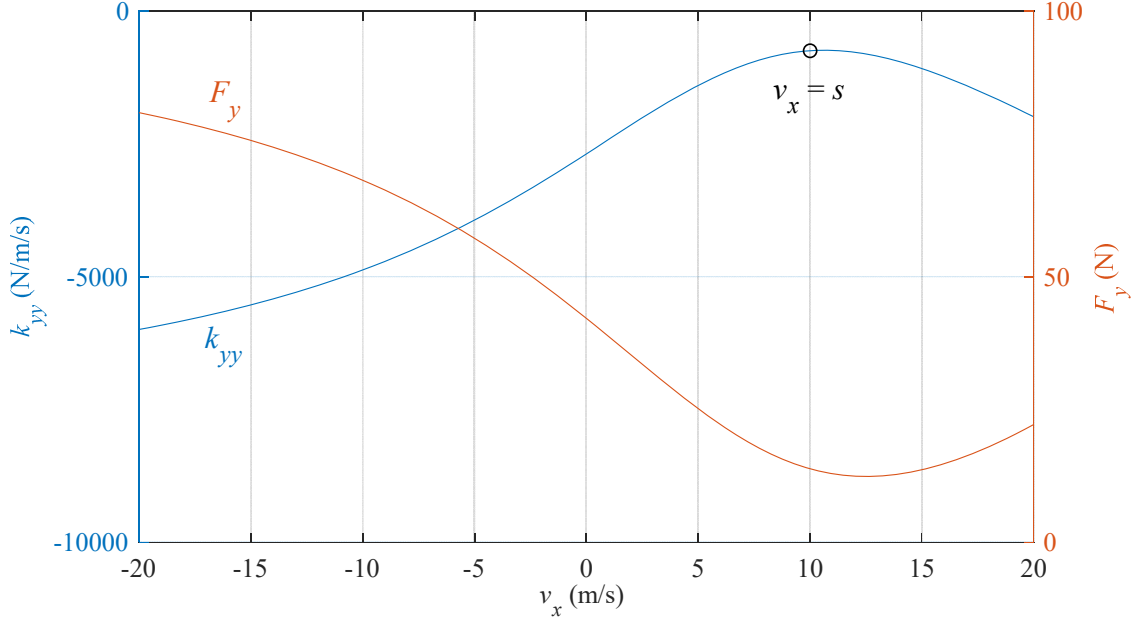


Fig. 63: Plot of k_{yy} and F_x vs. v_x when $(v_y, v_r) = (0, 10)$ m/s, $y = 10\text{mm}$ and all other positions and velocities zero

The variation of vertical force with respect to vertical velocity is shown in Fig. 64.

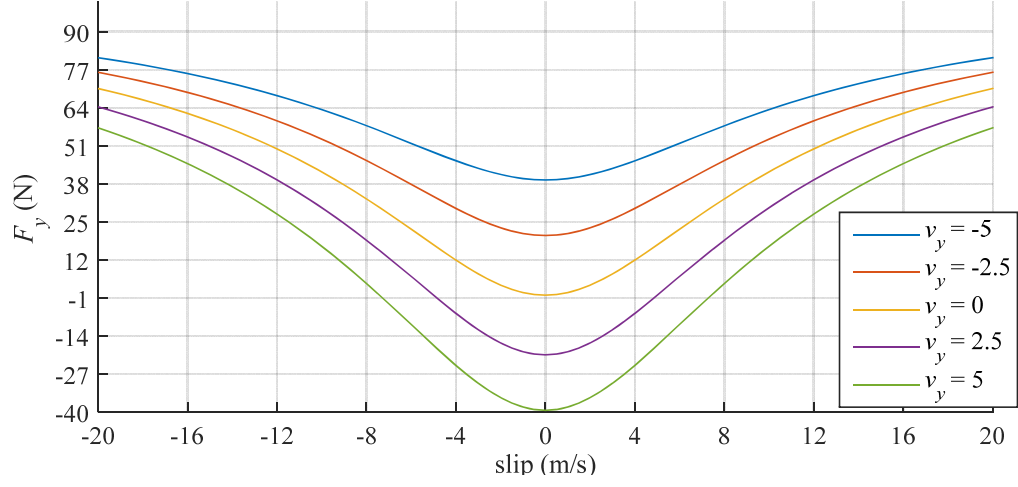


Fig. 64: F_y vs. slip for various values of v_y , $y = 10\text{mm}$, and all other positions and velocities zero

The surface and contour plots in Fig. 65 and Fig. 66 show how k_{yy} is affected by slip and v_y . k_{yy} and v_y are positively correlated, implying that increasing v_y reduces stabilizing action. More stability is observed as the slip magnitude increases. This is a fortunate dynamic, since one would expect a significant slip in order to maintain an airgap and provide thrust. Fig. 67 shows this strong linearity when rotational velocity is held such that $(v_x, v_r) = (0, 10)$ m/s. This can be exploited to simplify run-time re-calculations of k_{yy} in a state-space system.

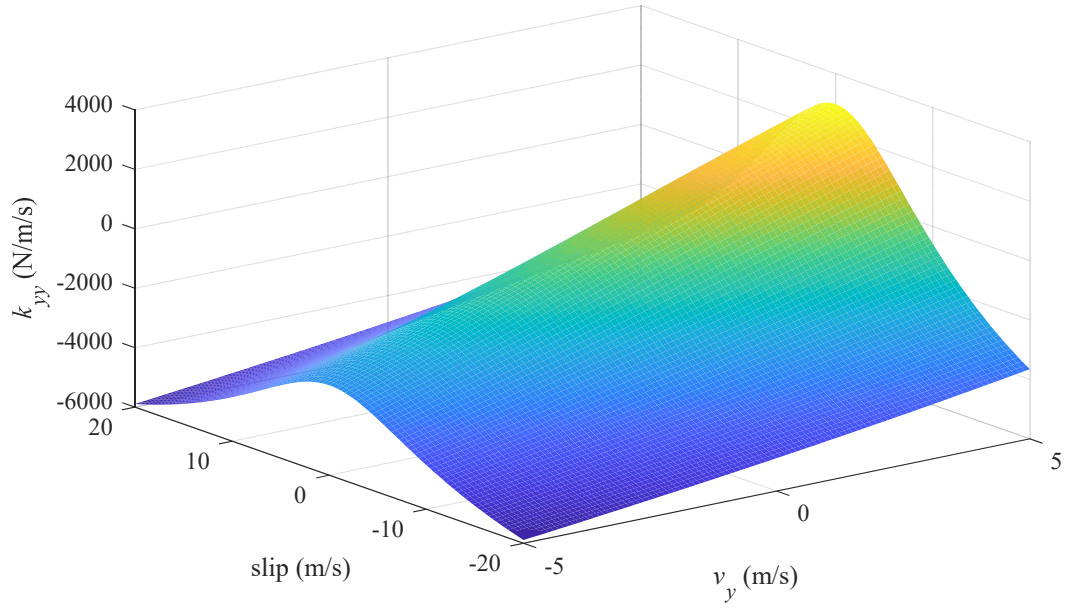


Fig. 65: Surface plot of k_{yy} vs. slip vs. v_y , $y = 10\text{mm}$, and all other positions and velocities zero (note $v_x = 0$, so slip is analogous to ω_m)

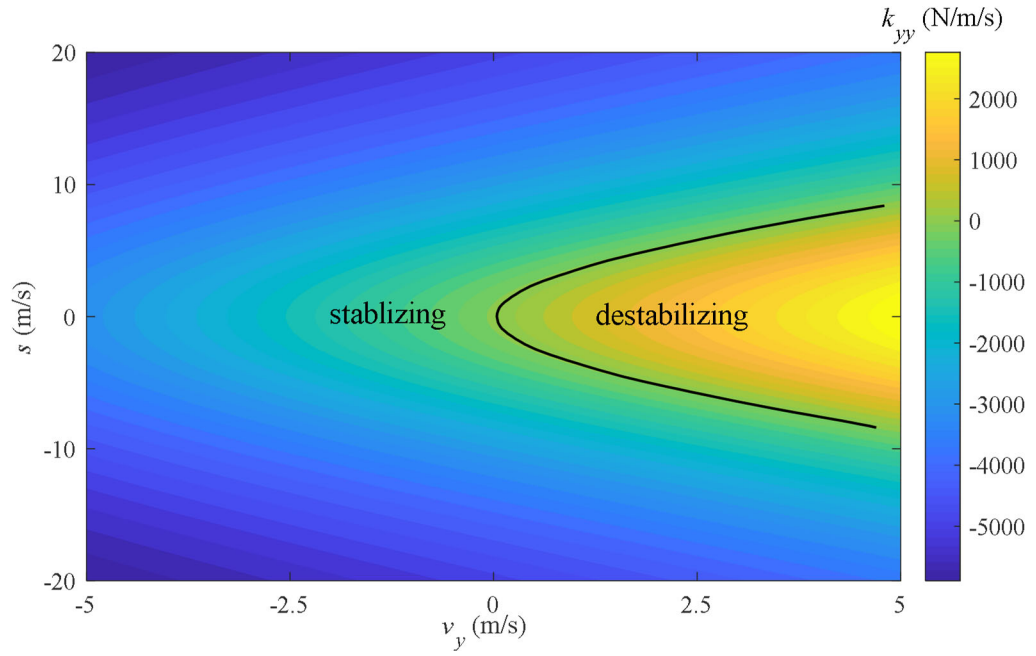


Fig. 66: Contour of k_{yy} vs. slip vs. v_y , $y = 10\text{mm}$, and all other positions and velocities zero (note $v_x = 0$, so slip is analogous to ω_m)

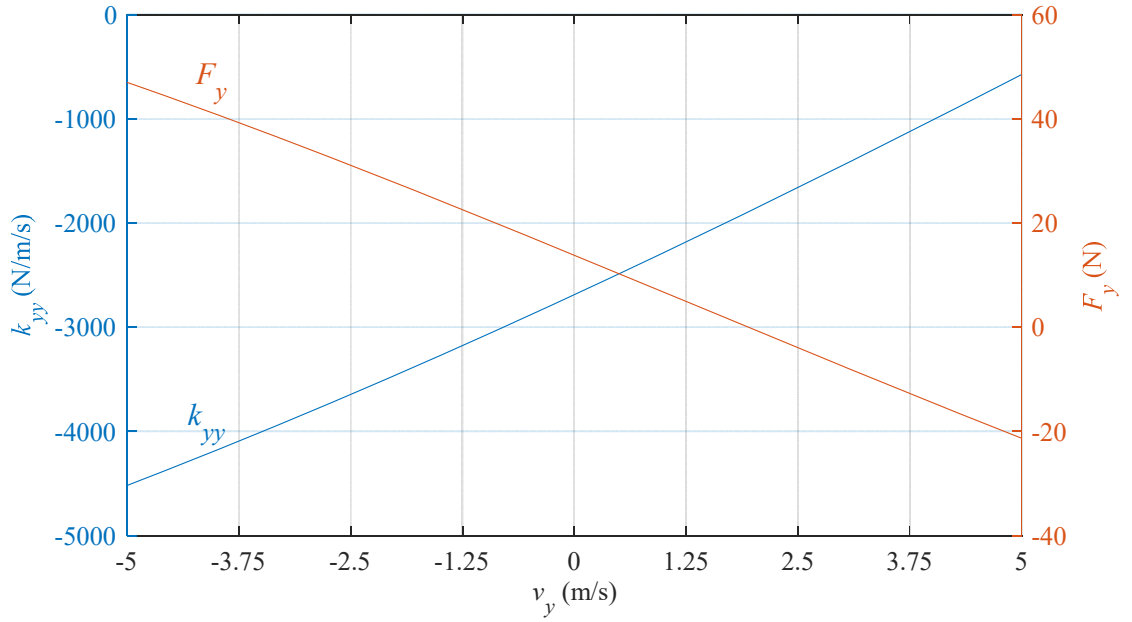


Fig. 67: Plot of k_{yy} and F_x vs. v_y when $(v_x, v_r) = (0, 10)$ m/s, $y = 10$ mm and all other positions and velocities zero

2.3.4 TRANSVERSE STIFFNESS

The transverse stiffness, k_{zz} , is defined by the partial derivative of F_z with respect to the transverse z -axis position.

$$k_{zz}(v_x, v_y, \omega_m) = \frac{\partial F_z}{\partial z} \quad (2.60)$$

The transverse stiffness is almost always destabilizing. Fig. 68 and Fig. 69 are surface and contour plots that show how it changes with slip and translational velocity and Fig. 70 and Fig. 71 are surface and contour plots that show how it changes with slip and vertical velocity, v_y . For the case when the vehicle's z -axis position is centered on the track ($\delta z = 0$), and vertical velocity is zero ($v_y = 0$), depicted by Fig. 68 and Fig. 69, the transverse force, F_z , is zero, and will become positive with any movement along the z -axis, since k_{zz}

will be positive. In fact, it is evident from the plots in the section that under most operating conditions, k_{zz} will be positive. A positive k_{zz} is deleterious to an EDW vehicle, as it causes the vehicle to move towards the side of the track, where the eddy currents will be influenced by edge effects, and finally the vehicle will catastrophically fall off the track.

Increases in slip are positively correlated with increasing k_{zz} . Interestingly increasing v_y tends to cause k_{zz} to decrease and can be a stabilizing influence. This means that the vehicle will experience a brief increase in transverse stability during an increase in the airgap (as when lifting off from a standstill), but conversely destabilization occurs when the heave velocity is in the direction that reduces the airgap.

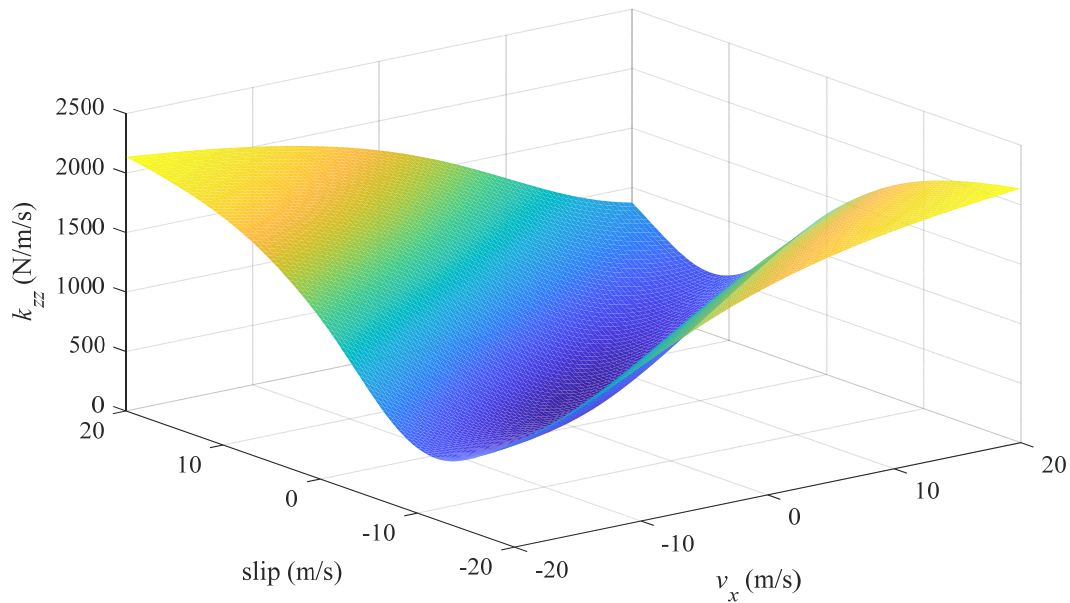


Fig. 68: Surface plot of the transverse stiffness, k_{zz} , as a function of slip, s , and translational velocity when $(x,y,z) = (0,10,0)$ mm and $(v_y,v_z) = (0, 0)$ m/s

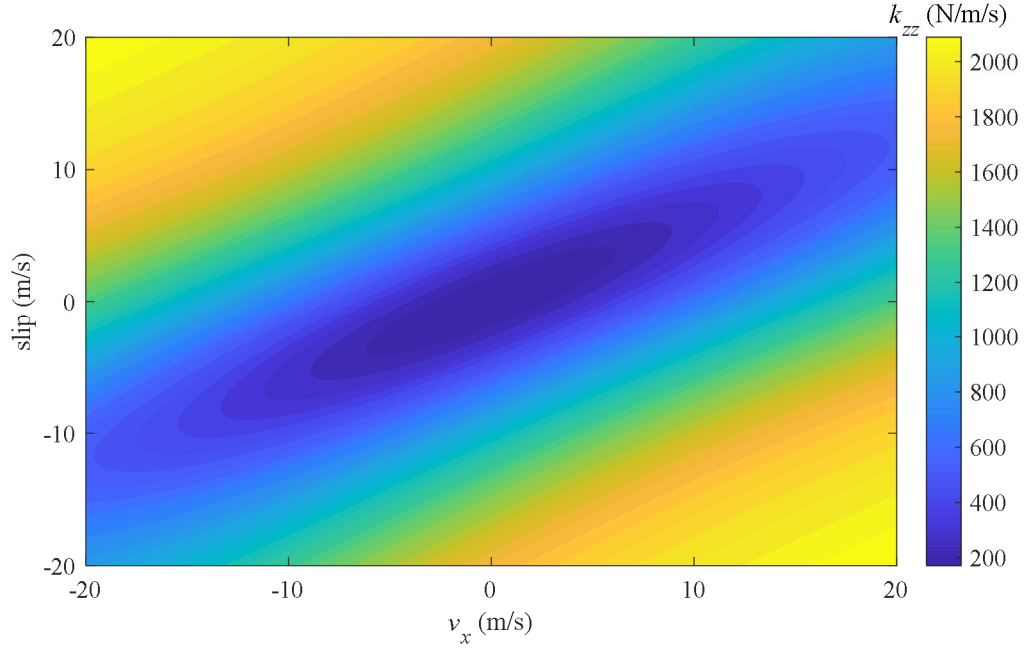


Fig. 69: Contour plot of the transverse stiffness, k_{zz} , as a function of slip, s , and translational velocity when $(x,y,z) = (0,10,0)$ mm and $(v_x,v_z) = (0, 0)$ m/s

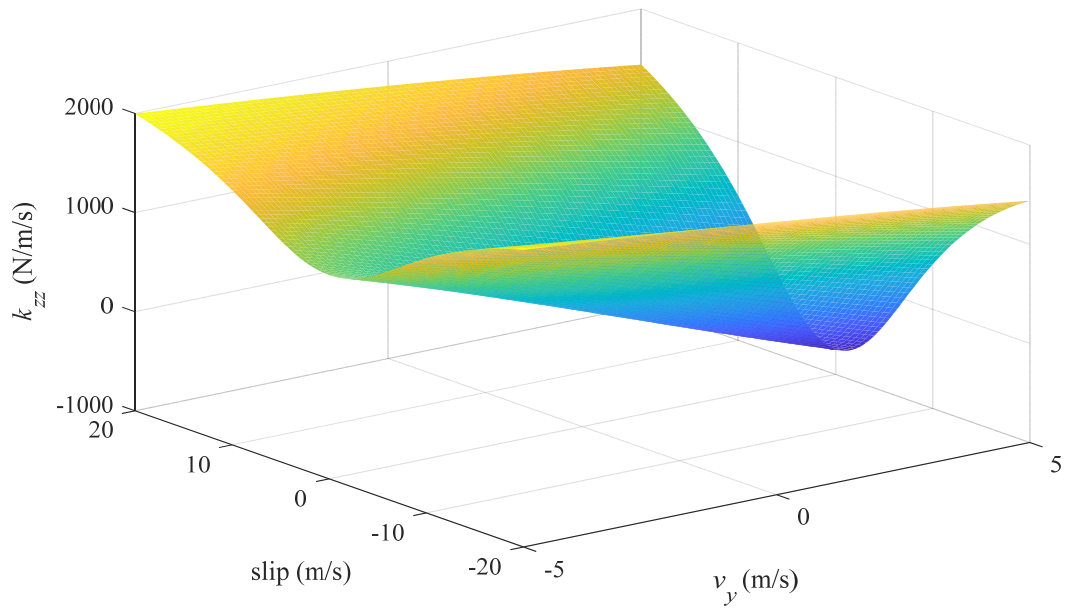


Fig. 70: Surface plot of the transverse stiffness k_{zz} vs. slip and heave, v_y when $(x,y,z) = (0,10,0)$ mm and $(v_x,v_z) = (0, 0)$ m/s

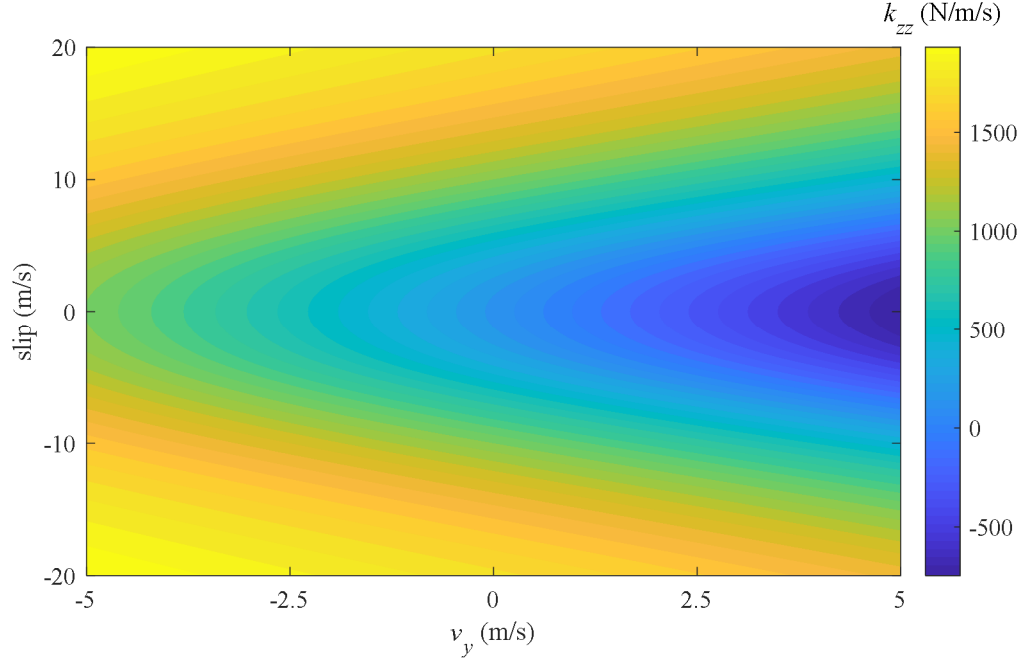


Fig. 71: Contour plot of the transverse stiffness k_{zz} vs. slip and heave, v_y , when $(x,y,z) = (0,10,0)$ mm and $(v_x,v_z) = (0, 0)$ m/s

2.3.5 TRANSVERSE THRUST STIFFNESS

The transverse thrust stiffness, k_{zx} , is defined by the partial derivative of transverse force with respect to horizontal position:

$$k_{zx}(v_x, v_y, \omega_m) = \frac{\partial F_z}{\partial x} \quad (2.61)$$

Both F_z and k_{zx} are zero when the rotor is centered above the track with no z -axis velocity. A transverse force and its partial derivatives appear when the rotor experiences a disturbance in the z direction. To illustrate how k_{zx} is affected by motion along x -axis, it is plotted versus slip and translational velocity in Fig. 72 and Fig. 73 for the case when the rotor is disturbed in the z -axis by allowing $z = 5$ mm and $v_z = 5$ m/s. It is most important to observe the behavior of k_{zx} as v_x varies, since it is expected that the vehicle will have a large

forward velocity that varies greatly during operation. The plot reveals that in the typical acceleration and cruising conditions, k_{zx} produces a restorative force, but during braking the contribution from k_{zx} will be destabilizing.

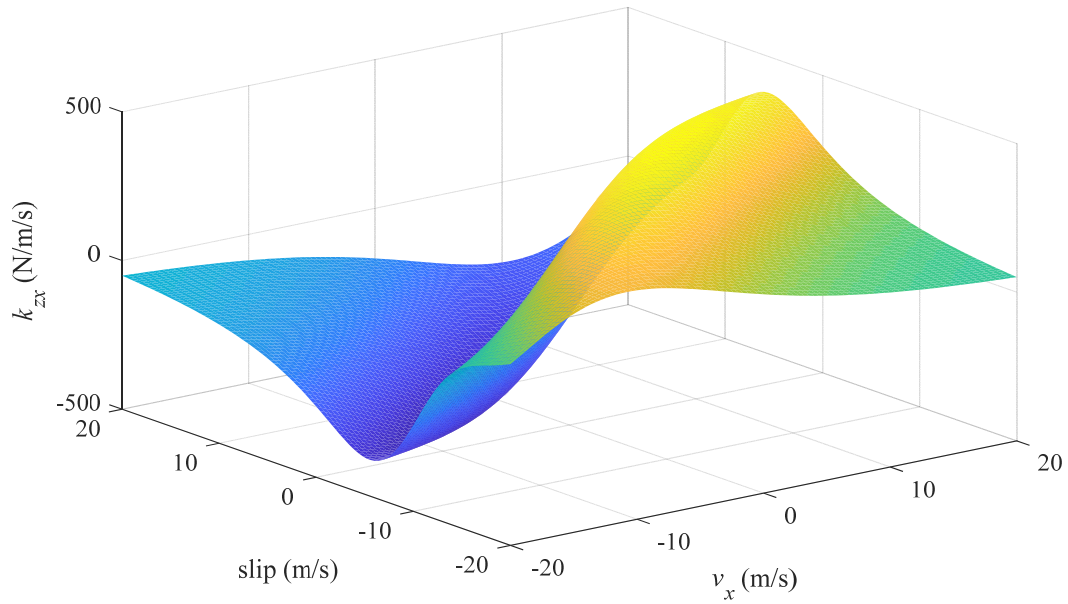


Fig. 72: Surface plot of the transverse thrust stiffness k_{zx} vs. slip and translational velocity, v_x when $(x,y,z) = (0, 10, 5)$ mm and $(v_y, v_z) = (0, 5)$ m/s

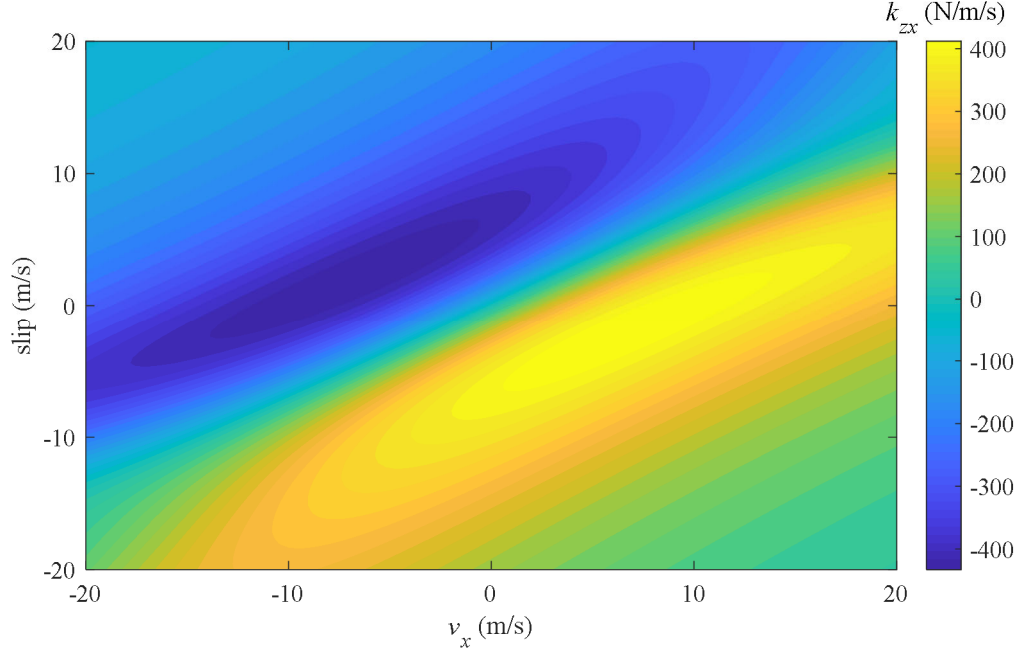


Fig. 73: Contour plot of the transverse thrust stiffness k_{zx} vs. slip and translational velocity, v_x when $(x,y,z) = (0, 10, 5)$ mm and $(v_y, v_z) = (0, 5)$ m/s

2.3.6 TRANSVERSE HEAVE STIFFNESS

The transverse heave stiffness, k_{zy} , is defined by the partial derivative of F_z with respect to the vertical y-axis position:

$$k_{zy}(v_x, v_y, \omega_m) = \frac{\partial F_z}{\partial y} \quad (2.62)$$

Similar to the transverse thrust stiffness, k_{zy} is zero for a rotor in which $(z, v_z) = (0, 0)$. Again, to observe the behavior as v_x changes, we simulate a rotor which has been disturbed in the z-axis such that $(z, v_z) = (5 \text{ mm}, 5 \text{ m/s})$, then plot the results versus slip and vertical velocity, shown in Fig. 74 and Fig. 75. The plot shows that the contribution from k_{zy} is always destabilizing in the z-axis but is particularly large roughly when $v_x = 2s$. Slip that is much larger than v_x tends to decrease k_{zy} , suggesting that lighter, more efficient vehicles

which don't require a large differential between forward velocity and slip will be more severely affected by transverse heave stiffness. A heavy vehicle with more drag will require more slip to levitate and overcome drag, thereby forcing k_{zy} closer to zero. It's also important to note that the destabilizing contribution of k_{zy} becomes significantly more pronounced in the braking region of operation.

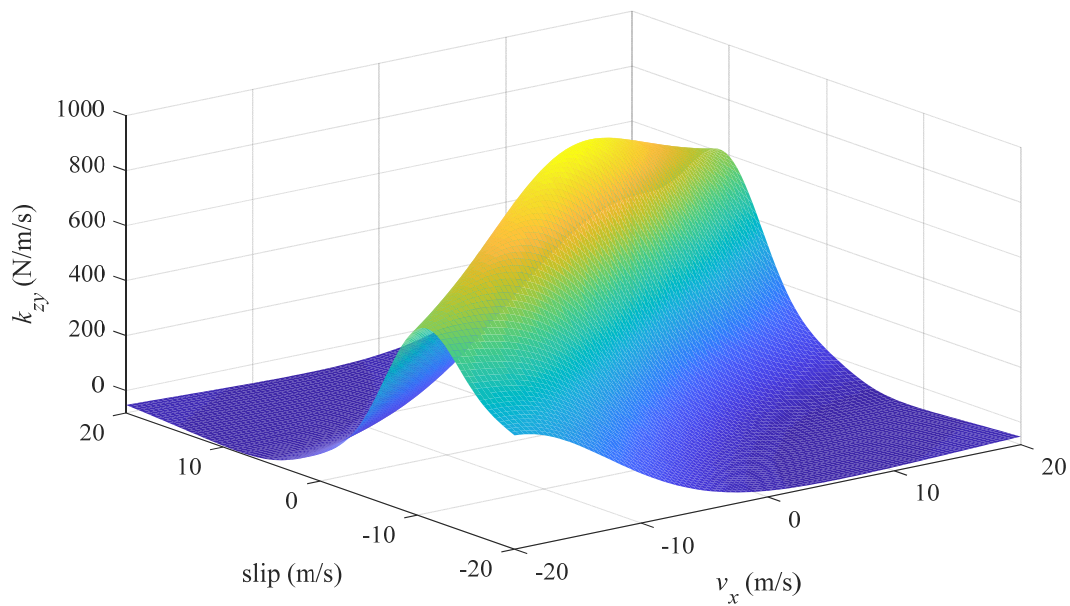


Fig. 74: Surface plot of the transverse heave stiffness k_{zy} vs. slip and translational velocity, v_x when $v_y = 0$, $v_z = 5$ m/s and $(x, y, z) = (0, 10, 5)$ mm and $(v_y, v_z) = (0, 5)$ m/s

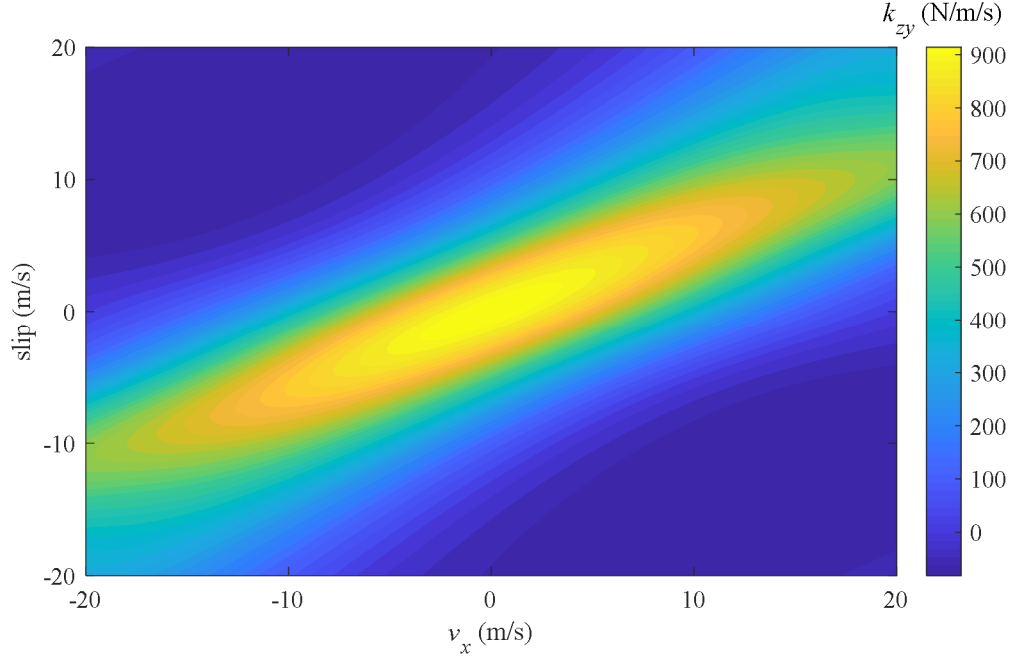


Fig. 75: Contour plot of the transverse heave stiffness k_{zy} vs. slip and translational velocity, v_x when $v_y = 0$, $v_z = 5$ m/s and $(x, y, z) = (0, 10, 5)$ mm and $(v_y, v_z) = (0, 5)$ m/s

2.3.7 THRUST TRANSLATIONAL DAMPING

Thrust translational damping is defined as the partial derivative of translational force with respect to translational velocity:

$$d_{xx}(v_x, v_y, \omega_m) = \frac{\partial F_x}{\partial v_x} \quad (2.63)$$

The surface and contour plots in Fig. 76 and Fig. 77 show how d_{xx} varies with slip and v_x . Stabilizing damping is observed near $s = v_x$. The damping increases nonlinearly as the system moves away from this line, plateauing near zero for large magnitude slip and v_x values. Fig. 78 shows the behavior of d_{xx} as v^x varies and $(v_y, v_r) = (0, 10)$ m/s. When the rotor's surface velocity matches the x velocity, the damping is minimized to produce more stable dynamics. The non-linear behavior means a more compute-intensive algorithm (ie.

the SOVP model) is required for re-calculating d_{xx} during run-time, rather than a linear interpolation. Steady-state cruising and mild to moderate braking will keep the EDW in the stable region. Heavy acceleration and emergency braking will push d_{xx} towards instability.

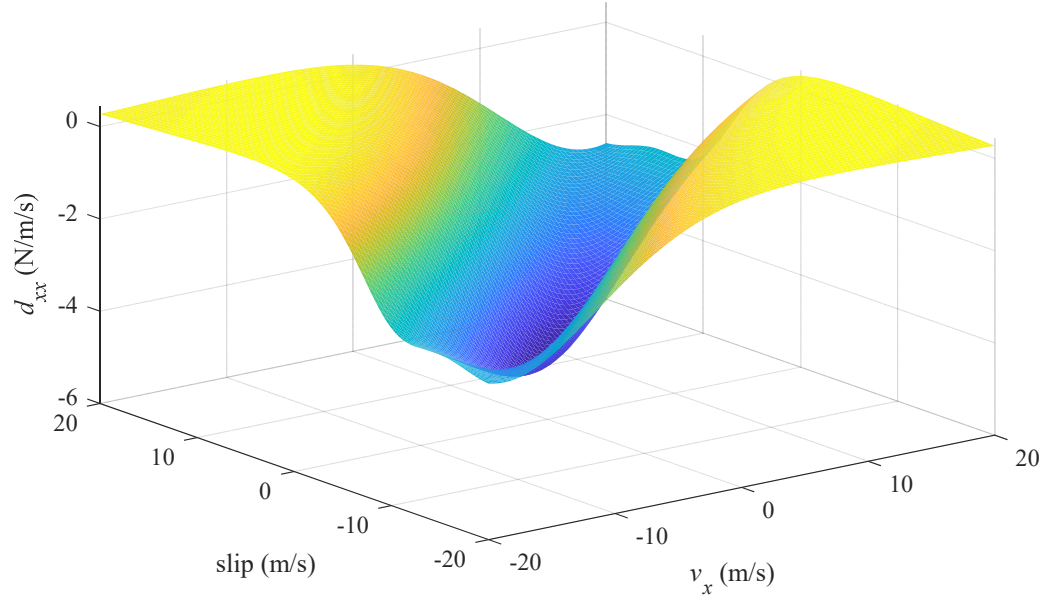


Fig. 76: Surface plot of d_{xx} vs. slip vs. v_x , ($v_y = 0$), all other positions and velocities zero

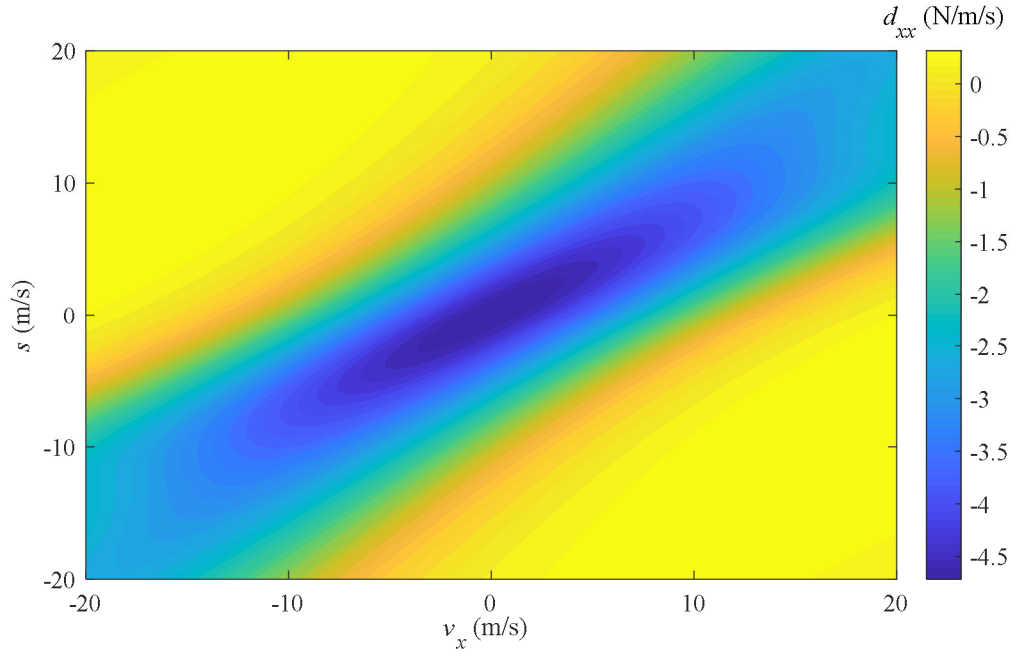


Fig. 77: Contour plot of d_{xx} vs. slip vs. v_x , ($v_y = 0$), all other positions and velocities zero

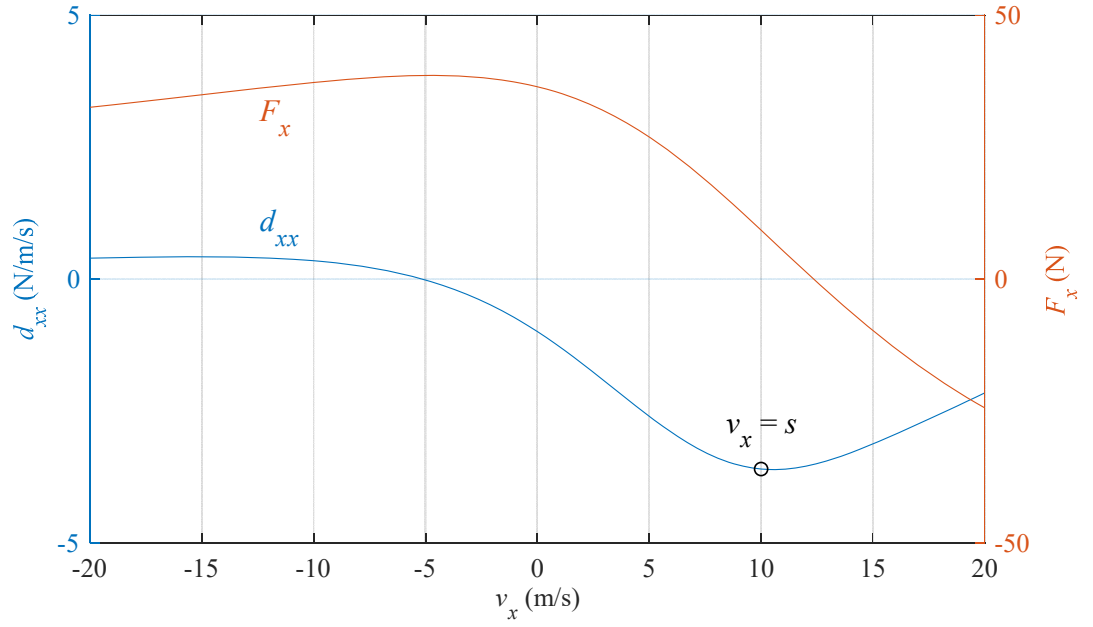


Fig. 78: Plot of d_{xx} and F_x vs. v_x when $(v_y, v_r) = (0, 10)$ m/s, all other positions and velocities zero

The surface and contour plots in Fig. 79 and Fig. 80 show the relationship of d_{xx} with respect to slip and v_y . While slices with respect to slip are non-linear, slices with respect to v_y are only weakly non-linear and for control purposes may be approximated as linear. Reduced slip magnitude and larger vertical velocities affect the stabilization on d_{xx} . During operation one would expect slip to be moderately large, which would lead to a near zero contribution on the x -axis dynamics from d_{xx} . Reduced slip during braking would cause d_{xx} to apply restorative force to the system. Fig. 81 confirms that while d_{xx} vs. v_y is not exactly linear, it could be approximated as linear within a subset of the operating region.

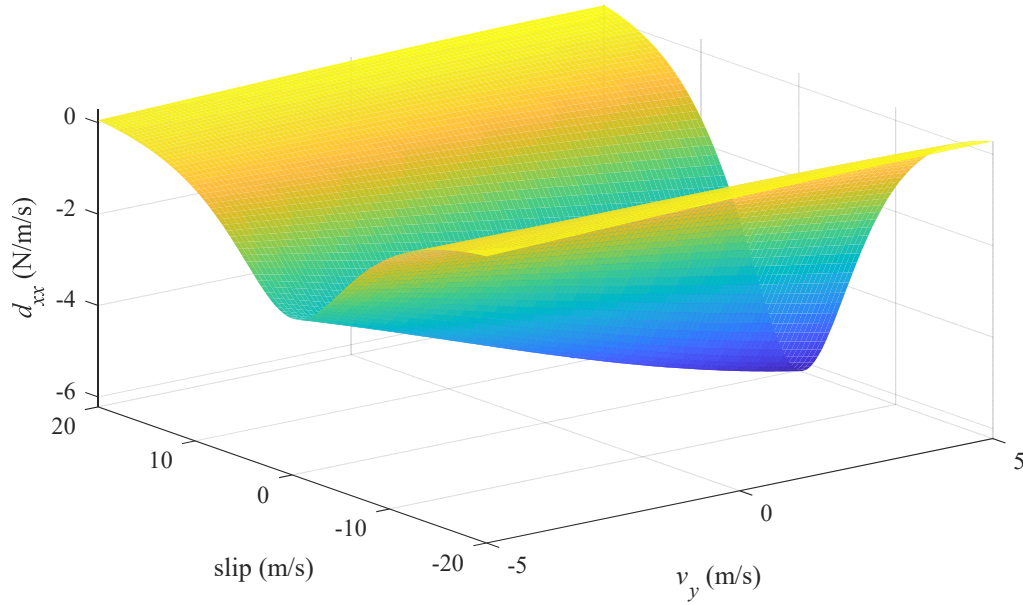


Fig. 79: Surface plot of d_{xx} vs. slip vs. v_y , all other positions and velocities zero
(note $v_x = 0$, so slip is analogous to ω_m)

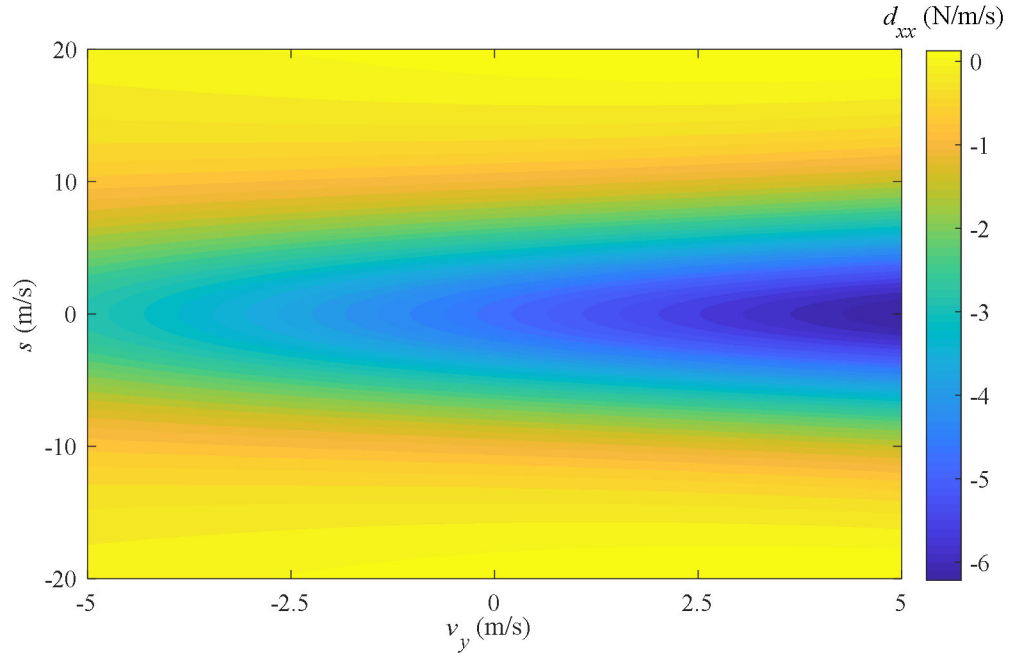


Fig. 80: Contour plot of d_{xx} vs. slip vs. v_y , all other positions and velocities zero
(note $v_x = 0$, so slip is analogous to ω_m)

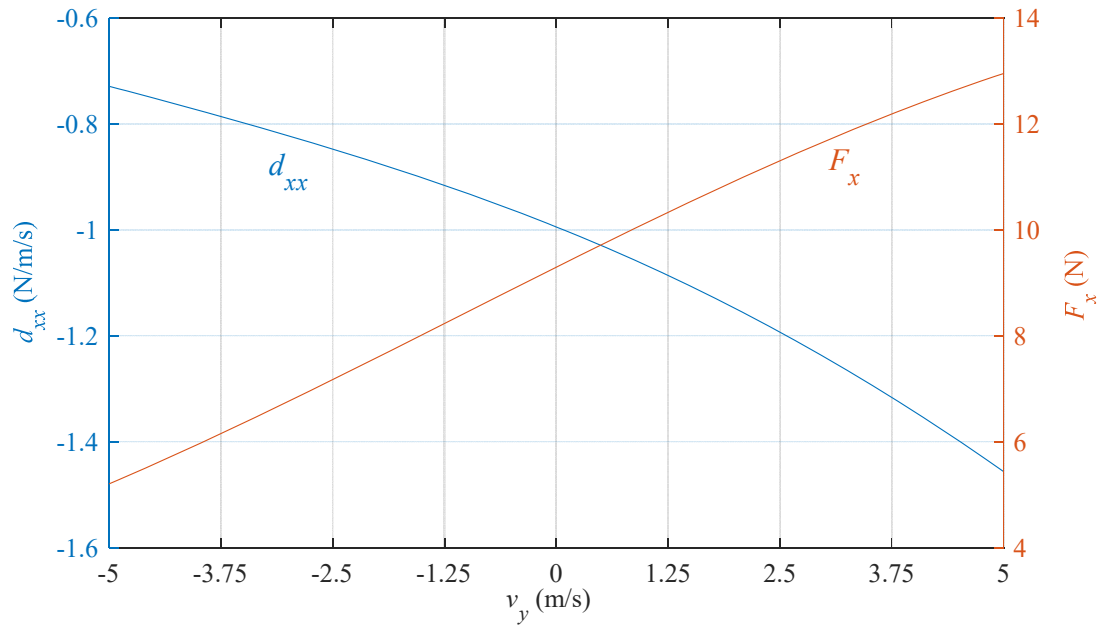


Fig. 81: Plots of d_{xx} and F_x vs. v_y when $(v_x, v_r) = (0, 10)$ m/s, all other positions and velocities zero

2.3.8 TRANSLATIONAL HEAVE DAMPING

The translational heave damping term is defined as the partial derivate of translational force with respect to vertical velocity:

$$d_{xy}(v_x, v_y, \omega_m) = \frac{\partial F_x}{\partial v_y} \quad (2.64)$$

The surface and contour plots Fig. 82 and Fig. 83 show that d_{xy} varies with v_x and slip non-linearly. The largest and smallest values of d_{xy} lie in the heavy braking operating region. Note that for negative values of the quantity $v_x - s$, the translational heave damping is stabilizing, while for positive values of $v_x - s$, it is destabilizing. The non-linearity complicates the linear modeling and control of the system, and will require updating the d_{xy} term using the analytic model during run-time to achieve high accuracy. A near-zero damping is observed when $s = v_x$. Fig. 84 shows one slice of d_{xy} vs. v_x when $(v_y, v_r) = (0, 10)$ m/s, again showing nonlinearity and the fact that faster translational velocity leads to instability in d_{xy} .

As the vehicle accelerates from a standstill, the thrust translational damping is pushed into the negative region. As v_x increases up to steady-state, the damping magnitude is decreased, but remains negative. Beyond mild braking ($s - v_x < 0$) the damping becomes positive and destabilizing.

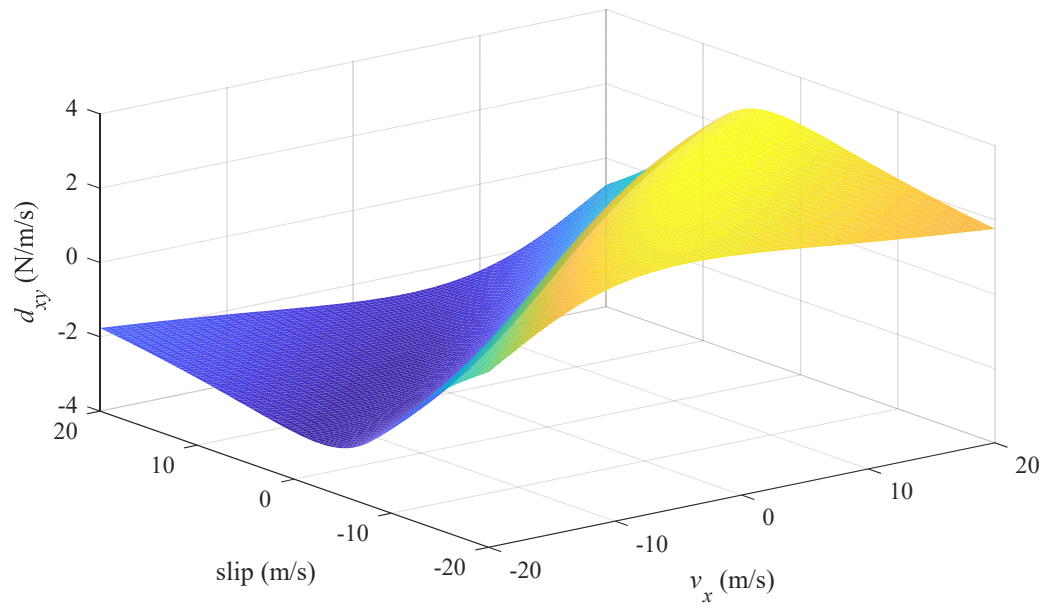


Fig. 82: Surface plot of d_{xy} vs. slip vs. v_x , ($v_y = 0$), all other positions and velocities zero

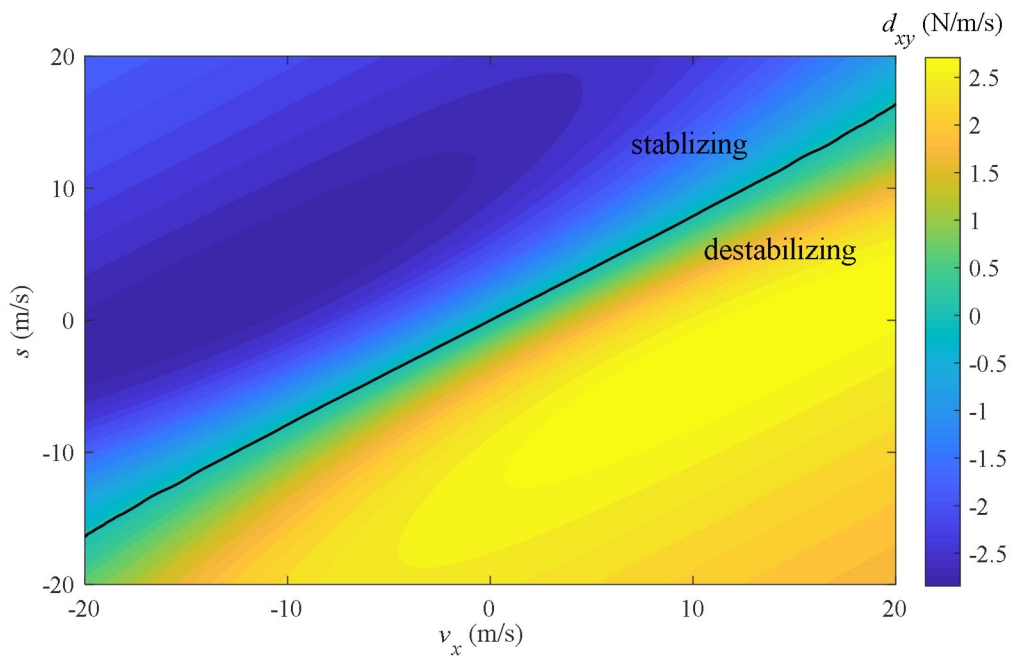


Fig. 83: Contour plot of d_{xy} vs. slip vs. v_x , ($v_y = 0$), all other positions and velocities zero

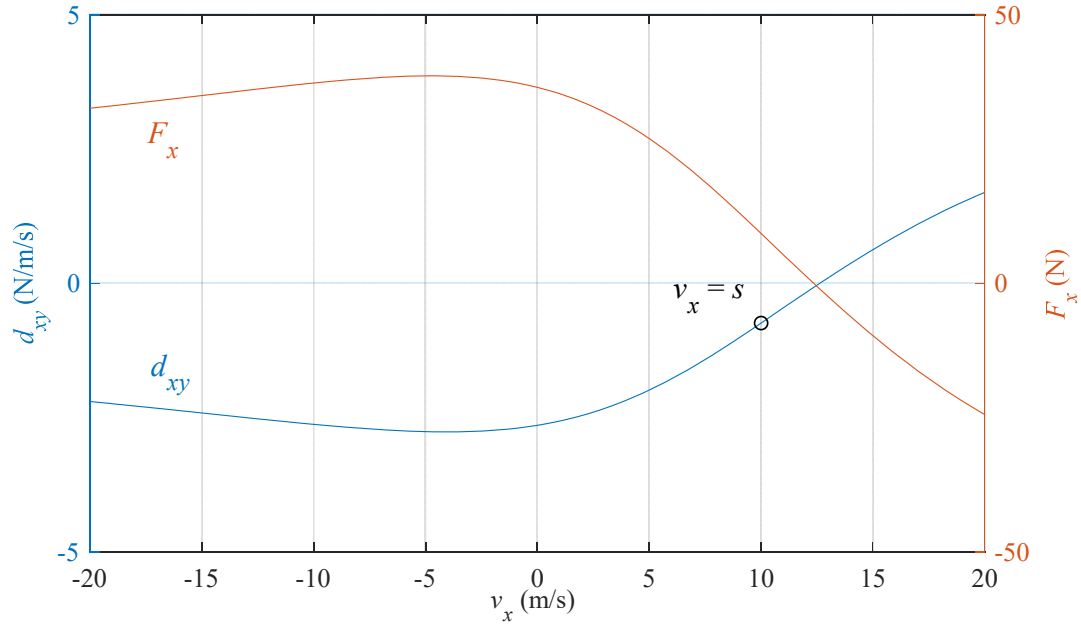


Fig. 84: Plot of d_{xy} and F_x vs. v_x when $(v_y, v_r) = (0, 10)$ m/s, all other positions and velocities zero

The surface and contour plots in Fig. 85 and Fig. 86 show how d_{xy} varies with slip and v_y . Within the reasonable operating region plotted, v_y does not have a large effect on d_{xy} . This is convenient for an accurate linearization around an operating point in this region. The nonlinear behavior with respect to slip shows that d_{xy} is negative in the expected steady-state cruising region as well as during acceleration and normal braking (where slip is positive) and is therefore stabilizing. Fig. 87 shows the approximately quadratic shape of d_{xy} with respect to v_y . To reduce compute time, d_{xy} could be approximated by a quadratic function during run-time. Note the stabilizing effect of d_{xy} when the when $(v_y, v_r) = (0, 10)$ m/s, although the stabilization becomes smaller as the magnitude of v_y increases.

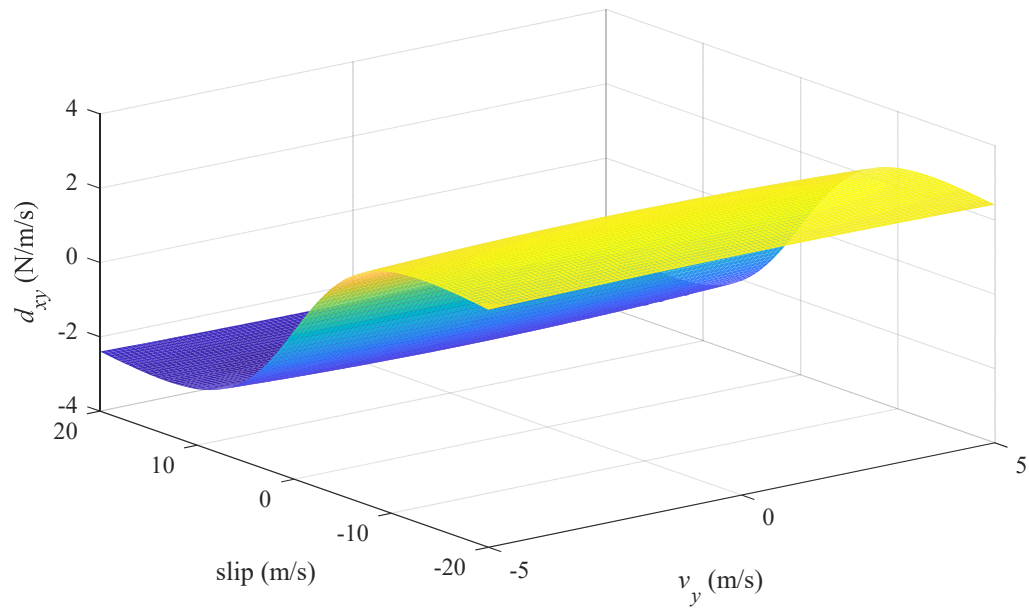


Fig. 85: Surface plot of d_{xy} vs. slip vs. v_y , all other positions and velocities zero
(note $v_x = 0$, so slip is analogous to ω_m)

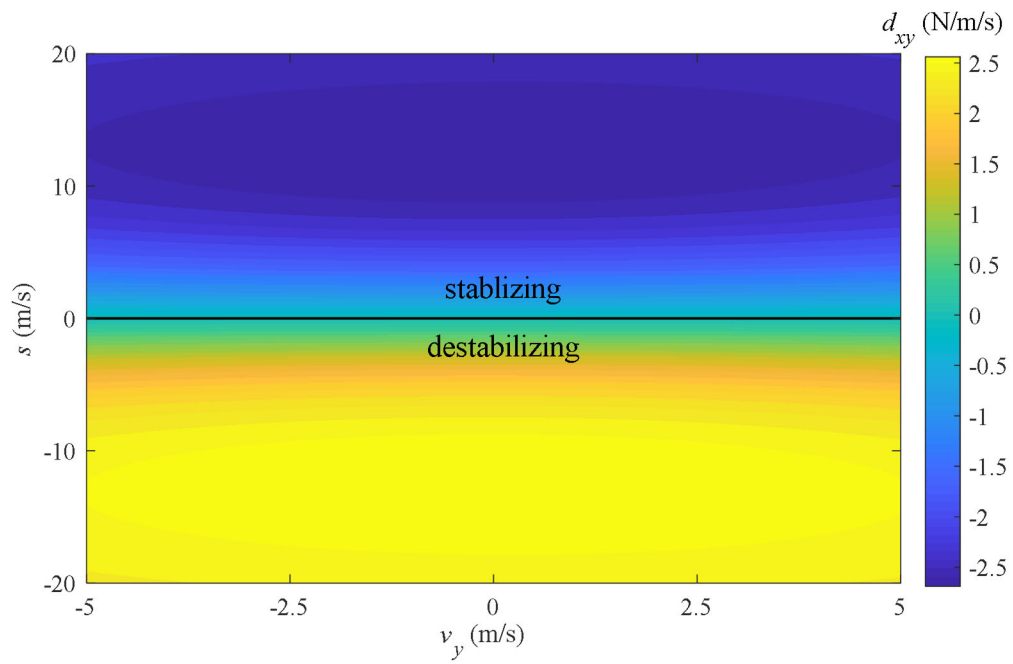


Fig. 86: Contour plot of d_{xy} vs. slip vs. v_y , all other positions and velocities zero
(note $v_x = 0$, so slip is analogous to ω_m)

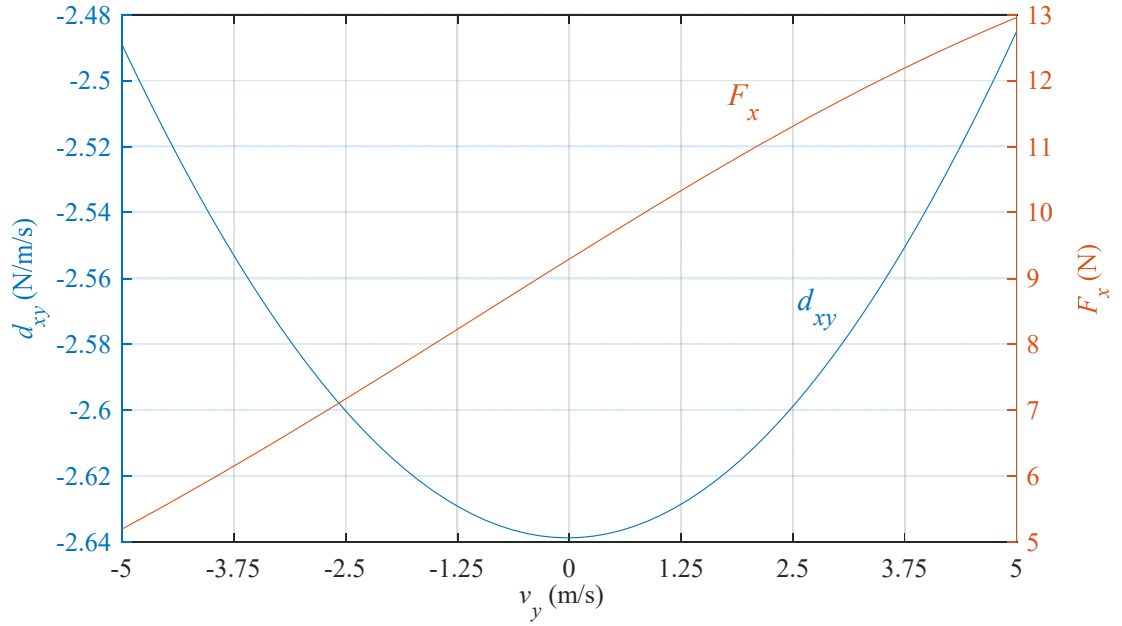


Fig. 87: Plot of d_{xy} and F_x vs. slip vs. v_y when $(v_x, v_r) = (0, 10)$ m/s, all other positions and velocities zero

2.4 CONCLUSION

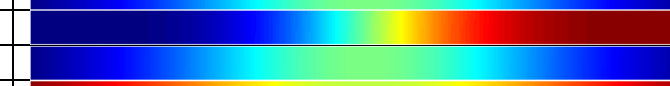
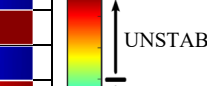
In this chapter, an exact 3-D eddy current based stiffness and damping model has been used to study the static stability of a 4-DOF EDW maglev system. The most significant damping and stiffness terms have been plotted in sections 2.3.1 through 2.3.8. Although many of the damping and stiffness terms are highly nonlinear, one can make general notes about the stability contribution of these terms in the operating region from $s = -20$ m/s to 20 m/s, $v_x = -20$ m/s to 20 m/s, and $v_y = -5$ m/s to 5 m/s.

This chapter also serves as a possible reference for real-world controller design outside of the forgiving realm of simulation-space. As discussed later in Chapter CHAPTER 5, real-time updating of the stiffness and damping terms in a controller's estimator is

important as the vehicle moves away from its starting operating conditions. The SOVP calculation time is not trivial, and with the constraints of finite computing power, knowing which terms strongly contribute destabilizing forces on the system allows a controller designer to prioritize which terms are updated first and/or more frequently.


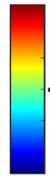





The stability of the selected damping and stiffness terms in relation to v_x when $(s, v_y) = (0, 0)$ is shown in Table 2. Note that k_{xy} and d_{xy} are unstable when v_x is positive, and d_{xx} becomes unstable if the magnitude of v_x becomes large enough. Another positive feedback loop exists between k_{xx} and d_{xy} for positive v_x values, since k_{xx} can exert more effect on F_x (and therefore v_x) with larger δy , and d_{xy} becomes increasingly unstable with larger v_x . The value of k_{zz} is infinitesimal as translational velocity moves towards zero, but grows large as the magnitude of v_x increases.

Table 2: Stability of damping and stiffness terms when $s = 0$, $v_y = 0$, and v_x varies

| Term | v_x (m/s) | | | | | Legend |
|----------|--|-----|---|----|----|---|
| | -20 | -10 | 0 | 10 | 20 | |
| k_{xx} |  | | | | |  |
| k_{xy} | | | | | | |
| k_{yy} | | | | | | |
| k_{zz} | | | | | | |
| d_{xx} | | | | | | |
| d_{xy} | | | | | | |

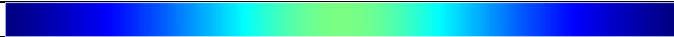
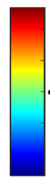

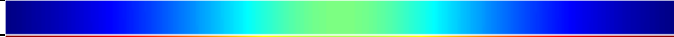



The stability in relation to v_y when $(s, v_x) = (0, 0)$ is shown in Table 3, which indicates that k_{xx} and k_{yy} are unstable when v_y is positive, and that v_y does not have a strong influence on k_{xy} and d_{xy} at this operating point. At $v_y = 0$, k_{zz} is zero, but becomes increasingly unstable with increasing vertical velocity and increasingly stable with decreasing vertical velocity.

Table 3: Stability of damping and stiffness terms when $s = 0$, $v_x = 0$, and v_y varies

| Term | v_y (m/s) | | | | | Legend |
|----------|--|------|---|-----|-----|---|
| | -5 | -2.5 | 0 | 2.5 | 2.5 | |
| k_{xx} |  | | | | |  UNSTABLE STABLE |
| k_{xy} |  | | | | | |
| k_{yy} |  | | | | | |
| k_{zz} |  | | | | | |
| d_{xx} |  | | | | | |
| d_{xy} |  | | | | | |

Finally, the stability in relation to s when $(v_x, v_y) = (0, 0)$ is shown in Table 4. In this case, k_{xy} and d_{xy} are unstable when s is negative and d_{xx} becomes weakly unstable when the magnitude of s becomes large. k_{zz} is always positive and tends to become further unstable as slip increases in magnitude. The synergistic effect, or a positive feedback loop, when k_{xy} and d_{xy} are both positive, is also present with the slip dynamic as it was with v_x .

Table 4: Stability of damping and stiffness terms when $v_y = 0$, $v_x = 0$, and s varies

| Term | s (m/s) | | | | | Legend |
|----------|--|-----|---|----|----|---|
| | -20 | -10 | 0 | 10 | 20 | |
| k_{xx} |  | | | | |  UNSTABLE STABLE |
| k_{xy} |  | | | | | |
| k_{yy} |  | | | | | |
| k_{zz} |  | | | | | |
| d_{xx} |  | | | | | |
| d_{xy} |  | | | | | |

It is worth noting that the damping exhibited by the EDW system is rather small in comparison to the stiffness. Using a simple mass-spring-damper system as an analogous example, where the system's equation of motion is:

$$m \frac{d^2 x}{dt^2} + c \frac{dx}{dt} + kx = 0 \quad (2.65)$$

where c is the damping coefficient and k is the stiffness coefficient. As an illustrative example, consider the 1-dimensional EDW system in the x -axis, such that

$$c = -d_{xx} \quad (2.66)$$

$$k = -k_{xx} \quad (2.67)$$

The critical damping ratio,

$$c_c = 2\sqrt{km} \quad (2.68)$$

would be quite large for a vehicle operating at cruise. For a cruising point of $v_x = 10$ m/s, $v_y = 0$ m/s, and $s = 16$ m/s, and parameters defined by Table 1,

$$c_c = 201.03 \text{ [N/m/s]} \quad (2.69)$$

$$c = 2.143 \text{ [N/m/s]} \quad (2.70)$$

The damping ratio is therefore

$$\zeta = \frac{c}{c_c} = 0.0107 \quad (2.71)$$

Although the system is stable, it is quite underdamped. This behavior is observed for other axes as well. Weak damping is one of the reasons that the EDW system necessitates an active control method.

CHAPTER 3: MAGLEV VEHICLE DYNAMIC MODEL

In this Chapter, equations of motion are derived for the prototype maglev vehicle in 4 degrees of freedom. These equations will be used later to represent the system in state-space form. Section 3.1 defines the vehicle motion about each axis, section 3.2 defines the forces generated by each EDW, and sections 3.3, 3.4, 3.5, and 3.6 define the vehicle's height, roll, pitch, and yaw motion, respectively. The equations of motion are written in terms of EDW rotational velocities, but will be expanded to include motor dynamics in chapter CHAPTER 4:. Note that while not explicitly notated in the equations, all of the vehicle's motions and forces are varying in time.

3.1 AXIS MOTION DEFINITIONS

The 2nd law of motion in an inertial system is:

$$\mathbf{F} = m\dot{\mathbf{v}} \quad (3.1)$$

where \mathbf{F} is the net force vector, m is the mass of the vehicle, \mathbf{v} is the net velocity vector, and

$$\mathbf{F} = F_x\hat{\mathbf{x}} + F_y\hat{\mathbf{y}} + F_z\hat{\mathbf{z}} \quad (3.2)$$

$$\mathbf{v} = v_x\hat{\mathbf{x}} + v_y\hat{\mathbf{y}} + v_z\hat{\mathbf{z}} \quad (3.3)$$

where F_x, F_y, F_z and v_x, v_y, v_z are the forces and velocities, respectively, acting in a reference frame $\hat{\mathbf{x}}, \hat{\mathbf{y}}, \hat{\mathbf{z}}$. The reference frame used for controlling the maglev vehicle is

$$[\hat{\mathbf{x}} \quad \hat{\mathbf{y}} \quad \hat{\mathbf{z}}]^T = \begin{bmatrix} 1 & 0 & 0 \\ 0 & 1 & 0 \\ 0 & 0 & 1 \end{bmatrix} \quad (3.4)$$

as described by Fig. 38 and Fig. 41 - Fig. 44, although the equations are left more general until necessary. The rotation in an inertial system is governed by

$$\mathbf{M} = \dot{\mathbf{H}} \quad (3.5)$$

The moment vector \mathbf{M} can be written as

$$\mathbf{M} = M_x \hat{\mathbf{x}} + M_y \hat{\mathbf{y}} + M_z \hat{\mathbf{z}} \quad [\text{Nm}] \quad (3.6)$$

where M_x , M_y , and M_z are the moments acting in the aforementioned reference frame and \mathbf{H} is the angular momentum:

$$\mathbf{H} = \mathbf{I}\boldsymbol{\omega}^T \quad (3.7)$$

Note that the superscript T denotes transposition and

$$\boldsymbol{\omega} = \omega_x \hat{\mathbf{x}} + \omega_y \hat{\mathbf{y}} + \omega_z \hat{\mathbf{z}} \quad [\text{rad/s}] \quad (3.8)$$

where ω_x , ω_y , and ω_z denote the vehicles rotation in the $\hat{\mathbf{x}}$, $\hat{\mathbf{y}}$, $\hat{\mathbf{z}}$ reference frame and the inertia matrix is

$$\mathbf{I} = \begin{bmatrix} I_{xx} & I_{xy} & I_{xz} \\ I_{yx} & I_{yy} & I_{yz} \\ I_{zx} & I_{zy} & I_{zz} \end{bmatrix} \quad [\text{kgm}^2] \quad (3.9)$$

The inertia components written in the form I_{pq} can be interpreted as the inertia in the p^{th} axis when the vehicle rotates about the q^{th} axis. Assuming our coordinate system is located at the principal axis of inertia then

$$\mathbf{I} = \begin{bmatrix} I_{xx} & 0 & 0 \\ 0 & I_{yy} & 0 \\ 0 & 0 & I_{zz} \end{bmatrix} \quad (3.10)$$

Equations (3.1) and (3.5) are only valid in an inertial frame [36]. If a body fixed frame is rotating with rotation vector $\boldsymbol{\omega}$ then for any vector \mathbf{u} the time derivative of \mathbf{u} is given by

$$\dot{\mathbf{u}}|_I = \dot{\mathbf{u}}|_B + \boldsymbol{\omega} \times \mathbf{u} \quad (3.11)$$

where subscripts I and B denote inertial and body fixed reference frame, respectively.

Therefore, utilizing (3.11) equations (3.1) and (3.5) become:

$$\mathbf{F} = m \dot{\mathbf{v}}|_B + m \boldsymbol{\omega} \times \mathbf{v} \quad (3.12)$$

$$\mathbf{M} = \dot{\mathbf{H}}|_B + \boldsymbol{\omega} \times \mathbf{H} \quad (3.13)$$

Expanding out (3.12) one obtains

$$\begin{bmatrix} F_x \\ F_y \\ F_z \end{bmatrix} = m \begin{bmatrix} \dot{v}_x \\ \dot{v}_y \\ \dot{v}_z \end{bmatrix} + m \begin{vmatrix} \hat{\mathbf{x}} & \hat{\mathbf{y}} & \hat{\mathbf{z}} \\ \omega_x & \omega_y & \omega_z \\ v_x & v_y & v_z \end{vmatrix} \quad (3.14)$$

Evaluating (3.14) gives

$$\begin{bmatrix} F_x \\ F_y \\ F_z \end{bmatrix} = m \begin{bmatrix} \dot{v}_x + \omega_y v_z - \omega_z v_y \\ \dot{v}_y - \omega_x v_z + \omega_z v_x \\ \dot{v}_z + \omega_x v_y - \omega_y v_x \end{bmatrix} \quad (3.15)$$

Substituting (3.7) into (3.13) gives

$$\mathbf{M} = \dot{\mathbf{H}}|_B + \boldsymbol{\omega} \times \mathbf{I} \boldsymbol{\omega}^T \quad (3.16)$$

Substituting (3.10) and (3.8) into (3.16) yields

$$\begin{bmatrix} M_x \\ M_y \\ M_z \end{bmatrix} = \begin{bmatrix} \dot{H}_x \\ \dot{H}_y \\ \dot{H}_z \end{bmatrix} + \boldsymbol{\omega} \times \begin{bmatrix} I_{xx} & 0 & 0 \\ 0 & I_{yy} & 0 \\ 0 & 0 & I_{zz} \end{bmatrix} \begin{bmatrix} \omega_x \\ \omega_y \\ \omega_z \end{bmatrix} \quad (3.17)$$

Substituting (3.8) and (3.10) into (3.7), the first term in (3.17) is:

$$\dot{\mathbf{H}} = \begin{bmatrix} I_{xx} & 0 & 0 \\ 0 & I_{yy} & 0 \\ 0 & 0 & I_{zz} \end{bmatrix} \begin{bmatrix} \dot{\omega}_x \\ \dot{\omega}_y \\ \dot{\omega}_z \end{bmatrix} = \begin{bmatrix} I_{xx} \dot{\omega}_x \\ I_{yy} \dot{\omega}_y \\ I_{zz} \dot{\omega}_z \end{bmatrix} \quad (3.18)$$

Evaluating the cross product term in (3.17) and substituting (3.18) into (3.17) gives

$$\begin{bmatrix} M_x \\ M_y \\ M_z \end{bmatrix} = \begin{bmatrix} I_{xx}\dot{\omega}_x + \omega_y\omega_z I_{zz} - \omega_z\omega_y I_{yy} \\ I_{yy}\dot{\omega}_y - \omega_x\omega_z I_{zz} + \omega_z\omega_x I_{xx} \\ I_{zz}\dot{\omega}_z + \omega_x\omega_y I_{yy} - \omega_y\omega_x I_{xx} \end{bmatrix} \quad (3.19)$$

Rearranging (3.15) and (3.19) yields a set of 6 first order differential equations

$$\dot{v}_x = \frac{F_x}{m} - \omega_y v_z + \omega_z v_y \quad (3.20)$$

$$\dot{v}_y = \frac{F_y}{m} + \omega_x v_z - \omega_z v_x \quad (3.21)$$

$$\dot{v}_z = \frac{F_z}{m} - \omega_x v_y + \omega_y v_x \quad (3.22)$$

$$\dot{\omega}_x = [M_x - \omega_y\omega_z I_{zz} + \omega_z\omega_y I_{yy}] / I_{xx} \quad (3.23)$$

$$\dot{\omega}_y = [M_y + \omega_x\omega_z I_{zz} - \omega_z\omega_x I_{xx}] / I_{yy} \quad (3.24)$$

$$\dot{\omega}_z = [M_z - \omega_x\omega_y I_{yy} + \omega_y\omega_x I_{xx}] / I_{zz} \quad (3.25)$$

3.2 FOUR DEGREES OF FREEDOM MODEL

The EWV, shown in Fig. 37, is constrained to move dynamically only in the vertical, or y -direction. Therefore it is assumed that

$$x = 0 \quad (3.26)$$

$$z = 0 \quad (3.27)$$

$$v_x \approx 0 \quad (3.28)$$

$$v_z \approx 0 \quad (3.29)$$

Note that although the vehicle's center of mass does not vary in the x or z direction, it is free to rotate about any axis. In order to model the EWV in this way, a 4-degree-of-freedom model is required. The variable definitions for the model are shown in Fig. 41 through Fig. 44 and the EDW numbering is shown in Fig. 38. The heights, y_1, y_2, y_3, y_4 are the airgaps between each EDW and the aluminum guideway. The average vehicle airgap height is:

$$y \cong (y_1 + y_2 + y_3 + y_4) / 4 \quad (3.30)$$

Defining:

$$y_{12} = \frac{y_1 + y_2}{2} \quad (3.31)$$

$$y_{34} = \frac{y_3 + y_4}{2} \quad (3.32)$$

$$\sin(\theta_x) = \frac{y_{34} - y_{12}}{2w} \quad (3.33)$$

Substituting (3.31) and (3.32) into (3.33) yields

$$\sin(\theta_x) = \frac{y_4 + y_3 - y_2 - y_1}{4w} \quad (3.34)$$

Equation (3.34) can be approximated using the small angle approximation of sine from the air-gap heights of each rotor:

$$\theta_x \cong \frac{y_3 + y_4 - y_1 - y_2}{4w} \quad (3.35)$$

and the vehicle pitch angle, θ_z , can be similarly approximated:

$$\theta_z \cong \frac{y_3 + y_2 - y_1 - y_4}{4l} \quad (3.36)$$

This is a practical method of measuring the angles as the rotor heights are measured using laser sensors. Using a small angle approximation is reasonable since the EWV is assumed to always operate with a small angle offset. The vehicles roll and pitch angular velocity are defined as

$$\dot{\theta}_x = \omega_x \quad (3.37)$$

$$\dot{\theta}_z = \omega_z \quad (3.38)$$

The vehicles *average* vertical velocity is defined as

$$\dot{y} = v_y \quad (3.39)$$

while the vertical velocity associated with each EDW air-gap will be

$$\dot{y}_n = v_{yn} \quad (3.40)$$

where subscript n denotes the corner number ($n = 1, 2, 3, 4$) as shown in Fig. 38. Assuming that the lateral force is zero

$$F_z = 0 \quad (3.41)$$

and with (3.26)-(3.29) equations (3.20)-(3.25) simplify down to

$$0 = F_x - \omega_z v_y \quad (3.42)$$

$$\dot{v}_y = F_y / m \quad (3.43)$$

$$0 = [-\omega_x v_y + \omega_y v_x] / m \quad (3.44)$$

$$\dot{\omega}_x = [M_x - \omega_y \omega_z I_{zz} + \omega_z \omega_y I_{yy}] / I_{xx} \quad (3.45)$$

$$\dot{\omega}_y = [M_y + \omega_x \omega_z I_{zz} - \omega_z \omega_x I_{xx}] / I_{yy} \quad (3.46)$$

$$\dot{\omega}_z = [M_z - \omega_x \omega_y I_{yy} + \omega_y \omega_x I_{xx}] / I_{zz} \quad (3.47)$$

Note that as it is assumed that ω_x , ω_y , ω_z , and v_y are all small (and less than 1), then, when linearized, the products $\omega_z v_y$, $\omega_x v_y$, $\omega_y v_x$, $\omega_y \omega_z$, $\omega_x \omega_z$, $\omega_x \omega_y$ will be very small. This makes (3.42) and (3.44) close enough to zero to be trivial, and components of (3.45)-(3.47) will also be approximately zero. The result is a set of four simplified second order differential equations

$$\dot{v}_y \cong F_y / m \quad (3.48)$$

$$\dot{\omega}_x \cong M_x / I_{xx} \quad (3.49)$$

$$\dot{\omega}_y \cong M_y / I_{yy} \quad (3.50)$$

$$\dot{\omega}_z \cong M_z / I_{zz} \quad (3.51)$$

The vehicle is prevented from moving along the x and z axes. The eddy current force created by each EDW is a function of the height, velocity and angular velocity. The force is calculated using the force terms given by Paul [31][35] in equation (2.25). The directions of the EDW forces are shown in Fig. 41 through Fig. 44. The total vertical force will be

$$\begin{aligned} F_y = & F_1^y(y_1, v_{y1}, \omega_{m1}) + F_2^y(y_2, v_{y2}, \omega_{m2}) \\ & + F_3^y(y_3, v_{y3}, \omega_{m3}) + F_4^y(y_4, v_{y4}, \omega_{m4}) - mg \end{aligned} \quad (3.52)$$

where F_n^y represents the vertical force on the n^{th} rotor. Note that sometimes force components are written using a subscript only notation rather than a subscript and superscript notation which is often used to shorten equations. These are used

interchangeably and can be thought of as equivalent, so that an arbitrary force F_n^m is equivalent to F_{mn} . Referring to Fig. 42 the moment vector around the x -axis will be

$$M_x = [F_3^y(y_2, v_{y2}, \omega_{m2}) + F_4^y(y_3, v_{y3}, \omega_{m3}) - F_1^y(y_4, v_{y4}, \omega_{m4}) - F_2^y(y_1, v_{y1}, \omega_{m1})]w \quad (3.53)$$

Referring to Fig. 44, the moment vector around the y -axis will be

$$M_y = [F_1^x(y_2, v_{y2}, \omega_{m2}) + F_2^x(y_3, v_{y3}, \omega_{m3}) - F_3^x(y_4, v_{y4}, \omega_{m4}) - F_4^x(y_1, v_{y1}, \omega_{m1})]w \quad (3.54)$$

where F_n^x represents the x -axis force on the n^{th} rotor. Referring Fig. 43, the moment vector around the z -axis will be

$$M_z = [F_2^y(y_1, v_{y1}, \omega_{m1}) + F_3^y(y_2, v_{y2}, \omega_{m2}) - F_1^y(y_3, v_{y3}, \omega_{m3}) - F_4^y(y_4, v_{y4}, \omega_{m4})]l + [-F_1^x(y_2, v_{y2}, \omega_{m2}) - F_4^x(y_3, v_{y3}, \omega_{m3}) + F_2^x(y_4, v_{y4}, \omega_{m4}) + F_3^x(y_1, v_{y1}, \omega_{m1})]d_s \quad (3.55)$$

where the moment caused by the x -axis forces are due to the vehicle's center of gravity being offset from the bottom of the rotors by a distance of d_s :

$$d_s = d \sin(\varphi) \quad (3.56)$$

Substituting (3.52) - (3.55) into (3.48) – (3.51) gives:

$$\dot{v}_y \cong [F_1^y(y_1, v_{y1}, \omega_{m1}) + F_2^y(y_2, v_{y2}, \omega_{m2}) + F_3^y(y_3, v_{y3}, \omega_{m3}) + F_4^y(y_4, v_{y4}, \omega_{m4})] \frac{1}{m} - g \quad (3.57)$$

$$\dot{\omega}_x \cong [F_3^y(y_2, v_{y2}, \omega_{m2}) + F_4^y(y_3, v_{y3}, \omega_{m3}) - F_1^y(y_4, v_{y4}, \omega_{m4}) - F_2^y(y_1, v_{y1}, \omega_{m1})] \frac{w}{I_{xx}} \quad (3.58)$$

$$\dot{\omega}_y \cong [F_2^x(y_3, v_{y3}, \omega_{m3}) - F_4^x(y_1, v_{y1}, \omega_{m1}) + F_1^x(y_2, v_{y2}, \omega_{m2}) - F_3^x(y_4, v_{y4}, \omega_{m4})] \frac{w}{I_{yy}} \quad (3.59)$$

$$\begin{aligned}
\dot{\omega}_z \cong & [F_2^y(y_2, v_{y2}, \omega_{m2}) + F_3^y(y_3, v_{y3}, \omega_{m3}) \\
& - F_1^y(y_1, v_{y1}, \omega_{m1}) - F_4^y(y_4, v_{y4}, \omega_{m4})] \frac{l}{I_{zz}} \\
& + [F_1^x(y_2, v_{y2}, \omega_{m2}) + F_4^x(y_3, v_{y3}, \omega_{m3}) \\
& + F_2^x(y_4, v_{y4}, \omega_{m4}) + F_3^x(y_1, v_{y1}, \omega_{m1})] \frac{d_s}{I_{zz}}
\end{aligned} \tag{3.60}$$

Assuming that each EDW is at a constant translational velocity $v_x = v_{x0}$, the lift force terms can be linearized around the equilibrium point. Note that motion in the x direction is of no concern for this 4-DOF model (because the vehicle can't fall off the track in the x -direction), as is the motion in the z direction, which is assumed to be constrained by track design. Although we expect the vehicle to maintain a level attitude during operation, the equations in this chapter are kept general so that the equilibrium point for each EDW can be different, as would be the case if the vehicle was required to maintain an angle for cornering maneuvers or to ascend/descend grades. Also note that even if the vehicle is level, the equilibrium velocity and force of each rotor can be different if the vehicle's mass were not uniform. The equilibrium operating point for each of the $n=1 - 4$ EDWs is

$$(y_n, v_{xn}, v_{yn}, \omega_{mn}) = (y_n^e, v_{xn}^e, 0, \omega_{mn}^e) \tag{3.61}$$

where ω_{mn} is the angular rotational velocity of the n th EDW rotor and superscript e denotes equilibrium and subscript n denotes corner that the EDW belongs to. The equilibrium operating point for the vehicle is assumed to be

$$(x, y, z, \theta_x, \theta_z, v_{xn}, v_{yn}, v_{zn}, \omega_x, \omega_z) = (0, y^e, 0, \theta_x^e, \theta_z^e, v_x^e, 0, 0, 0, 0) \tag{3.62}$$

The change in height from the equilibrium position for each EDW is defined as:

$$\delta y_n = y_n - y_n^e \tag{3.63}$$

and change in vertical velocity from the equilibrium is

$$\delta v_{yn} = v_{yn} - v_n^e \quad (3.64)$$

From (3.30), (3.35), and (3.36), the average equilibrium, height and angular position is given by

$$y^e = (y_1^e + y_2^e + y_3^e + y_4^e) / 4 \quad (3.65)$$

$$\theta_x^e \cong [y_3^e + y_4^e - y_1^e - y_2^e] / (4w) \quad (3.66)$$

$$\theta_z^e \cong [y_3^e + y_2^e - y_1^e - y_4^e] / (4l) \quad (3.67)$$

and referring to Fig. 41 and Fig. 42, the heights for each individual EDW are related to the angular positions by:

$$y_1 \approx y - w\theta_x - l\theta_z \quad (3.68)$$

$$y_2 \approx y - w\theta_x + l\theta_z \quad (3.69)$$

$$y_3 \approx y + w\theta_x + l\theta_z \quad (3.70)$$

$$y_4 \approx y + w\theta_x - l\theta_z \quad (3.71)$$

Similarly, the equilibrium heights are defined as:

$$y_1^e \approx y^e - w\theta_x^e - l\theta_z^e \quad (3.72)$$

$$y_2^e \approx y^e - w\theta_x^e + l\theta_z^e \quad (3.73)$$

$$y_3^e \approx y^e + w\theta_x^e + l\theta_z^e \quad (3.74)$$

$$y_4^e \approx y^e + w\theta_x^e - l\theta_z^e \quad (3.75)$$

This can be confirmed by substituting (3.72)-(3.75) into (3.30)-(3.36). Substituting $n = 1$ in (3.63) and substituting (3.68) into (3.63) gives

$$\delta y_1 \approx y - y_1^e - w\theta_x - l\theta_z \quad (3.76)$$

Similarly, for EDW $n = 2 - 4$:

$$\delta y_2 \approx y - y_2^e - w\theta_x + l\theta_z \quad (3.77)$$

$$\delta y_3 \approx y - y_3^e + w\theta_x + l\theta_z \quad (3.78)$$

$$\delta y_4 \approx y - y_4^e + w\theta_x - l\theta_z \quad (3.79)$$

Substituting (3.72) into (3.76) rearranging gives

$$\delta y_1 = y - [y^e - w\theta_x^e - l\theta_z^e] - w\theta_x - l\theta_z \quad (3.80)$$

Simplifying (3.80):

$$\delta y_1 = (y - y_e) - w(\theta_x - \theta_x^e) - l(\theta_z - \theta_z^e) \quad (3.81)$$

Defining the change in the vehicles *average* height as

$$\delta y = y - y^e \quad (3.82)$$

and the angular position difference is defined as

$$\delta\theta_x = \theta_x - \theta_x^e \quad (3.83)$$

$$\delta\theta_z = \theta_z - \theta_z^e \quad (3.84)$$

Then (3.76) reduces down to an equation for the height position of the 1st rotor

$$\delta y_1 = \delta y - w\delta\theta_x - l\delta\theta_z \quad (3.85)$$

Similarly, substituting (3.73)-(3.75) into (3.77)-(3.79) and utilizing (3.82), (3.83), and (3.84), we can obtain the heights of the other rotors

$$\delta y_2 = \delta y - w\delta\theta_x + l\delta\theta_z \quad (3.86)$$

$$\delta y_3 = \delta y + w\delta\theta_x + l\delta\theta_z \quad (3.87)$$

$$\delta y_4 = \delta y + w\delta\theta_x - l\delta\theta_z \quad (3.88)$$

Noting that $v_y^e = 0$. The time derivative of (3.85)-(3.88) gives the vertical velocities for each rotor

$$\delta v_{y1} = \delta v_y - w\delta\omega_x - l\delta\omega_z \quad (3.89)$$

$$\delta v_{y2} = \delta v_y - w\delta\omega_x + l\delta\omega_z \quad (3.90)$$

$$\delta v_{y3} = \delta v_y + w\delta\omega_x + l\delta\omega_z \quad (3.91)$$

$$\delta v_{y4} = \delta v_y + w\delta\omega_x - l\delta\omega_z \quad (3.92)$$

where

$$\delta v_y = v_y - v_y^e \quad (3.93)$$

$$\delta\omega_x = \omega_x - \omega_x^e \quad (3.94)$$

$$\delta\omega_z = \omega_z - \omega_z^e \quad (3.95)$$

The EDW lift force is linearized around the operating point defined by (3.61) for all four EDWs. Linearizing, the EDW lift force is approximated by using a first order Taylor series. Note that v_x terms are not included since the relatively large lift force will be negligibly affected by small movements about the x-axis (recall the vehicle is operating around a stationary point).

$$F_n^y(y_n, v_{yn}, \omega_n) \approx F_n^{ye} + k_{yyn}(y_n - y_n^e) + d_{yyn}v_{yn} + d_{y\theta n}(\omega_n - \omega_n^e) \quad (3.96)$$

where the “ n ” notation is taken to mean “of the n^{th} rotor”.

$$F_n^{ye} = F_n^y(y_n^e, 0, \omega_n^e) \quad (3.97)$$

$$k_{yyn} = \left. \frac{\partial F_n^y(y, 0, \omega_n^e)}{\partial y} \right|_{y=y_n^e} \quad (3.98)$$

$$d_{yyn} = \left. \frac{\partial F_n^y(y_n^e, v_y, \omega_n^e)}{\partial v_y} \right|_{v_y=0} \quad (3.99)$$

$$d_{y\theta n} = \left. \frac{\partial F_n^y(y_n^e, 0, \omega_n)}{\partial \omega_n} \right|_{\omega_n=\omega_n^e} \quad (3.100)$$

where ω_n is angular rotational velocity of the n^{th} rotor. The rotational direction is defined in Fig. 38. F_n^y is the force on the n^{th} rotor to maintain position at the operating point.

Linearizing the EDW thrust forces around a stable operating point gives:

$$\begin{aligned} F_n^x(y_n, v_{yn}, x_n, v_{xn}, \omega_n) \approx & F_n^{xe} + k_{xyn}(y_n - y_n^e) + d_{xyn}v_{yn} \\ & + k_{xxn}(x_n - x_n^e) + d_{yxn}(v_{xn} - v_{xn}^e) + d_{x\theta n}(\omega_n - \omega_n^e) \end{aligned} \quad (3.101)$$

where F_n^x is the force on the n^{th} rotor that is needed to maintain position at the operating point.

$$F_n^{xe} = F_n^x(y_n^e, v_{yn}^e, x_n^e, v_{xn}^e, \omega_n^e) \quad (3.102)$$

$$k_{xxn} = \left. \frac{\partial F_n^x(y, v_{yn}^e, x_n^e, v_{xn}^e, \omega_n^e)}{\partial y} \right|_{y=y_n^e} \quad (3.103)$$

$$d_{xyn} = \left. \frac{\partial F_n^x(y_n^e, v_y, x_n^e, v_{xn}^e, \omega_n^e)}{\partial v_y} \right|_{v_y=0} \quad (3.104)$$

$$k_{xxn} = \left. \frac{\partial F_n^x(y_n^e, v_{yn}^e, x_n, v_{xn}^e, \omega_n^e)}{\partial x_n} \right|_{x_n=0} \quad (3.105)$$

$$d_{yxn} = \left. \frac{\partial F_n^x(y_n^e, v_y, x_n^e, v_n, \omega_n^e)}{\partial v_{xn}} \right|_{v_x=0} \quad (3.106)$$

$$d_{x\theta n} = \left. \frac{\partial F_n^x(y_n^e, v_{yn}^e, x_n^e, v_{xn}^e, \omega_n)}{\partial \omega_n} \right|_{\omega_n=\omega_n^e} \quad (3.107)$$

Defining:

$$\delta x_n = x_n - x_n^e \quad (3.108)$$

$$\delta v_{xn} = v_{xn} - v_{xn}^e \quad (3.109)$$

$$\delta \omega_n = \omega_n - \omega_n^e \quad (3.110)$$

and utilizing (3.63) and (3.64) enables (3.96) and (3.101) to be written as

$$F_n^y(y_n, v_{yn}, \omega_n) \approx F_n^y + k_{yy} \delta y_n + d_{yy} \delta v_{yn} + d_{y\theta} \delta \omega_n \quad (3.111)$$

$$F_n^x(y_n, v_{yn}, \omega_n) \approx F_n^{xe} + k_{xy} \delta y_n + d_{xy} \delta v_{yn} + k_{xx} \delta x_n + d_{xx} \delta v_{xn} + d_{x\theta} \delta \omega_n \quad (3.112)$$

3.3 HEAVE DYNAMIC EQUATIONS

Recall the vehicle model's definition of vertical forces according to Fig. 41 and Fig. 42:

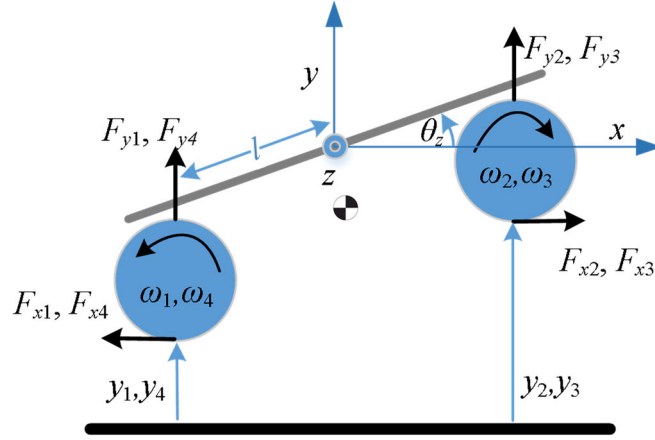


Fig. 41: 2-D sketch of vehicle pitch forces (x-y plane)

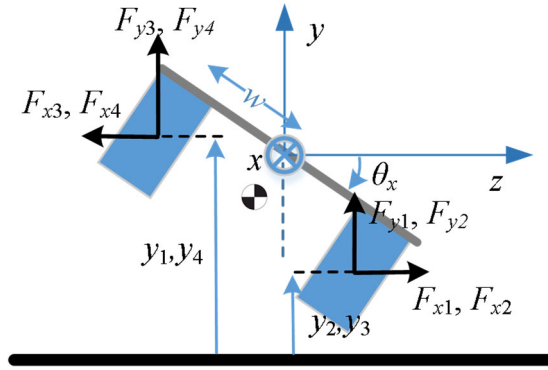


Fig. 42: 2-D sketch of vehicle roll forces (y-z plane)

Linearizing (3.57) by utilizing definition (3.93) gives

$$\begin{aligned}
 m\delta\dot{v}_y = & F_1^y(y_1, v_{y1}, w_{m1}) + F_2^y(y_2, v_{y2}, w_{m2}) \\
 & + F_3^y(y_3, v_{y3}, w_{m3}) + F_4^y(y_4, v_{y4}, w_{m4}) - mg
 \end{aligned} \tag{3.113}$$

Substituting (3.111) into (3.113) yields:

$$\begin{aligned}
m\delta\dot{v}_y &= F_1^{ye} + F_2^{ye} + F_3^{ye} + F_4^{ye} - mg \\
&\quad + [k_{yy1}\delta y_1 + k_{yy2}\delta y_2 + k_{yy3}\delta y_3 + k_{yy4}\delta y_4] \\
&\quad + [d_{yy1}\delta v_{y1} + d_{yy2}\delta v_{y2} + d_{yy3}\delta v_{y3} + d_{yy4}\delta v_{y4}] \\
&\quad + [d_{y\theta1}\delta\omega_1 + d_{y\theta2}\delta\omega_2 + d_{y\theta3}\delta\omega_3 + d_{y\theta4}\delta\omega_4]
\end{aligned} \tag{3.114}$$

Noting that

$$F_1^{ye} + F_2^{ye} + F_3^{ye} + F_4^{ye} = mg \tag{3.115}$$

Substituting (3.115) into (3.114):

$$\begin{aligned}
m\delta\dot{v}_y &= [k_{yy1}\delta y_1 + k_{yy2}\delta y_2 + k_{yy3}\delta y_3 + k_{yy4}\delta y_4] \\
&\quad + [d_{yy1}\delta v_{y1} + d_{yy2}\delta v_{y2} + d_{yy3}\delta v_{y3} + d_{yy4}\delta v_{y4}] \\
&\quad + [d_{y\theta1}\delta\omega_1 + d_{y\theta2}\delta\omega_2 + d_{y\theta3}\delta\omega_3 + d_{y\theta4}\delta\omega_4]
\end{aligned} \tag{3.116}$$

Substituting (3.85)-(3.88) and (3.89)-(3.92) into (3.116) gives

$$\begin{aligned}
m\delta\dot{v}_y &= [k_{yy1}(\delta y - w\delta\theta_x - l\delta\theta_z) + k_{yy2}(\delta y - w\delta\theta_x + l\delta\theta_z) \\
&\quad + k_{yy3}(\delta y + w\delta\theta_x + l\delta\theta_z) + k_{yy4}(\delta y + w\delta\theta_x - l\delta\theta_z)] \\
&\quad + [d_{yy1}(\delta v_y - w\delta\omega_x - l\delta\omega_z) + d_{yy2}(\delta v_y - w\delta\omega_x + l\delta\omega_z) \\
&\quad + d_{yy3}(\delta v_y + w\delta\omega_x + l\delta\omega_z) + d_{yy4}(\delta v_y + w\delta\omega_x - l\delta\omega_z)] \\
&\quad + [d_{y\theta1}\delta\omega_1 + d_{y\theta2}\delta\omega_2 + d_{y\theta3}\delta\omega_3 + d_{y\theta4}\delta\omega_4]
\end{aligned} \tag{3.117}$$

Rearranging (3.117) yields

$$\begin{aligned}
m\delta\dot{v}_y &= \delta y(k_{yy1} + k_{yy2} + k_{yy3} + k_{yy4}) + \delta\theta_x w(k_{yy3} + k_{yy4} - k_{yy1} - k_{yy2}) \\
&\quad + \delta\theta_z l(k_{yy2} + k_{yy3} - k_{yy1} - k_{yy4}) + \delta v_y(d_{yy1} + d_{yy2} + d_{yy3} + d_{yy4}) \\
&\quad + \delta\omega_x w(d_{yy3} + d_{yy4} - d_{yy1} - d_{yy2}) + \delta\omega_z l(d_{yy2} + d_{yy3} - d_{yy1} - d_{yy4}) \\
&\quad + [d_{y\theta1}\delta\omega_1 + d_{y\theta2}\delta\omega_2 + d_{y\theta3}\delta\omega_3 + d_{y\theta4}\delta\omega_4]
\end{aligned} \tag{3.118}$$

The vehicles total eddy current *vertical stiffness and damping* term can be defined as

$$4k_{yy} = k_{yy1} + k_{yy2} + k_{yy3} + k_{yy4} \tag{3.119}$$

$$4d_{yy} = d_{yy1} + d_{yy2} + d_{yy3} + d_{yy4} \tag{3.120}$$

The vehicle's average eddy current *vertical pitch angular stiffness and damping* is defined as:

$$k_{yy}^p = k_{yy2} + k_{yy3} - k_{yy1} - k_{yy4} \quad (3.121)$$

$$d_{yy}^p = d_{yy2} + d_{yy3} - d_{yy1} - d_{yy4} \quad (3.122)$$

and the vehicle's average eddy current *vertical roll angular stiffness and damping* can be defined as:

$$k_{yy}^r = k_{yy3} + k_{yy4} - k_{yy1} - k_{yy2} \quad (3.123)$$

$$d_{yy}^r = d_{yy3} + d_{yy4} - d_{yy1} - d_{yy2} \quad (3.124)$$

Utilizing definitions (3.119) - (3.122) allows (3.118) to be succinctly written as

$$\begin{aligned} m\delta\dot{v}_y = & 4\delta y k_{yy} + 4\delta v_y d_{yy} + [\delta\theta_x w k_{yy}^r + \delta\omega_x d_{yy}^r]w + [\delta\theta_z k_{yy}^p + \delta\omega_z d_{yy}^p]l \\ & + [d_{y\theta1}\delta\omega_1 + d_{y\theta2}\delta\omega_2 + d_{y\theta3}\delta\omega_3 + d_{y\theta4}\delta\omega_4] \end{aligned} \quad (3.125)$$

3.4 ROLL DYNAMIC EQUATIONS

Referring again to the definition of roll motion for the EWV in Fig. 42:

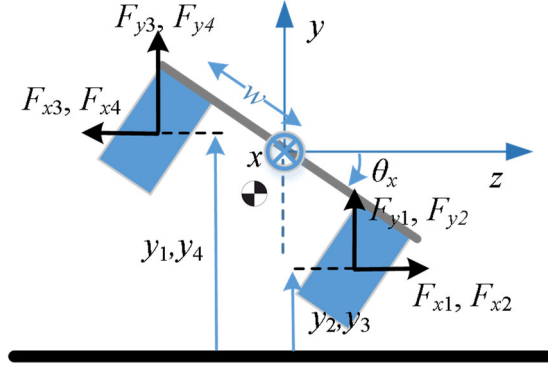


Fig. 42: 2-D sketch of vehicle roll forces (y-z plane)

Linearizing (3.60) and utilizing definition (3.94) gives

$$I_{xx}\delta\dot{\omega}_x = [-F_1^y(y_1, v_{y1}, \omega_1) - F_2^y(y_2, v_{y2}, \omega_2) + F_3^y(y_3, v_{y3}, \omega_3) + F_4^y(y_4, v_{y4}, \omega_4)]w \quad (3.126)$$

Equation (3.126) is written in terms of the individual EDW force dynamics. Recall equation (3.111):

$$F_n^y(y_n, v_{yn}, \omega_n) \approx F_n^y + k_{yyn}\delta y_n + d_{yyn}\delta v_{yn} + d_{y\theta n}\delta\omega_n \quad (3.111)$$

Substituting (3.111) into (3.126) yields:

$$\begin{aligned} I_{xx}\delta\dot{\omega}_x = & [-(F_1^{ye} + k_{yy1}\delta y_1 + d_{yy1}\delta v_{y1} + d_{y\theta1}\delta\omega_1) \\ & -(F_2^{ye} + k_{yy2}\delta y_2 + d_{yy2}\delta v_{y2} + d_{y\theta2}\delta\omega_2) \\ & + F_3^{ye} + k_{yy3}\delta y_3 + d_{yy3}\delta v_{y3} + d_{y\theta3}\delta\omega_3 \\ & + F_4^{ye} + k_{yy4}\delta y_4 + d_{yy4}\delta v_{y4} + d_{y\theta4}\delta\omega_4]w \end{aligned} \quad (3.127)$$

Equation (3.127) expresses the roll dynamics in terms of the EWV motion dynamics.

Further re-arranging (3.127):

$$\begin{aligned}
\frac{I_{xx}}{w} \delta \dot{\omega}_x = & (-F_1^{ye} - F_2^{ye} + F_3^{ye} + F_4^{ye}) \\
& + [-k_{yy1} \delta y_1 - k_{yy2} \delta y_2 + k_{yy3} \delta y_3 + k_{yy4} \delta y_4] \\
& + [-d_{yy1} \delta v_{y1} - d_{yy2} \delta v_{y2} + d_{yy3} \delta v_{y3} + d_{yy4} \delta v_{y4}] \\
& + [-d_{y\theta1} \delta \omega_1 - d_{y\theta2} \delta \omega_2 + d_{y\theta3} \delta \omega_3 + d_{y\theta4} \delta \omega_4]
\end{aligned} \tag{3.128}$$

Substituting (3.85)-(3.88) and (3.89)-(3.92) into (3.128) gives

$$\begin{aligned}
\frac{I_{xx}}{w} \delta \dot{\omega}_x = & (-F_1^{ye} - F_2^{ye} + F_3^{ye} + F_4^{ye}) \\
& + [-k_{yy1}(\delta y - w\delta\theta_x - l\delta\theta_z) - k_{yy2}(\delta y - w\delta\theta_x + l\delta\theta_z) \\
& + k_{yy3}(\delta y + w\delta\theta_x + l\delta\theta_z) + k_{yy4}(\delta y + w\delta\theta_x - l\delta\theta_z)] \\
& + [-d_{yy1}(\delta v_y - w\delta\omega_x - l\delta\omega_z) - d_{yy2}(\delta v_y - w\delta\omega_x + l\delta\omega_z) \\
& + d_{yy3}(\delta v_y + w\delta\omega_x + l\delta\omega_z) + d_{yy4}(\delta v_y + w\delta\omega_x - l\delta\omega_z)] \\
& + [-d_{y\theta1}\delta\omega_1 - d_{y\theta2}\delta\omega_2 + d_{y\theta3}\delta\omega_3 + d_{y\theta4}\delta\omega_4]
\end{aligned} \tag{3.129}$$

Rearranging further

$$\begin{aligned}
\frac{I_{xx}}{w} \delta \dot{\omega}_x = & (-F_1^{ye} - F_2^{ye} + F_3^{ye} + F_4^{ye}) \\
& + \delta y(-k_{yy1} - k_{yy2} + k_{yy3} + k_{yy4}) + w\delta\theta_x(k_{yy1} + k_{yy2} + k_{yy3} + k_{yy4}) \\
& + l\delta\theta_z(k_{yy1} - k_{yy2} + k_{yy3} - k_{yy4}) + \delta v_y(-d_{yy1} - d_{yy2} + d_{yy3} + d_{yy4}) \\
& + w\delta\omega_x(d_{yy1} + d_{yy2} + d_{yy3} + d_{yy4}) + l\delta\omega_z(d_{yy1} - d_{yy2} + d_{yy3} - d_{yy4}) \\
& + [-d_{y\theta1}\delta\omega_1 - d_{y\theta2}\delta\omega_2 + d_{y\theta3}\delta\omega_3 + d_{y\theta4}\delta\omega_4]
\end{aligned} \tag{3.130}$$

Defining average vertical yaw stiffness and damping terms as:

$$k_{yy}^y = k_{yy1} + k_{yy3} - k_{yy2} - k_{yy4} \tag{3.131}$$

$$d_{yy}^y = d_{yy1} + d_{yy3} - d_{yy2} - d_{yy4} \tag{3.132}$$

And utilizing definitions (3.119)-(3.122) and (3.131) and (3.132) allows (3.130) to be written as

$$\begin{aligned}
\frac{I_{xx}}{w} \delta \dot{\omega}_x = & (-F_1^{ye} - F_2^{ye} + F_3^{ye} + F_4^{ye}) \\
& + \delta y k_{yy}^r + \delta \theta_x k_{yy} w + \delta v_y d_{yy}^r + \delta \omega_x d_{yy} w + l \delta \theta_z k_{yy}^y + l \delta \omega_z d_{yy}^y \\
& + [d_{y\theta 3} \delta \omega_3 + d_{y\theta 4} \delta \omega_4 - d_{y\theta 1} \delta \omega_1 - d_{y\theta 2} \delta \omega_2]
\end{aligned} \tag{3.133}$$

The roll torque equilibrium is defined as

$$T_r^e = (F_3^{ye} + F_4^{ye} - F_1^{ye} - F_2^{ye})w \tag{3.134}$$

Substituting (3.134) into (3.133) gives

$$\begin{aligned}
I_{xx} \delta \dot{\omega}_x = & T_r^e + [\delta y k_{yy}^r + 4 \delta \theta_x k_{yy} w + \delta v_y d_{yy}^r + 4 \delta \omega_x d_{yy} w + l \delta \theta_z k_{yy}^y + l \delta \omega_z d_{yy}^y \\
& + d_{y\theta 3} \delta \omega_3 + d_{y\theta 4} \delta \omega_4 - d_{y\theta 1} \delta \omega_1 - d_{y\theta 2} \delta \omega_2]w
\end{aligned} \tag{3.135}$$

3.5 PITCH DYNAMIC EQUATIONS

Referring again to the EWV pitch angle definition as shown in Fig. 41:

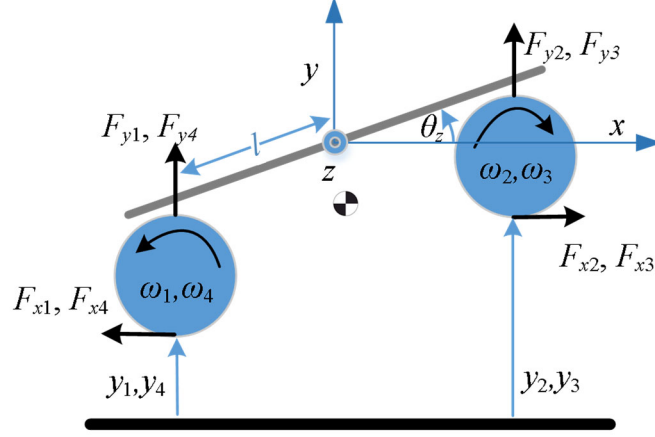


Fig. 41: 2-D sketch of vehicle pitch forces (x-y plane)

Linearizing (3.60) by utilizing definition (3.95) gives

$$I_{zz}\delta\dot{\omega}_z = [F_2^y(y_2, v_{y2}, \omega_2) + F_3^y(y_3, v_{y3}, \omega_3) - F_1^y(y_1, v_{y1}, \omega_1) - F_4^y(y_4, v_{y4}, \omega_4)]l + [F_2^x(y_2, v_{y2}, \omega_2) + F_3^x(y_3, v_{y3}, \omega_3) - F_1^x(y_4, v_{y4}, \omega_4) - F_4^x(y_1, v_{y1}, \omega_1)]d_s \quad (3.136)$$

where d_s is the vertical (the y -axis of the vehicle's body reference frame) distance between the rotor centers (their rotational axis) and the vehicle center of mass, which acts as the lever arm applying pitch torque from force components in the x -axis. Defining pitch equilibrium torque as:

$$T_p^e = (F_2^{ye} + F_3^{ye} - F_1^{ye} - F_4^{ye})l + (F_2^{xe} + F_3^{xe} - F_1^{xe} - F_4^{xe})d_s \quad (3.137)$$

and substituting (3.101) and (3.111) into (3.136), yields:

$$\begin{aligned}
I_{zz}\delta\dot{\omega}_z = T_p^e &+ \begin{bmatrix} (lk_{yy2} + d_s k_{xy2})\delta y_2 + (lk_{yy3} + d_s k_{xy3})\delta y_3 \\ -(lk_{yy1} + d_s k_{xy1})\delta y_1 - (lk_{yy4} + d_s k_{xy4})\delta y_4 \end{bmatrix} \\
&+ \begin{bmatrix} (ld_{yy2} + d_s d_{xy2})\delta v_{y2} + (ld_{yy3} + d_s d_{xy3})\delta v_{y3} \\ -(ld_{yy1} + d_s d_{xy1})\delta v_{y1} - (ld_{yy4} + d_s d_{xy4})\delta v_{y4} \end{bmatrix} \\
&+ \begin{bmatrix} (ld_{y\theta2} + d_s d_{x\theta2})\delta\omega_2 + (ld_{y\theta3} + d_s d_{x\theta3})\delta\omega_3 \\ -(ld_{y\theta1} + d_s d_{x\theta1})\delta\omega_1 - (ld_{y\theta4} + d_s d_{x\theta4})\delta\omega_4 \end{bmatrix}
\end{aligned} \tag{3.138}$$

Note that the horizontal position and velocity terms, δx_n and δv_{xn} , $n = 1-4$, are omitted since they will cancel out due to the front and rear rotors rotating in opposite directions. Then substituting (3.85)-(3.88) and (3.89)-(3.92) into (3.138) gives

$$\begin{aligned}
I_{zz}\delta\dot{\omega}_z = T_p^e &+ \begin{bmatrix} (lk_{yy2} + d_s k_{xy2})(\delta y - w\delta\theta_x + l\delta\theta_z) + (lk_{yy3} + d_s k_{xy3})(\delta y + w\delta\theta_x + l\delta\theta_z) \\ -(lk_{yy1} + d_s k_{xy1})(\delta y - w\delta\theta_x - l\delta\theta_z) - (lk_{yy4} + d_s k_{xy4})(\delta y + w\delta\theta_x - l\delta\theta_z) \end{bmatrix} \\
&+ \begin{bmatrix} (ld_{yy2} + d_s d_{xy2})(\delta v_y - w\delta\omega_x + l\delta\omega_z) + (ld_{yy3} + d_s d_{xy3})(\delta v_y + w\delta\omega_x + l\delta\omega_z) \\ -(ld_{yy1} + d_s d_{xy1})(\delta v_y - w\delta\omega_x - l\delta\omega_z) - (ld_{yy4} + d_s d_{xy4})(\delta v_y + w\delta\omega_x - l\delta\omega_z) \end{bmatrix} \\
&+ \begin{bmatrix} (ld_{y\theta2} + d_s d_{x\theta2})\delta\omega_2 + (ld_{y\theta3} + d_s d_{x\theta3})\delta\omega_3 \\ -(ld_{y\theta1} + d_s d_{x\theta1})\delta\omega_1 - (ld_{y\theta4} + d_s d_{x\theta4})\delta\omega_4 \end{bmatrix}
\end{aligned} \tag{3.139}$$

Rearranging (3.139) gives

$$\begin{aligned}
I_{zz}\delta\dot{\omega}_z = & T_p^e + \left[\begin{aligned} & \delta y(k_{yy2} + k_{yy3} - k_{yy1} - k_{yy4}) + w\delta\theta_x(k_{yy1} + k_{yy3} - k_{yy2} - k_{yy4}) \\ & + l\delta\theta_z(k_{yy1} + k_{yy2} + k_{yy3} + k_{yy4}) \end{aligned} \right] l \\
& + \left[\begin{aligned} & \delta y(k_{xy2} + k_{xy3} - k_{xy1} - k_{xy4}) + w\delta\theta_x(k_{xy1} + k_{xy3} - k_{xy2} - k_{xy4}) \\ & + l\delta\theta_z(k_{xy1} + k_{xy2} + k_{xy3} + k_{xy4}) \end{aligned} \right] d_s \\
& + \left[\begin{aligned} & \delta v_y(d_{yy2} + d_{yy3} - d_{yy1} - d_{yy4}) + w\delta\omega_x(d_{yy1} + d_{yy3} - d_{yy2} - d_{yy4}) \\ & + l\delta\omega_z(d_{yy1} + d_{yy2} + d_{yy3} + d_{yy4}) \end{aligned} \right] l \\
& + \left[\begin{aligned} & \delta v_y(d_{xy2} + d_{xy3} - d_{xy1} - d_{xy4}) + w\delta\omega_x(d_{xy1} + d_{xy3} - d_{xy2} - d_{xy4}) \\ & + l\delta\omega_z(d_{xy1} + d_{xy2} + d_{xy3} + d_{xy4}) \end{aligned} \right] d_s \\
& + \left[d_{y\theta2}\delta\omega_2 + d_{y\theta3}\delta\omega_3 - d_{y\theta4}\delta\omega_4 - d_{y\theta1}\delta\omega_1 \right] l \\
& + \left[d_{x\theta2}\delta\omega_2 + d_{x\theta3}\delta\omega_3 - d_{x\theta4}\delta\omega_4 - d_{x\theta1}\delta\omega_1 \right] d_s
\end{aligned} \tag{3.140}$$

Further rearrangement on (3.140) yields

$$\begin{aligned}
I_{zz}\delta\dot{\omega}_z = & T_p^e + \left[(k_{yy2} + k_{yy3} - k_{yy1} - k_{yy4})l + (k_{xy2} + k_{xy3} - k_{xy1} - k_{xy4})d_s \right] \delta y \\
& + \left[(d_{yy2} + d_{yy3} - d_{yy1} - d_{yy4})l + (d_{xy2} + d_{xy3} - d_{xy1} - d_{xy4})d_s \right] \delta v_y \\
& + \left[(k_{yy1} + k_{yy3} - k_{yy2} - k_{yy4})l + (k_{xy1} + k_{xy3} - k_{xy2} - k_{xy4})d_s \right] \delta\theta_x w \\
& + \left[(d_{yy1} + d_{yy3} - d_{yy2} - d_{yy4})l + (d_{xy1} + d_{xy3} - d_{xy2} - d_{xy4})d_s \right] \delta\omega_x w \\
& + \left[(k_{yy1} + k_{yy2} + k_{yy3} + k_{yy4})l + (k_{xy1} + k_{xy2} + k_{xy3} + k_{xy4})d_s \right] \delta\theta_z \\
& + \left[(d_{yy1} + d_{yy2} + d_{yy3} + d_{yy4})l + (d_{xy1} + d_{xy2} + d_{xy3} + d_{xy4})d_s \right] \delta\omega_z \\
& + \left[d_{y\theta2}\delta\omega_2 + d_{y\theta3}\delta\omega_3 - d_{y\theta4}\delta\omega_4 - d_{y\theta1}\delta\omega_1 \right] l \\
& + \left[d_{x\theta2}\delta\omega_2 + d_{x\theta3}\delta\omega_3 - d_{x\theta4}\delta\omega_4 - d_{x\theta1}\delta\omega_1 \right] d_s
\end{aligned} \tag{3.141}$$

Defining the total eddy current *horizontal stiffness and damping* terms as

$$4k_{xy} = k_{xy1} + k_{xy2} + k_{xy3} + k_{xy4} \tag{3.142}$$

$$4d_{xy} = d_{xy1} + d_{xy2} + d_{xy3} + d_{xy4} \tag{3.143}$$

the total eddy current *horizontal pitch stiffness and damping* terms as

$$k_{xy}^P = k_{xy2} + k_{xy3} - k_{xy1} - k_{xy4} \tag{3.144}$$

$$d_{xy}^p = d_{xy2} + d_{xy3} - d_{xy1} - d_{xy4} \quad (3.145)$$

and the average eddy-current *horizontal yaw stiffness and damping* terms as

$$k_{xy}^y = k_{xy1} + k_{xy3} - k_{xy2} - k_{xy4} \quad (3.146)$$

$$d_{xy}^y = d_{xy1} + d_{xy3} - d_{xy2} - d_{xy4} \quad (3.147)$$

and making use of the vertical stiffness and damping definitions from (3.119) - (3.122),

(3.131), and (3.132), equation (3.141) can be simplified down to

$$\begin{aligned} I_{zz}\delta\dot{\omega}_z = & T_p^e + \left[\delta y k_{yy}^p + w\delta\theta_x k_{yy}^y + 4l\delta\theta_z k_{yy} \right] l \\ & + \left[\delta y k_{yy}^p + w\delta\theta_x k_{xy}^y + 4l\delta\theta_z k_{xy} \right] d_s \\ & + \left[\delta v_y d_{yy}^p + w\delta\omega_x d_{yy}^y + 4l\delta\omega_z d_{yy} \right] l \\ & + \left[\delta v_y d_{xy}^p + w\delta\omega_x d_{xy}^y + 4l\delta\omega_z d_{xy} \right] d_s \\ & + \left[d_{y\theta2}\delta\omega_2 + d_{y\theta3}\delta\omega_3 - d_{y\theta4}\delta\omega_4 - d_{y\theta4}\delta\omega_1 \right] l \\ & + \left[d_{x\theta2}\delta\omega_2 + d_{x\theta3}\delta\omega_3 - d_{x\theta4}\delta\omega_4 - d_{x\theta1}\delta\omega_1 \right] d_s \end{aligned} \quad (3.148)$$

3.6 YAW DYNAMIC EQUATIONS

Referring again to the yaw angle definition for the EWV shown in Fig. 44:

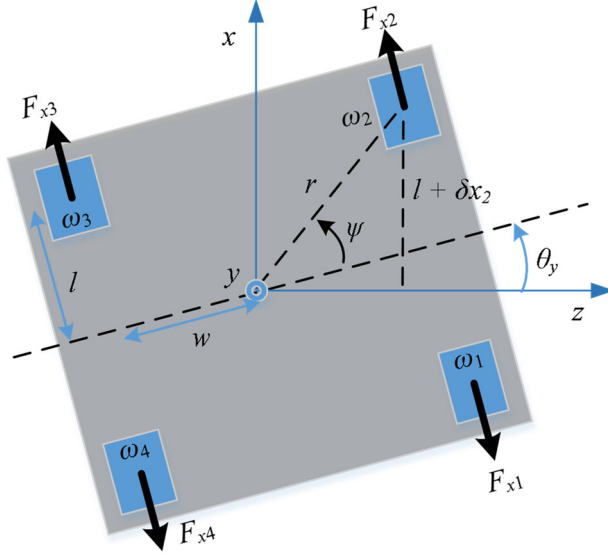


Fig. 44: 2-D sketch of yawed vehicle from above (x-z plane)

We can define the change in yaw velocity as follows:

$$\delta\omega_y = \omega_y - \omega_y^e \quad (3.149)$$

Linearizing (3.59) by using (3.149) gives

$$I_{yy} \frac{d^2\theta_y}{dt^2} = [F_2^x + F_4^x - F_1^x - F_3^x]w \quad (3.150)$$

Substituting (3.112) into (3.150)

$$\begin{aligned} I_{yy} \dot{\omega}_y = & [k_{xx1}y_1 + d_{xy1}v_{y1} + d_{x\theta1}\omega_1 + k_{xx1}x_1 + d_{xx1}v_{x1} + F_1^{xe} \\ & + k_{xx2}y_2 + d_{xy2}v_{y2} + d_{x\theta2}\omega_2 + k_{xx2}x_2 + d_{xx2}v_{x2} + F_2^{xe} \\ & - (k_{xx3}y_3 + d_{xy3}v_{y3} + d_{x\theta3}\omega_3 + k_{xx3}x_3 + d_{xx3}v_{x3} + F_3^{xe}) \\ & - (k_{xx4}y_4 + d_{xy4}v_{y4} + d_{x\theta4}\omega_4 + k_{xx4}x_4 + d_{xx4}v_{x4} + F_4^{xe})]w \end{aligned} \quad (3.151)$$

Linearizing and rearranging (3.151):

$$\begin{aligned}
\delta\dot{\omega}_y = \frac{w}{I_{yy}} & [(k_{xx2}\delta y_2 + k_{xx4}\delta y_4 - k_{xx1}\delta y_1 - k_{xx3}\delta y_3) \\
& + (d_{xy2}\delta v_{y2} + d_{xy4}\delta v_{y4} - d_{xy1}\delta v_{y1} - d_{xy3}\delta v_{y3}) \\
& + (k_{xx2}\delta x_2 + k_{xx4}\delta x_4 - k_{xx1}\delta x_1 - k_{xx3}\delta x_3) \\
& + (d_{xx2}\delta v_{x2} + d_{xx4}\delta v_{x4} - d_{xx1}\delta v_{x1} - d_{xx3}\delta v_{x3}) \\
& + (d_{x\theta2}\delta\omega_2 + d_{x\theta4}\delta\omega_4 - d_{x\theta1}\delta\omega_1 - d_{x\theta3}\delta\omega_3)]
\end{aligned} \tag{3.152}$$

Substituting equations (3.85) - (3.92) into (3.152) gives

$$\begin{aligned}
\delta\dot{\omega}_y = \frac{w}{I_{yy}} & [(k_{xx2}(\delta y - w\delta\theta_x + l\delta\theta_z) + k_{xx4}(\delta y + w\delta\theta_x - l\delta\theta_z) \\
& - k_{xx1}(\delta y - w\delta\theta_x - l\delta\theta_z) - k_{xx3}(\delta y + w\delta\theta_x + l\delta\theta_z)) \\
& + (d_{xy2}(\delta v_y - w\delta\omega_x + l\delta\omega_z) + d_{xy4}(\delta v_y + w\delta\omega_x - l\delta\omega_z) \\
& - d_{xy1}(\delta v_y - w\delta\omega_x - l\delta\omega_z) - d_{xy3}(\delta v_y + w\delta\omega_x + l\delta\omega_z)) \\
& + (k_{xx2}\delta x_2 + k_{xx4}\delta x_4 - k_{xx1}\delta x_1 - k_{xx3}\delta x_3) \\
& + (d_{xx2}\delta v_{x2} + d_{xx4}\delta v_{x4} - d_{xx1}\delta v_{x1} - d_{xx3}\delta v_{x3}) \\
& + (d_{x\theta2}\delta\omega_2 + d_{x\theta4}\delta\omega_4 - d_{x\theta1}\delta\omega_1 - d_{x\theta3}\delta\omega_3)]
\end{aligned} \tag{3.153}$$

Rewriting (3.153),

$$\begin{aligned}
\delta\dot{\omega}_y = \frac{w}{I_{yy}} & [\delta y(k_{xy2} + k_{xy4} - k_{xy1} - k_{xy3}) + w\delta\theta_x(k_{xy1} + k_{xy4} - k_{xy2} - k_{xy3}) \\
& + l\delta\theta_z(k_{xy1} + k_{xy2} - k_{xy3} - k_{xy4}) + \delta v_y(p_2^y + p_4^y - p_1^y - p_3^y) \\
& + w\delta\omega_x(d_{xy1} + d_{xy4} - d_{xy2} - d_{xy3}) + l\delta\omega_z(d_{xy1} + d_{xy2} - d_{xy3} - d_{xy4}) \\
& + (k_{xx2}\delta x_2 + k_{xx4}\delta x_4 - k_{xx1}\delta x_1 - k_{xx3}\delta x_3) \\
& + (d_{xx2}\delta v_{x2} + d_{xx4}\delta v_{x4} - d_{xx1}\delta v_{x1} - d_{xx3}\delta v_{x3}) \\
& + d_{x\theta2}\delta\omega_2 + d_{x\theta4}\delta\omega_4 - d_{x\theta1}\delta\omega_1 - d_{x\theta3}\delta\omega_3]
\end{aligned} \tag{3.154}$$

Utilizing (3.144) - (3.147), and defining the average eddy current *horizontal roll*

stiffness and damping terms as:

$$k_{xy}^r = k_{xy1} + k_{xy2} - k_{xy3} - k_{xy4} \tag{3.155}$$

$$d_{xy}^r = d_{xy2} + d_{xy3} - d_{xy1} - d_{xy4} \tag{3.156}$$

Substituting (3.121), (3.124), (3.132), (3.145), (3.147), and (3.156) into (3.154):

$$\begin{aligned}
 \delta \dot{\omega}_y = \frac{w}{I_{yy}} [& -k_{xy}^y \delta y - w k_{xy}^p \delta \theta_x + l k_{xy}^r \delta \theta_z - d_{yy}^y \delta v_y - w d_{yy}^p \delta \omega_x + l d_{yy}^r \delta \omega_z \\
 & + (k_{xx2} \delta x_2 + k_{xx4} \delta x_4 - k_{xx1} \delta x_1 - k_{xx3} \delta x_3) \\
 & + (d_{xx2} \delta v_{x2} + d_{xx4} \delta v_{x4} - d_{xx1} \delta v_{x1} - d_{xx3} \delta v_{x3}) \\
 & + d_{x\theta2} \delta \omega_2 + d_{x\theta4} \delta \omega_4 - d_{x\theta1} \delta \omega_1 - d_{x\theta3} \delta \omega_3]
 \end{aligned} \tag{3.157}$$

3.7 CONCLUSION

The prototype 4 rotor vehicle motions have been defined in this chapter. The definitions of the 4 degrees of freedom of interest are defined, along with the geometric identities necessary for the vehicle model. The motion of the vehicle is related to the forces generated at each rotor, which are then modeled as functions of various damping and stiffness terms. Finally, differential equations for each degree of freedom are derived, which are functions of vehicle states and the damping and stiffness values calculated using the SOVP model. These equations will be formulated into a system of dependent equations to model the system as a whole.

CHAPTER 4: FULL SYSTEM MODEL

In this chapter, we use the equations for heave (y), roll (θ_x), pitch (θ_z), and yaw (θ_y) to form a full 4-DOF model that can be used to analyze and apply control to a prototype model vehicle. Beginning with the 4 differential equations derived in Chapter CHAPTER 3, reasonable simplifications are made to arrive at a set of simpler equations in section 4.1. Then, unwanted x -position variables are converted into angles in section 4.2, which allows the system to be written in a state-space form in section 4.3. The system is broken down into smaller sub-systems by decoupling in section 4.4. Rather than treating rotor speeds as native inputs, section 4.5 adds motor dynamic equations to obtain a more practical input of voltage to each motor. Finally, in section 4.6, the model is compared to a real-time simulation to validate the analytic equations.

4.1 FULL SYSTEM MODEL EQUATIONS

Thus far, four equations, (3.125), (3.135), (3.148), and (3.157) describe the 4-DOF system have been derived. For vertical motion, we have:

$$m\delta\dot{v}_y = 4\delta y k_{yy} + 4\delta v_y d_{yy} + [\delta\theta_x w k_{yy}^r + \delta\omega_x d_{yy}^r]w + [\delta\theta_z k_{yy}^p + \delta\omega_z d_{yy}^p]l + [d_{y\theta1}\delta\omega_1 + d_{y\theta2}\delta\omega_2 + d_{y\theta3}\delta\omega_3 + d_{y\theta4}\delta\omega_4] \quad (3.125)$$

For roll, we have:

$$I_{xx}\delta\dot{\omega}_x = T_r^e + [\delta y k_{yy}^r + 4\delta\theta_x k_{yy} w + \delta v_y d_{yy}^r + 4\delta\omega_x d_{yy} w + l\delta\theta_z k_{yy}^y + l\delta\omega_z d_{yy}^y + d_{y\theta3}\delta\omega_3 + d_{y\theta4}\delta\omega_4 - d_{y\theta1}\delta\omega_1 - d_{y\theta2}\delta\omega_2]w \quad (3.135)$$

For pitch, we have:

$$\begin{aligned}
I_{zz}\delta\dot{\omega}_z = & T_p^e + \left[\delta y k_{yy}^p + w\delta\theta_x k_{yy}^y + 4l\delta\theta_z k_{yy} \right] l \\
& + \left[\delta y k_{yy}^p + w\delta\theta_x k_{xy}^y + 4l\delta\theta_z k_{xy} \right] d_s \\
& + \left[\delta v_y d_{yy}^p + w\delta\omega_x d_{yy}^y + 4l\delta\omega_z d_{yy} \right] l \\
& + \left[\delta v_y d_{xy}^p + w\delta\omega_x d_{xy}^y + 4l\delta\omega_z d_{xy} \right] d_s \\
& + \left[d_{y\theta 2}\delta\omega_2 + d_{y\theta 3}\delta\omega_3 - d_{y\theta 4}\delta\omega_4 - d_{y\theta 1}\delta\omega_1 \right] l \\
& + \left[d_{x\theta 2}\delta\omega_2 + d_{x\theta 3}\delta\omega_3 - d_{x\theta 4}\delta\omega_4 - d_{x\theta 1}\delta\omega_1 \right] d_s
\end{aligned} \tag{3.148}$$

and for yaw, we have:

$$\begin{aligned}
\delta\dot{\omega}_y = & \frac{w}{I_{yy}} \left[-k_{xy}^y \delta y - w k_{xy}^p \delta\theta_x + l k_{xy}^r \delta\theta_z - d_{yy}^y \delta v_y - w d_{yy}^p \delta\omega_x + l d_{yy}^r \delta\omega_z \right. \\
& + (k_{xx2} \delta x_2 + k_{xx4} \delta x_4 - k_{xx1} \delta x_1 - k_{xx3} \delta x_3) \\
& + (d_{xx2} \delta v_{x2} + d_{xx4} \delta v_{x4} - d_{xx1} \delta v_{x1} - d_{xx3} \delta v_{x3}) \\
& \left. + d_{x\theta 2} \delta\omega_2 + d_{x\theta 4} \delta\omega_4 - d_{x\theta 1} \delta\omega_1 - d_{x\theta 3} \delta\omega_3 \right]
\end{aligned} \tag{3.157}$$

We can make a very important assumption that allows the equations to be reduced to a smaller form: the vehicle is operating near a level equilibrium point. This is essential, since there would be no purpose in developing a linear control model of the vehicle if the vehicle is expected to move away from the equilibrium point. In other words, when using these equations to develop a control law, this assumption is necessary for a non-trivial solution. This assumption means that the linearization is to take place at the equilibrium point.

As a corollary to the previous assumption, and also making the basic assumption that the track is flat, the vehicle will be operating at a neutral or nearly neutral attitude (roll, pitch, and yaw angles near zero). Again, the model would not make sense if this assumption were omitted, as the vehicle is meant to travel smoothly down the track without subjecting the payload to any abnormal forces. The eddy current forces become very small

as the airgap becomes large, so the physics of the system actually enforce this assumption, as the vehicle is incapable of operating with excessive angles.

Finally, we can assume that the vehicle is designed to have a (nearly) symmetrical weight distribution, so that each corner requires equal forces around the equilibrium. As the designers of the vehicle, we can easily ensure this is true, especially as it makes design and construction more straightforward. This means the EDWs will all be operating at the same height above the track, and at the same rotational and translational speed at the equilibrium point. It then follows that each rotor has the same stiffness and damping terms at the equilibrium/linearization point. Therefore in this case the terms in (3.121) - (3.124), (3.131), (3.132), (3.144), (3.145), (3.155), and (3.156) will cancel out:

$$k_{xy}^r \cong k_{xy}^p \cong k_{xy}^y \cong d_{xy}^r \cong d_{xy}^p \cong d_{xy}^y \cong 0 \quad (4.1)$$

$$k_{yy}^r \cong k_{yy}^p \cong k_{yy}^y \cong d_{yy}^r \cong d_{yy}^p \cong d_{yy}^y \cong 0 \quad (4.2)$$

$$T_r^e \cong 0 \quad (4.3)$$

We can also expect the *horizontal yaw eddy current stiffness and damping* terms to be similar enough such that

$$k_{xx} \approx k_{xx1} \approx k_{xx2} \approx k_{xx3} \approx k_{xx4} \quad (4.4)$$

$$d_{xx} \approx d_{xx1} \approx d_{xx2} \approx d_{xx3} \approx d_{xx4} \quad (4.5)$$

and the vertical and horizontal damping terms will be approximately equal such that

$$d_{y\theta} \approx d_{y\theta1} \approx d_{y\theta2} \approx d_{y\theta3} \approx d_{y\theta4} \quad (4.6)$$

$$d_{x\theta} \approx d_{x\theta1} \approx d_{x\theta2} \approx d_{x\theta3} \approx d_{x\theta4} \quad (4.7)$$

By utilizing (4.2) and (4.6), the heave dynamic equation (3.125) can now be written as:

$$\delta \dot{v}_y = \delta y \frac{4k_{yy}}{m} + \delta v_y \frac{4d_{yy}}{m} + \frac{d_{y\theta}}{m} [\delta \omega_1 + \delta \omega_2 + \delta \omega_3 + \delta \omega_4] \quad (4.8)$$

and using (3.39), the accompanying height dynamic equation is

$$\delta \dot{y} = \delta v_y \quad (4.9)$$

The roll velocity dynamic equation (3.135) can be simplified by using (4.2) and (4.6)

$$\delta \dot{\omega}_x = \delta \theta_x \frac{4k_{yy}w^2}{I_{xx}} + \delta \omega_x \frac{4d_{yy}w^2}{I_{xx}} + \frac{d_{y\theta}w}{I_{xx}} (-\delta \omega_1 - \delta \omega_2 + \delta \omega_3 + \delta \omega_4) \quad (4.10)$$

Using (3.37), the accompanying roll angle dynamic equation is

$$\delta \dot{\theta}_x = \delta \omega_x \quad (4.11)$$

Given (4.1) - (4.7), the pitch velocity dynamic equation (3.148) simplifies to

$$\delta \dot{\omega}_z = \delta \theta_z \frac{4k_{yy}l^2}{I_{zz}} + \delta \omega_z \frac{4d_{yy}l^2}{I_{zz}} + \frac{ld_{y\theta} + d_s d_{x\theta}}{I_{zz}} (-\delta \omega_1 + \delta \omega_2 + \delta \omega_3 - \delta \omega_4) \quad (4.12)$$

and utilizing (3.38), the accompanying pitch angle dynamic equation is

$$\delta \dot{\theta}_z = \delta \omega_z \quad (4.13)$$

And with (4.1) - (4.7), equation (3.157) simplifies down to a new yaw velocity dynamic equation

$$\delta \dot{\omega}_y = \frac{w}{I_{yy}} \left[d_{x\theta} \delta \omega_2 + d_{x\theta} \delta \omega_4 - d_{x\theta} \delta \omega_1 - d_{x\theta} \delta \omega_3 + (k_{xx} \delta x_2 + k_{xx} \delta x_4 - k_{xx} \delta x_1 - k_{xx} \delta x_3) + (d_{xx} \delta v_{x2} + d_{xx} \delta v_{x4} - d_{xx} \delta v_{x1} - d_{xx} \delta v_{x3}) \right] \quad (4.14)$$

The accompanying yaw angle dynamic equation is defined as

$$\delta \dot{\theta}_y = \delta \omega_y \quad (4.15)$$

4.2 CONVERSION OF X-AXIS MOVEMENTS TO ANGLES

With our four simplified equations of motion, we now need to develop an expression for the horizontal position and velocity variables in terms of our intended states in order to develop a state-space model in matrix form. Note that although the vehicle in this model does not experience a net change in horizontal position or velocity, the yawing motion of the vehicle can cause small perturbations for each wheel along the x -axis. The angle is necessarily small (otherwise the vehicle would fall off the track), so the z -axis displacement is negligible. Referring once again to Fig. 44, we can start by first defining the x -position displacement of one of the rotors, arbitrarily selected. For rotor 2:

$$l + \delta x_2 = r \sin(\psi + \theta_y) \quad (4.16)$$

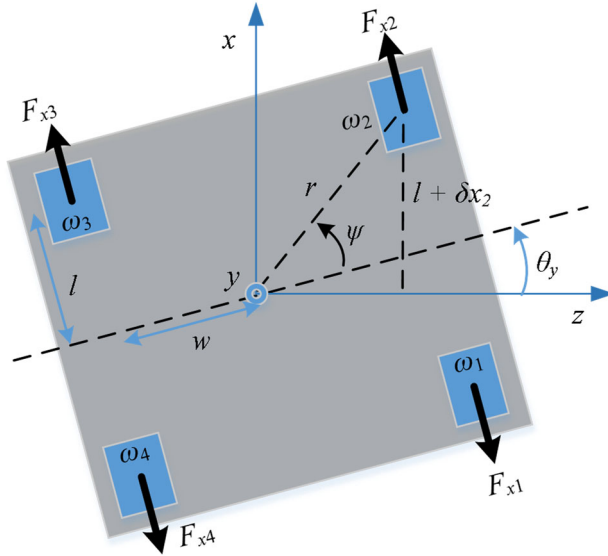


Fig. 44: 2-D sketch of yawed vehicle from above (x - z plane)

Since we expect θ_y to be small, we can linearize the sine function around ψ , such that (4.16) can be rewritten:

$$l + \delta x_2 \approx r[\sin(\psi) + \cos(\psi)(\psi - \theta_y)] \quad (4.17)$$

We can note that at the equilibrium position,

$$l = r \sin(\psi) \quad (4.18)$$

therefore, we can substitute (4.18) into (4.17), then linearize the result to obtain

$$\delta x_2 = r \cos(\psi) \delta \theta_y \quad (4.19)$$

We can similarly define the x-axis velocity due to yaw velocity:

$$\delta v_{x2} = r \cos(\psi) \delta \omega_y \quad (4.20)$$

Utilizing the same process used to obtain (4.19) and (4.20), we can define similar equations for the other 3 rotors:

$$\delta x_1 = -r \cos(\psi) \delta \theta_y \quad (4.21)$$

$$\delta x_3 = -r \cos(\psi) \delta \theta_y \quad (4.22)$$

$$\delta x_4 = r \cos(\psi) \delta \theta_y \quad (4.23)$$

$$\delta v_{x1} = -r \cos(\psi) \delta \omega_y \quad (4.24)$$

$$\delta v_{x3} = -r \cos(\psi) \delta \omega_y \quad (4.25)$$

$$\delta v_{x4} = r \cos(\psi) \delta \omega_y \quad (4.26)$$

Substituting (4.19) - (4.26) into the yaw velocity dynamic equation, (4.14):

$$\delta \dot{\omega}_y = \frac{w}{I_{yy}} \left[\begin{aligned} & d_{x\theta} \delta \omega_2 + d_{x\theta} \delta \omega_4 - d_{x\theta} \delta \omega_1 - d_{x\theta} \delta \omega_3 \\ & + (k_{xx} r \cos(\psi) \delta \theta_y + k_{xx} \delta x_4 + k_{xx} r \cos(\psi) \delta \theta_y + k_{xx} r \cos(\psi) \delta \theta_y) \\ & + (d_{xx} r \cos(\psi) \delta \omega_y + d_{xx} r \cos(\psi) \delta \omega_y + d_{xx} r \cos(\psi) \delta \omega_y + d_{xx} r \cos(\psi) \delta \omega_y) \end{aligned} \right] \quad (4.27)$$

We will define a shorthand variable, a , as

$$a = r \cos(\psi) \quad (4.28)$$

Substituting (4.28) into (4.27) and simplifying, we obtain a new equation which describes yaw motion using the desired states (and eliminating the variables which denote variations in the x -position):

$$\delta\dot{\omega}_y = \frac{w}{I_{yy}} [4ak_{xx}\delta\theta_y + 4ad_{xx}\delta\omega_y + d_{x\theta}\delta\omega_2 + d_{x\theta}\delta\omega_4 - d_{x\theta}\delta\omega_1 - d_{x\theta}\delta\omega_4] \quad (4.29)$$

4.3 4-DOF STATE SPACE MODEL

Combining (4.8), (4.9), (4.10), (4.11), (4.12), (4.13), (4.15), and (4.29) together yields a complete set of equations describing the vehicle motion in 4-DOF:

$$\delta\dot{y} = \delta v_y \quad (4.9)$$

$$\delta\dot{\theta}_x = \delta\omega_x \quad (4.11)$$

$$\delta\dot{\theta}_z = \delta\omega_z \quad (4.13)$$

$$\delta\dot{\theta}_y = \delta\omega_y \quad (4.15)$$

$$\delta\dot{v}_y = \delta y \frac{4k_{yy}}{m} + \delta v_y \frac{4d_{yy}}{m} + \frac{d_{y\theta}}{m} [\delta\omega_1 + \delta\omega_2 + \delta\omega_3 + \delta\omega_4] \quad (4.8)$$

$$\delta\dot{\omega}_x = \delta\theta_x \frac{4k_{yy}w^2}{I_{xx}} + \delta\omega_x \frac{4d_{yy}w^2}{I_{xx}} + \frac{d_{y\theta}w}{I_{xx}} (-\delta\omega_1 - \delta\omega_2 + \delta\omega_3 + \delta\omega_4) \quad (4.10)$$

$$\delta\dot{\omega}_z = \delta\theta_z \frac{4k_{yy}l^2}{I_{zz}} + \delta\omega_z \frac{4d_{yy}l^2}{I_{zz}} + \frac{ld_{y\theta} + d_s d_{x\theta}}{I_{zz}} (-\delta\omega_1 + \delta\omega_2 + \delta\omega_3 - \delta\omega_4) \quad (4.12)$$

$$\delta\dot{\omega}_y = \frac{w}{I_{yy}} [4ak_{xx}\delta\theta_y + 4ad_{xx}\delta\omega_y + d_{x\theta}\delta\omega_2 + d_{x\theta}\delta\omega_4 - d_{x\theta}\delta\omega_1 - d_{x\theta}\delta\omega_4] \quad (4.30)$$

The system can be described in linear state space form, where a single matrix equation is used to represent the entire set of state equations:

$$\dot{\mathbf{x}} = \mathbf{A}\mathbf{x} + \mathbf{B}\mathbf{u} \quad (4.31)$$

$$\mathbf{y} = \mathbf{C}\mathbf{x} + \mathbf{D}\mathbf{u} \quad (4.32)$$

where \mathbf{x} is a $p_s \times 1$ column of state variables, where p_s is the number of states, \mathbf{y} is a $p_o \times 1$ column of output variables, where p_o is the number of outputs, \mathbf{u} is a $p_i \times 1$ column of input variables, where p_i is the number of inputs, \mathbf{A} is a $p_s \times p_s$ state matrix of coefficients that describe each states' contribution to each differential equation, \mathbf{B} is a $p_s \times p_i$ column of coefficients that describe how each input affects the differential equations, \mathbf{C} is a $p_o \times p_s$ matrix of coefficients describing each states' contribution to the output, and \mathbf{D} is a $p_o \times p_i$ feedforward matrix with coefficients describing each inputs' contribution to the output.

The state-space system for (4.9) - (4.12) and (4.30) is given by following subscripts to differentiate it from state space systems in future chapters:

$$\dot{\mathbf{x}}_e = \mathbf{A}_e \mathbf{x}_e + \mathbf{B}_e \mathbf{u}_e \quad (4.33)$$

$$\mathbf{y} = \mathbf{C}_e \mathbf{x}_e + \mathbf{D}_e \mathbf{u}_e \quad (4.34)$$

where \mathbf{x}_e is the state vector, \mathbf{A}_e is the system matrix, \mathbf{B}_e is the input matrix, \mathbf{u}_e is the input vector, \mathbf{y} is the output vector, \mathbf{C}_e is the output matrix, and \mathbf{D}_e is the feedforward matrix for the 8 state prototype system. Note that it is implied that states, inputs, and outputs are time-varying values, despite the lack of explicitly writing each in terms of time variable t . This applies to all state-space and vehicle equations in this document. Defining the state vector:

$$\mathbf{x}_e = [\delta y \quad \delta \theta_x \quad \delta \theta_z \quad \delta \theta_y \quad \delta v_y \quad \delta \omega_x \quad \delta \omega_z \quad \delta \omega_y]^T \quad (4.35)$$

The input vector is defined as:

$$\mathbf{u}_e = [\delta \omega_1 \quad \delta \omega_2 \quad \delta \omega_3 \quad \delta \omega_4]^T \quad (4.36)$$

The system matrix is:

$$\mathbf{A}_e = \begin{bmatrix} 0 & 0 & 0 & 0 & 1 & 0 & 0 & 0 \\ 0 & 0 & 0 & 0 & 0 & 1 & 0 & 0 \\ 0 & 0 & 0 & 0 & 0 & 0 & 1 & 0 \\ 0 & 0 & 0 & 0 & 0 & 0 & 0 & 1 \\ \frac{4k_{yy}}{m} & 0 & 0 & 0 & \frac{4d_{yy}}{m} & 0 & 0 & 0 \\ 0 & \frac{4k_{yy}w^2}{I_{xx}} & 0 & 0 & 0 & \frac{4d_{yy}w^2}{I_{xx}} & 0 & 0 \\ 0 & 0 & \frac{4k_{yy}l^2}{I_{zz}} & 0 & 0 & 0 & \frac{4d_{yy}l^2}{I_{zz}} & 0 \\ 0 & 0 & 0 & \frac{4k_{xx}a}{I_{yy}} & 0 & 0 & 0 & \frac{4d_{xx}a}{I_{yy}} \end{bmatrix} \quad (4.37)$$

The input matrix is:

$$\mathbf{B}_e = \begin{bmatrix} 0 & 0 & 0 & 0 \\ 0 & 0 & 0 & 0 \\ 0 & 0 & 0 & 0 \\ 0 & 0 & 0 & 0 \\ \frac{d_{y\theta}}{m} & \frac{d_{y\theta}}{m} & \frac{d_{y\theta}}{m} & \frac{d_{y\theta}}{m} \\ \frac{d_{y\theta}w}{I_{xx}} & \frac{d_{y\theta}w}{I_{xx}} & -\frac{d_{y\theta}w}{I_{xx}} & -\frac{d_{y\theta}w}{I_{xx}} \\ -\frac{ld_{y\theta} + d_sd_{x\theta}}{I_{zz}} & \frac{ld_{y\theta} + d_sd_{x\theta}}{I_{zz}} & \frac{ld_{y\theta} + d_sd_{x\theta}}{I_{zz}} & -\frac{ld_{y\theta} + d_sd_{x\theta}}{I_{zz}} \\ -\frac{wd_{x\theta}}{I_{yy}} & \frac{wd_{x\theta}}{I_{yy}} & -\frac{wd_{x\theta}}{I_{yy}} & \frac{wd_{x\theta}}{I_{yy}} \end{bmatrix} \quad (4.38)$$

The output matrix is generated to output the 4 position states, y-position, roll, pitch, and yaw:

$$\mathbf{C}_e = \begin{bmatrix} 1 & 0 & 0 & 0 & 0 & 0 & 0 & 0 \\ 0 & 1 & 0 & 0 & 0 & 0 & 0 & 0 \\ 0 & 0 & 1 & 0 & 0 & 0 & 0 & 0 \\ 0 & 0 & 0 & 1 & 0 & 0 & 0 & 0 \\ 0 & 0 & 0 & 0 & 0 & 0 & 0 & 0 \\ 0 & 0 & 0 & 0 & 0 & 0 & 0 & 0 \\ 0 & 0 & 0 & 0 & 0 & 0 & 0 & 0 \\ 0 & 0 & 0 & 0 & 0 & 0 & 0 & 0 \end{bmatrix} \quad (4.39)$$

Note that the feedforward matrix is null.

4.4 DECOUPLING OUTPUTS

An 8th order coupled system is difficult to develop a simple controller for. Instead, it is beneficial, if possible, to break the system down in to 2nd order linear time invariant (LTI) single input single output (SISO) systems. These 2nd order systems are easier to analyze than an 8th order system, and each can have its own optimized controller. The inputs to the smaller systems are y-axis linear acceleration, a_y , and the rotational accelerations about the y-axis, α_y , x-axis, α_x , and z-axis, α_z . The state flow diagram shown in Fig. 88 conveniently separates the coupled system dynamics described by (4.33) from the coupled inputs to arrive at 4 simple 2nd order LTI SISO systems.

The input into each of the four 2nd order systems can be determined by summing the effect of each rotor on each of the 4 degrees of freedom. Extracting this information from the input matrix (4.38), we can define the input into each DOF using the coupling matrix:

$$\begin{bmatrix} \delta a_y \\ \delta \alpha_x \\ \delta \alpha_z \\ \delta \alpha_y \end{bmatrix} = \begin{bmatrix} \frac{d_{y\theta}}{m} & \frac{d_{y\theta}}{m} & \frac{d_{y\theta}}{m} & \frac{d_{y\theta}}{m} \\ \frac{d_{y\theta}w}{I_{xx}} & \frac{d_{y\theta}w}{I_{xx}} & -\frac{d_{y\theta}w}{I_{xx}} & -\frac{d_{y\theta}w}{I_{xx}} \\ -\frac{ld_{y\theta} + d_s d_{x\theta}}{I_{zz}} & \frac{ld_{y\theta} + d_s d_{x\theta}}{I_{zz}} & \frac{ld_{y\theta} + d_s d_{x\theta}}{I_{zz}} & -\frac{ld_{y\theta} + d_s d_{x\theta}}{I_{zz}} \\ -\frac{wd_{x\theta}}{I_{yy}} & \frac{wd_{x\theta}}{I_{yy}} & -\frac{wd_{x\theta}}{I_{yy}} & \frac{wd_{x\theta}}{I_{yy}} \end{bmatrix} \begin{bmatrix} \delta \omega_1 \\ \delta \omega_2 \\ \delta \omega_3 \\ \delta \omega_4 \end{bmatrix} \quad (4.40)$$

Any combination of motions to the 4 wheels can now be directly translated into changes in accelerations in each degree of freedom. The workings of this coupling matrix on the overall system can also be shown graphically in Fig. 88:

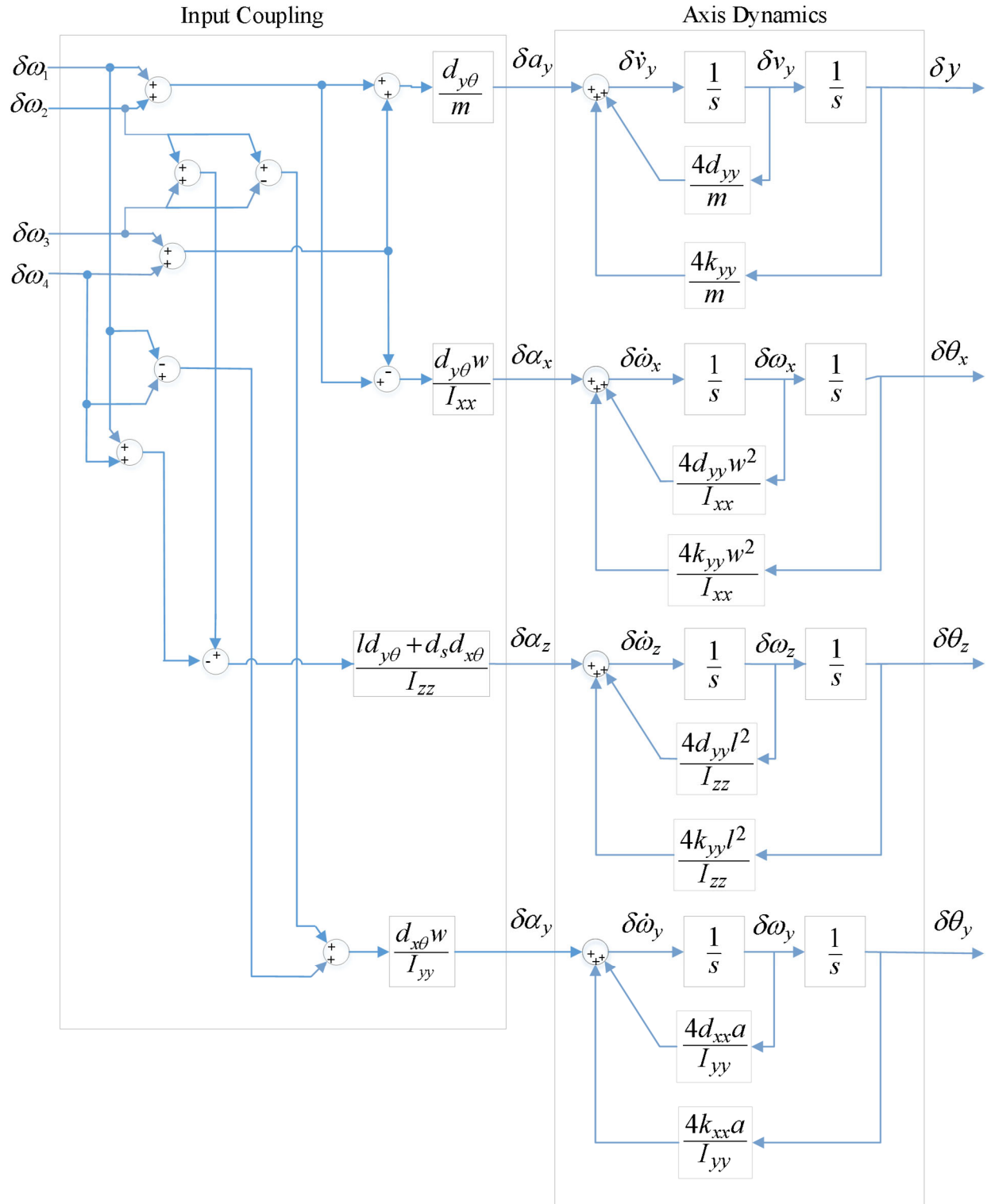


Fig. 88: 4-DOF radial EDW vehicle system decoupled state flow diagram

There are only four input vectors that are used to control the heave, pitch, roll, and yaw. The height input vector is

$$\mathbf{\Omega}_h = \begin{bmatrix} \delta\omega^h \\ \delta\omega^h \\ \delta\omega^h \\ \delta\omega^h \end{bmatrix} \quad (4.41)$$

where $\delta\omega^h$ is the change in EDW speeds to enact the desired rate of change of heave.

The roll vector is

$$\mathbf{\Omega}_x = \begin{bmatrix} -\delta\omega^x \\ \delta\omega^x \\ \delta\omega^x \\ -\delta\omega^x \end{bmatrix} \quad (4.42)$$

where $\delta\omega^x$ is the change in EDW speeds to enact the desired roll acceleration.

The pitch vector is

$$\mathbf{\Omega}_z = \begin{bmatrix} \delta\omega^z \\ \delta\omega^z \\ -\delta\omega^z \\ -\delta\omega^z \end{bmatrix} \quad (4.43)$$

where $\delta\omega^z$ is the change in EDW speeds to enact the desired pitch acceleration.

The yaw vector is

$$\mathbf{\Omega}_y = \begin{bmatrix} -\delta\omega^y \\ \delta\omega^y \\ -\delta\omega^y \\ \delta\omega^y \end{bmatrix} \quad (4.44)$$

where $\delta\omega^y$ is the change in EDW speeds to enact the desired yaw acceleration.

By using one of these input vectors, inputs can be decoupled to control height, roll, pitch, or yaw separately. For example, to enact a height change only, substitute (4.41) into (4.40):

$$\begin{bmatrix} \delta a_y \\ \delta \alpha_x \\ \delta \alpha_z \\ \delta \alpha_y \end{bmatrix} = \begin{bmatrix} \frac{d_{y\theta}}{m} & \frac{d_{y\theta}}{m} & \frac{d_{y\theta}}{m} & \frac{d_{y\theta}}{m} \\ \frac{d_{y\theta}w}{I_{xx}} & \frac{d_{y\theta}w}{I_{xx}} & -\frac{d_{y\theta}w}{I_{xx}} & -\frac{d_{y\theta}w}{I_{xx}} \\ -\frac{ld_{y\theta} + d_s d_{x\theta}}{I_{zz}} & \frac{ld_{y\theta} + d_s d_{x\theta}}{I_{zz}} & \frac{ld_{y\theta} + d_s d_{x\theta}}{I_{zz}} & -\frac{ld_{y\theta} + d_s d_{x\theta}}{I_{zz}} \\ -\frac{wd_{x\theta}}{I_{yy}} & \frac{wd_{x\theta}}{I_{yy}} & -\frac{wd_{x\theta}}{I_{yy}} & \frac{wd_{x\theta}}{I_{yy}} \end{bmatrix} \mathbf{\Omega}_h \quad (4.45)$$

Multiplying through to solve, the resulting height acceleration change would be:

$$\delta a_y = \frac{4d_{y\theta}}{m} \delta\omega^h \quad (4.46)$$

while the other accelerations, $\delta\alpha_x$, $\delta\alpha_z$ and $\delta\alpha_y$, are zero.

To change roll acceleration only, substitute (4.42) into (4.40):

$$\begin{bmatrix} \delta a_y \\ \delta \alpha_x \\ \delta \alpha_z \\ \delta \alpha_y \end{bmatrix} = \begin{bmatrix} \frac{d_{y\theta}}{m} & \frac{d_{y\theta}}{m} & \frac{d_{y\theta}}{m} & \frac{d_{y\theta}}{m} \\ \frac{d_{y\theta}w}{I_{xx}} & \frac{d_{y\theta}w}{I_{xx}} & -\frac{d_{y\theta}w}{I_{xx}} & -\frac{d_{y\theta}w}{I_{xx}} \\ -\frac{ld_{y\theta} + d_s d_{x\theta}}{I_{zz}} & \frac{ld_{y\theta} + d_s d_{x\theta}}{I_{zz}} & \frac{ld_{y\theta} + d_s d_{x\theta}}{I_{zz}} & -\frac{ld_{y\theta} + d_s d_{x\theta}}{I_{zz}} \\ -\frac{wd_{x\theta}}{I_{yy}} & \frac{wd_{x\theta}}{I_{yy}} & -\frac{wd_{x\theta}}{I_{yy}} & \frac{wd_{x\theta}}{I_{yy}} \end{bmatrix} \Omega_x \quad (4.47)$$

Multiplying through, the resulting roll acceleration change would be:

$$\delta \alpha_z = \frac{4ld_{y\theta} + 4d_s d_{x\theta}}{I_{zz}} \delta \omega^x \quad (4.48)$$

while the other accelerations, δa_y , $\delta \alpha_x$ and $\delta \alpha_y$, are zero.

To change pitch acceleration only, substitute (4.43) into (4.40):

$$\begin{bmatrix} \delta a_y \\ \delta \alpha_x \\ \delta \alpha_z \\ \delta \alpha_y \end{bmatrix} = \begin{bmatrix} \frac{d_{y\theta}}{m} & \frac{d_{y\theta}}{m} & \frac{d_{y\theta}}{m} & \frac{d_{y\theta}}{m} \\ \frac{d_{y\theta}w}{I_{xx}} & \frac{d_{y\theta}w}{I_{xx}} & -\frac{d_{y\theta}w}{I_{xx}} & -\frac{d_{y\theta}w}{I_{xx}} \\ -\frac{ld_{y\theta} + d_s d_{x\theta}}{I_{zz}} & \frac{ld_{y\theta} + d_s d_{x\theta}}{I_{zz}} & \frac{ld_{y\theta} + d_s d_{x\theta}}{I_{zz}} & -\frac{ld_{y\theta} + d_s d_{x\theta}}{I_{zz}} \\ -\frac{wd_{x\theta}}{I_{yy}} & \frac{wd_{x\theta}}{I_{yy}} & -\frac{wd_{x\theta}}{I_{yy}} & \frac{wd_{x\theta}}{I_{yy}} \end{bmatrix} \Omega_z \quad (4.49)$$

Multiplying through, the resulting pitch acceleration change would be:

$$\delta \alpha_x = \frac{4d_{y\theta}w}{I_{xx}} \delta \omega^z \quad (4.50)$$

while the other accelerations δa_y , $\delta \alpha_z$ and $\delta \alpha_y$, are zero.

To change yaw acceleration only, substitute (4.44) into (4.40):

$$\begin{bmatrix} \delta a_y \\ \delta \alpha_x \\ \delta \alpha_z \\ \delta \alpha_y \end{bmatrix} = \begin{bmatrix} \frac{d_{y\theta}}{m} & \frac{d_{y\theta}}{m} & \frac{d_{y\theta}}{m} & \frac{d_{y\theta}}{m} \\ \frac{d_{y\theta}w}{I_{xx}} & \frac{d_{y\theta}w}{I_{xx}} & -\frac{d_{y\theta}w}{I_{xx}} & -\frac{d_{y\theta}w}{I_{xx}} \\ -\frac{ld_{y\theta} + d_s d_{x\theta}}{I_{zz}} & \frac{ld_{y\theta} + d_s d_{x\theta}}{I_{zz}} & \frac{ld_{y\theta} + d_s d_{x\theta}}{I_{zz}} & -\frac{ld_{y\theta} + d_s d_{x\theta}}{I_{zz}} \\ -\frac{wd_{x\theta}}{I_{yy}} & \frac{wd_{x\theta}}{I_{yy}} & -\frac{wd_{x\theta}}{I_{yy}} & \frac{wd_{x\theta}}{I_{yy}} \end{bmatrix} \Omega_y \quad (4.51)$$

Multiplying through, the resulting yaw acceleration change would be:

$$\delta \alpha_y = \frac{4wd_{x\theta}}{I_{yy}} \delta \omega^y \quad (4.52)$$

while the other acceleration values, δa_y , $\delta \alpha_z$ and $\delta \alpha_x$, are zero.

We can use equations (4.46), (4.50), (4.48), and (4.52) to solve for $\delta \omega^h$, $\delta \omega^x$, $\delta \omega^z$, and $\delta \omega^y$, respectively:

$$\delta \omega^h = \frac{m}{4d_{y\theta}} \delta a_y \quad (4.53)$$

$$\delta \omega^x = \frac{I_{xx}}{4d_{y\theta}w} \delta \alpha_x \quad (4.54)$$

$$\delta \omega^z = \frac{I_{zz}}{4ld_{y\theta} + 4d_s d_{x\theta}} \delta \alpha_z \quad (4.55)$$

$$\delta \omega^y = \frac{I_{yy}}{4wd_{x\theta}} \delta \alpha_y \quad (4.56)$$

Then, the contribution from each of the EDW velocity terms $\delta \omega^h$, $\delta \omega^x$, $\delta \omega^z$, and $\delta \omega^y$ must be summed to arrive at the desired EDW speed to enact the desired change in system input:

$$\begin{bmatrix} \delta\omega_1 \\ \delta\omega_2 \\ \delta\omega_3 \\ \delta\omega_4 \end{bmatrix} = \mathbf{\Omega}_h + \mathbf{\Omega}_x + \mathbf{\Omega}_z + \mathbf{\Omega}_y \quad (4.57)$$

Ideally, we would like to command a desired y -acceleration, D_y , desired yaw acceleration, $D_{\angle y}$, desired roll acceleration, $D_{\angle x}$, and desired pitch acceleration, $D_{\angle z}$. In order to accomplish this, we can run our desired inputs through an input decoupling block, which cancels out the input coupling block:

$$\begin{bmatrix} \delta\omega_1 \\ \delta\omega_2 \\ \delta\omega_3 \\ \delta\omega_4 \end{bmatrix} = \begin{bmatrix} \frac{m}{d_{y\theta}} & \frac{m}{d_{y\theta}} & \frac{m}{d_{y\theta}} & \frac{m}{d_{y\theta}} \\ -\frac{I_{xx}}{wd_{y\theta}} & -\frac{I_{xx}}{wd_{y\theta}} & \frac{I_{xx}}{wd_{y\theta}} & \frac{I_{xx}}{wd_{y\theta}} \\ -\frac{I_{zz}}{ld_{y\theta} + d_s d_{x\theta}} & \frac{I_{zz}}{ld_{y\theta} + d_s d_{x\theta}} & \frac{I_{zz}}{ld_{y\theta} + d_s d_{x\theta}} & -\frac{I_{zz}}{ld_{y\theta} + d_s d_{x\theta}} \\ \frac{I_{yy}}{wd_{x\theta}} & \frac{I_{yy}}{wd_{x\theta}} & -\frac{I_{yy}}{wd_{x\theta}} & -\frac{I_{yy}}{wd_{x\theta}} \end{bmatrix} \begin{bmatrix} D_y \\ D_{\angle x} \\ D_{\angle z} \\ D_{\angle y} \end{bmatrix} \quad (4.58)$$

A graphical representation of the decoupling block is shown in Fig. 89.

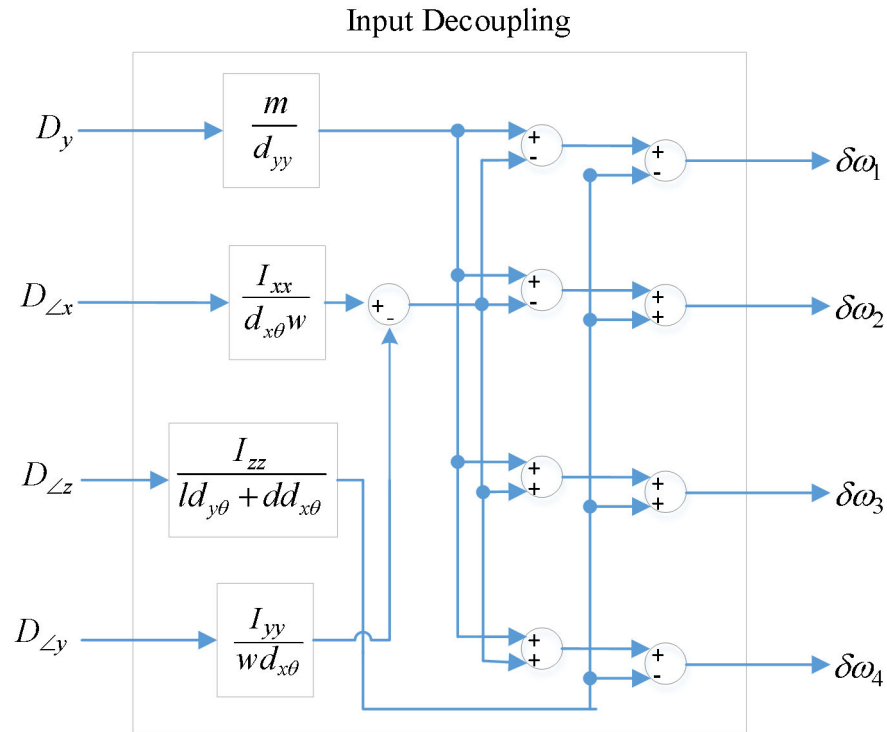


Fig. 89: State flow diagram of input decoupling block

To further simplify, we can separate the system dynamics block shown in Fig. 88 into 4 simpler LTI SISO blocks, as shown in Fig. 90:

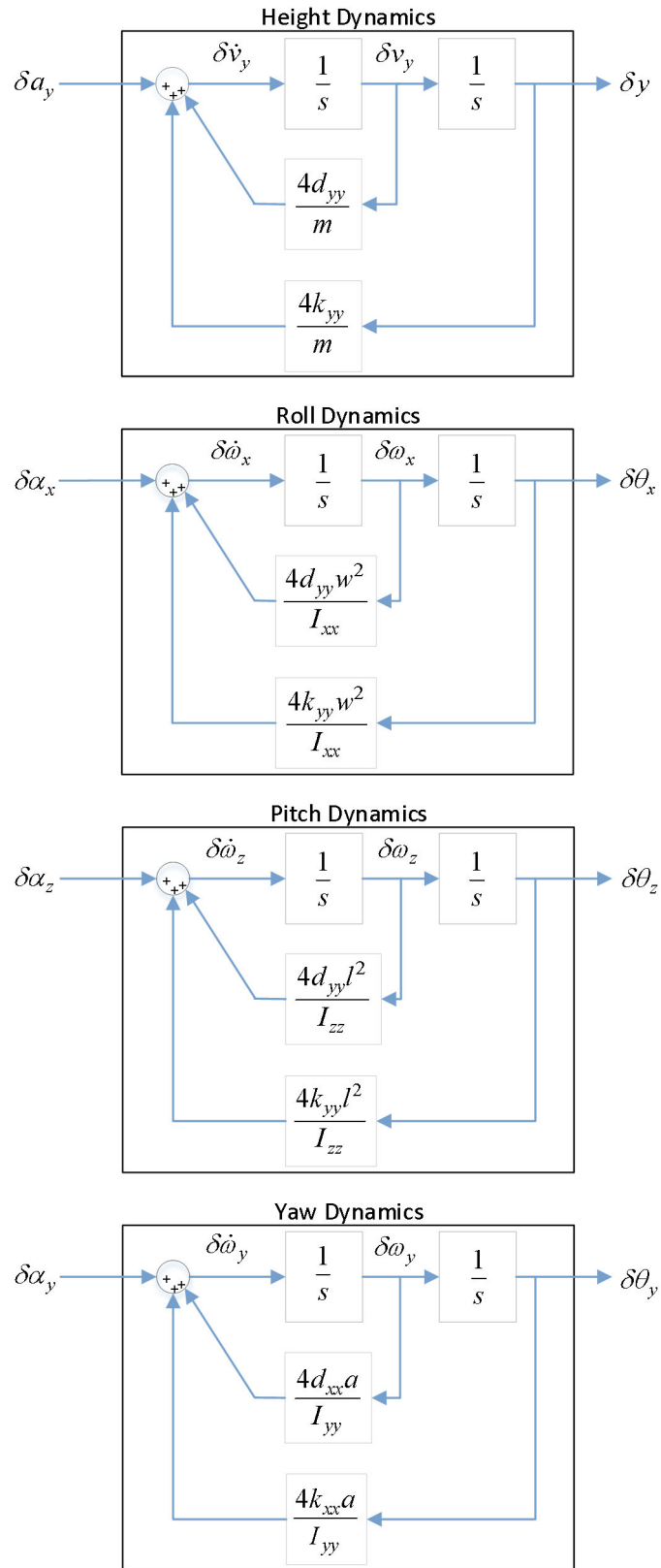


Fig. 90: Separated dynamics systems of prototype radial EDW vehicle linearized model

Fig. 91 shows the entire decoupled and axis-separated system block diagram:

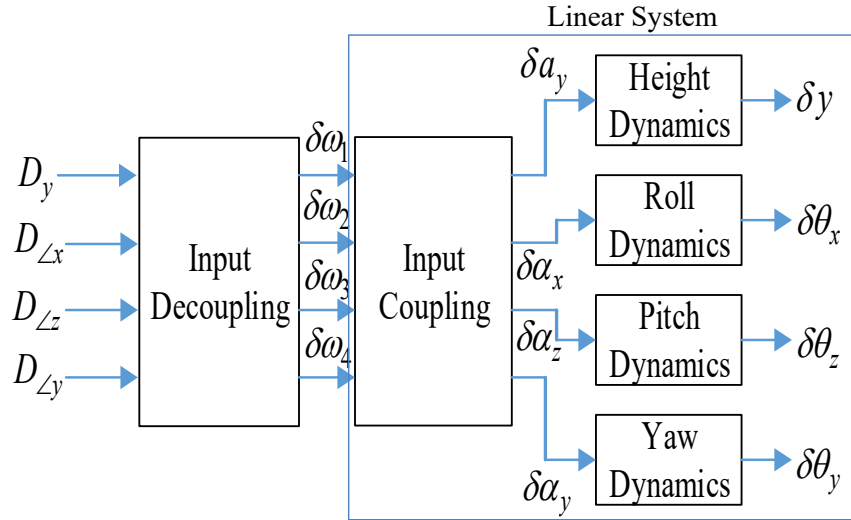


Fig. 91: Decoupled system state flow diagram

By applying inputs through the input decoupling block, we achieve the following equivalences that allow accelerations to be commanded as if inputs were being directly applied to the dynamics blocks:

$$D_y = \delta a_y \quad (4.59)$$

$$D_{\angle x} = \delta\alpha_x \quad (4.60)$$

$$D_{\angle z} = \delta\alpha_z \quad (4.61)$$

$$D_{\angle y} = \delta\alpha_y \quad (4.62)$$

These 2nd order system blocks can be represented in state space form,

$$\dot{\mathbf{x}}_d = \mathbf{A}_d \mathbf{x}_d + \mathbf{B}_d \mathbf{u}_d \quad (4.63)$$

$$y_d = \mathbf{C}_d \mathbf{x}_d + \mathbf{D}_d \mathbf{u}_d \quad (4.64)$$

where \mathbf{A}_d is the plant state matrix \mathbf{B}_d is the plant input matrix, \mathbf{C}_d is the output matrix, \mathbf{D}_d is the feedthrough matrix, \mathbf{x}_d is the state vector, \mathbf{u}_d is the input vector, and y_d is the output.

This form is useful for simple controller design as well as analyzing each DOF's dynamics separately. The height dynamics are:

$$\begin{bmatrix} \delta \dot{y} \\ \delta \dot{v}_y \end{bmatrix} = \begin{bmatrix} 0 & 1 \\ \frac{k_{yy}}{m} & \frac{d_{yy}}{m} \end{bmatrix} \begin{bmatrix} \delta y \\ \delta v_y \end{bmatrix} + \begin{bmatrix} 0 \\ 1 \end{bmatrix} D_y \quad (4.65)$$

The roll dynamics are:

$$\begin{bmatrix} \delta \dot{\theta}_x \\ \delta \dot{\omega}_x \end{bmatrix} = \begin{bmatrix} 0 & 1 \\ \frac{k_{yy} w^2}{I_{xx}} & \frac{d_{yy} w^2}{I_{xx}} \end{bmatrix} \begin{bmatrix} \delta \theta_x \\ \delta \omega_x \end{bmatrix} + \begin{bmatrix} 0 \\ 1 \end{bmatrix} D_{\angle x} \quad (4.66)$$

The pitch dynamics are:

$$\begin{bmatrix} \delta \dot{\theta}_z \\ \delta \dot{\omega}_z \end{bmatrix} = \begin{bmatrix} 0 & 1 \\ \frac{k_{yy} l^2}{I_{zz}} & \frac{d_{yy} l^2}{I_{zz}} \end{bmatrix} \begin{bmatrix} \delta \theta_z \\ \delta \omega_z \end{bmatrix} + \begin{bmatrix} 0 \\ 1 \end{bmatrix} D_{\angle z} \quad (4.67)$$

The yaw dynamics are:

$$\begin{bmatrix} \delta \dot{\theta}_y \\ \delta \dot{\omega}_y \end{bmatrix} = \begin{bmatrix} 0 & 1 \\ \frac{4k_{xx} a}{I_{yy}} & \frac{4d_{xx} a}{I_{yy}} \end{bmatrix} \begin{bmatrix} \delta \theta_y \\ \delta \omega_y \end{bmatrix} + \begin{bmatrix} 0 \\ 1 \end{bmatrix} D_{\angle y} \quad (4.68)$$

For these systems, we can assume that the output matrix will be formulated to output position and feedthrough matrix will be empty:

$$\mathbf{C}_d = \begin{bmatrix} 1 & 0 \end{bmatrix} \quad (4.69)$$

$$\mathbf{D}_d = \begin{bmatrix} 0 \end{bmatrix} \quad (4.70)$$

4.5 INCLUSION OF MOTOR DYNAMICS

The EDWs rotational angular velocity, ω_n for the n^{th} rotor is controlled by varying the stator voltage of that rotor. The dynamics of the n^{th} brushless brushless DC (BLDC) motor is given by

$$\dot{u}_n = -u_n \frac{R_a}{L_a} - \frac{k_t}{L_a} \omega_n + \frac{V_n}{L_a} \quad (4.71)$$

$$\dot{\omega}_n = \frac{k_t}{J} u_n - \frac{b}{J} \omega_n - \frac{1}{J} T_n \quad (4.72)$$

where V_n = stator voltage of n^{th} rotor, u_n = stator current of n^{th} rotor, R_a = winding resistance, L_a = stator inductance, k_e = back-emf constant, J = rotor inertia, b = motor viscous force constant, k_t = motor torque constant. Performing a linearization on the current and angular velocity equations from (4.71) and (4.72):

$$\dot{u}_n = \dot{u}_n^0 - \delta u_n \frac{R_a}{L_a} - \delta \omega_n \frac{k_t}{L_a} + \frac{\delta V_n}{L_a} \quad (4.73)$$

$$\dot{\omega}_n = \dot{\omega}_n^0 + \delta u_n \frac{k_t}{J} - \delta \omega_n \frac{b}{J} - \delta T_n \frac{1}{J} \quad (4.74)$$

where

$$\delta V_n = V_n - V_n^0 \quad (4.75)$$

$$\delta \dot{u}_n = \dot{u}_n - \dot{u}_n^0 \quad (4.76)$$

$$\delta \dot{\omega}_n = \dot{\omega}_n - \dot{\omega}_n^0 \quad (4.77)$$

where V_n^0 , u_n^0 and ω_n^0 denote the motor voltage, motor current, and rotor angular velocity at the linearization point.

This allows the current and angular velocity dynamic equations to be written as linear around the operating point:

$$\delta \dot{u}_n = -\delta u_n \frac{R_a}{L_a} - \delta \omega_n \frac{k_t}{L_a} + \frac{\delta V_n}{L_a} \quad (4.78)$$

$$\delta \dot{\omega}_n = \delta u_n \frac{k_t}{J} - \delta \omega_n \frac{b}{J} - \delta T_n \frac{1}{J} \quad (4.79)$$

The load torque, T_n on the n^{th} rotor is caused by the eddy current forces. This load torque can be modeled using approach given in [11]. The torque equation is defined by equation (2.27). Assuming that each EDW is at the average height point defined in (3.61) then linearizing the eddy current torque on the n^{th} rotor yields

$$T_n(y_n, \dot{y}_n, x_n, \dot{x}_n, \omega_n) \approx k_{yn} \delta y_n + d_{yn} \delta \dot{y}_n + k_{xn} \delta x_n + d_{xn} \delta \dot{x}_n + d_{\theta n} \delta \omega_n + T_n^e \quad (4.80)$$

where

$$T_n^e = T_n(y_n^e, 0, x_n^e, \dot{x}_n^e, \omega_n^e) \quad (4.81)$$

$$k_{yn} = \left. \frac{\partial T_n(y_n, 0, x_n^e, \dot{x}_n^e, \omega_n^e)}{\partial y_n} \right|_{y_n=y_n^e} \quad (4.82)$$

$$d_{yn} = \left. \frac{\partial T_n(y_n^e, \dot{y}_n, x_n^e, \dot{x}_n^e, \omega_n^e)}{\partial \dot{y}_n} \right|_{\dot{y}_n=0} \quad (4.83)$$

$$k_{xn} = \left. \frac{\partial T_n(y_n^e, 0, x_n, \dot{x}_n^e, \omega_n^e)}{\partial x_n} \right|_{x_n=x_n^e} \quad (4.84)$$

$$d_{xn} = \left. \frac{\partial T_n(y_n^e, \dot{y}_n, x_n, \dot{x}_n, \omega_n^e)}{\partial \dot{x}_n} \right|_{\dot{x}_n=0} \quad (4.85)$$

$$d_{\theta n} = \left. \frac{\partial T_n(y_n^e, 0, x_n^e, \dot{x}_n^e, \omega_n)}{\partial \omega_n} \right|_{\omega_n=\omega_n^e} \quad (4.86)$$

Note that the z -axis movement is not included in the torque equation because the vehicle's center of gravity is physically constrained around $z = 0$. To eliminate the weak non-linearity, we use the linearization of torque to describe the behavior around the operating point:

$$\delta T_n \approx T_n(y_n, \dot{y}_n, x_n, \dot{x}_n, \omega_n) - T_n^e \quad (4.87)$$

Substituting (4.80) into (4.87):

$$\delta T_n(y_n, \dot{y}_n, x_n, \dot{x}_n, \omega_n) \approx k_{yn} \delta y_n + d_{yn} \delta \dot{y}_n + k_{xn} \delta x_n + d_{xn} \delta \dot{x}_n + d_{\theta n} \delta \omega_n \quad (4.88)$$

Substituting the torque equation (4.88) into the rotor velocity equation (4.79):

$$\frac{d\delta\omega_n}{dt} \approx \frac{k_t}{J} \delta i_n - \frac{b}{J} \delta \omega_n - \frac{k_{yn}}{J} \delta y_n - \frac{d_{yn}}{J} \delta \dot{y}_n - \frac{k_{xn}}{J} \delta x_n - \frac{d_{xn}}{J} \delta \dot{x}_n - \frac{d_{\theta n}}{J} \delta \omega_n \quad (4.89)$$

Substituting the δy_n and $\delta \dot{y}_n$ terms from (3.85) - (3.92) into (4.89) allows each rotors' vertical motion to be represented as a function of average vehicle height, roll, and pitch angles. Also, substituting (4.19) - (4.26) into (4.89) allows each rotors' translational movement, δx_n and $\delta \dot{x}_n$, to be expressed in terms of the vehicle yaw movements. This gives a set of state equations for the rotors' angular velocities:

$$\begin{aligned} \delta \dot{\omega}_1 = & \left(\frac{k_t}{J} \right) \delta u_1 - \left(\frac{b + d_{\theta 1}}{J} \right) \delta \omega_1 - \frac{k_{y1}}{J} (\delta y + w \delta \theta_x - l \delta \theta_z) \\ & - \frac{d_{y1}}{J} (\delta v_y + w \delta \dot{\theta}_x - l \delta \dot{\theta}_z) + \left(\frac{a k_{xn}}{J} \right) \delta \theta_y + a \left(\frac{a d_{xn}}{J} \right) \delta \omega_y \end{aligned} \quad (4.90)$$

$$\begin{aligned} \delta \dot{\omega}_2 = & \left(\frac{k_t}{J} \right) \delta u_2 - \left(\frac{b + d_{\theta 2}}{J} \right) \delta \omega_2 - \frac{k_{y2}}{J} (\delta y + w \delta \theta_x + l \delta \theta_z) \\ & - \frac{d_{y2}}{J} (\delta v_y + w \delta \dot{\theta}_x + l \delta \dot{\theta}_z) - \left(\frac{a k_{xn}}{J} \right) \delta \theta_y - a \left(\frac{a d_{xn}}{J} \right) \delta \omega_y \end{aligned} \quad (4.91)$$

$$\begin{aligned}\delta\dot{\omega}_3 = & \left(\frac{k_t}{J}\right)\delta u_3 - \left(\frac{b+d_{\theta 3}}{J}\right)\delta\omega_3 - \frac{k_{y3}}{J}(\delta y - w\delta\theta_x + l\delta\theta_z) \\ & - \frac{d_{y3}}{J}(\delta v_y - w\delta\dot{\theta}_x + l\delta\dot{\theta}_z) + \left(\frac{ak_{xn}}{J}\right)\delta\theta_y + a\left(\frac{ad_{xn}}{J}\right)\delta\omega_y\end{aligned}\quad (4.92)$$

$$\begin{aligned}\delta\dot{\omega}_4 = & \left(\frac{k_t}{J}\right)\delta u_4 - \left(\frac{b+d_{\theta 4}}{J}\right)\delta\omega_4 - \frac{k_{y4}}{J}(\delta y - w\delta\theta_x - l\delta\theta_z) \\ & - \frac{d_{y4}}{J}(\delta v_y - w\delta\dot{\theta}_x - l\delta\dot{\theta}_z) - \left(\frac{ak_{xn}}{J}\right)\delta\theta_y - a\left(\frac{ad_{xn}}{J}\right)\delta\omega_y\end{aligned}\quad (4.93)$$

The state space system from (4.33) can be augmented to include these additional states.

Writing out the complete set of states and inputs:

States: $\delta y, \delta v_y, \delta\theta_x, \delta\dot{\theta}_x, \delta\theta_z, \delta\dot{\theta}_z, \delta\omega_1, \delta\omega_2, \delta\omega_3, \delta\omega_4, \delta u_1, \delta u_2, \delta u_3, \delta u_4$

Inputs: $\delta V_1, \delta V_2, \delta V_3, \delta V_4$

The new state space system is defined by:

$$\dot{\mathbf{x}}_c = \mathbf{A}_c \mathbf{x}_c + \mathbf{B}_c \mathbf{u}_c \quad (4.94)$$

The new state vector is:

$$\mathbf{x}_c = [\mathbf{x}_e \quad \delta\omega_1 \quad \delta\omega_2 \quad \delta\omega_3 \quad \delta\omega_4 \quad \delta u_1 \quad \delta u_2 \quad \delta u_3 \quad \delta u_4]^T \quad (4.95)$$

Recall that \mathbf{x}_e is defined by:

$$\mathbf{x}_e = [\delta y \quad \delta\theta_x \quad \delta\theta_z \quad \delta\theta_y \quad \delta v_y \quad \delta\omega_x \quad \delta\omega_z \quad \delta\omega_y]^T \quad (4.35)$$

The new input vector is:

$$\mathbf{u}_c = [\delta V_1 \quad \delta V_2 \quad \delta V_3 \quad \delta V_4]^T \quad (4.96)$$

The new state and input matrices are

$$\mathbf{A}_c = \begin{bmatrix} \mathbf{A}_e & \mathbf{B}_e & \mathbf{0}_{4,6} \\ \mathbf{A}_m & \mathbf{B}_d & \frac{k_t}{J} \mathbf{I}_{4,4} \\ \mathbf{0}_{6,4} & -\frac{k_e}{L_a} \mathbf{I}_{4,4} & -\frac{R_a}{L_a} \mathbf{I}_{4,4} \end{bmatrix} \quad (4.97)$$

$$\mathbf{B}_c = \frac{1}{L_a} \begin{bmatrix} \mathbf{0}_{4,10} \\ \mathbf{I}_{4,4} \end{bmatrix} \quad (4.98)$$

Note that \mathbf{A}_c is composed of a set of other matrices. Recall that \mathbf{A}_e and \mathbf{B}_e are the state and input matrices from (4.33) that describes how the vehicle's movement affects the states and are defined by (4.37) and (4.38). \mathbf{A}_m and \mathbf{B}_d describe rotor angular velocities' effect on the states. The last row and column in (4.97) describe the effect of rotor current on the states, where $\mathbf{I}_{n \times q}$ is an $n \times q$ identity matrix. \mathbf{A}_m and \mathbf{B}_d are described by:

$$\mathbf{A}_m = \frac{1}{J} \begin{bmatrix} -k_{y1} & -d_{y1} & wk_{y1} & wd_{y1} & -lk_{y1} & -ld_{y1} & ak_{x1} & ad_{x1} \\ -k_{y2} & -d_{y2} & wk_{y2} & wd_{y2} & lk_{y2} & ld_{y2} & ak_{x2} & ad_{x2} \\ -k_{y3} & -d_{y3} & -wk_{y3} & -wd_{y3} & lk_{y3} & ld_{y3} & ak_{x3} & ad_{x3} \\ -k_{y4} & -d_{y4} & -wk_{y4} & -wd_{y3} & -lk_{y4} & -ld_{y4} & ak_{x4} & ad_{x4} \end{bmatrix} \quad (4.99)$$

$$\mathbf{B}_d = \frac{-1}{J} \begin{bmatrix} b + d_{\theta 1} & 0 & 0 & 0 \\ 0 & b + d_{\theta 2} & 0 & 0 \\ 0 & 0 & b + d_{\theta 3} & 0 \\ 0 & 0 & 0 & b + d_{\theta 4} \end{bmatrix} \quad (4.100)$$

Note that if the vehicle is evenly loaded and operating near a level operating point, then

$$k_{y1} = k_{y2} = k_{y3} = k_{y4} \quad (4.101)$$

$$d_{y1} = d_{y2} = d_{y3} = d_{y4} \quad (4.102)$$

$$k_{x1} = k_{x2} = k_{x3} = k_{x4} \quad (4.103)$$

$$d_{x1} = d_{x2} = d_{x3} = d_{x4} \quad (4.104)$$

$$d_{\theta 1} = d_{\theta 2} = d_{\theta 3} = d_{\theta 4} \quad (4.105)$$

Representing the vehicle in linear state-space form is ideal due to the wide selection of effective control strategies that are easily applied to such systems, some of which are explored in chapter CHAPTER 5:. This is also a milestone for EDWmaglev, since it is now possible to quickly analyze the system's behavior without having to resort to either compute-intensive numerical methods which can take days or weeks to simulate, or inaccurate lumped parameter approaches. If the system remains close to the operating point for which the damping and stiffness terms were calculated for, then the behavior of the highly nonlinear EDW system will be qualitatively the same as the linear system derived above [80].

If the system undergoes a large change in operating point, or if a linear system is undesirable, the stiffness and damping terms can instead be replaced with functions to form a nonlinear model using the the SOVP analytical solution. The nonlinear system can then be thought of as being approximated by a series of first order Taylor expansions such that it can be called *piecewise linear*. Smaller linearization error occurs as the *piecewise* system becomes more segmented, which is possible with an analytical force model that is orders of magnitude faster than previous models [71]. The suitability for the analytical solution to be used in a piecewise linear model is discussed in further detail at the end of chapter CHAPTER 5:.

4.6 MODEL VALIDATION

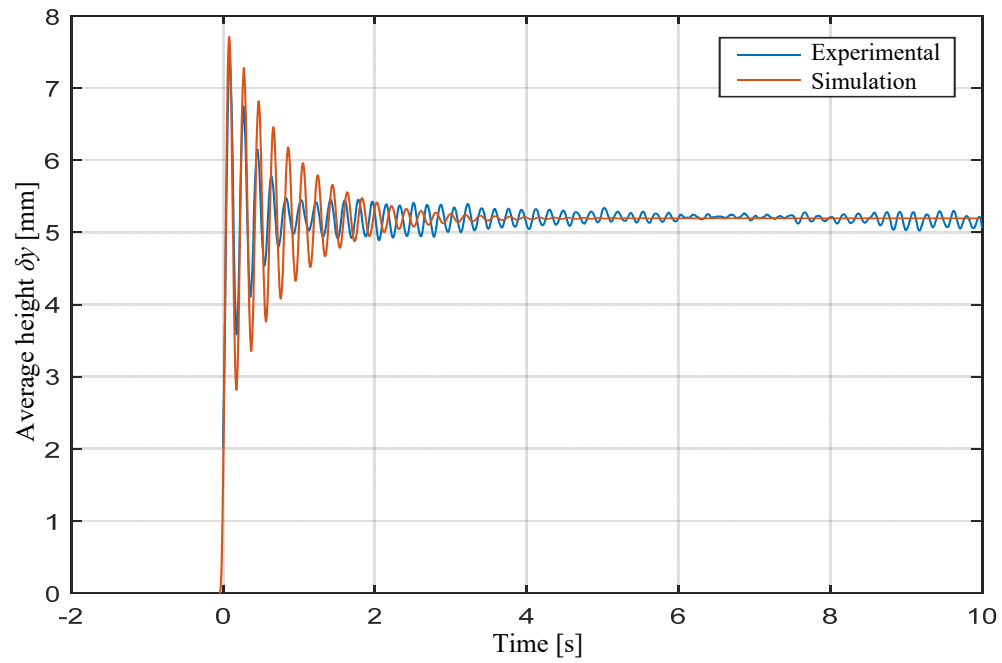
The system was simulated by using the values given in Table 1. The simulation was around the steady-state equilibrium point:

$$(y, v_y, \theta_x, \theta_y, \theta_z, \omega_x, \omega_y, \omega_z, \omega_n, V_n) = (9.29\text{mm}, 0, 0, 0, 0, 0, 0, 0, 3937\text{rpm}, 12\text{V}) \quad (4.106)$$

where $n=1 - 4$. Equation (4.94) was used to simulate the dynamics. At $t = 0$ the EWV was disturbed by applying a $\delta V_n=12\text{V}$ change to all of the rotors. The resulting simulation and experimental results are shown in Fig. 92 through Fig. 95 and the prolonged oscillations seen in the simulation results indicate that the system is underdamped. Note that yaw was not simulated because on the prototype testbed, the vehicle was constrained in the y rotational axis. Because of the phase differences between each corner of the vehicle, the average vehicle height, y , fails to provide the expected result. These phase differences are due to the vehicle's weight not being uniformly distributed and each motor/rotor having slightly different physical parameters, and provide a natural averaging/filtering of the rotor heights. Therefore, the oscillation that the vehicle exhibits is damped significantly faster than predicted by the model. Note that the pitch angle has more damping than the roll angle due to the physical vehicle restrains that prevent it from leaving the ideal location on the track.

Table 5: Radial EDW vehicle state-space simulation parameters

| Parameter | Value | Unit |
|---------------|----------|--------|
| k_{xx} | -1832.6 | N/m |
| d_{xx} | 1.174 | Ns/m |
| k_{xy} | -6009.1 | Ns/m |
| d_{xy} | -5.106 | Ns/m |
| k_{yy} | -2113.1 | N/m |
| d_{yy} | -5.21 | Ns/m |
| $d_{x\theta}$ | 0.0221 | Ns/m |
| $d_{y\theta}$ | -0.1087 | Ns/m |
| k_y | -48.71 | N/m |
| d_y | 0.0221 | Ns/m |
| k_x | 0 | N/m |
| d_x | 0 | Ns/m |
| d_θ | 0.000316 | Ns/rad |

Fig. 92: Vehicle average height vs. time using Table 5 and $\delta V_n=12V$

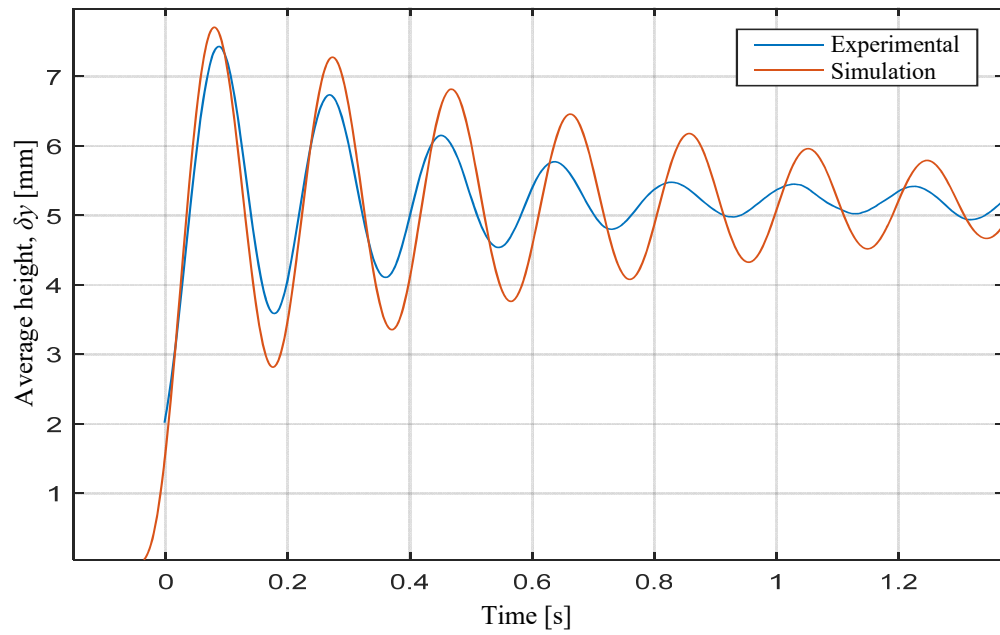


Fig. 93: Zoomed-in view of height vs. time using Table 5 and $\delta V_n=12\text{V}$

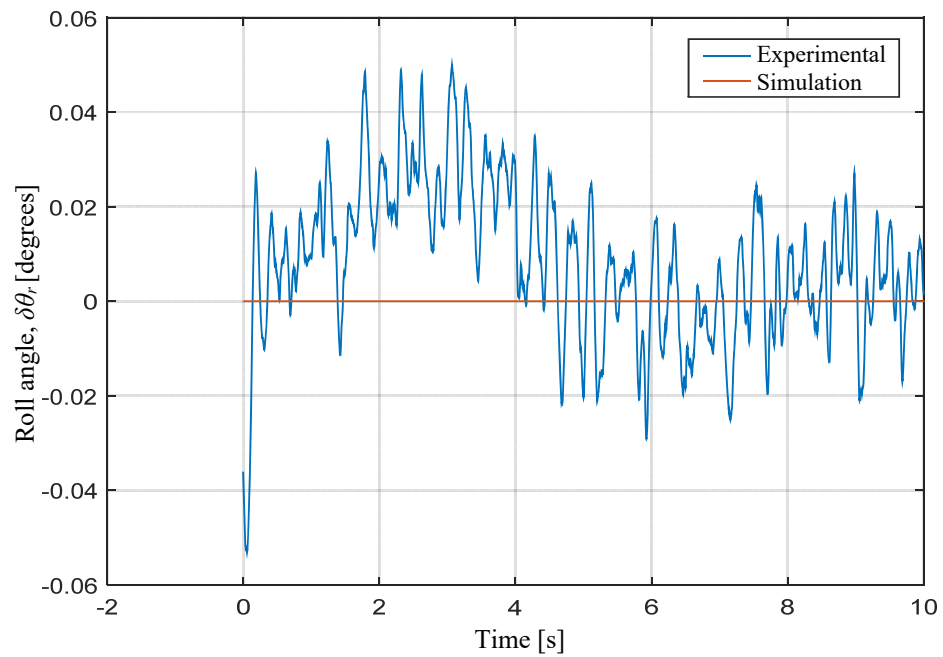


Fig. 94: Vehicle roll angle vs. time using Table 5 and $\delta V_n=12\text{V}$

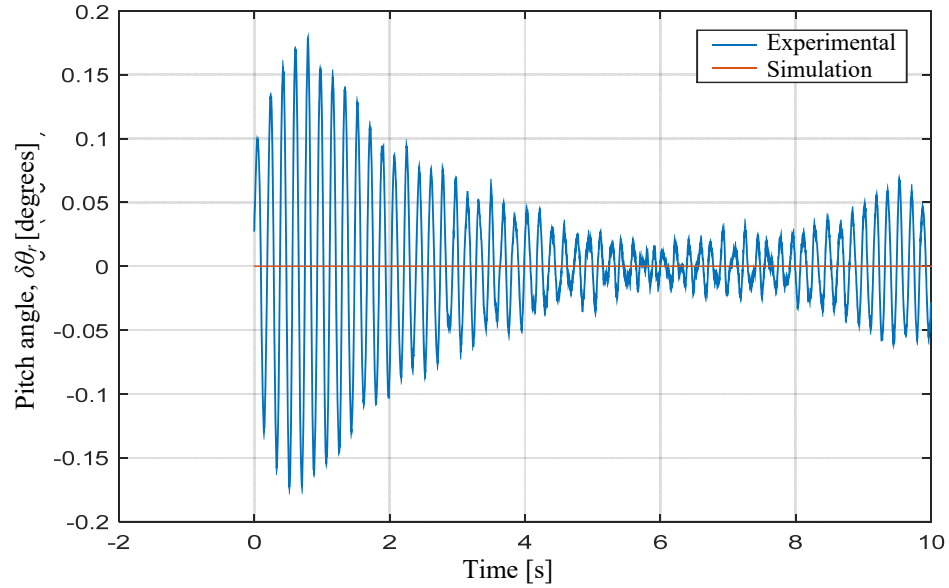


Fig. 95: Vehicle pitch angle vs. time using Table 5 and $\delta V_n = 12V$

Fig. 96 and Fig. 97 show the height change only on rotor 3. The simulation model still predicts less damping than actually exists, and the predicted overshoot of 85.1% is actually only 56.4%. However, the state-space model accurately predicts that oscillations, which are at 5.8Hz. It is also apparent that the vehicle has some steady-state oscillation that the model does not predict. The steady-state oscillations are likely caused by irregularities in the guideway height. The track irregularities are measured to be up to ± 0.71 mm, as shown in Fig. 98.

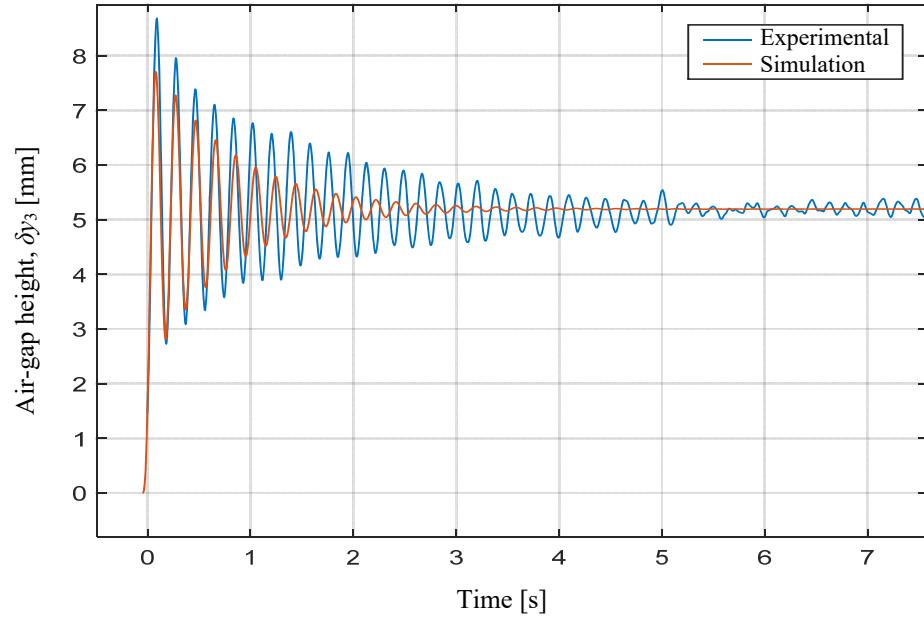


Fig. 96: Air-gap height of rotor 3 vs. time using Table 5 and $\delta V_n=12V$

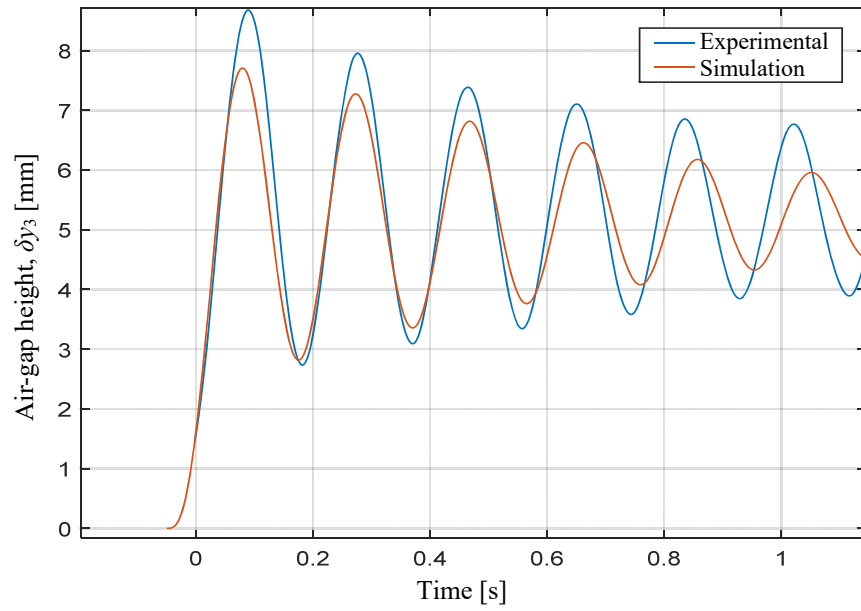


Fig. 97: Zoomed-in view of air-gap height of rotor 3 vs. time using Table 5 and $\delta V_n=12V$

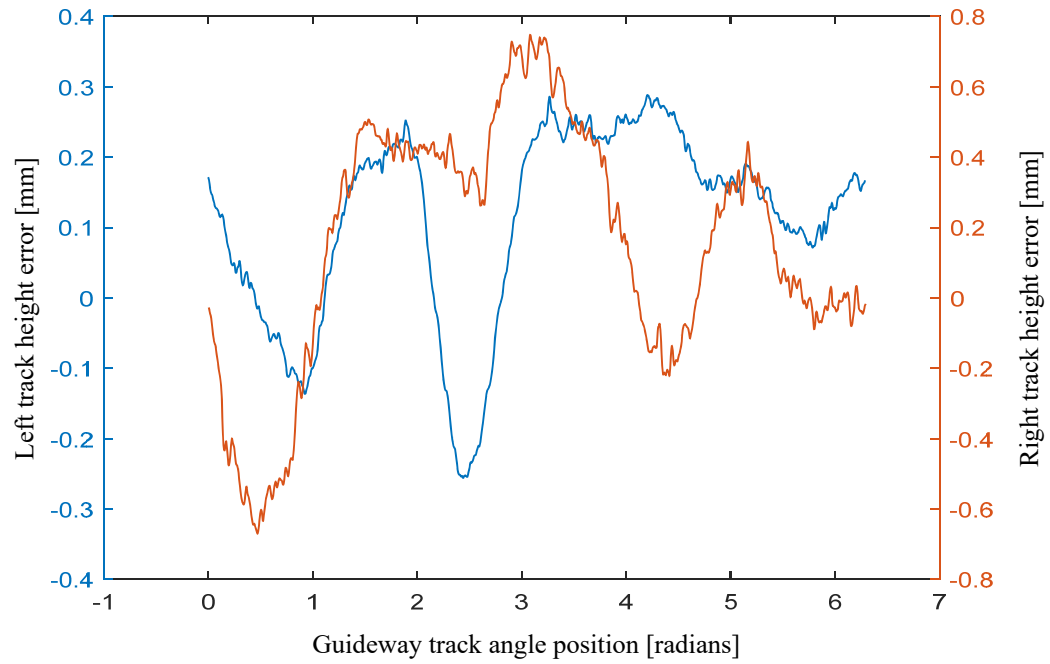


Fig. 98. Height irregularities in the left and right side of the guideway track

4.7 CONCLUSION

This chapter has used the linear differential equations from Chapter CHAPTER 3: to formulate a 4-DOF state-space system. Model complexity has been reduced by making reasonable assumptions about the vehicle operating parallel (or near parallel) to the track surface, so that many of the damping and stiffness expressions cancel each other out. In addition, x coordinates are converted into yaw, as yaw is a desired state while x -position is not. It was shown that a decoupling block could be used to directly apply inputs to each of the 4 individual subsystems (degrees of freedom). A simulation was compared to experimental results which showed that the model could predict the general behavior of the system, although the model was significantly more damped than the experimental system. The reason for this discrepancy is perhaps due to a combination of track variances as well as the EDW's being out-of-phase with each other due to manufacturing tolerances and uneven weights. This model will be used to develop a control strategy for the prototype system.

CHAPTER 5: CONTROL OF PROTOTYPE 4-DOF SYSTEM

In this chapter, classical control methods are applied to the prototype 4-DOF system to achieve a set of desired performance objectives. The purpose of modeling a controller for this system is to show that the SOVP damping and stiffness terms can be used to create an effective controller that: (a) can be tuned for performance a-priori, rather than tuning from experimental trials, and (b) does not necessitate compute-intensive dynamic force calculations (from an FEA model, for example). In Chapter CHAPTER 4:, it was shown that the EDWs could be modeled with driving motors such that the input to each wheel is voltage. With the knowledge that an EDW maglev system model based on damping and stiffness terms can be easily augmented with motor dynamics, we can then focus solely on the maglev dynamics in this chapter.

5.1 TRANSFER FUNCTIONS

We can write the transfer function to each of the 2nd order LTI systems from (4.65) - (4.68) to gain an understanding of how our system parameters affect the system's response. Writing the differential equations for heave from equation (4.65):

$$\delta \ddot{y} = \frac{4k_{yy}}{m} \delta y + \frac{4d_{yy}}{m} \delta \dot{y} + D_y \quad (5.1)$$

Taking the Laplace Transform of (5.1):

$$s^2 \delta y(s) - s \delta y(0) - \delta y(0) = \frac{4k_{yy}}{m} \delta y(s) + s \frac{4d_{yy}}{m} \delta y(s) + D_y(s) \quad (5.2)$$

Noting that

$$\delta y(0) = 0 \quad (5.3)$$

then simplifying and rearranging (5.2), the heave transfer function is formed:

$$G_y = \frac{\delta y(s)}{\delta D_y(s)} = \frac{m}{ms^2 + 4d_{yy}s + 4k_{yy}} \quad (5.4)$$

Using the same method, the transfer function for the roll system is determined to be:

$$G_{\angle x} = \frac{\delta \theta_x(s)}{\delta D_{\angle x}(s)} = \frac{I_{xx}}{I_{xx}s^2 + 4d_{yy}w^2s + 4k_{yy}w^2} \quad (5.5)$$

Similarly for the pitch system:

$$G_{\angle z} = \frac{\delta \theta_z(s)}{\delta D_{\angle z}(s)} = \frac{I_{zz}}{I_{zz}s^2 + 4d_{yy}l^2s + 4k_{yy}l^2} \quad (5.6)$$

Again using the same method for the yaw system:

$$G_{\angle y} = \frac{\delta \theta_y(s)}{\delta D_{\angle y}(s)} = \frac{I_{yy}}{I_{yy}s^2 + 4d_{xx}as + 4k_{xx}a} \quad (5.7)$$

We can define the transfer function in terms of the eigenvalues as well. For the height dynamics:

$$G_y = \frac{1}{(s + \lambda_{y1})(s + \lambda_{y2})} \quad (5.8)$$

Using the quadratic equation to solve for the eigenvalues yields:

$$\lambda_{y1} = -\frac{2d_{yy}}{m} + \frac{1}{2} \sqrt{\left(\frac{4d_{yy}}{m}\right)^2 - \frac{16k_{yy}}{m}} \quad (5.9)$$

$$\lambda_{y2} = -\frac{2d_{yy}}{m} - \frac{1}{2} \sqrt{\left(\frac{4d_{yy}}{m}\right)^2 - \frac{16k_{yy}}{m}} \quad (5.10)$$

Since stability requires all eigenvalues of a system to have negative real parts, it is evident from (5.9) that the stability criteria for the height system are:

$$k^y > 0 \quad (5.11)$$

$$d^y > 0 \quad (5.12)$$

Damping and stiffness values from Table 6 are used to simulate the vehicle hovering with a 9.29 mm airgap on all rotors, with each rotor centered over the track. These values are used to form a Bode plot for the height system as shown in Fig. 99.

Table 6: Radial EDW vehicle simulation damping and stiffness terms

| Parameter | Value | Unit |
|-----------|---------|------|
| k_{xx} | -1832.6 | N/m |
| d_{xx} | 1.17 | Ns/m |
| k_{yy} | -6009.1 | Ns/m |
| d_{xy} | -5.106 | Ns/m |

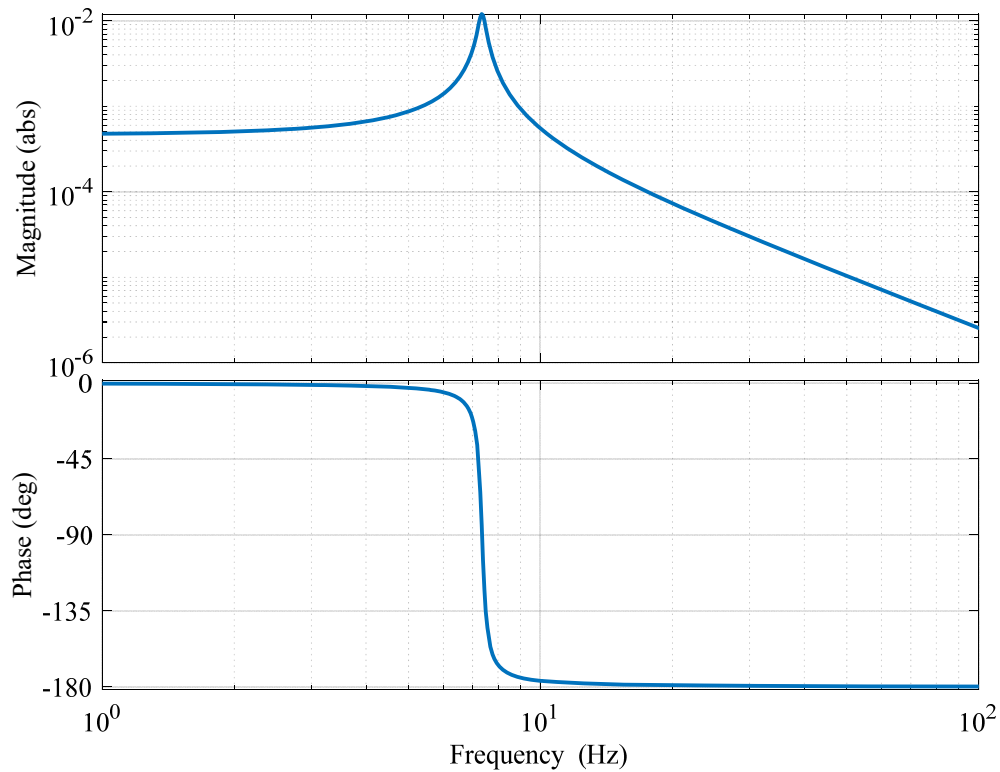


Fig. 99: Height system open-loop Bode plot, using parameters from Table 6

The Bode plot shows infinite gain margin and phase margin, implying strong stability for the height system. It also shows a resonant frequency at 7.34 Hz.

For the roll dynamics, the transfer function is:

$$G_{\angle x} = \frac{1}{(s + \lambda_{\angle x1})(s + \lambda_{\angle x2})} \quad (5.13)$$

Where the quadratic equation once again is used to find the eigenvalues:

$$\lambda_{\angle x1} = -\frac{2d_{yy}w^2}{I_{xx}} + \frac{1}{2} \sqrt{\left(\frac{4d_{yy}w^2}{I_{xx}}\right)^2 - \frac{16k_{yy}w^2}{I_{xx}}} \quad (5.14)$$

$$\lambda_{\angle x2} = -\frac{2d_{yy}w^2}{I_{xx}} - \frac{1}{2} \sqrt{\left(\frac{4d_{yy}w^2}{I_{xx}}\right)^2 - \frac{16k_{yy}w^2}{I_{xx}}} \quad (5.15)$$

Despite having different eigenvalues, the stability criterion for the roll system is the same as the height system, shown in equations (5.11) and (5.12). The Bode plot for the roll system using parameters from Table 6 is shown in Fig. 100. Similarly to the height system, the gain and phase margin are infinite, guaranteeing stability. The resonant frequency occurs at 25.1 Hz.

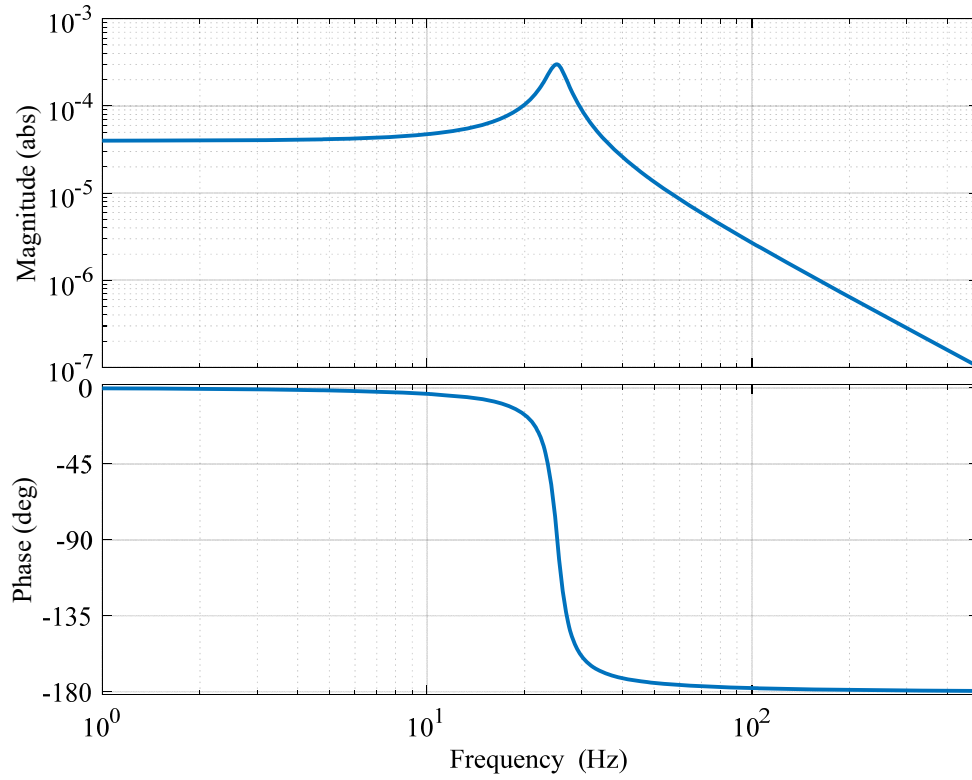


Fig. 100: Roll system open-loop Bode plot, using parameters from Table 6

For the pitch dynamics, the transfer function is:

$$G_{\zeta z} = \frac{1}{(s + \lambda_{\zeta z1})(s + \lambda_{\zeta z2})} \quad (5.16)$$

Where the eigenvalues are:

$$\lambda_{\zeta z1} = -\frac{2d_{yy}l^2}{I_{zz}} + \frac{1}{2} \sqrt{\left(\frac{4d_{yy}l^2}{I_{zz}}\right)^2 - \frac{16k_{yy}l^2}{I_{zz}}} \quad (5.17)$$

$$\lambda_{\zeta z2} = -\frac{2d_{yy}l^2}{I_{zz}} - \frac{1}{2} \sqrt{\left(\frac{4d_{yy}l^2}{I_{zz}}\right)^2 - \frac{16k_{yy}l^2}{I_{zz}}} \quad (5.18)$$

Again, the stability criteria are defined by (5.11) and (5.12). Fig. 101 shows a Bode plot for the system using Table 6. Stability in the pitch axis is guaranteed due to the infinite gain and phase margins. A resonant frequency occurs at 24.4 Hz.

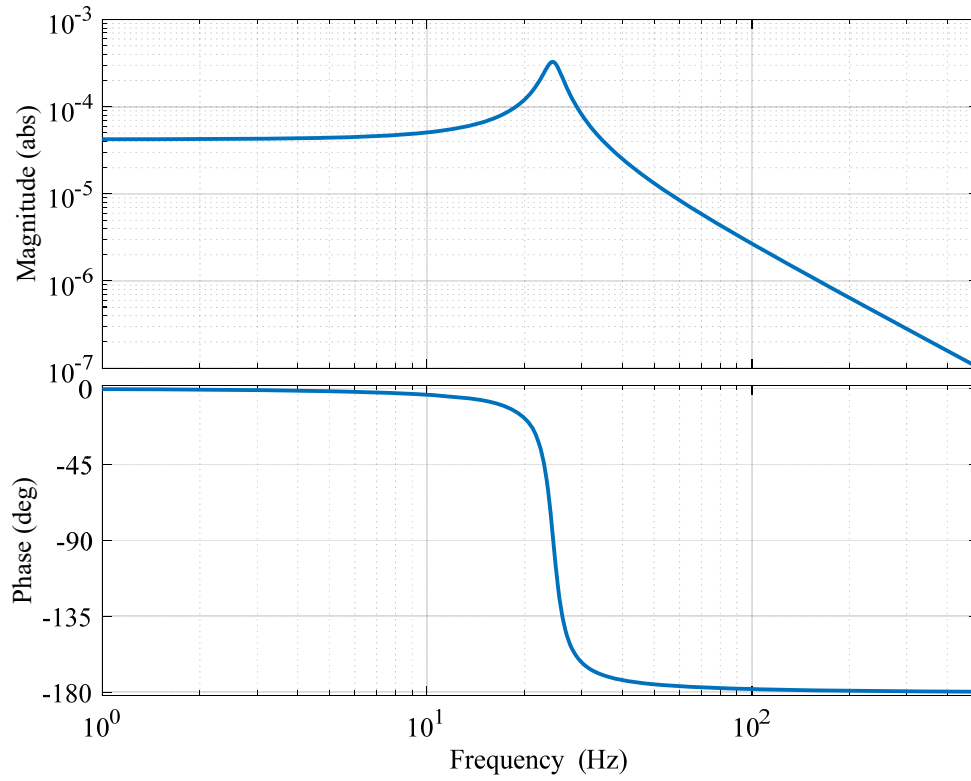


Fig. 101: Pitch system open-loop Bode plot, using parameters from Table 6

For the yaw dynamics, the transfer function is:

$$G_{\angle y} = \frac{1}{(s + \lambda_{\angle y1})(s + \lambda_{\angle y2})} \quad (5.19)$$

With the eigenvalues calculated from:

$$\lambda_{\angle y1} = -\frac{2d_{xx}a}{I_{yy}} + \frac{1}{2} \sqrt{\left(\frac{4d_{xx}a}{I_{yy}}\right)^2 - \frac{16k_{xx}a}{I_{yy}}} \quad (5.20)$$

$$\lambda_{\angle y1} = -\frac{2d_{xx}a}{I_{yy}} - \frac{1}{2}\sqrt{\left(\frac{4d_{xx}a}{I_{yy}}\right)^2 - \frac{16k_{xx}a}{I_{yy}}} \quad (5.21)$$

The stability criteria for the yaw dynamic system are:

$$p^x > 0 \quad (5.22)$$

$$c^x > 0 \quad (5.23)$$

Fig. 102 shows a Bode plot for the yaw system simulated using parameters from Table 6. Unlike the other degrees of freedom, the phase plot does not approach -180 degrees as frequency approaches infinity. In fact, increases to approach +180 degrees and is positive for all frequencies. This system is unstable, and will have an unstable oscillation at the resonant frequency of 21.8 Hz.

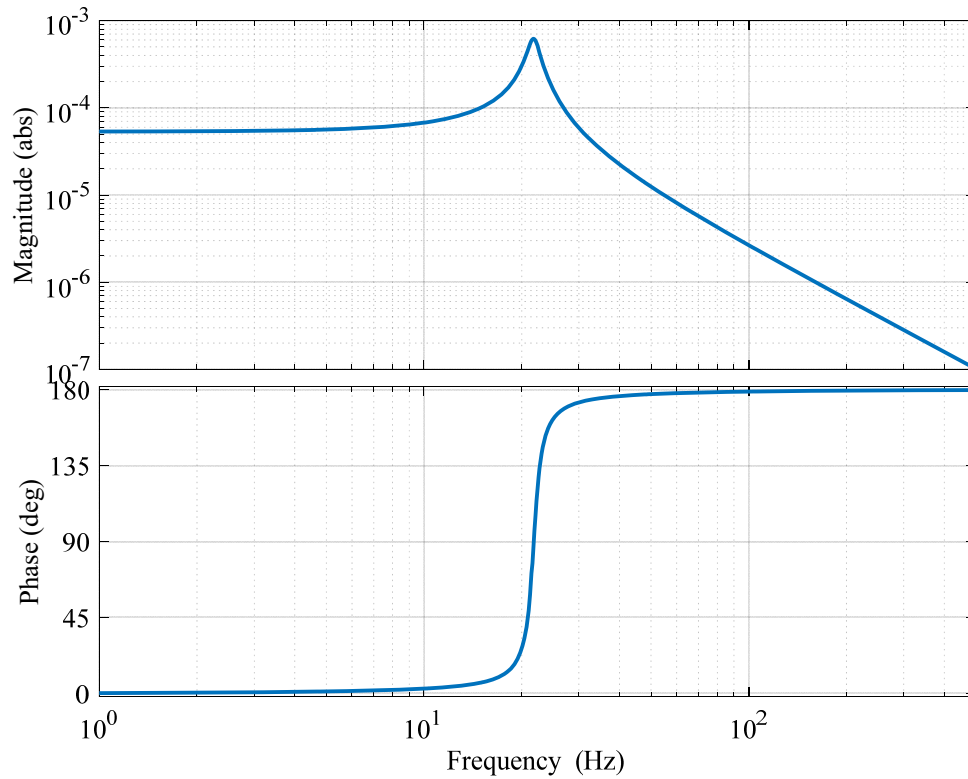


Fig. 102: Yaw system open-loop Bode plot, using parameters from Table 6

We should note that while the vehicle's physical dimensional and mass distribution terms such as w , l , a , m , I_{xx} , I_{yy} , I_{zz} cannot be altered, we can affect the system's response by selecting the damping and stiffness values. This is accomplished by choosing an effective operating point at which these values are calculated for. In other words, the system's open loop dynamics are determined by the chosen operating point.

5.2 LINEAR CONTROL OF SYSTEM DYNAMICS BLOCKS

The four decoupled 2nd order LTI systems derived in Section 4.4 in equations (4.65) - (4.68) can be simulated and compared with a set of systems that employ linear quadratic regulators (LQR). Each system must satisfy a cost function of the general form [58]:

$$J_d = \int_0^{\infty} (\mathbf{x}_d^T \mathbf{Q}_d \mathbf{x}_d + u_d^T R_d u_d + 2\mathbf{x}_d^T \mathbf{N}_d u_d) dt \quad (5.24)$$

where J_d is the cost, \mathbf{Q}_d , R_d , and \mathbf{N}_d are matrices carrying the relative cost weights. Note that the “ d ” nomenclature is to signify that these variables will come from the 4 LTI *dynamic* systems, and will be replaced with y , θx , θz , or θy , which represent height, roll, pitch, and yaw, respectively. To simplify the controller, we will make the reasonable assumption that we have a strong motor driver that can supply any reasonable amount of current and voltage without overheating, so that

$$R_d \approx 0 \quad (5.25)$$

$$\mathbf{N}_d = 0 \quad (5.26)$$

This allows us to penalize the state error exclusively, which is of most importance. Another factor that allows this assumption to be realistic will be the realistic choice of \mathbf{Q}_d , which will not allow the vehicle to undergo excessive changes in velocity, which will naturally limit the drive current to the motors.

Maintaining close proximity to desired displacement is critical for the vehicle to remain contactless with the track, while keeping velocities error small, though still important to minimize mechanical stresses, is less critical. As such, a \mathbf{Q}_d matrix that places displacement error an order of magnitude larger than velocity error is appropriate.

$$\mathbf{Q}_d = \begin{bmatrix} 10 & 0 \\ 0 & 1 \end{bmatrix} \quad (5.27)$$

This cost function is implemented by applying a control signal determined by a feedback gain, \mathbf{K}_d , and the states of the selected system, \mathbf{x}_d [58]:

$$u_d = r_d - \mathbf{K}_d \mathbf{x}_d \quad (5.28)$$

where r_d is the reference signal (the system's external input).

Recall the general form of a state-space system in matrix form:

$$\dot{\mathbf{x}}_d = \mathbf{A}_d \mathbf{x}_d - \mathbf{B}_d u_d \quad (5.29)$$

Substituting (5.28) into (5.29) and rearranging [75]:

$$\dot{\mathbf{x}}_d = (\mathbf{A}_d - \mathbf{B}_d \mathbf{K}_d) \mathbf{x}_d + \mathbf{B}_d r_d \quad (5.30)$$

This input closes the plant loop, such that the new system has the same state space form, with the new \mathbf{A} , or state matrix of the state-space system being [58]:

$$\mathbf{A}_{d,cl} = \mathbf{A}_d - \mathbf{B}_d \mathbf{K}_d \quad (5.31)$$

where “ cl ” nomenclature denotes *closed loop*. The gain, when assuming an infinite control horizon, is calculated from [58]:

$$\mathbf{K}_d = R_d^{-1} (\mathbf{B}_d^T \mathbf{P}_d + \mathbf{N}_d^T) \quad (5.32)$$

where the algebraic Riccati equation [58]:

$$\mathbf{A}_d^T \mathbf{P}_d + \mathbf{P}_d \mathbf{A}_d - (\mathbf{P}_d \mathbf{B}_d + \mathbf{N}_d) R_d^{-1} (\mathbf{B}_d^T \mathbf{P}_d + \mathbf{N}_d^T) + \mathbf{Q}_d = 0 \quad (5.33)$$

is used to solve for \mathbf{P}_d in (5.32) [75]. The systems with LQR control will take on the form shown by Fig. 103.

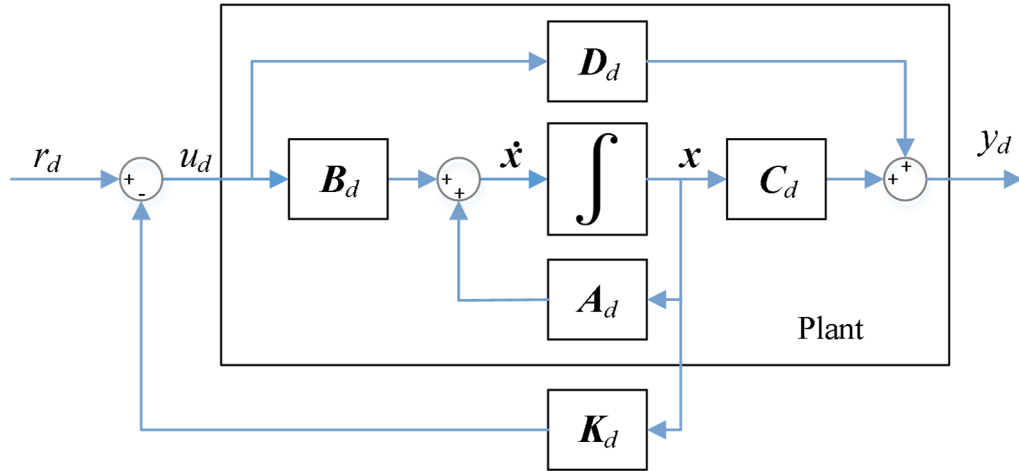


Fig. 103: Block diagram of dynamic system with LQR control

An operating point allowing the vehicle to levitate at a steady state height of 9.29mm and roll, pitch, and yaw angles of zero is chosen, with parameters defined in Table 1 and the damping and stiffness values shown in Table 6.

Table 1: Rotor, Guideway, and Vehicle Parameters for the Experimental Setup

| Parameter | | Value | Unit |
|--|--|------------------------|------------------|
| Rotor | Outer radius, r_o | 26 ± 0.58 | mm |
| | Inner radius, r_i | 9.6 | mm |
| | Width of rotor, w_o | 52 | mm |
| | Residual flux density, B_{rem} | 1.42 | T |
| | relative permeability, μ_r | 1.108 | - |
| | Pole-pairs, P | 2 | - |
| Guideway | Outer radius, r_g | 600 ± 0.73 | mm |
| | Guideway width, w_g | 77 | mm |
| | Thickness, h | 6.3 | mm |
| | Conductivity, σ (Al, 6061-T06) | 2.459×10^{-7} | Sm^{-1} |
| Vehicle | Total mass, m | 10.315 | kg |
| | Length, $2l$ | 0.173 | m |
| | Width, $2w$ | 0.3254 | m |
| | z -axis rotational Inertia, I_{zz} | 0.08821 | kgm^2 |
| | x -axis rotational Inertia, I_{xx} | 0.1977 | kgm^2 |
| | y -axis rotational inertia, I_{yy} | 0.259 | kgm^2 |
| BLDC motors (Scorpion SII-4035-250KV) | Winding inductance, L_a | 4.7×10^{-6} H | H |
| | Winding resistance, R_a | 0.037 | Ω |
| | Back-emf constant, K_e | 0.036 | Vs/rad |
| | Torque constant, K_t | 0.0295 | Nm/s |
| | rotational inertia, J | 0.00386 | kgm^2 |
| | Viscous damping coefficient, b | 2.295×10^{-6} | Nm·s/rad |

Table 6:

| Parameter | Value | Unit |
|-----------|---------|------|
| k_{xx} | -1832.6 | N/m |
| d_{xx} | 1.17 | Ns/m |
| k_{yy} | -6009.1 | Ns/m |
| d_{xy} | -5.106 | Ns/m |

Table 7: Radial EDW vehicle simulation step disturbance

| State | Value | Unit |
|-------------------|-------|----------------|
| δy | 0 | <i>m</i> |
| δv_y | 1 | <i>m/s</i> |
| $\delta \theta_x$ | 0 | <i>radians</i> |
| $\delta \omega_x$ | 1 | <i>rad/s</i> |
| $\delta \theta_z$ | 0 | <i>radians</i> |
| $\delta \omega_z$ | -0.7 | <i>rad/s</i> |
| $\delta \theta_y$ | 0 | <i>radians</i> |
| $\delta \omega_y$ | 0.5 | <i>rad/s</i> |

Fig. 104 and Fig. 105 show the simulated height and heave behavior when the disturbance defined in Table 7 is applied at $t = 1$ seconds. The value of \mathbf{K}_y calculated from (5.32) is:

$$\mathbf{K}_y = [599.62 \quad 317.67] \quad (5.34)$$

The open loop system is stable, but is slow to reject the disturbance, with the height still oscillating with an amplitude of 34.7% of the first oscillation magnitude 5 seconds after the disturbance is applied. The LQR controller quickly recovered from the disturbance within with a settling time of less than 0.3 seconds for the height dynamic. We will define the settling time error band to be 2%.

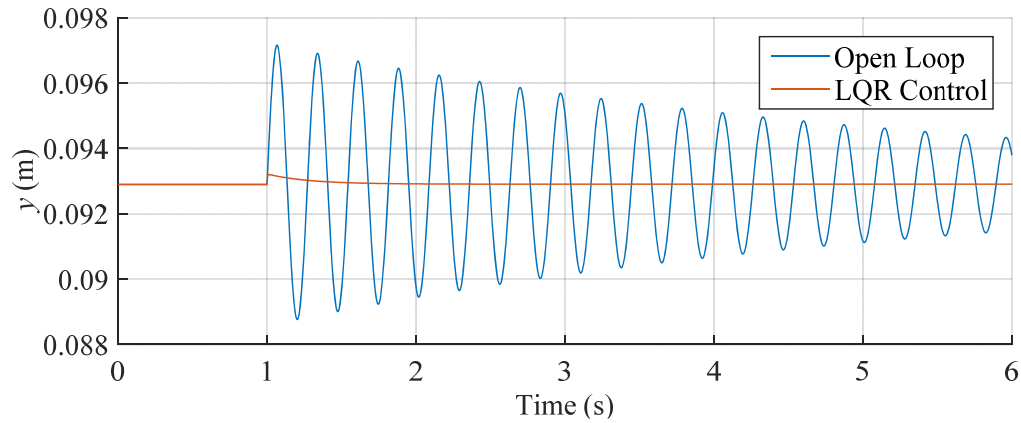


Fig. 104: Height dynamics open loop vs LQR control (parameters from Table 1, Table 6, and Table 7)

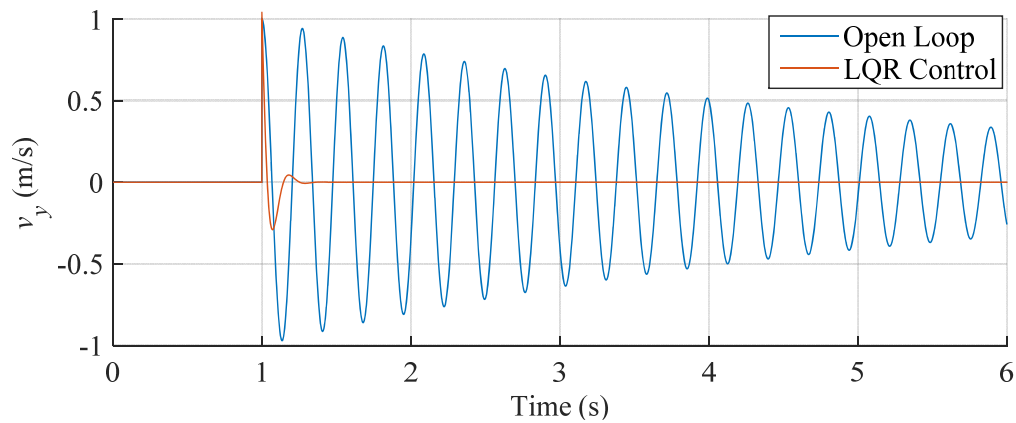


Fig. 105: Heave dynamics open loop vs LQR control (parameters from Table 1, Table 6, and Table 7)

The roll angle and roll velocity simulation results are shown in Fig. 106 and Fig. 107. The gain value was calculated to be:

$$\mathbf{K}_{\theta_x} = [79.36 \quad 311.25] \quad (5.35)$$

Again, the LQR recovers from the disturbance much quicker with fewer oscillations, settling in roughly 0.6 seconds, while the open loop takes roughly 2.6 seconds.

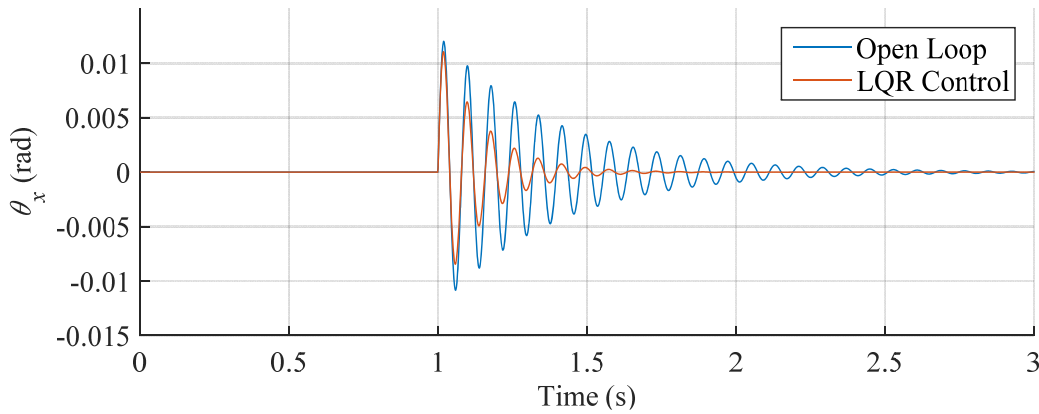


Fig. 106: Roll dynamics: open loop vs LQR control (parameters from Table 1, Table 6, and Table 7)

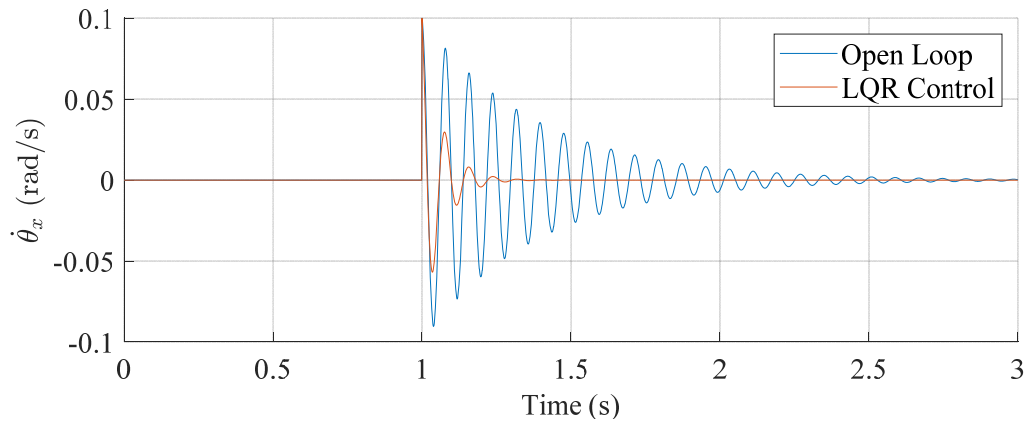


Fig. 107: Roll Velocity dynamics: open loop vs LQR control
(parameters from Table 1, Table 6, and Table 7)

The pitch dynamics simulation results, shown in Fig. 108 and Fig. 109, show a very similar performance to the roll dynamics. The gain was calculated to be:

$$\mathbf{K}_{\theta_z} = [83.94 \quad 311.55] \quad (5.36)$$

The pitch angle with the LQR system has fewer oscillations and a settling time of less than 0.6 seconds, while the open loop system takes about 2.6 seconds to settle.

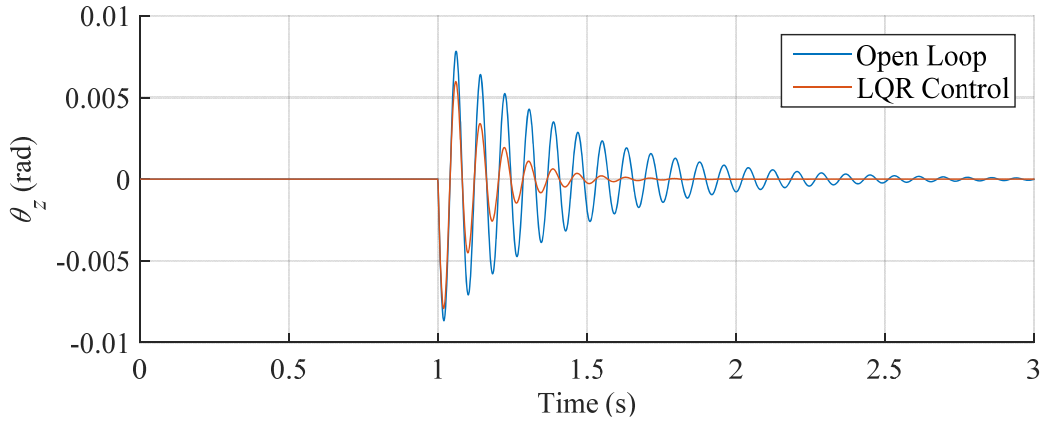


Fig. 108: Pitch dynamics: open loop vs LQR control (parameters from Table 1, Table 6, and Table 7)

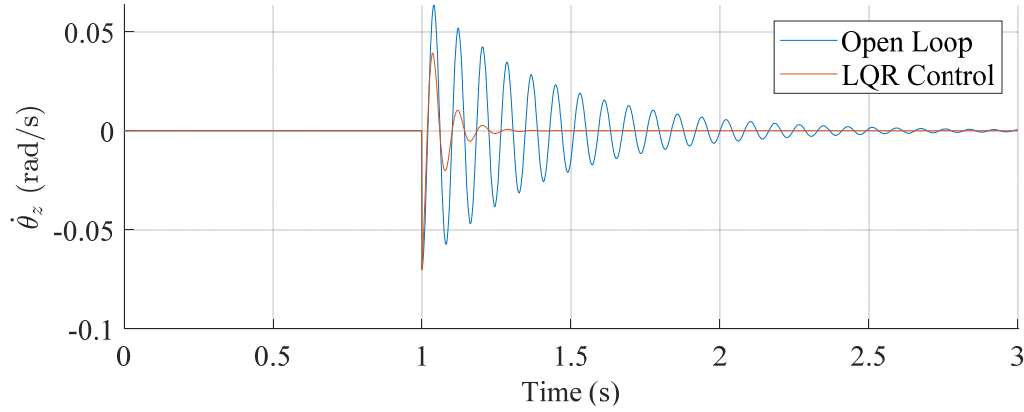


Fig. 109: Pitch velocity dynamics: open loop vs LQR control
(parameters from Table 1, Table 6, and Table 7)

For the yaw simulation, the gain value was calculated to be:

$$\mathbf{K}_{\theta_y} = [26.67 \quad 328.32] \quad (5.37)$$

Calculating the eigenvalues of the state matrix for the yaw dynamic system and observing the positive real parts shows that the system is unstable:

$$\lambda_{\angle y} = 5.892 \pm j136.76 \quad (5.38)$$

The controllability matrix for this system is:

$$\mathbf{M}_{\angle y} = [\mathbf{B}_y \quad \mathbf{A}_y \mathbf{B}_y] = \begin{bmatrix} 0 & 1 \\ 1 & 11.78 \end{bmatrix} \quad (5.39)$$

The full rank of 2 of the controllability matrix in (5.39) ensures that the system is controllable. Fig. 110 and Fig. 111 confirm that the system is open loop unstable but is stabilized by the LQR controller. The LQR system has a settling time of approximately 0.57 seconds.

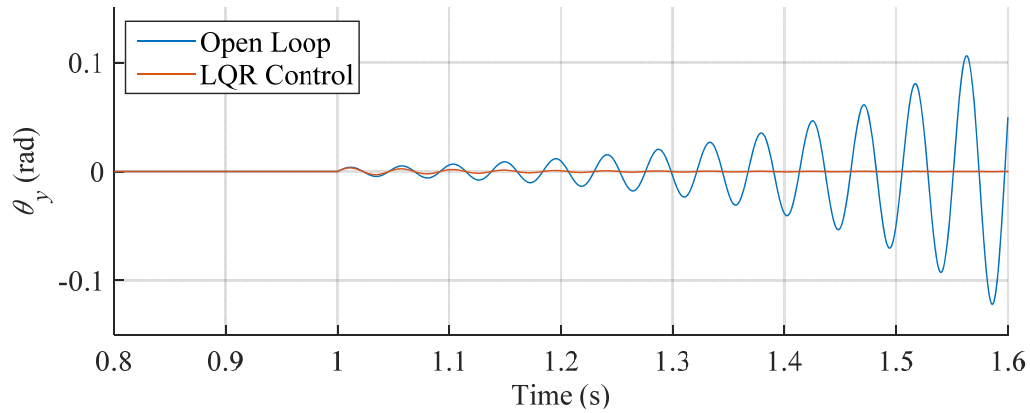


Fig. 110: Yaw dynamics: open loop vs LQR control (parameters from Table 1, Table 6, and Table 7)

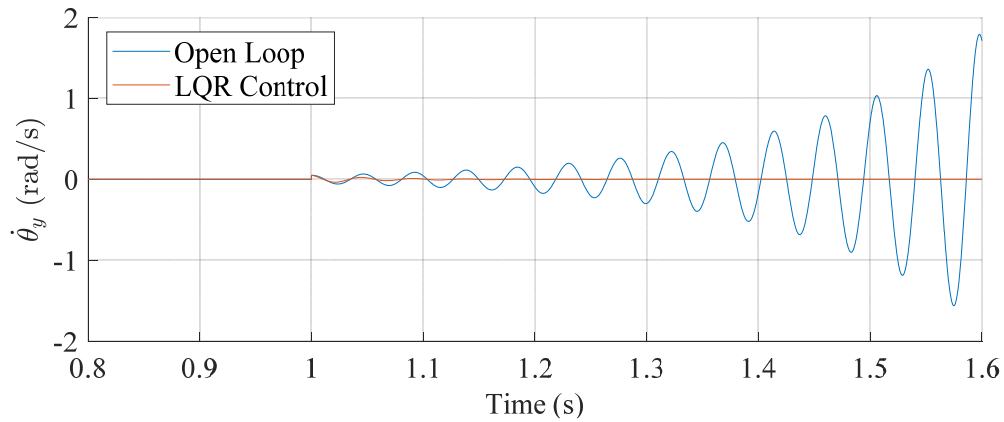


Fig. 111: Yaw velocity dynamics: open loop vs LQR control
(parameters from Table 1, Table 6, and Table 7)

Fig. 112 shows each rotors' rotational velocity over the course of the 4-DOF simulation of the open loop system. Instability in the y rotational axis is the dominant contributor the rotor speeds, as evidenced by the oscillations that increase with time which have the same frequency as the yaw position and yaw velocity from Fig. 110 and Fig. 111.

The change in rotor rotational velocities causes the torque and y force from each rotor to vary, as shown in Fig. 113. Both the y forces and the torques exhibit similar oscillation frequency as yaw. These rotational speeds, torques, and forces are unrealistic for the prototype system, since we have estimated the maximum rotational speed to 5000 rpm for safety, the motor manufacturer stated maximum torque is 2.48 Nm [74], and the 4-40 hardware securing the rotors will begin to yield if a force of more than 951 N is applied [73]. Note that after $t = 1.125$ seconds, the oscillations cross zero, implying that the rotors are changing directions very rapidly which is yet again unrealistic due to rotor inertia.

The rotor rotational velocities for the closed loop system are shown in Fig. 114. Each rotors' unique velocity profile can be determined by summing the effect of each degree of freedom as shown in equation (4.57).

$$\begin{bmatrix} \delta\omega_1 \\ \delta\omega_2 \\ \delta\omega_3 \\ \delta\omega_4 \end{bmatrix} = \mathbf{\Omega}_h + \mathbf{\Omega}_x + \mathbf{\Omega}_z + \mathbf{\Omega}_y \quad (4.57)$$

The closed loop system ensures that the rotor speeds stay positive and within reasonable speeds, never deviating from the initial operating point by more than 1000 rpm, and eventually settling back to the initial speeds of 3691 rpm. The torques and vertical forces exerted by the rotors are also kept within reasonable mechanical limits, as evidenced in Fig. 115. The vehicle is stabilized while maintaining a peak force less than 56.4 N and peak torque less than 1.51 Nm and a deviation of torque less than 0.55 Nm.

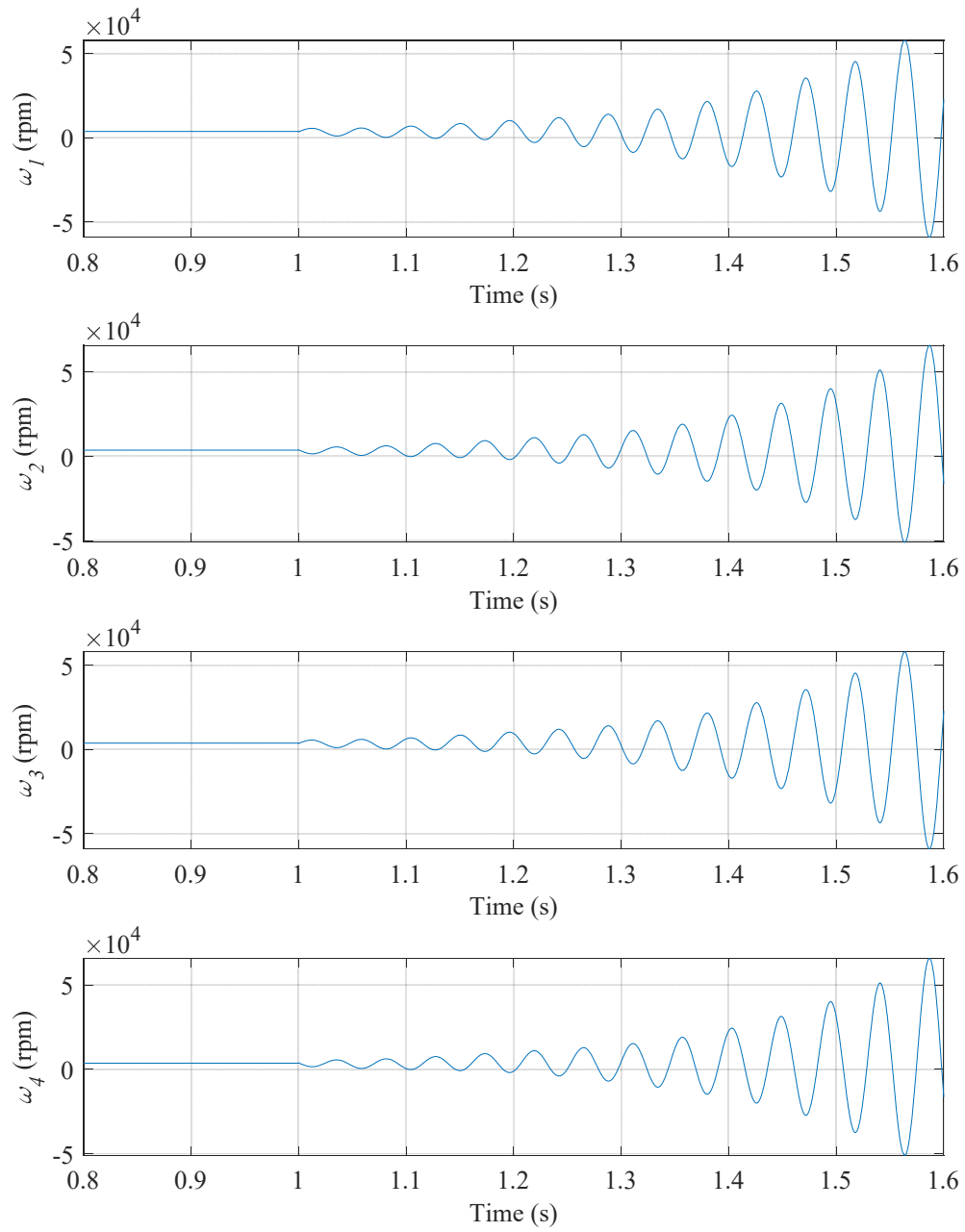


Fig. 112: Individual rotor rotational velocities for open loop system simulation
(parameters from Table 1, Table 6, and Table 7)

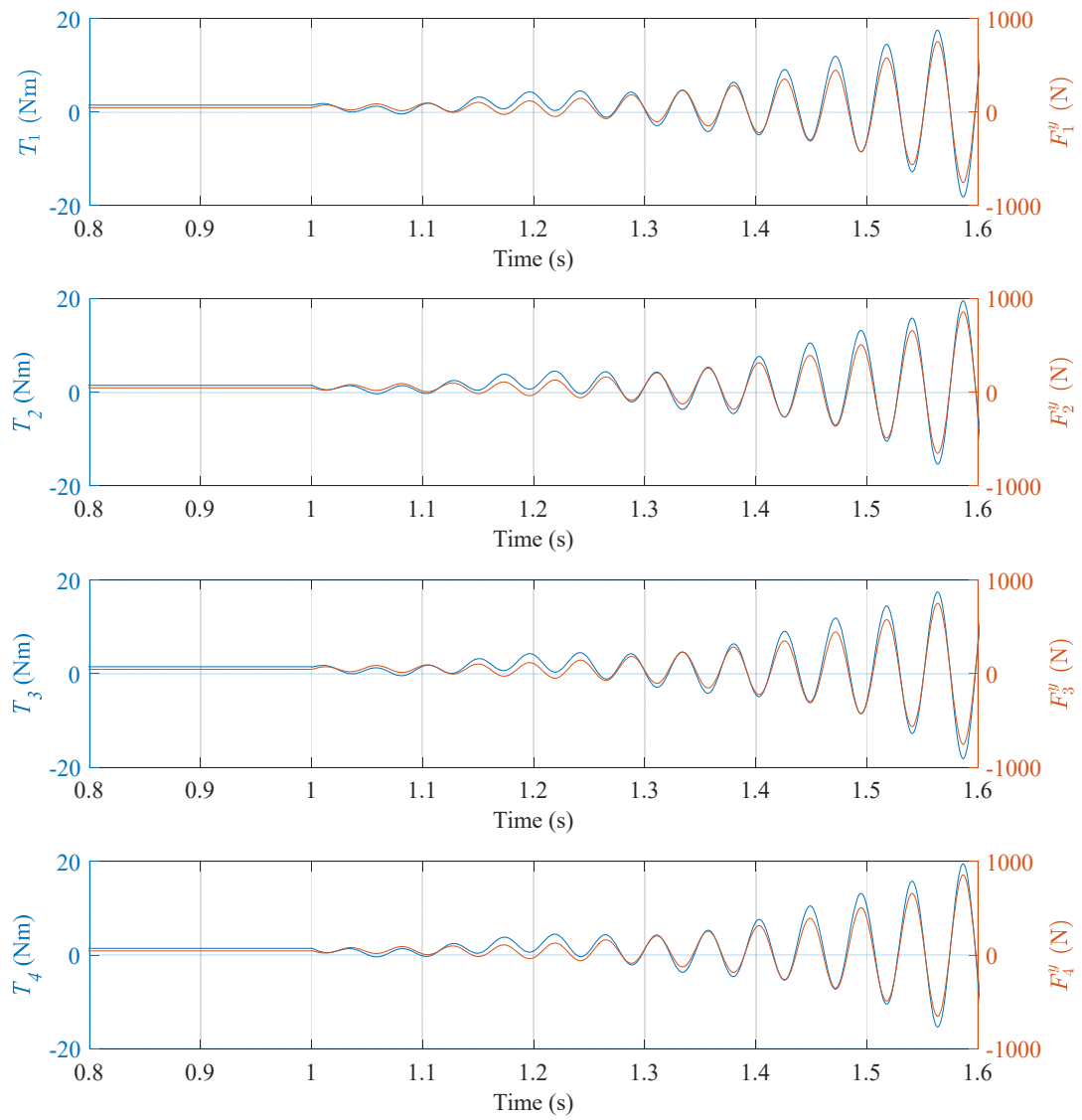


Fig. 113: Individual rotor torque and force plots for open loop system simulation
(parameters from Table 1, Table 6, and Table 7)

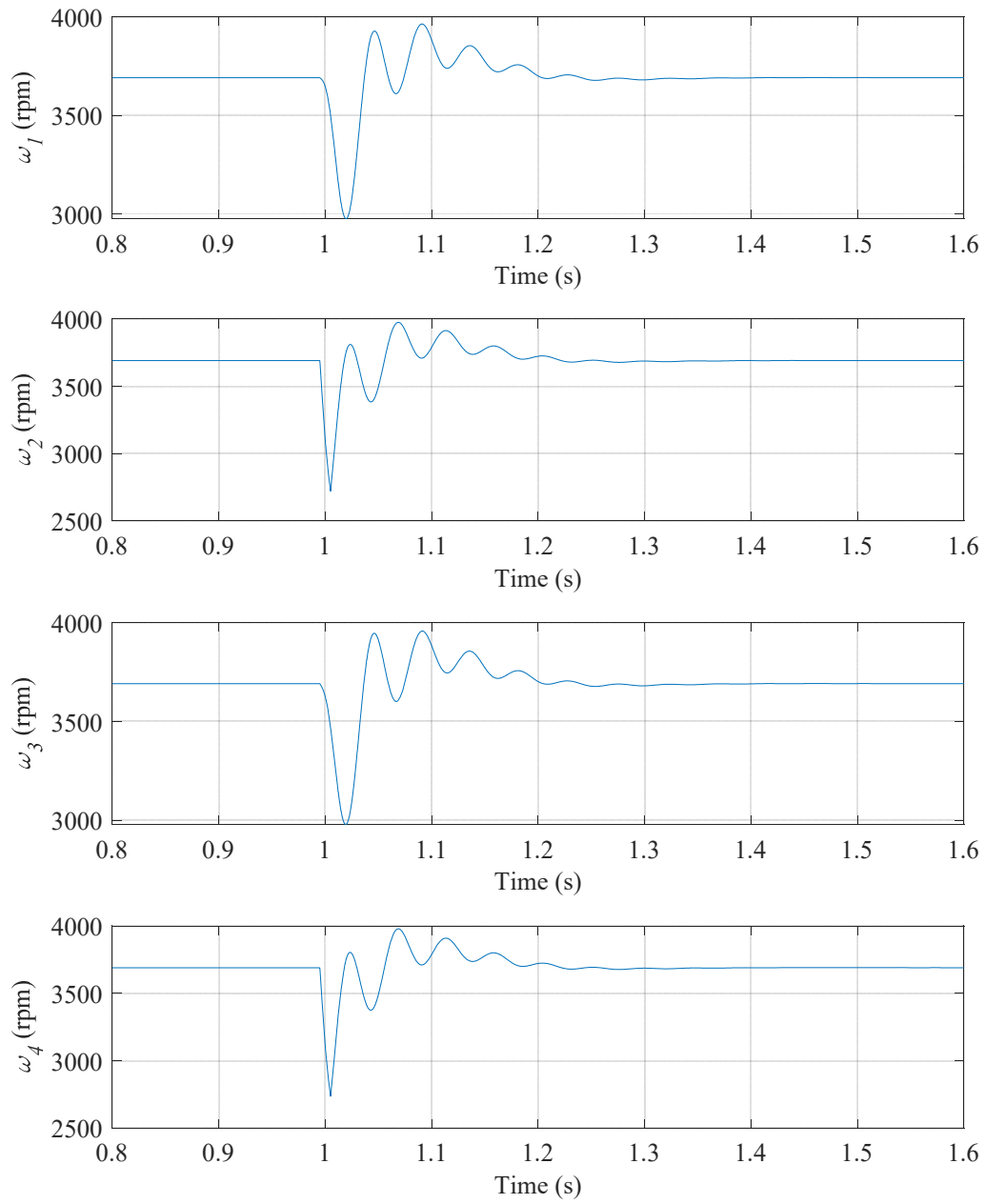


Fig. 114: Individual rotor rotational velocities for closed loop LQR system simulation (parameters from Table 1, Table 6, and Table 7)

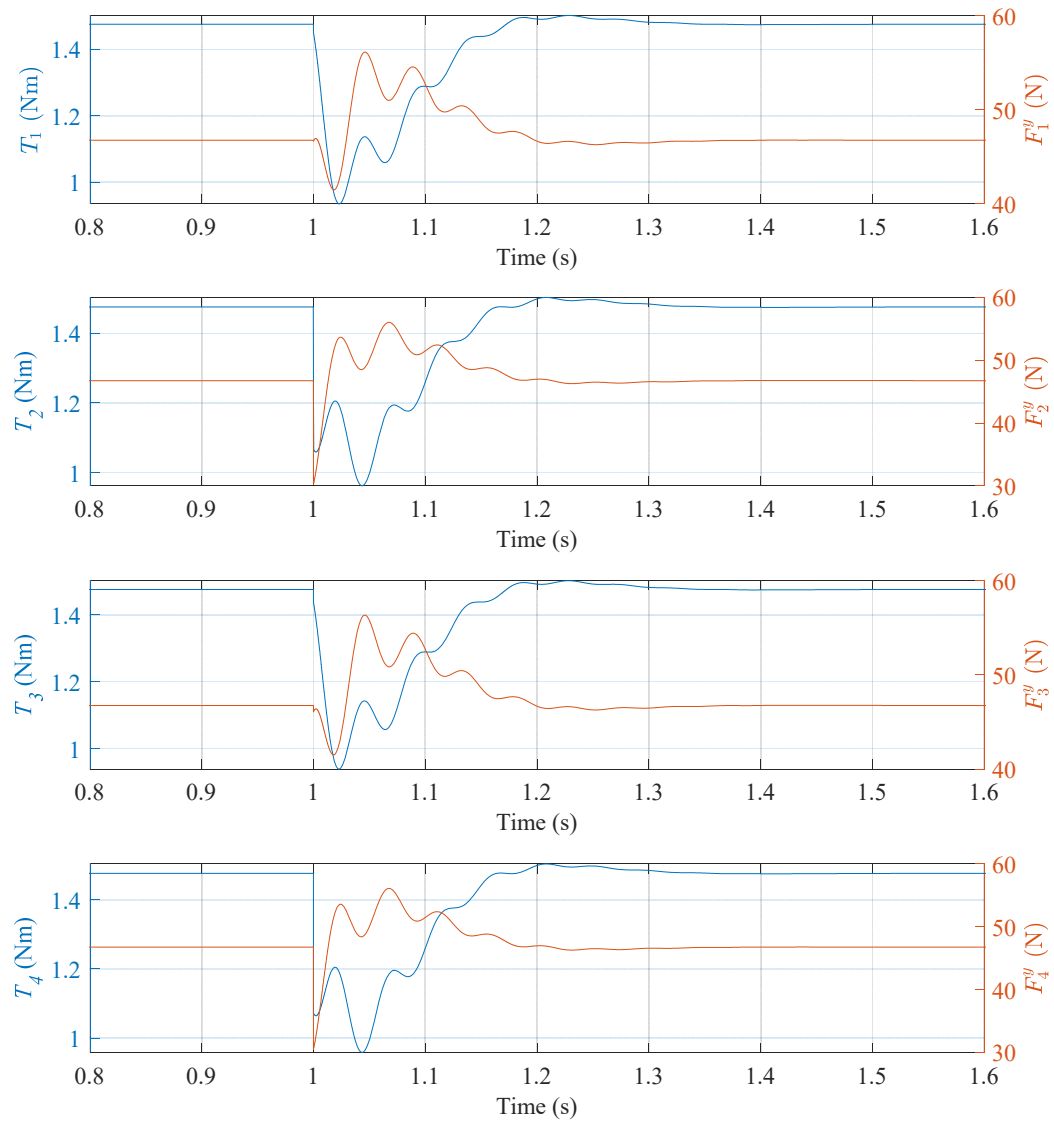


Fig. 115: Individual rotor torque and force plots for closed loop LQR system simulation
(parameters from Table 1, Table 6, and Table 7)

5.3 SETPOINT TRACKING

In this section, we will discuss and simulate two methods of obtaining steady-state setpoint tracking for the LTI systems; pre-compensation and linear quadratic integral control.

5.3.1 LINEAR QUADRATIC REGULATOR WITH PRE-COMPENSATED REFERENCE

The LTI systems simulated in section 5.2 do not achieve steady-state tracking of a reference signal because the error signal is derived from the difference between the reference signal and the states, rather than the reference signal and the output [58]. This can be remedied with careful selection of a pre-compensation value, \bar{N}_d , which scales the reference signal, denoted by r in the generalized block diagram in Fig. 116.

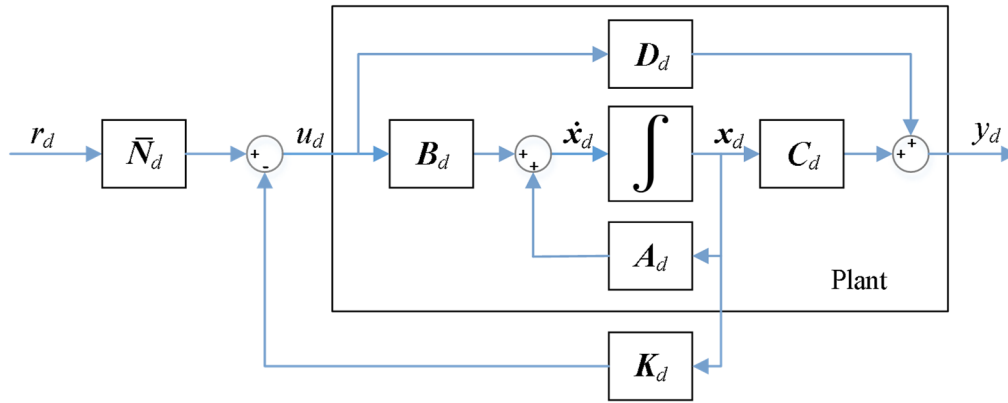


Fig. 116: Generalized LQR controller with pre-compensator to achieve steady-state tracking

Pre-compensation adjusts the reference signal so that when states reach steady-state, the output matches the reference signal. The input matrix of the state-space system is modified [58]:

$$\mathbf{B}_{d,ss} = \mathbf{B}_d \bar{\mathbf{N}}_d \quad (5.40)$$

where $\mathbf{B}_{d,ss}$ is the input matrix which drives steady-state error to zero. For illustrative purposes, the height dynamic system was simulated using a pre-compensator block and the parameters from Table 1, Table 6, and Table 8. The pre-compensator value is:

$$\bar{N}_y = 1133.67 \quad (5.41)$$

The reference signal in this case is the desired height of the vehicle. The results are shown in Fig. 117. From steady state (level at $y = 9.29\text{mm}$), the system is given a reference signal of $r = 0.01029\text{m}$ at $t = 1\text{s}$ (i.e.: commanded to move 1mm up). The system reaches steady state 0.282 seconds after the command is sent. Note that previous simulations had a reference signal of

$$r_d = 0 \quad (5.42)$$

and were only tested for disturbance rejection because the reference signal was meaningless. Without the pre-compensator, the resulting δy as $t \rightarrow \infty$ is 1133.67 times smaller (the value of \bar{N}_d) and is not useful to plot in comparison as it appears as a horizontal line at this scale.

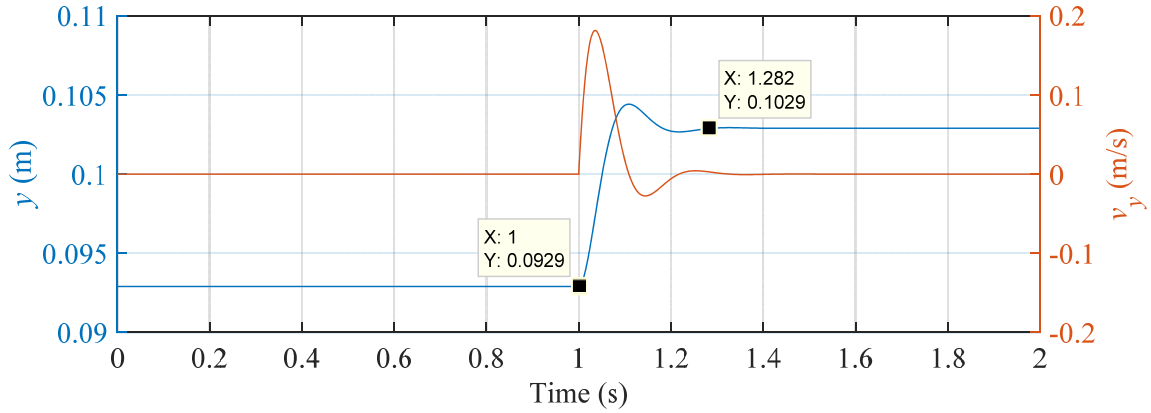


Fig. 117: Height dynamics simulation with LQR and pre-compensation controller (parameters from Table 1, Table 6, and Table 7)

5.3.2 LINEAR QUADRATIC INTEGRAL CONTROL

While a pre-compensator method works to achieve desired steady-state response, the pre-compensator values rely on a very accurate model. Uncertainties in the model, noise, and discretization error will lead to nonzero steady-state error. To add robustness to the system, an error integrator is preferred. This creates a Linear Quadratic Integral (LQI) controller as shown in Fig. 118.

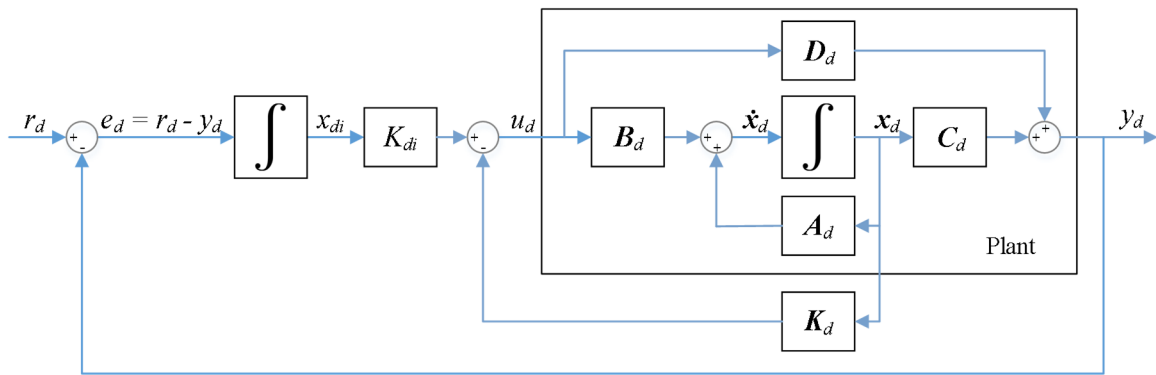


Fig. 118: Generalized block diagram of LQI controller, where e_d is the error signal, x_{di} is the integrator state, K_d is the LQR (feedback) gain matrix, and K_{di} is the integrator gain

The plant model,

$$\dot{\mathbf{x}}_d = \mathbf{A}_d \mathbf{x}_d + \mathbf{B}_d \mathbf{u}_d \quad (5.43)$$

is augmented to include a new state, x_{di} , which is the integral of the error, e_d , between the reference signal, r_d , and the output [58]:

$$e_d = \dot{x}_{di} = -\mathbf{C}_d \mathbf{x}_d \quad (5.44)$$

For convenience in relating x_{di} to its derivative, the \dot{x}_{di} notation will be used rather than e_d .

The resulting system in state-space form can be written as [75]:

$$\dot{\mathbf{z}}_d = \begin{bmatrix} \mathbf{A}_d & 0 \\ -\mathbf{C}_d & 0 \end{bmatrix} \mathbf{z}_d + \begin{bmatrix} \mathbf{B}_d \\ 0 \end{bmatrix} \mathbf{u}_d \quad (5.45)$$

where the new state vector that is augmented to include error is

$$\mathbf{z}_d = \begin{bmatrix} \mathbf{x}_d \\ x_{di} \end{bmatrix} \quad (5.46)$$

Note that the subscript “ d ” nomenclature again signifies that state-space matrices from the degree-of-freedom dynamics being simulated will replace those written in (5.45), (5.46), and in the following equations in this chapter.

Choosing a controller gain matrix using either pole placement or the Algebraic Riccati Equation on the augmented system, the input is described by [75]:

$$\mathbf{u}_d = -[\mathbf{K}_d \quad K_{di}] \mathbf{z}_d \quad (5.47)$$

where the linear quadratic gain matrix is \mathbf{K}_d , and the integrator gain is K_{di} . Substituting (5.47) into (5.45), we arrive at the closed loop system representation [75]:

$$\dot{\mathbf{z}}_d = \begin{bmatrix} \mathbf{A}_d - \mathbf{B}_d \mathbf{K}_d & -\mathbf{B}_d K_{di} \\ -\mathbf{C}_d & 0 \end{bmatrix} \mathbf{z}_d + \begin{bmatrix} 0 \\ 1 \end{bmatrix} r_d \quad (5.48)$$

$$y_d = [C_d \quad D_d K_{di}] z_d \quad (5.49)$$

Note that since D_d is zero, (5.49) is simplified to

$$y_d = [C_d \quad 0] z_d \quad (5.50)$$

and the linear quadratic (LQ) gain matrix is

$$K_d = [K_{d1} \quad K_{d2}] \quad (5.51)$$

Using the LQI equation (5.48), the height dynamic LQI system is:

$$\begin{bmatrix} \delta \dot{y} \\ \delta \dot{v}_y \\ \delta \dot{x}_{yi} \end{bmatrix} = \begin{bmatrix} 0 & 1 & 0 \\ \frac{k_{yy}}{m} - K_{y1} & \frac{d_{yy}}{m} - K_{y2} & K_{yi} \\ -1 & 0 & 0 \end{bmatrix} \begin{bmatrix} \delta y \\ \delta v_y \\ \delta x_{yi} \end{bmatrix} + \begin{bmatrix} 0 \\ 0 \\ 1 \end{bmatrix} \delta y_{des} \quad (5.52)$$

where the error state, x_{yi} , is the difference between the height and the commanded height, y_{des} :

$$x_{yi} = y - y_{des} \quad (5.53)$$

The LQI roll dynamics are described by:

$$\begin{bmatrix} \delta \dot{\theta}_x \\ \delta \dot{\omega}_x \\ \dot{x}_{\theta xi} \end{bmatrix} = \begin{bmatrix} 0 & 1 & 0 \\ \frac{k_{yy} w^2}{I_{xx}} - K_{\theta x1} & \frac{d_{yy} w^2}{I_{xx}} - K_{\theta x2} & K_{\theta xi} \\ -1 & 0 & 0 \end{bmatrix} \begin{bmatrix} \delta \theta_x \\ \delta \omega_x \\ x_{\theta xi} \end{bmatrix} + \begin{bmatrix} 0 \\ 0 \\ 1 \end{bmatrix} \delta \theta_{x,des} \quad (5.54)$$

where the error state, $x_{\theta xi}$, is the difference between roll angle and the commanded roll, $\theta_{x,des}$:

$$x_{\theta xi} = \theta_x - \theta_{x,des} \quad (5.55)$$

The LQI pitch dynamics are described by:

$$\begin{bmatrix} \delta\dot{\theta}_z \\ \delta\dot{\omega}_z \\ \dot{x}_{\theta zi} \end{bmatrix} = \begin{bmatrix} 0 & 1 & 0 \\ \frac{k_{yy}l^2}{I_{zz}} - K_{\theta z1} & \frac{d_{yy}l^2}{I_{zz}} - K_{\theta z2} & K_{\theta zi} \\ -1 & 0 & 0 \end{bmatrix} \begin{bmatrix} \delta\theta_z \\ \delta\omega_z \\ x_{\theta zi} \end{bmatrix} + \begin{bmatrix} 0 \\ 0 \\ 1 \end{bmatrix} \delta\theta_{z,des} \quad (5.56)$$

where the error state, $e_{\theta z}$, is the difference between pitch angle and the commanded pitch angle, $\theta_{z,des}$:

$$e_{\theta z} = \theta_z - \theta_{z,des} \quad (5.57)$$

The LQI yaw dynamics are described by:

$$\begin{bmatrix} \delta\dot{\theta}_y \\ \delta\dot{\omega}_y \\ \dot{x}_{\theta yi} \end{bmatrix} = \begin{bmatrix} 0 & 1 & 0 \\ \frac{4k_{xx}a}{I_{yy}} - K_{\theta y1} & \frac{4d_{xx}a}{I_{yy}} - K_{\theta y2} & K_{\theta yi} \\ -1 & 0 & 0 \end{bmatrix} \begin{bmatrix} \delta\theta_y \\ \delta\omega_y \\ x_{\theta yi} \end{bmatrix} + \begin{bmatrix} 0 \\ 0 \\ 1 \end{bmatrix} \delta\theta_{y,des} \quad (5.58)$$

where the error state, $x_{\theta yi}$, is the difference between yaw angle and the commanded yaw, $\theta_{y,des}$:

$$x_{\theta yi} = \theta_y - \theta_{y,des} \quad (5.59)$$

Again using the simulation parameters from Table 1 and Table 6 and reference signal commands shown in Table 8, which are applied from equilibrium at $t = 1$ s.

Table 8: Radial EDW vehicle simulation position command (reference signals)

| Parameter | Value | Unit |
|----------------|-------|------|
| r_y | 10.29 | mm |
| $r_{\theta x}$ | 4 | deg |
| $r_{\theta z}$ | -3 | deg |
| $r_{\theta y}$ | 2 | deg |

The LQI cost function weights defined as

$$Q_d = Q_y = Q_{\theta x} = Q_{\theta z} = Q_{\theta y} = \begin{bmatrix} 1 & 0 & 0 \\ 0 & 1 & 0 \\ 0 & 0 & 1000 \end{bmatrix} \quad (5.60)$$

$$R_d = R_y = R_{\theta x} = R_{\theta z} = \frac{1}{30} R_{\theta y} = 10^{-6} \quad (5.61)$$

The costs are chosen to minimize error between the output and reference signals. Note that the very small input cost weights are necessary since the state signals are small (on the order of hundredths and thousandths), and we must make sure the input costs are small by comparison. Also note that the input cost weight for the yaw dynamic is 30 times larger than the other axes in order to slow down yaw movement, since it is not as critical as roll or pitch (yaw will not cause the rotor to come into contact with the track surface), and since yaw has the largest moment of inertia. Using the cost weights from (5.60) and (5.61), the feedback values were calculated by solving for the Algebraic Riccati Equation:

$$\begin{bmatrix} K_{y1} \\ K_{y2} \\ K_{yi} \end{bmatrix} = \begin{bmatrix} 7528.5 \\ 1007.1 \\ -31622.8 \end{bmatrix} \quad (5.62)$$

$$\begin{bmatrix} K_{\theta x1} \\ K_{\theta x2} \\ K_{\theta xi} \end{bmatrix} = \begin{bmatrix} 3922.2 \\ 998.7 \\ -31622.8 \end{bmatrix} \quad (5.63)$$

$$\begin{bmatrix} K_{\theta z1} \\ K_{\theta z2} \\ K_{\theta zi} \end{bmatrix} = \begin{bmatrix} 4059.7 \\ 999.1 \\ -31622.8 \end{bmatrix} \quad (5.64)$$

$$\begin{bmatrix} K_{\theta y1} \\ K_{\theta y2} \\ K_{\theta yi} \end{bmatrix} = \begin{bmatrix} 4059.7 \\ 202.7 \\ -5773.5 \end{bmatrix} \quad (5.65)$$

The simulation results, shown in Fig. 119, Fig. 120, Fig. 121, and Fig. 122, show that the LQI controller yields a stable system with zero steady-state error, and a settling time of

less than 1.2 seconds for the height system, less than 1.0 seconds for the roll and pitch systems, and less than 1.4 seconds for the yaw system.

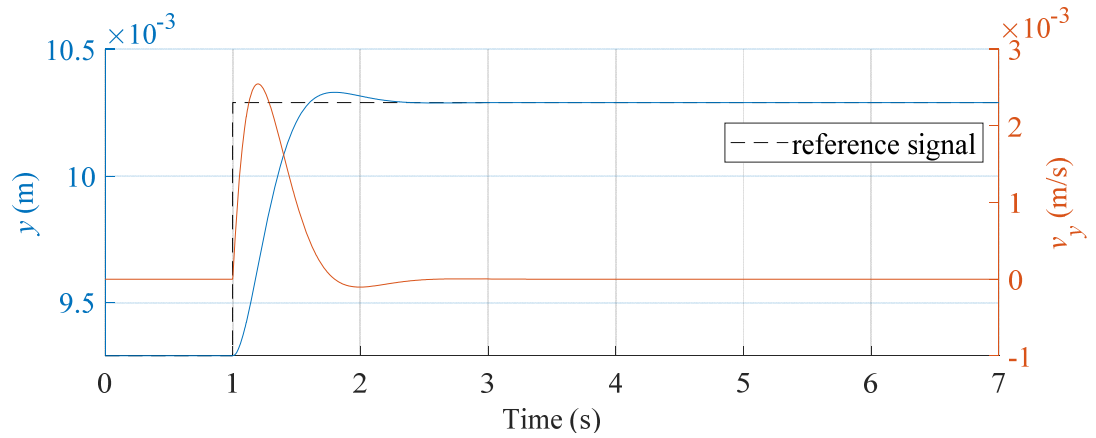


Fig. 119: Vertical displacement simulation with LQI control
(parameters from Table 1, Table 6, and Table 8)

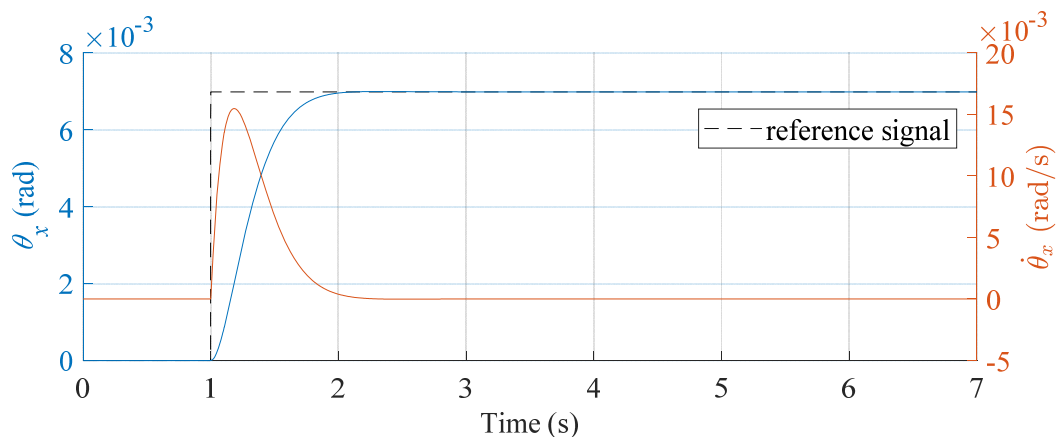


Fig. 120: Roll simulation with LQI control (parameters from Table 1, Table 6, and Table 8)

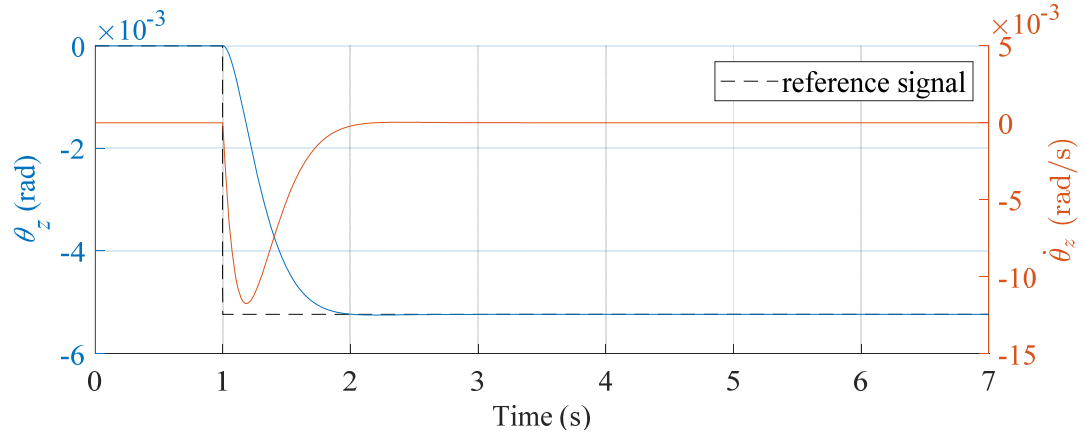


Fig. 121: Pitch simulation with LQI control (parameters from Table 1, Table 6, and Table 8)

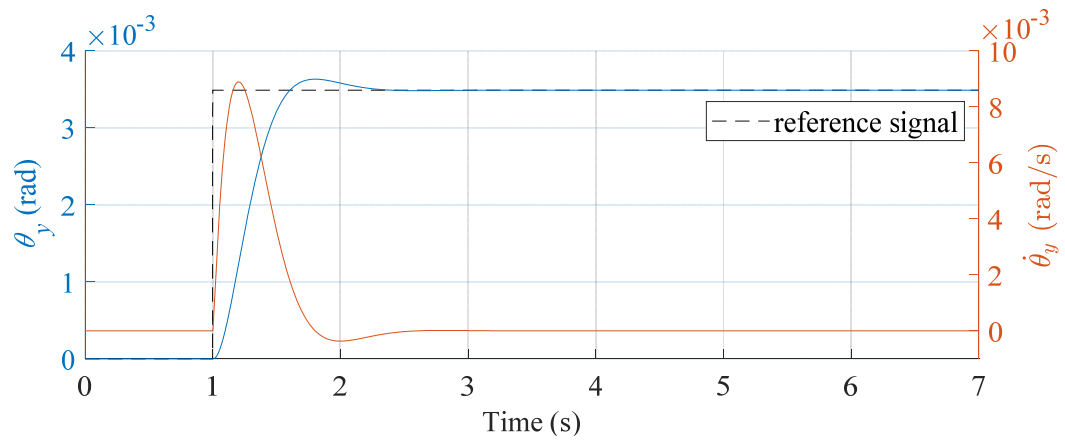


Fig. 122: Yaw simulation with LQI control (parameters from Table 1, Table 6, and Table 8)

Fig. 123 shows the rotor rotational velocities for the LQI simulation. The change in rotational velocities required to move to the reference signal is relatively small to achieve a reasonable settling times of 1 to 1.4 seconds, the largest being rotor 3 with a maximum deviation of 480 rpm. Note that rotors 2 and 3 experienced increased rotational velocity while rotors 1 and 4 experienced reduced rotational velocity.

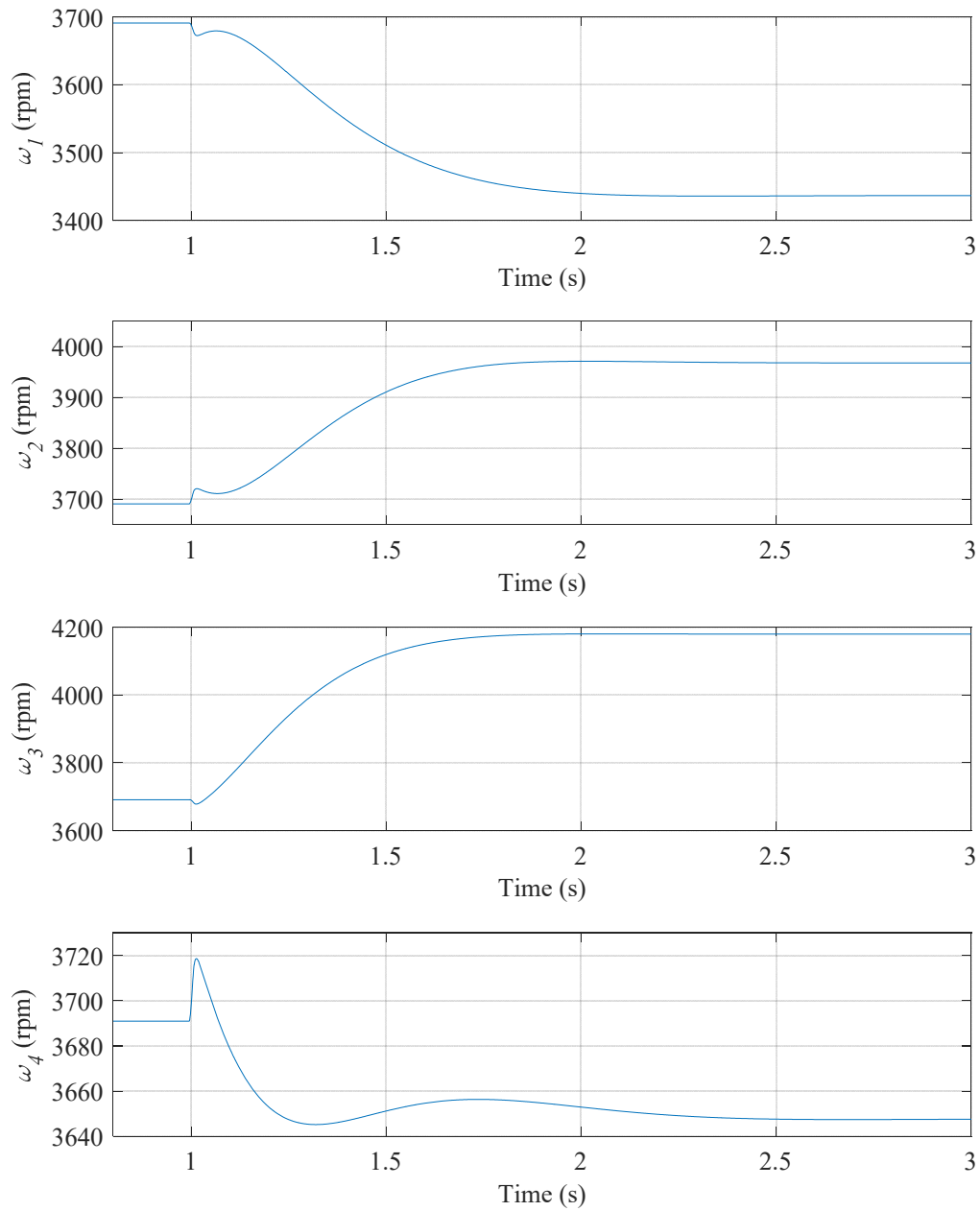


Fig. 123: Individual rotor rotational velocity plots for closed loop LQI system simulation (parameters from Table 1, Table 6, and Table 8)

Fig. 124 shows the rotor torques and vertical forces for the LQI simulation. Clearly the vehicle attitude has a pronounced effect on the resulting forces and torques because the pattern of decreased speeds on rotors 1 and 4 and increased speeds on rotors 2 and 3 is not

reflected by the torques and forces. Instead, we see increased torque on only rotor 2 due to it being pushed closer to the track by both roll and pitch angles. While the total cumulative vertical force is increased, rotor 3 experiences reduced force as roll and pitch move it further from the track.

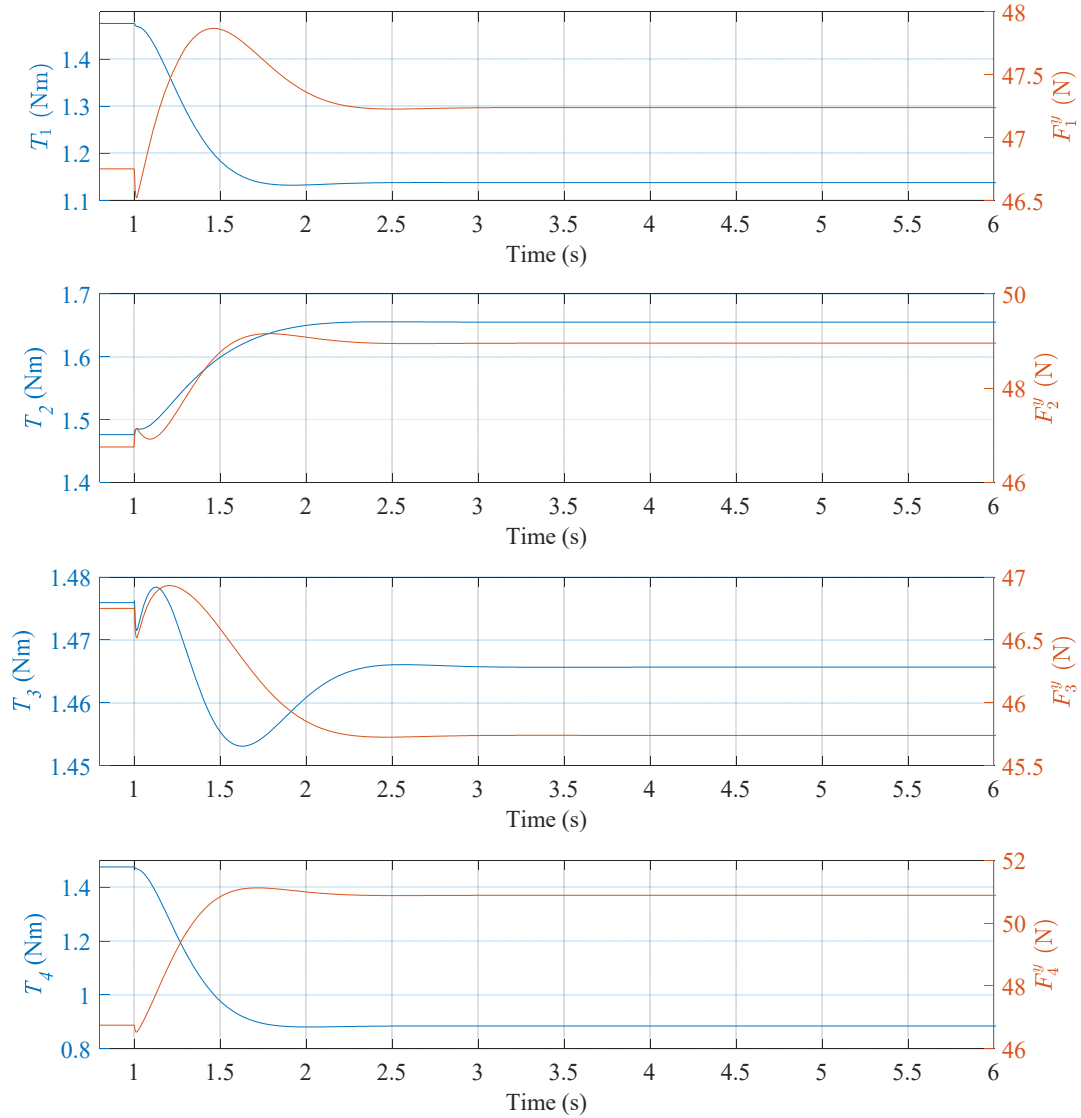


Fig. 124: Individual rotor torque and force plots for closed loop LQI system simulation (parameters from Table 1, Table 6, and Table 8)

5.4 OBSERVER-BASED CONTROL

On the prototype vehicle, it is easy to measure height, the pitch, and the roll angles using laser displacement sensors, but vehicle velocities are more challenging to measure in real-time without delay. A state observer on each 1-DOF subsystem can be used to estimate these unknown quantities so that state control methods can be used.

5.4.1 STATE OBSERVER DERIVATION

A state observer or estimator consists of a virtual plant model that is identical to the physical plant, which is fed measurable data (often the output), so that its states closely match the systems' actual states. These estimated states can then be used for control. A block diagram of a control system utilizing an observer is shown in Fig. 125. Similar to previous sections, feedforward is neglected for this section, so $\mathbf{D}_d = []$.

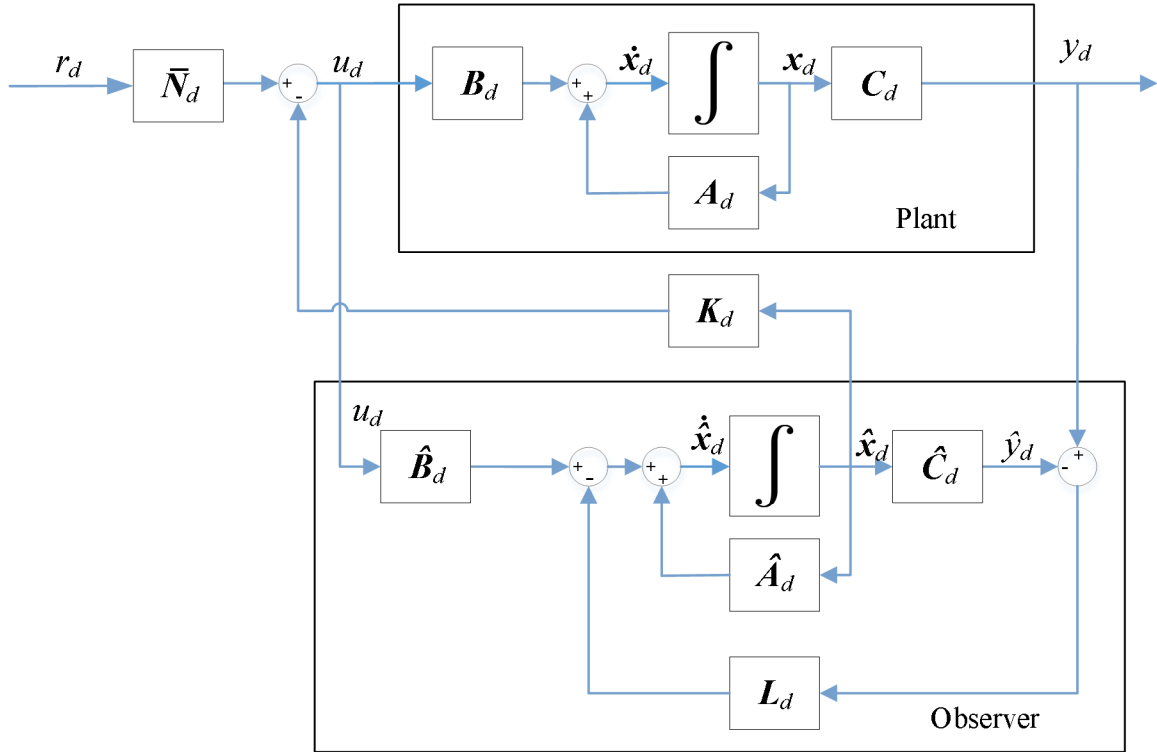


Fig. 125: General block diagram of system control using state observer, $D_d = []$

The general plant states are:

$$\dot{\mathbf{x}}_d = \mathbf{A}_d \mathbf{x}_d + \mathbf{B}_d u_d \quad (5.66)$$

$$y_d = \mathbf{C}_d \mathbf{x}_d \quad (5.67)$$

where y_d is the system output. The estimator is governed by [58][75]:

$$\dot{\hat{\mathbf{x}}}_d = \hat{\mathbf{A}}_d \hat{\mathbf{x}}_d + \hat{\mathbf{B}}_d u_d + \mathbf{L}_d (y_d - \hat{y}_d) \quad (5.68)$$

$$\hat{y}_d = \hat{\mathbf{C}}_d \hat{\mathbf{x}}_d \quad (5.69)$$

where the caret notation signifies estimation, \hat{y}_d is the estimator output, and \mathbf{L}_d is the estimator feedback gain. Note that the system matrices for the estimator are subject to modeling error and are estimated values as well. Recall the full order estimated state equation, (5.68), while substituting in (5.69) and (5.78) - (5.80) :

$$\dot{\hat{\mathbf{x}}}_d = \mathbf{A}_d \hat{\mathbf{x}}_d + \mathbf{B}_d u_d + \mathbf{L}_d (y_d - \mathbf{C}_d \hat{\mathbf{x}}_d) \quad (5.70)$$

The control signal for the system is [75]:

$$u_d = \bar{N}_d r_d - \mathbf{K}_d \hat{\mathbf{x}}_d \quad (5.71)$$

Substituting (5.67), (5.69), and (5.71) into (5.68) yields:

$$\dot{\hat{\mathbf{x}}}_d = (\hat{\mathbf{A}}_d - \hat{\mathbf{B}}_d \mathbf{K}_d) \hat{\mathbf{x}}_d + \mathbf{L}_d (\mathbf{C}_d \mathbf{x}_d - \hat{\mathbf{C}}_d \hat{\mathbf{x}}_d) + \mathbf{B}_d \bar{N}_d r_d \quad (5.72)$$

Substituting (5.71) into (5.66):

$$\dot{\mathbf{x}}_d = \mathbf{A}_d \mathbf{x}_d + \mathbf{B}_d (\bar{N}_d r_d - \mathbf{K}_d \hat{\mathbf{x}}_d) \quad (5.73)$$

The state error dynamics can be described by a new state:

$$\mathbf{e}_x = \mathbf{x}_d - \hat{\mathbf{x}}_d \quad (5.74)$$

A similar definition holds for the derivative of the error:

$$\dot{\mathbf{e}}_x = \dot{\mathbf{x}}_d - \dot{\hat{\mathbf{x}}}_d \quad (5.75)$$

Substituting (5.73) and (5.72) into (5.75):

$$\begin{aligned} \mathbf{e}_x &= \mathbf{A}_d \mathbf{x}_d + \mathbf{B}_d (\bar{N}_d r_d - \mathbf{K}_d \hat{\mathbf{x}}_d) \\ &\quad - (\hat{\mathbf{A}}_d - \hat{\mathbf{B}}_d \mathbf{K}_d) \hat{\mathbf{x}}_d - \mathbf{L}_d (\mathbf{C}_d \mathbf{x}_d - \hat{\mathbf{C}}_d \hat{\mathbf{x}}_d) - \mathbf{B}_d \bar{N}_d r_d \end{aligned} \quad (5.76)$$

Grouping like terms in (5.76):

$$\mathbf{e}_x = (\mathbf{A}_d - \mathbf{L}_d \mathbf{C}_d) \mathbf{x}_d - (\hat{\mathbf{A}}_d - \hat{\mathbf{B}}_d \mathbf{K}_d - \mathbf{L}_d \hat{\mathbf{C}}_d + \mathbf{B}_d \mathbf{K}_d) \hat{\mathbf{x}}_d \quad (5.77)$$

For the purposes of creating a simple linear system model, we can assume that the observer model is sufficiently close to the plant such that:

$$\hat{\mathbf{A}}_d = \mathbf{A}_d \quad (5.78)$$

$$\hat{\mathbf{B}}_d = \mathbf{B}_d \quad (5.79)$$

$$\hat{\mathbf{C}}_d = \mathbf{C}_d \quad (5.80)$$

Substituting (5.78), (5.79), and (5.80) into (5.77) and rearranging:

$$\dot{\mathbf{e}}_x = \mathbf{A}_d(\mathbf{x}_d - \hat{\mathbf{x}}_d) - \mathbf{L}_d\mathbf{C}_d(\mathbf{x}_d - \hat{\mathbf{x}}_d) \quad (5.81)$$

Finally, substituting (5.74) into (5.81) and factoring:

$$\dot{\mathbf{e}}_x = (\mathbf{A}_d - \mathbf{L}_d\mathbf{C}_d)\mathbf{e}_x \quad (5.82)$$

The \mathbf{L}_d gain is selected to drive the estimator to the system's actual value by driving error to zero. Since control is dependent on the observer states, it is important for the estimates to converge to the actual states quickly without amplifying noise. Typically, it is desired to use poles of the estimator, $\mathbf{A}_d - \mathbf{L}_d\mathbf{C}_d$, that are 2 to 5 times faster than the slowest pole of the controller, $\mathbf{A}_d - \mathbf{B}_d\mathbf{K}_d$ [77].

We can now define our plant state dynamics as functions of plant and error states. By substituting (5.74) into (5.73), $\dot{\mathbf{x}}_d$ can be written in terms of \mathbf{x}_d and \mathbf{e}_d such that:

$$\dot{\mathbf{x}}_d = (\mathbf{A}_d - \mathbf{B}_d\mathbf{K}_d)\mathbf{x}_d + \mathbf{B}_d\mathbf{K}_d\mathbf{e}_d + \mathbf{B}_d\bar{\mathbf{N}}_d r_d \quad (5.83)$$

Equations (5.83) and (5.82) can now be combined into matrix form to form the observer system dynamic model [75]:

$$\begin{bmatrix} \dot{\mathbf{x}}_d \\ \dot{\mathbf{e}}_x \end{bmatrix} = \begin{bmatrix} \mathbf{A}_d - \mathbf{B}_d\mathbf{K}_d & \mathbf{B}_d\mathbf{K}_d \\ 0 & \mathbf{A}_d - \mathbf{L}_d\mathbf{C}_d \end{bmatrix} \begin{bmatrix} \mathbf{x}_d \\ \mathbf{e}_x \end{bmatrix} + \begin{bmatrix} \mathbf{B}_d\bar{\mathbf{N}}_d \\ 0 \end{bmatrix} r_d \quad (5.84)$$

$$\mathbf{y}_d = \begin{bmatrix} \mathbf{C}_d & 0 \end{bmatrix} \begin{bmatrix} \mathbf{x}_d \\ \mathbf{e}_x \end{bmatrix} \quad (5.85)$$

Note that the system described by (5.84) and (5.85) observes the separation principle which states that designing the optimal feedback controller can be achieved by designing an

optimal observer [77]. It also follows that LQR methods (solving the Algebraic Riccati Equation) can be used to solve the feedback control gain matrix, \mathbf{K}_d , completely separately from the pole placement methods which can be used to solve for the estimator gain matrix, \mathbf{L}_d [77].

It can sometimes be useful to directly monitor the observer states of a system rather than the error. The same system can be written as functions of plant and observer states by combining equations (5.73) and (5.72) in matrix form:

$$\begin{bmatrix} \dot{\mathbf{x}}_d \\ \dot{\hat{\mathbf{x}}}_d \end{bmatrix} = \begin{bmatrix} \mathbf{A}_d & -\hat{\mathbf{B}}_d \mathbf{K}_d \\ \mathbf{L}_d \mathbf{C}_d & \hat{\mathbf{A}}_d - \mathbf{L}_d \mathbf{C}_d - \hat{\mathbf{B}}_d \mathbf{K}_d \end{bmatrix} \begin{bmatrix} \mathbf{x}_d \\ \hat{\mathbf{x}}_d \end{bmatrix} + \begin{bmatrix} \mathbf{B}_d \bar{\mathbf{N}}_d \\ \mathbf{B}_d \bar{\mathbf{N}}_d \end{bmatrix} r_d \quad (5.86)$$

5.4.2 REDUCED ORDER OBSERVER METHODS

Even well designed state observers will have some error in their estimations, so if some of the states are measurable, it is preferable to use those measurements for those states instead of the observer. For the prototype vehicle, the 2nd order LTI system for yaw requires a full observer since the prototype vehicle does not have provisions to measure horizontal motion. However, the height, roll, and pitch systems can more accurately be modeled using a reduced order observer, since vertical displacement at each corner is measurable (while instantaneous real-time velocity data is not). The reduced-order observer system can be derived without modifying a full observer system. Starting with the standard state space system from equations (5.66) and (5.67), we can break down the

matrices into components that describe the states that are available to measure, $\mathbf{x}_{d,a}$, and states that are unmeasurable, $\mathbf{x}_{d,u}$ [77]:

$$\mathbf{A}_d = \begin{bmatrix} \mathbf{A}_{d,aa} & \mathbf{A}_{d,au} \\ \mathbf{A}_{d,ua} & \mathbf{A}_{d,uu} \end{bmatrix} \quad (5.87)$$

$$\mathbf{B}_d = \begin{bmatrix} \mathbf{B}_{d,a} \\ \mathbf{B}_{d,u} \end{bmatrix} \quad (5.88)$$

$$\mathbf{C}_d = [\mathbf{C}_{d1} \quad \mathbf{C}_{d2}] \quad (5.89)$$

where the subscript notation a implies available to measure and u implies unavailable to measure (estimated state), and d denotes the system being analyzed. Substituting (5.87) and (5.88) into (5.66), and (5.89) into (5.67), and writing breaking the state vector into its measureable and unmeasurable components, we can rewrite the state space system:

$$\begin{bmatrix} \dot{\mathbf{x}}_{d,a}(t) \\ \dot{\mathbf{x}}_{d,u}(t) \end{bmatrix} = \begin{bmatrix} \mathbf{A}_{d,aa} & \mathbf{A}_{d,au} \\ \mathbf{A}_{d,ua} & \mathbf{A}_{d,uu} \end{bmatrix} \begin{bmatrix} \mathbf{x}_{d,a}(t) \\ \mathbf{x}_{d,u}(t) \end{bmatrix} + \begin{bmatrix} \mathbf{B}_{d,a} \\ \mathbf{B}_{d,u} \end{bmatrix} u_d(t) \quad (5.90)$$

$$y = [\mathbf{C}_{d1} \quad \mathbf{C}_{d2}] \begin{bmatrix} \mathbf{x}_{d,a}(t) \\ \mathbf{x}_{d,u}(t) \end{bmatrix} \quad (5.91)$$

The measured state dynamic equation is:

$$\dot{\mathbf{x}}_{d,a} = \mathbf{A}_{d,aa}\mathbf{x}_{d,a} + \mathbf{A}_{d,au}\mathbf{x}_{d,u} + \mathbf{B}_{d,a}u_d \quad (5.92)$$

The unmeasured state dynamic equation is:

$$\dot{\mathbf{x}}_{d,u} = \mathbf{A}_{d,ua}\mathbf{x}_{d,a} + \mathbf{A}_{d,uu}\mathbf{x}_{d,u} + \mathbf{B}_{d,u}u_d \quad (5.93)$$

Re-arranging (5.92) yields:

$$\dot{\mathbf{x}}_{d,a} - \mathbf{A}_{d,aa}\mathbf{x}_{d,a} - \mathbf{B}_{d,a}u_d = \mathbf{A}_{d,au}\mathbf{x}_{d,u} \quad (5.94)$$

We can take equations (5.93) and (5.94) and compare them to the standard state space form from (5.66) and (5.67). The comparison is shown in Table 9.

Table 9: Cross-comparison of full-order and reduced order observer expressions [77]

| Full-order observer terms | Reduced order observer terms |
|-------------------------------|--|
| $\dot{\mathbf{x}}_d$ | $\dot{\mathbf{x}}_{d,u}$ |
| \mathbf{A}_d | $\mathbf{A}_{d,uu}$ |
| $\mathbf{B}_d \mathbf{u}_d$ | $\mathbf{A}_{d,ua} \mathbf{x}_{d,a} - \mathbf{B}_{d,u} \mathbf{u}_d$ |
| y_d | $\dot{\mathbf{x}}_{d,a} - \mathbf{A}_{d,aa} \mathbf{x}_{d,a} - \mathbf{B}_{d,a} u_d$ |
| \mathbf{C}_d | $\mathbf{A}_{d,au}$ |
| $\mathbf{L}_d \ (n \times 1)$ | $\mathbf{L}_d \ ((n-1) \times 1)$ |

Rewriting the observed state equation, (5.70):

$$\dot{\hat{\mathbf{x}}}_d = (\mathbf{A}_d - \mathbf{L}_d \mathbf{C}_d) \hat{\mathbf{x}}_d + \mathbf{B}_d u_d + \mathbf{L}_d y_d \quad (5.95)$$

Since the system formed by (5.94) and (5.93) fits the standard state space form as shown by the equivalency in Table 9, we can form the reduced-order estimated state equation by substituting in the terms from the first column of Table 9 with the terms from the second column of Table 9 in equation (5.95):

$$\begin{aligned} \dot{\hat{\mathbf{x}}}_{d,u} = & (\mathbf{A}_{d,uu} - \mathbf{L}_d \mathbf{A}_{d,au}) \hat{\mathbf{x}}_{d,u} + \mathbf{A}_{d,ua} \mathbf{x}_{d,a} \\ & + \mathbf{B}_{d,u} \mathbf{u}_d + \mathbf{L}_d (\dot{\mathbf{x}}_{d,a} - \mathbf{A}_{d,aa} \mathbf{x}_{d,a} - \mathbf{B}_{d,a} u_d) \end{aligned} \quad (5.96)$$

Grouping like-terms in (5.96):

$$\begin{aligned} \dot{\hat{\mathbf{x}}}_{d,u} = & (\mathbf{A}_{d,uu} - \mathbf{L}_d \mathbf{A}_{d,au}) \hat{\mathbf{x}}_{d,u} + (\mathbf{A}_{d,ua} - \mathbf{L}_d \mathbf{A}_{d,aa}) \mathbf{x}_{d,a} \\ & + \mathbf{L}_d \dot{\mathbf{x}}_{d,a} + (\mathbf{B}_{d,u} - \mathbf{L}_d \mathbf{B}_{d,a}) u_d \end{aligned} \quad (5.97)$$

By substituting (5.92) into (5.97), we obtain an expression for the estimated state:

$$\begin{aligned} \dot{\hat{\mathbf{x}}}_{d,u} = & (\mathbf{A}_{d,uu} - \mathbf{L}_d \mathbf{A}_{d,au}) \hat{\mathbf{x}}_{d,u} + (\mathbf{A}_{d,ua} - \mathbf{L}_d \mathbf{A}_{d,aa}) \mathbf{x}_{d,a} \\ & + \mathbf{L}_d (\mathbf{A}_{d,aa} \mathbf{x}_{d,a} + \mathbf{A}_{d,au} \mathbf{x}_{d,u} + \mathbf{B}_{d,a} u_d) + (\mathbf{B}_{d,u} - \mathbf{L}_d \mathbf{B}_{d,a}) u_d \end{aligned} \quad (5.98)$$

Defining the error of the unmeasurable state so that it can be minimized to allow the estimate to approach the real state:

$$\mathbf{e}_{d,u} = \mathbf{x}_{d,u} - \hat{\mathbf{x}}_{d,u} \quad (5.99)$$

The derivative of error is:

$$\dot{\mathbf{e}}_{d,u} = \dot{\mathbf{x}}_{d,u} - \dot{\hat{\mathbf{x}}}_{d,u} \quad (5.100)$$

Substituting (5.93) and (5.97) into (5.100):

$$\begin{aligned} \dot{\mathbf{e}}_{d,u} = & \mathbf{A}_{d,ua}\mathbf{x}_{d,a} + \mathbf{A}_{d,uu}\mathbf{x}_{d,u} + \mathbf{B}_{d,u}u_d \\ & - (\mathbf{A}_{d,uu} - \mathbf{L}_d\mathbf{A}_{d,au})\hat{\mathbf{x}}_{d,u} - (\mathbf{A}_{d,ua} - \mathbf{L}_d\mathbf{A}_{d,aa})\mathbf{x}_{d,a} \\ & - \mathbf{L}_d\dot{\mathbf{x}}_{d,a} - (\mathbf{B}_{d,u} - \mathbf{L}_d\mathbf{B}_{d,a})u_d \end{aligned} \quad (5.101)$$

Substituting (5.92) into (5.101):

$$\begin{aligned} \dot{\mathbf{e}}_{d,u} = & \mathbf{A}_{d,ua}\mathbf{x}_{d,a} + \mathbf{A}_{d,uu}\mathbf{x}_{d,u} + \mathbf{B}_{d,u}u_d \\ & - (\mathbf{A}_{d,uu} - \mathbf{L}_d\mathbf{A}_{d,au})\hat{\mathbf{x}}_{d,u} - (\mathbf{A}_{d,ua} - \mathbf{L}_d\mathbf{A}_{d,aa})\mathbf{x}_{d,a} \\ & - \mathbf{L}_d(\mathbf{A}_{d,aa}\mathbf{x}_{d,a} + \mathbf{A}_{d,au}\mathbf{x}_{d,u} + \mathbf{B}_{d,a}u_d) - (\mathbf{B}_{d,u} - \mathbf{L}_d\mathbf{B}_{d,a})u_d \end{aligned} \quad (5.102)$$

Simplifying (5.102):

$$\dot{\mathbf{e}}_{d,u} = (\mathbf{A}_{d,uu} - \mathbf{L}_d\mathbf{A}_{d,au})\mathbf{x}_{d,u} - (\mathbf{A}_{d,uu} - \mathbf{L}_d\mathbf{A}_{d,au})\hat{\mathbf{x}}_{d,u} \quad (5.103)$$

Finally, substituting (5.99) into (5.103) [77]:

$$\dot{\mathbf{e}}_{d,u} = (\mathbf{A}_{d,uu} - \mathbf{L}_d\mathbf{A}_{d,au})\mathbf{e}_{d,u} \quad (5.104)$$

Equations (5.83), the measured states, and (5.104), the observed states, can now be combined to form a state-space system in matrix form for the reduced-order observer:

$$\begin{bmatrix} \dot{\mathbf{x}}_d \\ \dot{\mathbf{e}}_{d,u} \end{bmatrix} = \begin{bmatrix} \mathbf{A}_d - \mathbf{B}_d\mathbf{K}_d & \mathbf{B}_d\mathbf{K}_{d,u} \\ 0 & \mathbf{A}_{d,uu} - \mathbf{L}_d\mathbf{A}_{d,au} \end{bmatrix} \begin{bmatrix} \mathbf{x}_d \\ \mathbf{e}_{d,u} \end{bmatrix} + \begin{bmatrix} \mathbf{B}_d\bar{\mathbf{N}}_d \\ 0 \end{bmatrix} r_d \quad (5.105)$$

The reduced-order observer from (5.105) can also be represented as a block diagram as shown in Fig. 126.

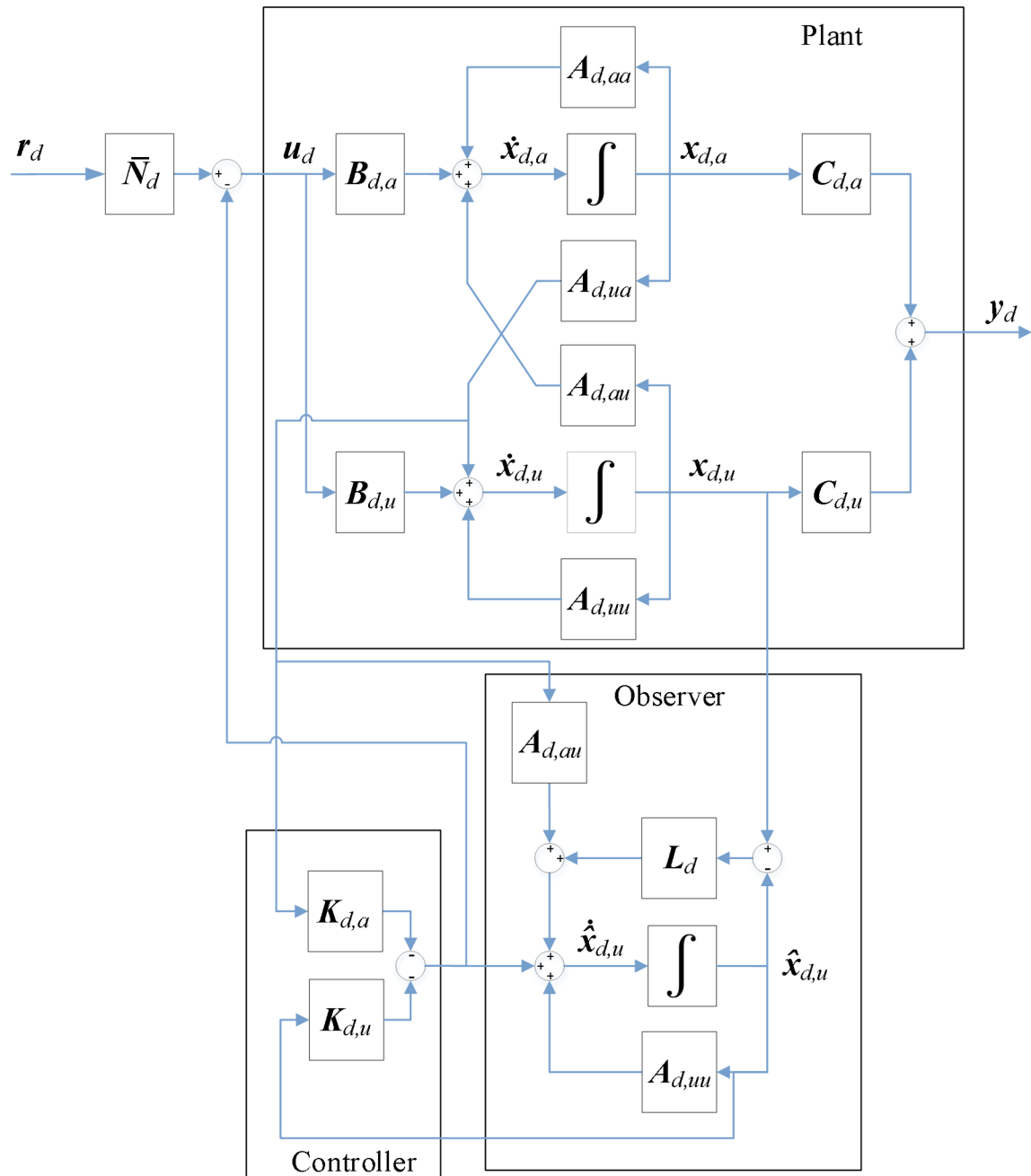


Fig. 126: Reduced-order observer general block diagram

Note that the observer error should decay to zero as long as the eigenvalues of $A_{d,uu} - L_d A_{d,au}$ have negative real parts. We must also assume that the system's observability matrix,

$$M_d = \begin{bmatrix} C_d \\ C_d A_d \end{bmatrix} \quad (5.106)$$

has a rank of n . It is also necessary to ensure the system can be controlled by checking the controllability matrix for full rank:

$$N_d = [B_d \quad A_d B_d] \quad (5.107)$$

We can apply gains to the input in order to control the system, again using the Algebraic Riccati Equation [77]:

$$u(t) = -K_d \begin{bmatrix} x_{d,a}(t) \\ x_{d,u}(t) \end{bmatrix} \quad (5.108)$$

where

$$K_d = [K_{d,a} \quad K_{d,u}] \quad (5.109)$$

and $K_{d,a}$ and $K_{d,u}$ are the feedback gains of the measured and observed states, respectively. Note that this notation facilitates the derivation of a reduced order observer, but for a 2nd order system, the notation of K_d from section 5.3 (equation (5.51)) is synonymous:

$$[K_{d,a} \quad K_{d,u}] = [K_{d1} \quad K_{d2}] \quad (5.110)$$

Note that the gains L_d and K_d can be chosen independently of each other to obtain desired system response. The control law is then given by:

$$u_d = -K_{d,a} x_{d,a} - K_{d,u} \hat{x}_{d,u} \quad (5.111)$$

Grouping like-terms and substituting (5.111) into equation (5.98) yields:

$$\begin{aligned}
\dot{\hat{\mathbf{x}}}_{d,u} = & \left(\mathbf{A}_{d,uu} - \mathbf{B}_{d,u} \mathbf{K}_{d,u} - \mathbf{L}_d \mathbf{A}_{d,au} \right) \hat{\mathbf{x}}_{d,u} \\
& + \left(\mathbf{A}_{d,ua} - \mathbf{B}_{d,u} \mathbf{K}_{d,a} \right) \mathbf{x}_{d,a} + \mathbf{L}_d \mathbf{A}_{d,au} \mathbf{x}_{d,u}
\end{aligned} \tag{5.112}$$

5.4.3 OBSERVER EXAMPLES AND SIMULATIONS

5.4.3.1 VERTICAL VELOCITY SYSTEM OBSERVER

Checking the controllability, \mathbf{M}_y , and observability, \mathbf{O}_y , matrices for the height system:

$$\mathbf{M}_y = \begin{bmatrix} 0 & 1 \\ 1 & \frac{4d_{yy}}{m} \end{bmatrix} \quad (5.113)$$

$$\mathbf{O}_y = \begin{bmatrix} 1 & 0 \\ 0 & 1 \end{bmatrix} \quad (5.114)$$

We can see that the rank of both \mathbf{M}_y and \mathbf{O}_y is 2 (full), so the system is observable and controllable. For the height-heave system, we can define the parameters:

$$A_{y,aa} = [0] \quad (5.115)$$

$$A_{y,au} = [1] \quad (5.116)$$

$$A_{y,ua} = \begin{bmatrix} \frac{4k_{yy}}{m} \end{bmatrix} \quad (5.117)$$

$$A_{y,uu} = \begin{bmatrix} \frac{4d_{yy}}{m} \end{bmatrix} \quad (5.118)$$

$$B_{y,a} = [0] \quad (5.119)$$

$$B_{y,u} = [1]v \quad (5.120)$$

From (5.111), the control law for the reduced-order observer system is

$$\delta u_y = -K_{y,a} \delta y - K_{y,u} \delta \hat{v}_y \quad (5.121)$$

where the estimated state is:

$$\delta \dot{\hat{v}}_y = \left(\frac{4d_{yy}}{m} - K_{y,u} - L_y \right) \delta \hat{v}_y + \left(\frac{4k_{yy}}{m} - K_{y,a} \right) \delta y + L_y \delta v_y \quad (5.122)$$

Evaluating terms in (5.105) with $y = d$ by substituting (5.115) - (5.120) into (5.105) gives

$$\mathbf{A}_d - \mathbf{B}_d \mathbf{K}_d = \begin{bmatrix} 0 & 1 \\ \frac{4k_{yy}}{m} - K_{y,a} & \frac{4d_{yy}}{m} - K_{y,u} \end{bmatrix} \quad (5.123)$$

$$\mathbf{B}_d \mathbf{K}_{d,u} = \begin{bmatrix} 0 \\ K_{y,u} \end{bmatrix} \quad (5.124)$$

$$\mathbf{A}_{d,uu} - \mathbf{L}_d \mathbf{A}_{d,au} = \frac{4d_{yy}}{m} - L_y \quad (5.125)$$

$$\mathbf{B}_d \bar{\mathbf{N}}_d = \begin{bmatrix} 0 \\ \bar{N}_y \end{bmatrix} \quad (5.126)$$

Substituting (5.123) - (5.126) into (5.105) the reduced-order observer state-space height system:

$$\begin{bmatrix} \delta \dot{y} \\ \delta \dot{v}_y \\ \delta \dot{e}_y \end{bmatrix} = \begin{bmatrix} 0 & 1 & 0 \\ \frac{4k_{yy}}{m} - K_{y,a} & \frac{4d_{yy}}{m} - K_{y,u} & K_{y,u} \\ 0 & 0 & \frac{4d_{yy}}{m} - L_y \end{bmatrix} \begin{bmatrix} \delta y \\ \delta v_y \\ \delta e_y \end{bmatrix} + \begin{bmatrix} 0 \\ \bar{N}_y \\ 0 \end{bmatrix} r_y \quad (5.127)$$

It's interesting to note that this system is a special case where the measured output is equal to the measured state, so the output is not directly dependent on the estimated state. Although the system is observable, the error will always be zero if it starts with zero error, since

$$\delta \hat{y} = \delta y \quad (5.128)$$

Therefore, L_y would have no effect on the system and it would behave similar to an LQR system. This assumption breaks down if the system starts with error or if there are modeling errors, which is likely. If error exists then the error will decay according to:

$$\delta \dot{e}_y = \left(\frac{4d_{yy}}{m} - L_y \right) \delta e_y \quad (5.129)$$

From (5.129), we can see that a negative damping term d_{yy} will help drive the system error toward zero, but even if a system has a positive d_{yy} , the observer will converge to the plant states as long as L_y is sufficiently large.

Although a more accurate reduced order observer would be used on an actual vehicle, it further verifies the validity of using the SOVP model for modeling and control if we implement an observer which must actively correct for error using output feedback. Therefore, the full state observer is derived by evaluating the terms in (5.84) with $d = y$:

$$\mathbf{A}_d - \mathbf{B}_d \mathbf{K}_d = \begin{bmatrix} 0 & 1 \\ \frac{4k_{yy}}{m} - K_{y2} & \frac{4d_{yy}}{m} - K_{y2} \end{bmatrix} \quad (5.130)$$

$$\mathbf{B}_d \mathbf{K}_d = \begin{bmatrix} 0 & 0 \\ K_{y1} & K_{y2} \end{bmatrix} \quad (5.131)$$

$$\mathbf{A}_d - \mathbf{L}_d \mathbf{C}_d = \begin{bmatrix} L_{y1} & 1 \\ \frac{4k_{yy}}{m} - L_{y2} & \frac{4d_{yy}}{m} \end{bmatrix} \quad (5.132)$$

$$\mathbf{B}_d \bar{\mathbf{N}}_d = \begin{bmatrix} 0 \\ \bar{N}_y \end{bmatrix} \quad (5.133)$$

Substituting (5.130) - (5.133) into (5.84) yields the height system full observer state space equation:

$$\begin{bmatrix} \delta \dot{y} \\ \delta \dot{v}_y \\ \delta \dot{e}_y \\ \delta \dot{e}_{vy} \end{bmatrix} = \begin{bmatrix} 0 & 1 & 0 & 0 \\ \frac{4k_{yy}}{m} - K_{y1} & \frac{4d_{yy}}{m} - K_{y2} & K_{y1} & K_{y2} \\ 0 & 0 & L_{y1} & 1 \\ 0 & 0 & \frac{4k_{yy}}{m} - L_{y2} & \frac{4d_{yy}}{m} \end{bmatrix} \begin{bmatrix} \delta y \\ \delta v_y \\ \delta e_y \\ \delta e_{vy} \end{bmatrix} + \begin{bmatrix} 0 \\ \bar{N}_y \\ 0 \\ 0 \end{bmatrix} \delta y_{des} \quad (5.134)$$

Using simulation parameters from Table 1 and Table 6, choosing a level operating (starting) height of 9.29mm, and using a cost matrix that penalizes position error,

$$\mathbf{Q}_y = \begin{bmatrix} 100 & 0 \\ 0 & 1 \end{bmatrix} \quad (5.135)$$

we can use the LQR method to obtain a controller gain:

$$\mathbf{K}_y = \begin{bmatrix} 9480.21 \\ 10000.50 \end{bmatrix} \quad (5.136)$$

Table 1. Rotor, guideway, and vehicle parameters for the radial experimental setup

| Parameter | | Value | Unit |
|--|--|------------------------|------------------|
| Rotor | Outer radius, r_o | 26 ± 0.58 | mm |
| | Inner radius, r_i | 9.6 | mm |
| | Width of rotor, w_o | 52 | mm |
| | Residual flux density, B_{rem} | 1.42 | T |
| | relative permeability, μ_r | 1.108 | - |
| | Pole-pairs, P | 2 | - |
| Guideway | Outer radius, r_g | 600 ± 0.73 | mm |
| | Guideway width, w_g | 77 | mm |
| | Thickness, h | 6.3 | mm |
| | Conductivity, σ (Al, 6061-T06) | 2.459×10^{-7} | Sm^{-1} |
| Vehicle | Total mass, m | 10.315 | kg |
| | Length, $2l$ | 0.173 | m |
| | Width, $2w$ | 0.3254 | m |
| | z -axis rotational Inertia, I_{zz} | 0.08821 | kgm^2 |
| | x -axis rotational Inertia, I_{xx} | 0.1977 | kgm^2 |
| | y -axis rotational inertia, I_{yy} | 0.259 | kgm^2 |
| BLDC motors (Scorpion SII-4035-250KV)[74] | Winding inductance, L_a | 4.7×10^{-6} H | H |
| | Winding resistance, R_a | 0.037 | Ω |
| | Back-emf constant, K_e | 0.036 | Vs/rad |
| | Torque constant, K_t | 0.0295 | Nm/s |
| | rotational inertia, J | 0.00386 | kgm^2 |
| | Viscous damping coefficient, b | 2.295×10^{-6} | Nm·s/rad |

Table 6:

| Parameter | Value | Unit |
|-----------|---------|------|
| k_{xx} | -1832.6 | N/m |
| d_{xx} | 1.17 | Ns/m |
| k_{yy} | -6009.1 | Ns/m |
| d_{xy} | -5.106 | Ns/m |

The eigenvalues of the controller system $A_y - B_y K_y$ are (noting that the superscript “ cl ” notation signifies the closed loop poles):

$$\lambda_{y1}^{cl} = -10.00 \quad (5.137)$$

$$\lambda_{y2}^{cl} = -10000 \quad (5.138)$$

Choosing observer poles roughly 10 times faster than the slowest controller pole (note the superscript “ o ” signifies poles of the observer):

$$p_{y1}^o = -100 \quad (5.139)$$

$$p_{y2}^o = -101 \quad (5.140)$$

From (5.82), the error dynamics of the observer system are derived from the poles of $A_y - L_y C_y$, so pole placement can be used to find the observer gain for the system:

$$L_y = \begin{bmatrix} 200.55 \\ 9475.77 \end{bmatrix} \quad (5.141)$$

A simulation of the system is performed with a command at $t = 0$ s according to Table 7. The system's initial conditions are shown in Table 10. Note that the observer begins with non-zero error (position offset by -0.5mm and velocity offset by -0.1m/s). Results for the simulation are shown in Fig. 127.

Table 7: Radial EDW vehicle simulation step disturbance

| State | Value | Unit |
|-------------------|-------|----------------|
| δy | 0 | <i>m</i> |
| δv_y | 1 | <i>m/s</i> |
| $\delta \theta_x$ | 0 | <i>radians</i> |
| $\delta \omega_x$ | 1 | <i>rad/s</i> |
| $\delta \theta_z$ | 0 | <i>radians</i> |
| $\delta \omega_z$ | -0.7 | <i>rad/s</i> |
| $\delta \theta_y$ | 0 | <i>radians</i> |
| $\delta \omega_y$ | 0.5 | <i>rad/s</i> |

Table 10: Height observer system initial conditions

| Parameter | Value | Unit |
|----------------|-------|------|
| $y(0)$ | 9.29 | mm |
| $v_y(0)$ | 0 | m/s |
| $\hat{y}(0)$ | 8.79 | mm |
| $\hat{v}_y(0)$ | -0.1 | m/s |

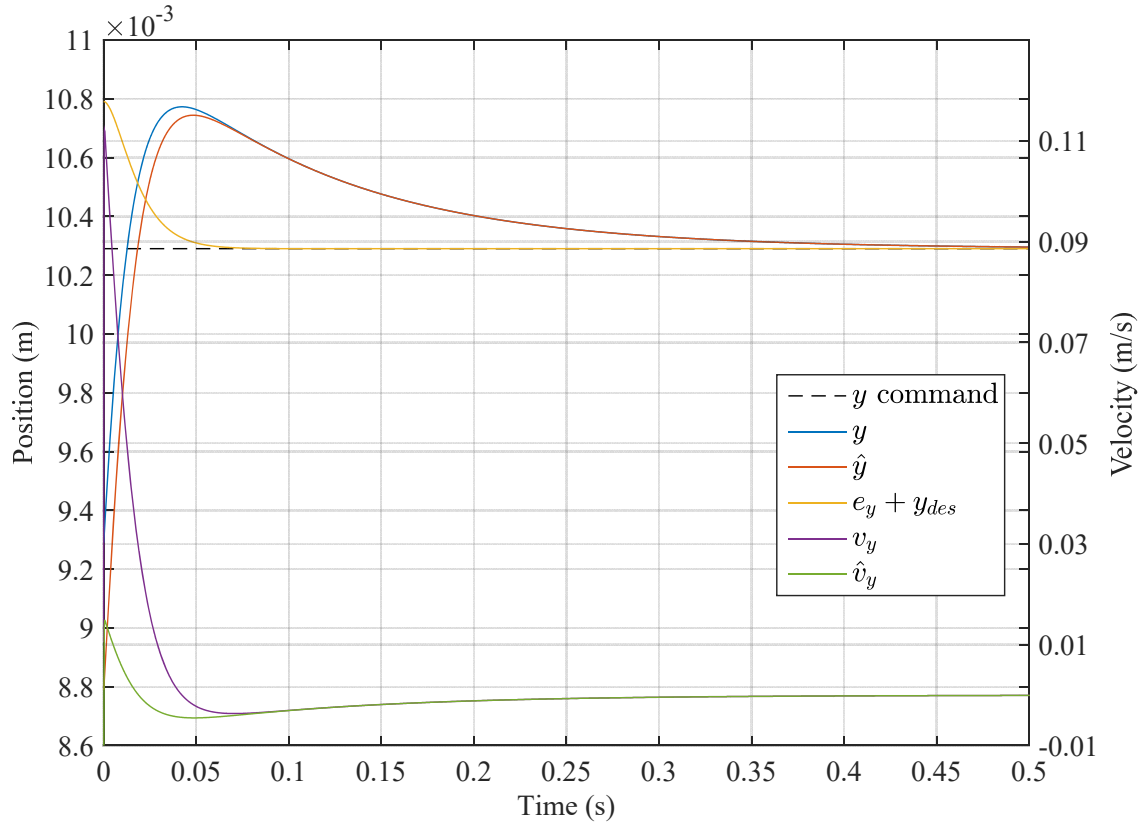


Fig. 127: Height dynamics observer simulation (parameters from Table 1, Table 6, Table 7, Table 10)

Although the estimated system begins with error on both the position and velocity while a new position is commanded, the observer state converge to the plant states and the system settles to its desired state ($\pm 2\%$) in 0.4 seconds. The error approaches zero after 0.1 seconds.

5.4.3.2 ROLL VELOCITY SYSTEM OBSERVER

Checking the controllability, $\mathbf{M}_{\angle x}$, and observability, $\mathbf{O}_{\angle x}$, matrices for the roll system:

$$\mathbf{M}_{\angle x} = \begin{bmatrix} 0 & 1 \\ 1 & -\frac{4d_{yy}w^2}{I_{xx}} \end{bmatrix} \quad (5.142)$$

$$\mathbf{O}_{\angle x} = \begin{bmatrix} 1 & 0 \\ 0 & 1 \end{bmatrix} \quad (5.143)$$

We can see that the rank of both $\mathbf{M}_{\angle x}$ and $\mathbf{O}_{\angle x}$ is 2 (full), so the system is observable and controllable. Defining the observer system:

$$A_{\theta x, aa} = [0] \quad (5.144)$$

$$A_{\theta x, au} = [1] \quad (5.145)$$

$$A_{\theta x, ua} = \begin{bmatrix} \frac{4k_{yy}w^2}{I_{xx}} \end{bmatrix} \quad (5.146)$$

$$A_{\theta x, uu} = \begin{bmatrix} \frac{4d_{yy}w^2}{I_{xx}} \end{bmatrix} \quad (5.147)$$

$$B_{\theta x, a} = [0] \quad (5.148)$$

$$B_{\theta x, u} = [1] \quad (5.149)$$

From (5.111) the control law for a reduced order observer system is

$$\delta u_{\theta x} = -K_{\theta x, a} \delta \theta_x - K_{\theta x, u} \delta \hat{\omega}_x \quad (5.150)$$

where the estimated state is:

$$\delta \dot{\hat{\omega}}_x = \left(\frac{4d_{yy}w^2}{I_{xx}} - K_{\theta x, u} - L_{\theta x} \right) \delta \hat{\omega}_x + \left(\frac{4k_{yy}w^2}{I_{xx}} - K_{\theta x, a} \right) \delta \theta_x + L_{\theta x} \delta \omega_x \quad (5.151)$$

Similarly to obtaining the equation for the height dynamics reduced-order observer system, substituting (5.144) - (5.149) into (5.105) yields the reduced-order observer state-space roll system:

$$\begin{bmatrix} \dot{\theta}_x \\ \dot{\omega}_x \\ \dot{e}_{\theta x} \end{bmatrix} = \begin{bmatrix} 0 & 1 & 0 \\ \frac{4k_{yy}w^2}{I_{xx}} - K_{\theta x,a} & \frac{4d_{yy}w^2}{I_{xx}} - K_{\theta x,u} & K_{\theta x,u} \\ 0 & 0 & \frac{4d_{yy}w^2}{I_{xx}} - L_{\theta x} \end{bmatrix} \begin{bmatrix} \theta_x \\ \omega_x \\ e_{\theta x} \end{bmatrix} + \begin{bmatrix} 0 \\ \bar{N}_{\theta x} \\ 0 \end{bmatrix} r_{\theta x} \quad (5.152)$$

Also similarly to the height system, the reduced order observer for the roll system is trivial and behaves similarly to a standard LQR unless there is modeling error or the system begins with error. The error will decay according to:

$$\delta \dot{e}_{\theta x} = \left(\frac{4d_{yy}w^2}{I_{xx}} - L_{\theta x} \right) \delta e_{\theta x} \quad (5.153)$$

To further verify the validity of using the SOVP model for modeling and control, the full state observer is derived from (5.84), again using the same method as section 5.4.3.1:

$$\begin{bmatrix} \delta \dot{\theta}_x \\ \delta \dot{\omega}_x \\ \delta \dot{e}_{\theta x} \\ \delta \dot{e}_{\omega x} \end{bmatrix} = \begin{bmatrix} 0 & 1 & 0 & 0 \\ \frac{4k_{yy}w^2}{I_{xx}} - K_{\theta x1} & \frac{4d_{yy}w^2}{I_{xx}} - K_{\theta x2} & K_{\theta x1} & K_{\theta x2} \\ 0 & 0 & L_{\theta x1} & 1 \\ 0 & 0 & \frac{4k_{yy}w^2}{I_{xx}} - L_{\theta x2} & \frac{4d_{yy}w^2}{I_{xx}} \end{bmatrix} \begin{bmatrix} \delta \theta_x \\ \delta \omega_x \\ \delta e_{\theta x} \\ \delta e_{\omega x} \end{bmatrix} + \begin{bmatrix} 0 \\ \bar{N}_{\theta x} \\ 0 \\ 0 \end{bmatrix} \delta \theta_{x,des} \quad (5.154)$$

As in section 5.4.3.1, we can use a cost weighting matrix and the Algebraic Riccati to obtain the controller gain:

$$\mathbf{Q}_{\theta x} = \begin{bmatrix} 100 & 0 \\ 0 & 1 \end{bmatrix} \quad (5.155)$$

$$\mathbf{K}_{\theta_x} = \begin{bmatrix} 93935.1 \\ 10004.1 \end{bmatrix} \quad (5.156)$$

The eigenvalues of $\mathbf{A}_{\theta_x} - \mathbf{B}_{\theta_x}\mathbf{K}_{\theta_x}$ are:

$$\lambda_{\theta_{x1}}^{cl} = -10.02 \quad (5.157)$$

$$\lambda_{\theta_{x2}}^{cl} = -9999.4 \quad (5.158)$$

Observer poles are chosen to be:

$$p_{\theta_{x1}}^o = -100 \quad (5.159)$$

$$p_{\theta_{x2}}^o = -101 \quad (5.160)$$

Using pole placement on $\mathbf{A}_{\theta_x} - \mathbf{L}_{\theta_x}\mathbf{C}_{\theta_x}$ to obtain the observer gain:

$$\mathbf{L}_{\theta_x} = \begin{bmatrix} 195.72 \\ 2807.40 \end{bmatrix} \quad (5.161)$$

A simulation of the system is performed with a disturbance at $t = 0$ s specified by Table 7 and initial conditions defined in Table 11. Note that the observer begins with non-zero error (rotational position offset by 0.02 radians and rotational velocity offset by -0.01 rad/s). Results for the simulation are shown in Fig. 128.

Table 11: Roll observer system initial conditions

| Parameter | Value | Unit |
|---------------------|-------|-------|
| $\theta_x(0)$ | 0 | rad |
| $\omega_x(0)$ | 0 | rad/s |
| $\hat{\theta}_x(0)$ | 0.02 | rad |
| $\hat{\omega}_x(0)$ | -0.01 | rad/s |

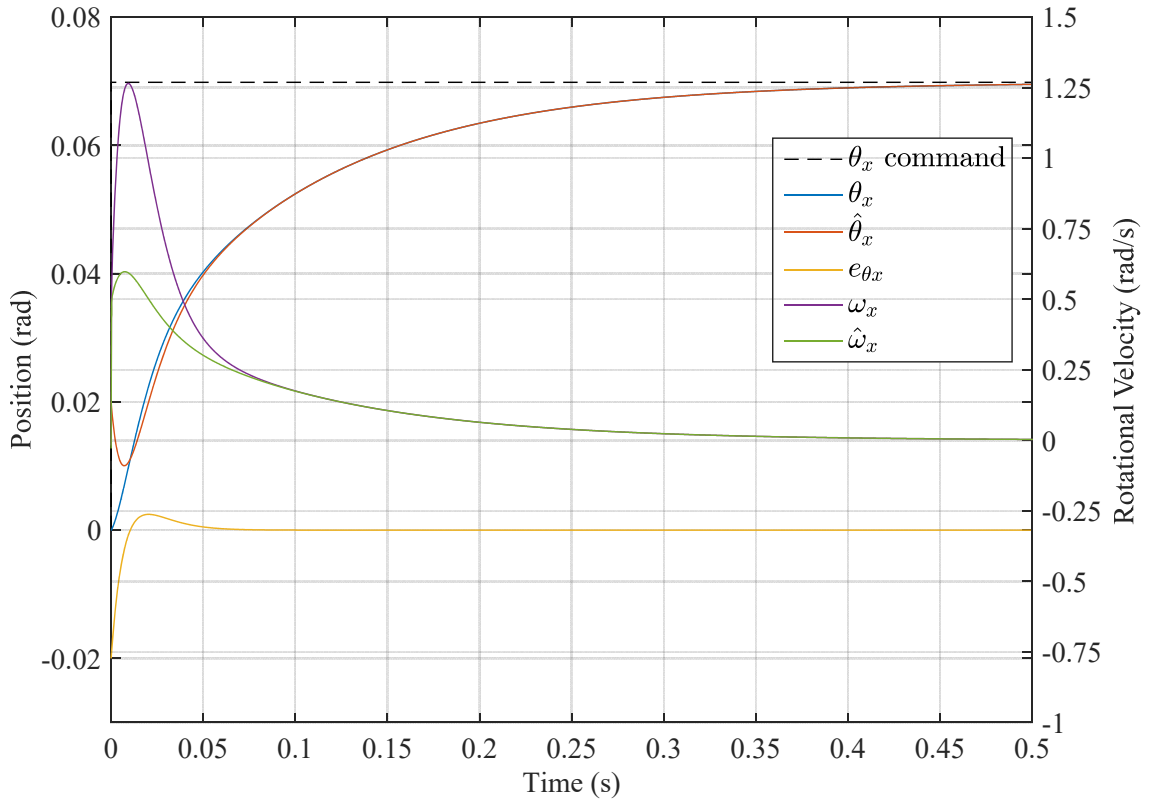


Fig. 128: Roll dynamics observer simulation (parameters from Table 1, Table 6, Table 7, Table 11)

Similarly to the height system, the roll system settles to within 2% of its' steady state value in 0.4 seconds, and observer approaches zero before 0.1 seconds. In order for the observer to correct for positional error, velocity error (not shown since it's not a state or an input to any system blocks) briefly becomes large, as is desired since positional error accrues more cost than velocity error.

5.4.3.3 PITCH VELOCITY SYSTEM OBSERVER

Checking the controllability, $\mathbf{M}_{\angle z}$, and observability, $\mathbf{O}_{\angle z}$, matrices for the pitch system:

$$\mathbf{M}_{\angle z} = \begin{bmatrix} 0 & 1 \\ 1 & \frac{4d_{yy}l^2}{I_{zz}} \end{bmatrix} \quad (5.162)$$

$$\mathbf{O}_{\angle z} = \begin{bmatrix} 1 & 0 \\ 0 & 1 \end{bmatrix} \quad (5.163)$$

We can see that the rank of both $\mathbf{M}_{\angle z}$ and $\mathbf{O}_{\angle z}$ is 2 (full), so the system is observable and controllable. Defining the observer system:

$$A_{\theta z,aa} = [0] \quad (5.164)$$

$$A_{\theta z,au} = [1] \quad (5.165)$$

$$A_{\theta z,ua} = \begin{bmatrix} \frac{4k_{yy}l^2}{I_{zz}} \end{bmatrix} \quad (5.166)$$

$$A_{\theta z,uu} = \begin{bmatrix} \frac{4d_{yy}l^2}{I_{zz}} \end{bmatrix} \quad (5.167)$$

$$B_{\theta z,a} = [0] \quad (5.168)$$

$$B_{\theta z,u} = [1] \quad (5.169)$$

From (5.111) the control law for the reduced order observer system is

$$\delta u_{\theta z} = -K_{\theta z,a} \delta \theta_z - K_{\theta z,u} \delta \hat{\omega}_z \quad (5.170)$$

where the estimated state is:

$$\delta \dot{\hat{\omega}}_z = \left(\frac{4d_{yy}l^2}{I_{zz}} - K_{\theta z,u} - L_{\theta z} \right) \delta \hat{\omega}_z + \left(\frac{4k_{yy}l^2}{I_{zz}} - K_{\theta z,a} \right) \delta \theta_z + L_{\theta z} \delta \omega_z \quad (5.171)$$

Substituting (5.164) - (5.169) into (5.105) yields the reduced-order observer state-space pitch system:

$$\begin{bmatrix} \dot{\theta}_z \\ \dot{\omega}_z \\ \dot{e}_{\theta z} \end{bmatrix} = \begin{bmatrix} 0 & 1 & 0 \\ \frac{4k_{yy}l^2}{I_{zz}} - K_{\theta z,a} & \frac{4d_{yy}l^2}{I_{zz}} - K_{\theta z,u} & K_{\theta z,u} \\ 0 & 0 & \frac{4d_{yy}l^2}{I_{zz}} - L_{\theta z} \end{bmatrix} \begin{bmatrix} \theta_z \\ \omega_z \\ e_{\theta z} \end{bmatrix} + \begin{bmatrix} 0 \\ \bar{N}_{\theta z} \\ 0 \end{bmatrix} r_{\theta z} \quad (5.172)$$

Assuming the system either begins with error or has modeling errors, then the error will decay according to:

$$\delta \dot{e}_{\theta z} = \left(\frac{4d_{yy}l^2}{I_{zz}} - L_{\theta z} \right) \delta e_{\theta z} \quad (5.173)$$

The full state observer is derived from (5.84) and (4.67):

$$\begin{bmatrix} \delta \dot{\theta}_z \\ \delta \dot{\omega}_z \\ \delta \dot{e}_{\theta z} \\ \delta \dot{e}_{\omega z} \end{bmatrix} = \begin{bmatrix} 0 & 1 & 0 & 0 \\ \frac{4k_{yy}l^2}{I_{zz}} - K_{\theta z1} & \frac{4d_{yy}l^2}{I_{zz}} - K_{\theta z2} & K_{\theta z1} & K_{\theta z2} \\ 0 & 0 & L_{\theta z1} & 1 \\ 0 & 0 & \frac{4k_{yy}l^2}{I_{zz}} - L_{\theta z2} & \frac{4d_{yy}l^2}{I_{zz}} \end{bmatrix} \begin{bmatrix} \delta \theta_z \\ \delta \omega_z \\ \delta e_{\theta z} \\ \delta e_{\omega z} \end{bmatrix} + \begin{bmatrix} 0 \\ \bar{N}_{\theta z} \\ 0 \\ 0 \end{bmatrix} \delta \theta_{z,des} \quad (5.174)$$

Similarly to section 5.4.3.1 and 5.4.3.2, we can use a cost weighting matrix and the Algebraic Riccati to obtain the controller gain:

$$\mathbf{Q}_{\theta z} = \begin{bmatrix} 100 & 0 \\ 0 & 1 \end{bmatrix} \quad (5.175)$$

$$\mathbf{K}_{\theta z} = \begin{bmatrix} 94260.3 \\ 10004.4 \end{bmatrix} \quad (5.176)$$

The eigenvalues of $A_{\theta z} - B_{\theta z}K_{\theta z}$ are:

$$\lambda_{\theta z 1}^{cl} = -10.01 \quad (5.177)$$

$$\lambda_{\theta z 2}^{cl} = -9999.41 \quad (5.178)$$

Observer poles are chosen to be:

$$p_{\theta z 1}^o = -100 \quad (5.179)$$

$$p_{\theta z 2}^o = -101 \quad (5.180)$$

Using pole placement on $A_{\theta z} - L_{\theta z}C_{\theta z}$ to obtain the observer gain:

$$L_{\theta z} = \begin{bmatrix} 198.02 \\ 3401.28 \end{bmatrix} \quad (5.181)$$

A simulation of the system is performed with a disturbance at $t = 0$ s specified by Table 7 and initial conditions defined in Table 12. Note that the observer begins with non-zero error (rotational position offset by 0.01 radians and rotational velocity offset by -0.07 rad/s). Results for the simulation are shown in Fig. 129.

Table 12: Pitch observer system initial conditions

| Parameter | Value | Unit |
|---------------------|-------|-------|
| $\theta_z(0)$ | 0 | rad |
| $\omega_z(0)$ | 0 | rad/s |
| $\hat{\theta}_z(0)$ | 0.01 | rad |
| $\hat{\omega}_z(0)$ | -0.07 | rad/s |

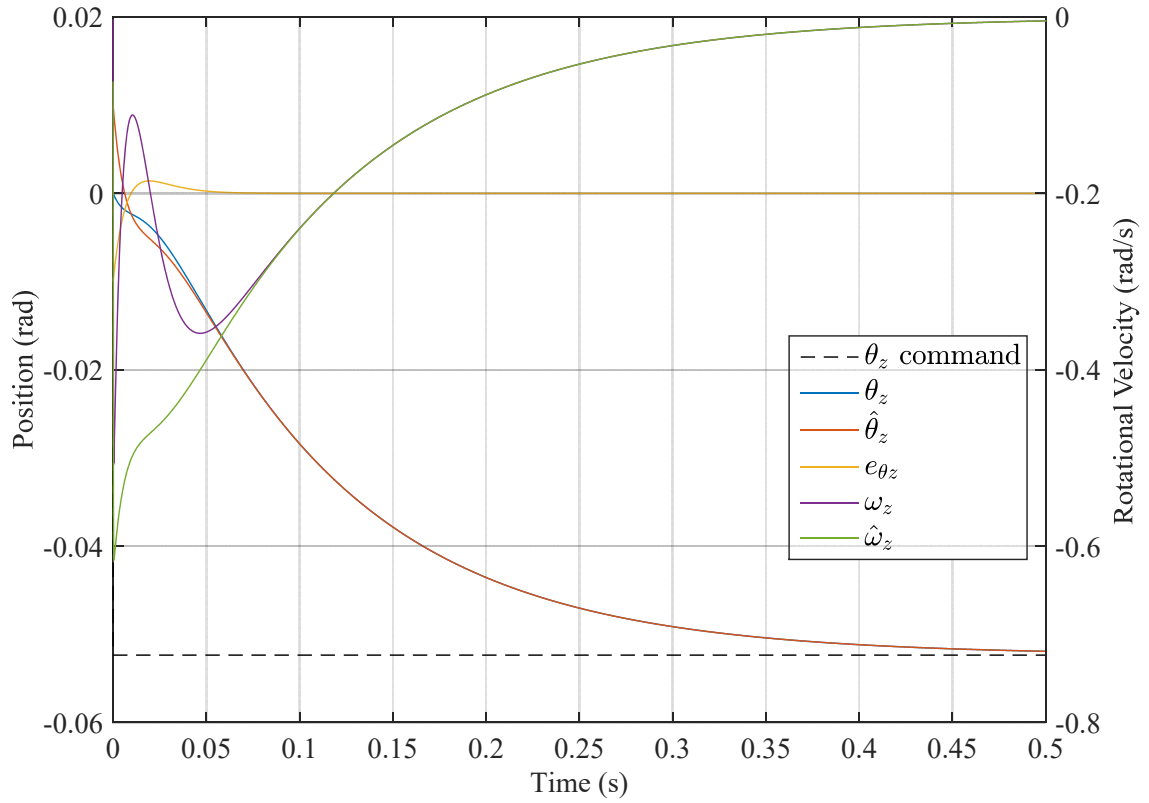


Fig. 129: Pitch dynamics observer simulation (parameters from Table 1, Table 6, Table 7, Table 12)

The pitch system settles within 2% of its' steady state in 0.5 seconds. Positional error, which is fed into the \mathbf{L}_{θ_z} block, quickly settles to zero within 0.1 seconds. We can observe a period of large velocity error from $t = 0\text{s}$ to $t = 0.05\text{s}$, which allows the estimated position to quickly converge to the plant state.

5.4.3.4 YAW SYSTEM FULL OBSERVER

Checking the controllability, $\mathbf{M}_{\angle y}$, and observability, $\mathbf{O}_{\angle y}$, matrices for the roll system:

$$\mathbf{M}_{\angle y} = \begin{bmatrix} 0 & 1 \\ 1 & \frac{4d_{xx}a}{I_{yy}} \end{bmatrix} \quad (5.182)$$

$$\mathbf{O}_{\angle y} = \begin{bmatrix} 1 & 0 \\ 0 & 1 \end{bmatrix} \quad (5.183)$$

We can see that the rank of both $\mathbf{M}_{\angle y}$ and $\mathbf{O}_{\angle y}$ is 2 (full), so the system is observable and controllable. A combination magnetometer – gyroscope device can be used to approximately detect yaw position, although these devices are orders of magnitude less accurate than the laser sensors used for the other degrees of freedom, especially at smaller time scales. As such, it will be more important to trust the plant modeling and use slower estimator poles. Although this will make the estimator slower to recover from error, the system will have more time to average yaw readings. Alternatively, and discussed in a later section, a filter can be used on the measurements to reduce the noise.

Defining the observer system:

$$A_{\theta y, aa} = [0] \quad (5.184)$$

$$A_{\theta y, au} = [1] \quad (5.185)$$

$$A_{\theta y, ua} = \begin{bmatrix} \frac{4k_{xx}a}{I_{yy}} \end{bmatrix} \quad (5.186)$$

$$A_{\theta y, uu} = \begin{bmatrix} \frac{4d_{xx}a}{I_{yy}} \end{bmatrix} \quad (5.187)$$

$$B_{\theta y, a} = [0] \quad (5.188)$$

$$B_{\theta y, u} = [1] \quad (5.189)$$

From (5.111) the control law for the reduced order observer system is

$$\delta u_{\theta y} = -K_{\theta y, a} \delta \theta_y - K_{\theta y, u} \delta \hat{\omega}_y \quad (5.190)$$

where the estimated state is:

$$\delta \dot{\hat{\omega}}_y = \left(\frac{4d_{xx}a}{I_{yy}} - K_{\theta y,u} - L_{\theta y} \right) \delta \hat{\omega}_y + \left(\frac{4k_{xx}a}{I_{yy}} - K_{\theta y,a} \right) \delta \theta_y + L_{\theta y} \delta \omega_y \quad (5.191)$$

Substituting (5.164) - (5.169) into (5.84) yields the reduced-order observer state-space pitch system:

$$\begin{bmatrix} \dot{\theta}_y \\ \dot{\omega}_y \\ \dot{e}_{\theta y} \end{bmatrix} = \begin{bmatrix} 0 & 1 & 0 \\ \frac{4k_{xx}a}{I_{yy}} - K_{\theta y,a} & \frac{4d_{xx}a}{I_{yy}} - K_{\theta y,u} & K_{\theta y,u} \\ 0 & 0 & \frac{4d_{xx}a}{I_{yy}} - L_{\theta y} \end{bmatrix} \begin{bmatrix} \theta_y \\ \omega_y \\ e_{\theta y} \end{bmatrix} + \begin{bmatrix} 0 \\ \bar{N}_{\theta y} \\ 0 \end{bmatrix} r_{\theta y} \quad (5.192)$$

Again, modeling uncertainties and initial error will cause error to follow the following dynamic equation:

$$\delta \dot{e}_{\theta y} = \left(\frac{4d_{xx}a}{I_{yy}} - L_{\theta y} \right) \delta e_{\theta y} \quad (5.193)$$

The full state observer is derived from (5.84) and (4.67):

$$\begin{bmatrix} \delta \dot{\theta}_y \\ \delta \dot{\omega}_y \\ \delta \dot{e}_{\theta y} \\ \delta \dot{e}_{\omega y} \end{bmatrix} = \begin{bmatrix} 0 & 1 & 0 & 0 \\ \frac{4k_{xx}a}{I_{yy}} - K_{\theta y1} & \frac{4d_{xx}a}{I_{yy}} - K_{\theta y2} & K_{\theta y1} & K_{\theta y2} \\ 0 & 0 & L_{\theta y1} & 1 \\ 0 & 0 & \frac{4k_{xx}a}{I_{yy}} - L_{\theta y2} & \frac{4d_{xx}a}{I_{yy}} \end{bmatrix} \begin{bmatrix} \delta \theta_y \\ \delta \omega_y \\ \delta e_{\theta y} \\ \delta e_{\omega y} \end{bmatrix} + \begin{bmatrix} 0 \\ \bar{N}_{\theta y} \\ 0 \\ 0 \end{bmatrix} \delta \theta_{y,des} \quad (5.194)$$

Similarly to section 5.4.3.1, 5.4.3.2, and 5.4.3.3, we can use a cost weighting matrix and the Algebraic Riccati to obtain the controller gain:

$$\mathbf{Q}_{\theta_y} = \begin{bmatrix} 100 & 0 \\ 0 & 1 \end{bmatrix} \quad (5.195)$$

$$\mathbf{K}_{\theta_y} = \begin{bmatrix} 83003.1 \\ 10020.1 \end{bmatrix} \quad (5.196)$$

The eigenvalues of $\mathbf{A}_{\theta_y} - \mathbf{B}_{\theta_y}\mathbf{K}_{\theta_y}$ are:

$$\lambda_{\theta_{y1}}^{cl} = -10.17 \quad (5.197)$$

$$\lambda_{\theta_{y2}}^{cl} = -9998.13 \quad (5.198)$$

Observer poles are chosen to be:

$$p_{\theta_{y1}}^o = -100 \quad (5.199)$$

$$p_{\theta_{y2}}^o = -101 \quad (5.200)$$

Using pole placement on $\mathbf{A}_{\theta_y} - \mathbf{L}_{\theta_y}\mathbf{C}_{\theta_y}$ to obtain the observer gain:

$$\mathbf{L}_{\theta_y} = \begin{bmatrix} 2014.78 \\ 1008006.36 \end{bmatrix} \quad (5.201)$$

A simulation of the system is performed with a disturbance at $t = 0$ s specified by Table 7 and initial conditions defined in Table 13. Note that the observer begins with non-zero error (rotational position offset by -0.05 radians and rotational velocity offset by 0.05 rad/s). Results for the simulation are shown in Fig. 130.

Table 13: Yaw observer system initial conditions

| Parameter | Value | Unit |
|---------------------|-------|-------|
| $\theta_y(0)$ | 0 | rad |
| $\omega_y(0)$ | 0 | rad/s |
| $\hat{\theta}_y(0)$ | -0.05 | rad |
| $\hat{\omega}_y(0)$ | 0.05 | rad/s |

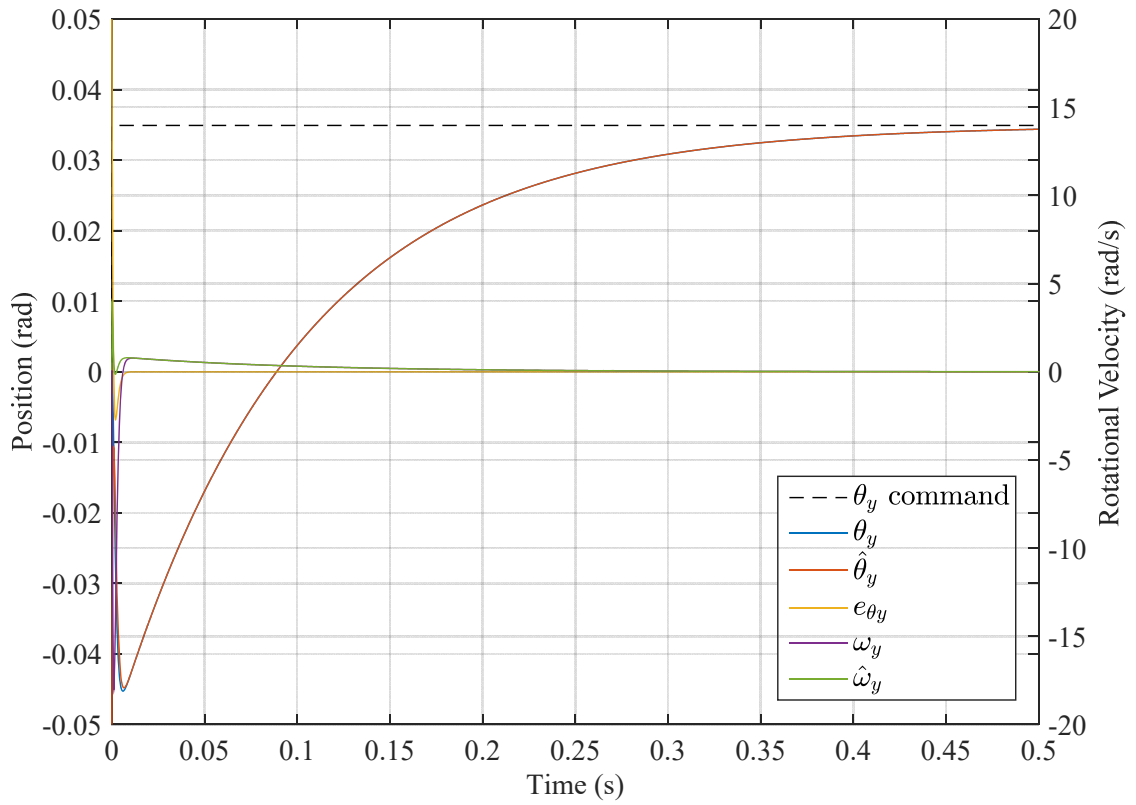


Fig. 130: Yaw dynamics observer simulation (parameters from Table 1, Table 6, Table 7, Table 13)

The yaw state settles to within 2% of its steady state value in roughly 10 times faster than the other states, at 0.05 seconds. When the simulation begins, yaw error is aggressively reduced using large observer velocities to force the estimation to approach the plant yaw state. A closer inspection of the result plot is shown in Fig. 131.

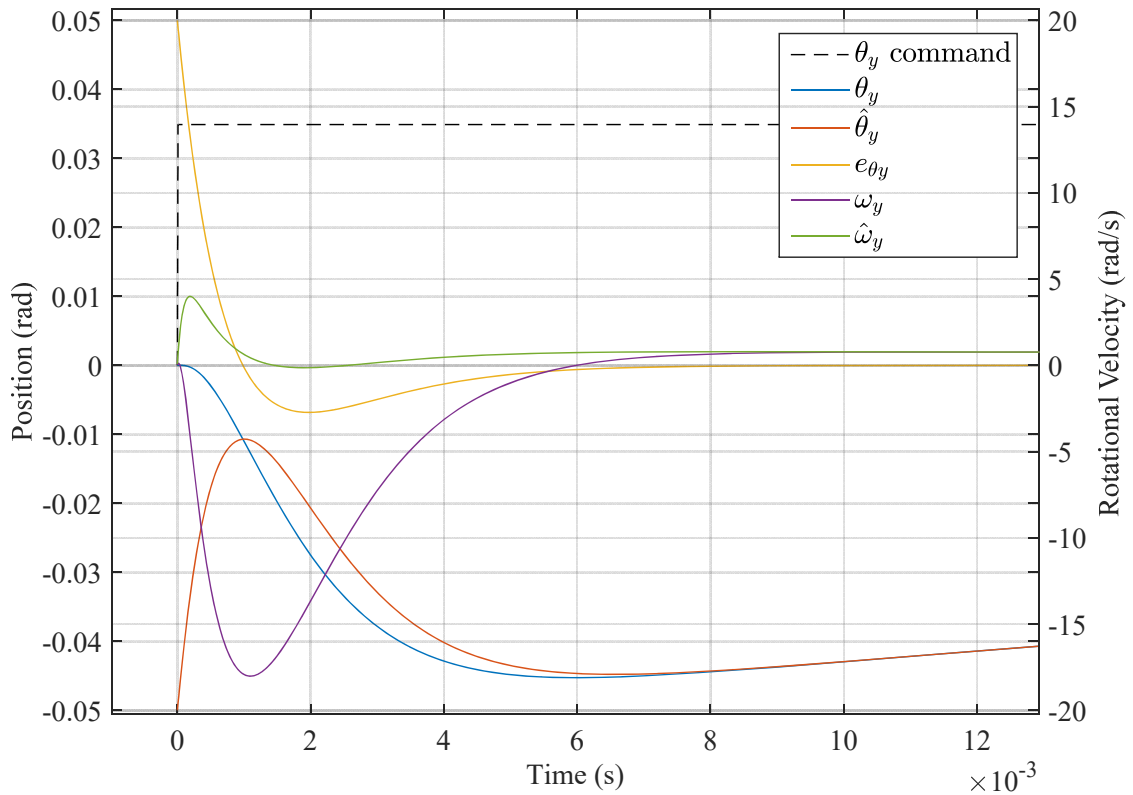


Fig. 131: First moments of yaw dynamics observer simulation
(parameters from Table 1, Table 6, Table 7, Table 13)

The zoomed plot shows that the large initial yaw error forces the velocity error to be large. Only when the position error becomes small does the estimated velocity begin to approach the plant velocity. The observer's error actually causes the position to move away from the desired value (rather than begin from 0, the position drops to -0.045 radians before moving towards the desired 0.035 radians). This simulation therefore shows that observer error can have a significant impact on overall system performance.

Since the system is decoupled, the four independent simulations represent the movement of the entire 4-DOF system. When they are all simulated simultaneously, we

can observe the individual rotor behavior that determines the vehicle's movement. Fig. 132 shows the rotor rotational velocities, and Fig. 133 shows each rotors' torque and vertical force. Note that rotor 1 slows down dramatically and actually begins rotating in reverse, while rotor 3 experiences a much larger rotational speed than the rest.

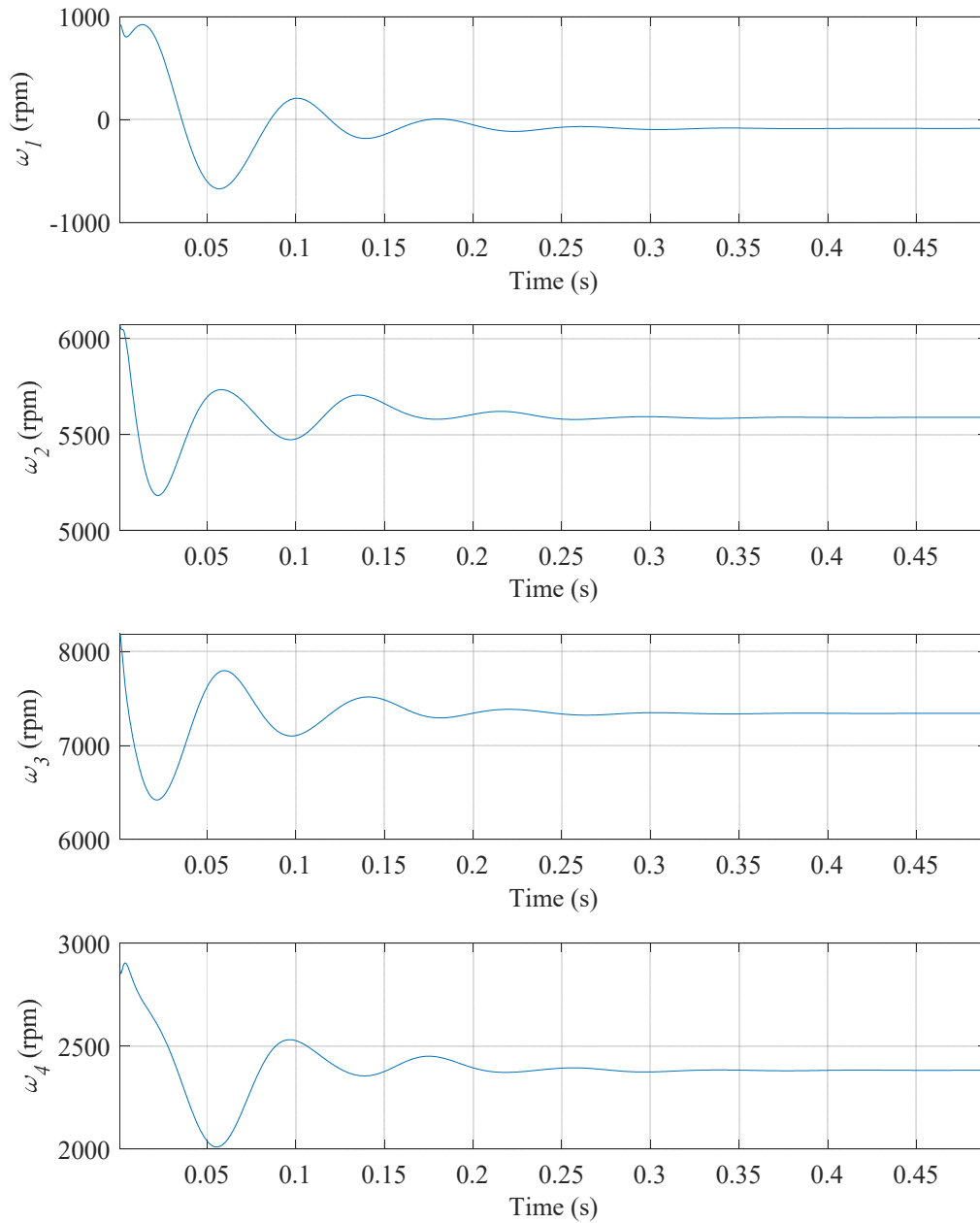


Fig. 132: Individual rotor rotational velocity during simulations from Fig. 127 to Fig. 131

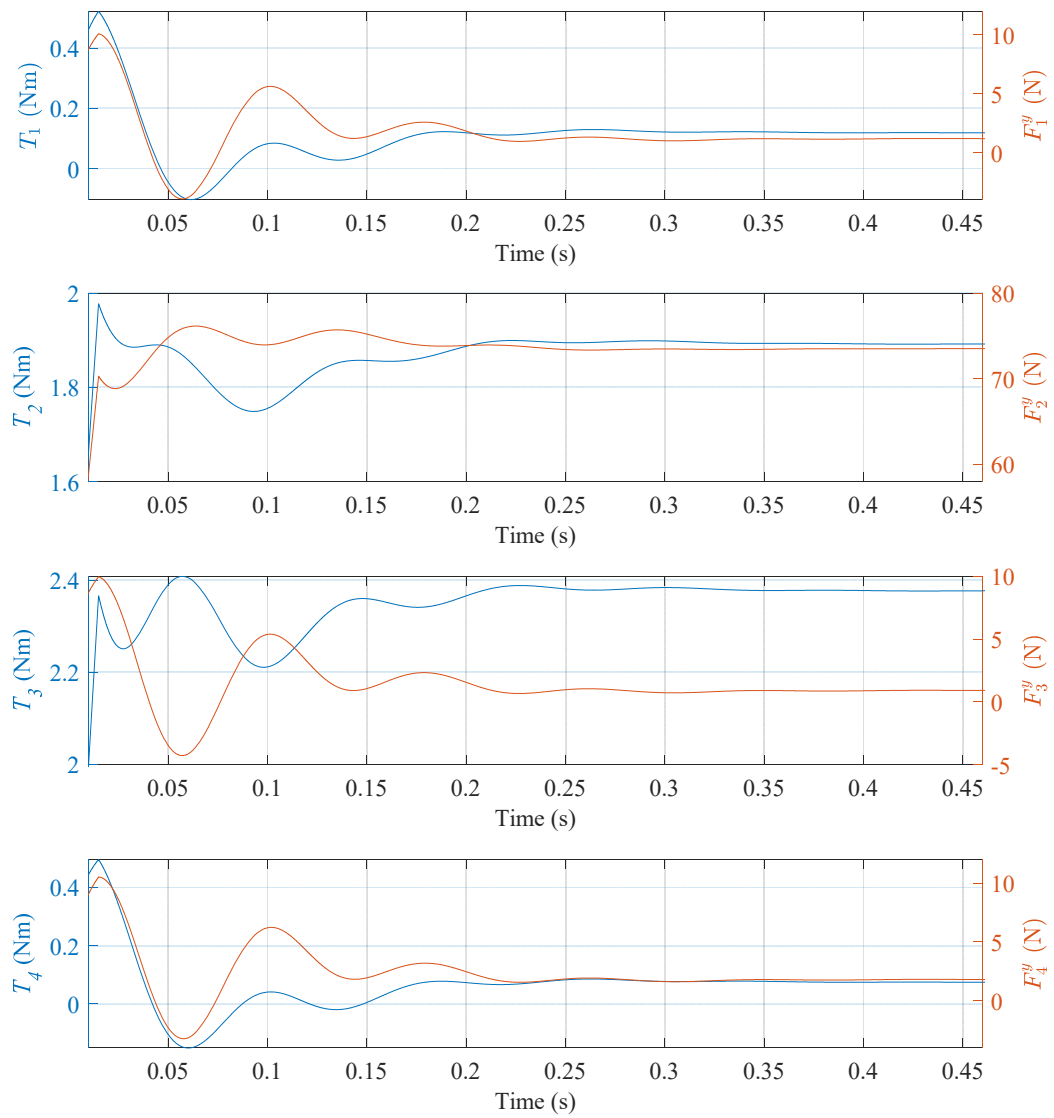


Fig. 133: Individual rotor torque and vertical force during simulations from Fig. 127 to Fig. 131

5.5 NONLINEAR OBSERVER CONTROL

In this section, the plant and observer dynamics are updated in run-time using state information to create a more accurate model. First, the Linear Quadratic Gaussian Integral (LQGI) methodology is introduced, then the LQG system is augmented so that the governing equations become non-linear.

5.5.1 LINEAR QUADRATIC GAUSSIAN INTEGRAL CONTROL

An LQGI controller can be formed by combining a Linear Quadratic Estimator (LQE) with an LQR [78] and a PI (Proportional Integral) integrator. The estimator employs a Kalman filter which estimates the plant's states while they are subject to process noise and the output is subject to measurement noise. The Kalman filter produces an optimal estimation of the states such that the mean value of the squared error is minimized. We wish this system to achieve zero steady-state error without prescalars that are highly dependent on model accuracy, so the system is augmented with an integrator similar to that used in section 5.3.2.

Suppose we want to minimize the following objective function:

$$J = E \left[\mathbf{x}_d^T(t_f) \mathbf{F}_d \mathbf{x}_d(t_f) + \int_0^T \left(\mathbf{x}_d^T(t) \mathbf{Q}_d \mathbf{x}_d(t) + u_d^T(t) R_d(t) u_d(t) \right) dt \right] \quad (5.202)$$

where E is the expected value, T is the horizon length, t_f is the final time, \mathbf{F}_d scales the relative weight of the states at t_f , \mathbf{Q}_d scales the weight of the states, and R_d scales the weight of the input. If we take the horizon to be infinite, then the first part of the objective function becomes irrelevant. The objective function is also scaled by T^{-1} so that it does not become infinite. Rewriting (5.202) with the assumption of an infinite horizon:

$$J = \frac{1}{T} \mathbb{E} \left[\int_0^T \left(\mathbf{x}_d^T(t) \mathbf{Q}_d \mathbf{x}_d + u_d^T(t) R_d(t) u_d(t) \right) dt \right] \quad (5.203)$$

We should assume that a real world system will have some degree of random white noise acting on both the states and the output measurement. The plant noise on the states (also known as process noise) is denoted by the vector:

$$\mathbf{d}_d = \begin{bmatrix} d_{d1} \\ d_{d2} \end{bmatrix} \quad (5.204)$$

The process noise is scaled by a (typically diagonal) matrix \mathbf{G}_d . Referring to Fig. 134, the plant states with noise can be modeled by

$$\dot{\mathbf{x}}_d = \mathbf{A}_d \mathbf{x}_d + \mathbf{B}_d u_d + \mathbf{G}_d \mathbf{d}_d \quad (5.205)$$

The estimator states are

$$\dot{\hat{\mathbf{x}}}_d = \hat{\mathbf{A}}_d \hat{\mathbf{x}}_d + \hat{\mathbf{B}}_d u_d + \mathbf{L}_d \mathbf{e}_d \quad (5.206)$$

where once again the estimator error is

$$\mathbf{e}_d = y_d - \hat{y}_d \quad (5.207)$$

and the outputs to these systems are

$$y_d = \mathbf{C}_d \mathbf{x}_d + \mathbf{I}_{1 \times 1} n_d \quad (5.208)$$

$$\hat{y}_d = \hat{\mathbf{C}}_d \hat{\mathbf{x}}_d \quad (5.209)$$

Substituting (5.208) and (5.209) into (5.207) gives:

$$\mathbf{e}_d = \mathbf{C}_d \mathbf{x}_d - \hat{\mathbf{C}}_d \hat{\mathbf{x}}_d + \mathbf{I}_{1 \times 1} n_d \quad (5.210)$$

The integrator, which drives the steady-state error to zero, is defined by

$$\dot{x}_{di} = r_d - \mathbf{C}_d \mathbf{x}_d - \mathbf{I}_{1 \times 1} n_d \quad (5.211)$$

The estimated states drive a regulator that, along with the integrator, form the plant's input:

$$u_d = K_{di}x_{di} - K_{dc}\hat{x}_d \quad (5.212)$$

The system block diagram is shown in Fig. 134.

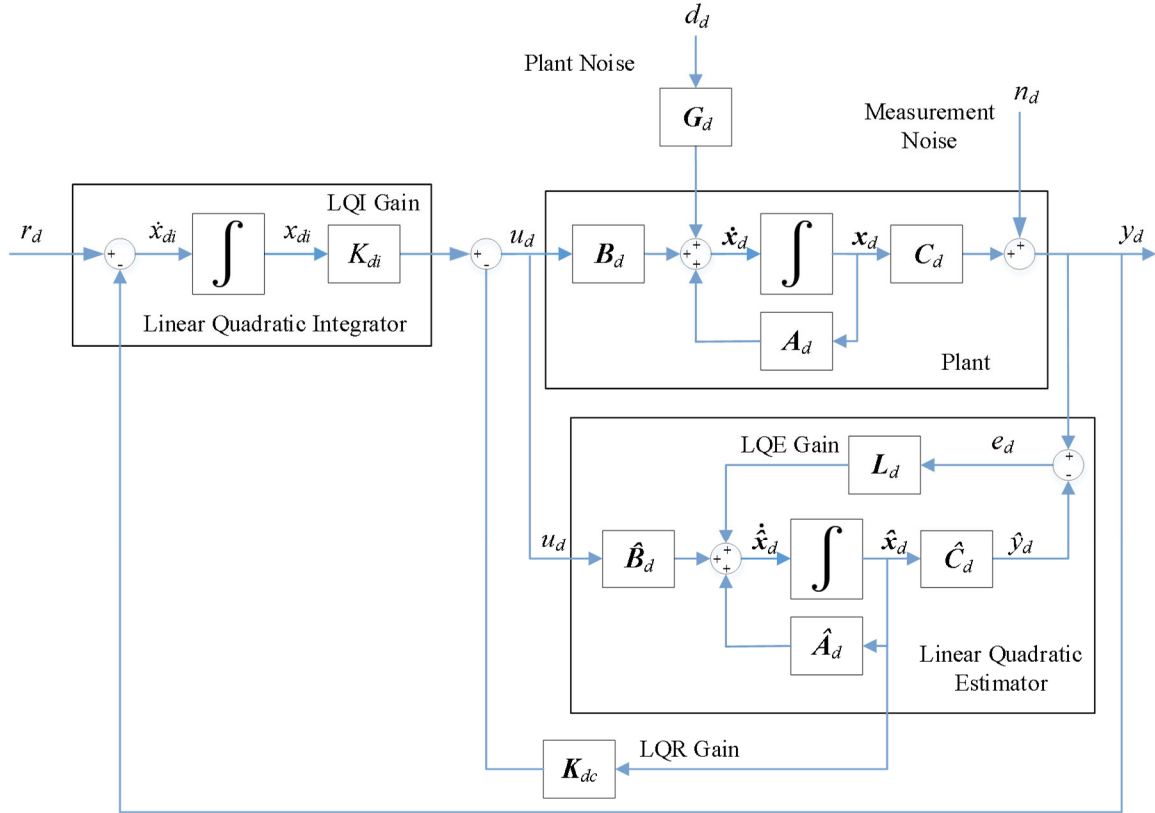


Fig. 134: LQG block diagram, where K_{dc} is the LQR controller gain and G_d defines how the noise is distributed across the states

Substituting (5.212) into (5.205) and (5.206) gives

$$\dot{x}_d = A_d x_d + B_d K_{di} x_{di} - B_d K_{dc} \hat{x}_d + G_d d_d \quad (5.213)$$

$$\dot{\hat{x}}_d = \hat{A}_d \hat{x}_d + \hat{B}_d K_{di} x_{di} - \hat{B}_d K_{dc} \hat{x}_d + L_d e_d \quad (5.214)$$

The estimator can be described in terms of its native states, x , \hat{x} , and x_i by substituting (5.208) and (5.209) into (5.207), then substituting the result into (5.214):

$$\dot{\hat{x}}_d = \hat{A}_d \hat{x}_d + \hat{B}_d K_{di} x_{di} - \hat{B}_d K_{dc} \hat{x}_d + L_d C_d x_d + L_d n_d - L_d \hat{C}_d \hat{x}_d \quad (5.215)$$

Equation (5.215) can be simplified to

$$\dot{\hat{\mathbf{x}}}_d = \mathbf{A}_d \hat{\mathbf{x}}_d + \mathbf{B}_d [K_{di} \mathbf{x}_{di} - \mathbf{K}_{dc} \hat{\mathbf{x}}_d] + \mathbf{L}_d [C_d \mathbf{x}_d - C_d \hat{\mathbf{x}}_d + n_d] \quad (5.216)$$

In order to ensure that the principle of separation of estimation and control holds, and to form a convenient linear state-space system, a new augmented state can be defined [78]:

$$\bar{\mathbf{x}}_d = \mathbf{x}_d - \hat{\mathbf{x}}_d \quad (5.217)$$

The plant input, (5.212), can then be redefined by substituting the augmented state, (5.217), into (5.212):

$$u_d = K_{di} \mathbf{x}_{di} + \mathbf{K}_{dc} \bar{\mathbf{x}}_d - \mathbf{K}_{dc} \mathbf{x}_d \quad (5.218)$$

Substituting (5.217) and the new input from (5.218) into the plant and estimator state equations, (5.205) and (5.206),

$$\dot{\mathbf{x}}_d = \mathbf{A}_d \mathbf{x}_d + \mathbf{B}_d (K_{di} \mathbf{x}_{di} + \mathbf{K}_{dc} \bar{\mathbf{x}}_d - \mathbf{K}_{dc} \mathbf{x}_d) + \mathbf{G}_d \mathbf{d}_d \quad (5.219)$$

$$\dot{\hat{\mathbf{x}}}_d = \hat{\mathbf{A}}_d (\mathbf{x}_d - \bar{\mathbf{x}}_d) + \hat{\mathbf{B}}_d (K_{di} \mathbf{x}_{di} + \mathbf{K}_{dc} \bar{\mathbf{x}}_d - \mathbf{K}_{dc} \mathbf{x}_d) + \mathbf{L}_d (C_d \mathbf{x}_d + n_d - \hat{C}_d (\mathbf{x}_d - \bar{\mathbf{x}}_d)) \quad (5.220)$$

Noting that (5.217) also implies

$$\dot{\bar{\mathbf{x}}}_d = \dot{\mathbf{x}}_d - \dot{\hat{\mathbf{x}}}_d \quad (5.221)$$

Equations (5.219) and (5.220) can be substituted into (5.221) to obtain the state equation for the augmented state:

$$\begin{aligned} \dot{\bar{\mathbf{x}}}_d = & \left[\mathbf{A}_d \mathbf{x}_d + \mathbf{B}_d (K_{di} \mathbf{x}_{di} + \mathbf{K}_{dc} \bar{\mathbf{x}}_d - \mathbf{K}_{dc} \mathbf{x}_d) + \mathbf{G}_d \mathbf{d}_d \right] \\ & - \left[\hat{\mathbf{A}}_d (\mathbf{x}_d - \bar{\mathbf{x}}_d) + \hat{\mathbf{B}}_d (K_{di} \mathbf{x}_{di} + \mathbf{K}_{dc} \bar{\mathbf{x}}_d - \mathbf{K}_{dc} \mathbf{x}_d) \right. \\ & \left. + \mathbf{L}_d (C_d \mathbf{x}_d + n_d - \hat{C}_d (\mathbf{x}_d - \bar{\mathbf{x}}_d)) \right] \end{aligned} \quad (5.222)$$

If we assume that the estimator model is sufficiently accurate such that

$$\hat{\mathbf{A}}_d \cong \mathbf{A}_d \quad (5.223)$$

$$\hat{\mathbf{B}}_d \cong \mathbf{B}_d \quad (5.224)$$

$$\hat{\mathbf{C}}_d \cong \mathbf{C}_d \quad (5.225)$$

Then common terms in (5.222) reduce down to

$$\dot{\bar{\mathbf{x}}}_d = (\mathbf{A}_d - \mathbf{L}_d \mathbf{C}_d) \bar{\mathbf{x}}_d + \mathbf{G}_d \mathbf{d}_d - \mathbf{L}_d n_d \quad (5.226)$$

Equations (5.211), (5.219), and (5.226) form a new set of state equations that can fully describe the system. They can be written in state space matrix form:

$$\begin{bmatrix} \dot{\mathbf{x}} \\ \dot{\bar{\mathbf{x}}} \\ \dot{\mathbf{x}}_i \end{bmatrix} = \begin{bmatrix} \mathbf{A}_d - \mathbf{B}_d \mathbf{K}_{dc} & \mathbf{B}_d \mathbf{K}_{dc} & \mathbf{B}_d \mathbf{K}_{di} \\ \bar{\mathbf{0}} & \mathbf{A}_d - \mathbf{L}_d \mathbf{C}_d & \mathbf{0} \\ -\mathbf{C}_d & \bar{\mathbf{0}} & \mathbf{0} \end{bmatrix} \begin{bmatrix} \mathbf{x} \\ \bar{\mathbf{x}} \\ \mathbf{x}_i \end{bmatrix} + \begin{bmatrix} \bar{\mathbf{0}} & \mathbf{G}_d & \bar{\mathbf{0}} \\ \bar{\mathbf{0}} & \mathbf{G}_d & -\mathbf{L}_d \\ 1 & \mathbf{0} & 1 \end{bmatrix} \begin{bmatrix} r_d \\ d_d \\ n_d \end{bmatrix} \quad (5.227)$$

The separation principle applies to the LQG system in (5.227), where the gains \mathbf{K}_{dc} and \mathbf{K}_{di} can be selected similarly to section 5.3.2 by creating an augmented system defined by:

$$\dot{\mathbf{z}}_d = \begin{bmatrix} \mathbf{A}_d & \mathbf{0} \\ -\mathbf{C}_d & \mathbf{0} \end{bmatrix} \mathbf{z}_d + \begin{bmatrix} \mathbf{B}_d \\ \mathbf{0} \end{bmatrix} u_d \quad (5.45)$$

where

$$\mathbf{z}_d = \begin{bmatrix} \mathbf{x}_d \\ \mathbf{x}_{di} \end{bmatrix} \quad (5.46)$$

The cost function state weighting matrix, \mathbf{Q}_d , is $n_z \times n_z$, where n_z is the number of states of \mathbf{z}_d . Once this is chosen, along with R_d , a scalar representing the relative weight of the input in the cost function, LQR methods are used to calculate \mathbf{K}_d , where

$$\mathbf{K}_d = \begin{bmatrix} \mathbf{K}_{dc} \\ \mathbf{K}_{di} \end{bmatrix} \quad (5.228)$$

Since we are assuming that the system in question is an LTI system, the auto-covariances of the estimated states and error pseudo-states are constant. With no time-varying matrices in the Algebraic Riccati Equation, the estimator can then be solved like an LQR problem through the use of a simple variable conversion [76][78]:

$$\mathbf{A}_d \rightarrow \mathbf{A}_d^T \quad (5.229)$$

$$\mathbf{B}_d \rightarrow \mathbf{C}_d^T \quad (5.230)$$

$$\mathbf{Q}_d \rightarrow \mathbf{W}_d \quad (5.231)$$

$$\mathbf{R}_d \rightarrow \mathbf{V}_d \quad (5.232)$$

where \mathbf{W}_d is the $n \times n$ auto-covariance matrix of the process noise (where n is the system order) and \mathbf{V}_d is the output noise auto-covariance. An LQGI simulation of each LTI system is performed using the command specified in Table 7 and initial conditions defined in Table 14. The LQR costs are chosen to reflect a heavy emphasis on integrator error so that the system will aggressively follow the reference signal. The fixed state and output covariances are tuned to allow the estimator to closely follow the noisy plant while still rejecting much of the high frequency component of the noise.

Table 7: Radial EDW vehicle simulation step disturbance

| State | Value | Unit |
|-------------------|-------|----------------|
| δy | 0 | <i>m</i> |
| δv_y | 1 | <i>m/s</i> |
| $\delta \theta_x$ | 0 | <i>radians</i> |
| $\delta \omega_x$ | 1 | <i>rad/s</i> |
| $\delta \theta_z$ | 0 | <i>radians</i> |
| $\delta \omega_z$ | -0.7 | <i>rad/s</i> |
| $\delta \theta_y$ | 0 | <i>radians</i> |
| $\delta \omega_y$ | 0.5 | <i>rad/s</i> |

Table 14: LQGI observer system initial conditions

| Parameter | Value | Unit |
|---------------------|-------|--------------|
| $y(0)$ | 9.29 | <i>mm</i> |
| $v_y(0)$ | 0 | <i>m/s</i> |
| $\hat{y}(0)$ | 8.79 | <i>mm</i> |
| $\hat{v}_y(0)$ | -0.1 | <i>m/s</i> |
| $\theta_x(0)$ | 0 | <i>rad</i> |
| $\omega_x(0)$ | 0 | <i>rad/s</i> |
| $\hat{\theta}_x(0)$ | 0.02 | <i>rad</i> |
| $\hat{\omega}_x(0)$ | -0.01 | <i>rad/s</i> |
| $\theta_z(0)$ | 0 | <i>rad</i> |
| $\omega_z(0)$ | 0 | <i>rad/s</i> |
| $\hat{\theta}_z(0)$ | 0.01 | <i>rad</i> |
| $\hat{\omega}_z(0)$ | -0.07 | <i>rad/s</i> |
| $\theta_y(0)$ | 0 | <i>rad</i> |
| $\omega_y(0)$ | 0 | <i>rad/s</i> |
| $\hat{\theta}_y(0)$ | -0.05 | <i>rad</i> |
| $\hat{\omega}_y(0)$ | 0.05 | <i>rad/s</i> |

In the following simulations, for the height, roll, pitch, and yaw systems, the state cost and noise covariance weights are defined by:

$$\mathbf{Q}_d^a = \begin{bmatrix} 1 & 0 & 0 \\ 0 & 0.1 & 0 \\ 0 & 0 & 10^6 \end{bmatrix} \quad (5.233)$$

$$\mathbf{W}_d = \begin{bmatrix} 10^3 & 0 \\ 0 & 10^7 \end{bmatrix} \quad (5.234)$$

$$V_d = 0.01 \quad (5.235)$$

Note that in (5.233), (5.237) and future definitions of cost weight terms, the superscript “*a*” notation signifies the *augmented* system (including integrator state). The process noise weighting matrix for the height system is:

$$G_y = \begin{bmatrix} 4 \\ 5 \end{bmatrix} \quad (5.236)$$

and the input cost weight for the height system is:

$$R_y^a = 10^{-5} \quad (5.237)$$

The process noise, d_y , is specified to be white Gaussian noise with a magnitude of $d_y = 2 \times 10^{-3}$ and the measurement noise, n_y , is white Gaussian noise with a magnitude of $n_y = 8 \times 10^{-3}$. The simulation results are shown in Fig. 135.

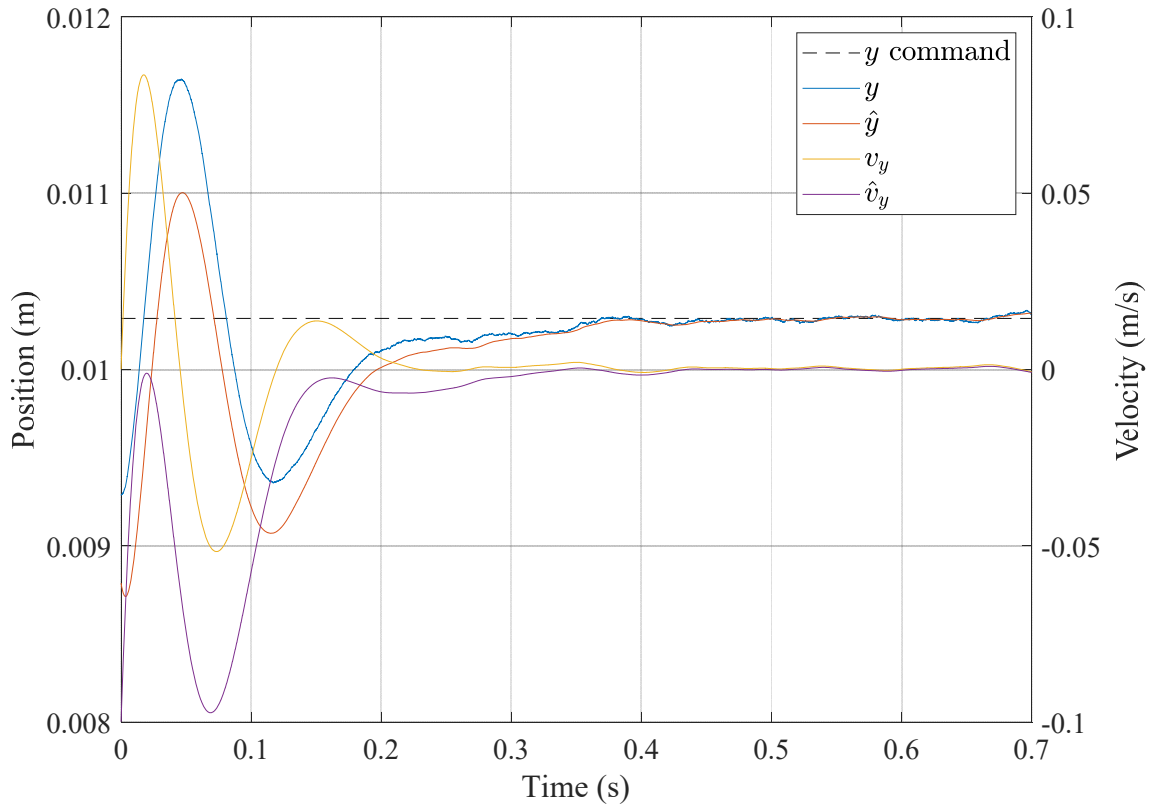


Fig. 135: Height dynamics LQGI simulation for initial conditions $(y, \hat{y}) = (9.29, 8.79)$ mm, $(v_y, \hat{v}_y) = (0, -0.1)$ m/s, and $r_y = 10.29$ mm, (parameters from Table 1, Table 6, Table 7, Table 14)

The simulation shows the height settling by 0.41 seconds, which is approximately when the estimation error, e_y , between the observed state and the actual state becomes very small. The system is able track a reference command and hold its position within ± 0.5 mm even while subjected to noise.

For the roll system, the cost and covariance weights are defined by (5.233) - (5.235).

The process noise weighting matrix is:

$$G_{\angle x} = \begin{bmatrix} 10 \\ 1 \end{bmatrix} \quad (5.238)$$

and the input cost weight is:

$$R_{\theta_x}^a = 0.0001 \quad (5.239)$$

The process noise, $d_{\angle x}$, is specified to be white Gaussian noise with a magnitude of 0.2 and the measurement noise, $n_{\angle x}$, is white Gaussian noise with a magnitude of 2×10^{-4} . Note that the noise magnitudes are chosen arbitrarily to demonstrate the systems' noise rejecting performance. The roll system LQGI simulation is shown in Fig. 136.

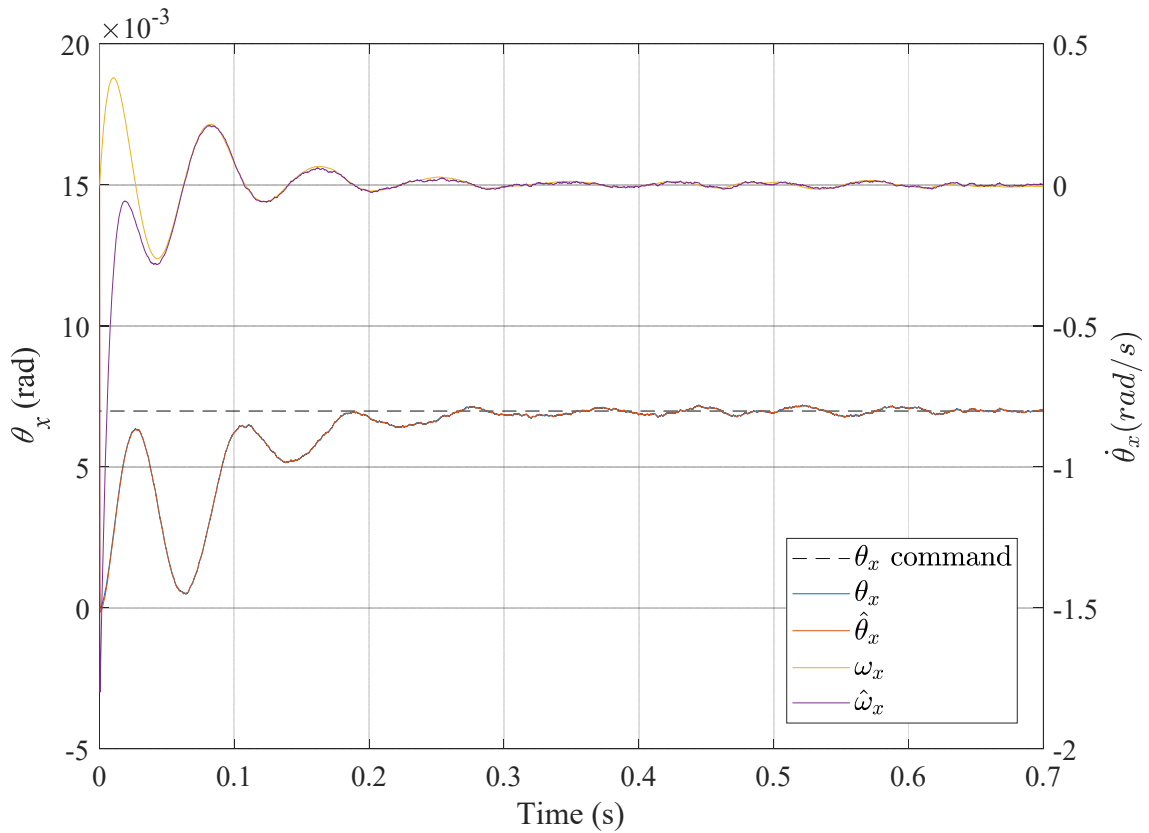


Fig. 136: Roll dynamics LQGI simulation for initial conditions $(\theta_x, \hat{\theta}_x) = (0, 0.02)$ rad, $(\omega_x, \hat{\omega}_x) = (0, -0.1)$ rad/s, and $r_y = 0.00698$ rad, (parameters from Table 1, Table 6, Table 7, Table 14)

The roll system, depending on the random noise, tended to achieve a settling time (within 2% of the reference) of 0.32 seconds. The system recovers from the initial

estimation error such that the estimator error is negligible after 0.06 seconds. The quick system response can be attributed to the small input cost. A slower, smoother response could be achieved by placing heavier costs on the input as well as velocity.

For the pitch system, the cost and covariance weights are defined by (5.233) - (5.235)

. The process noise weighting matrix is:

$$G_{\angle z} = \begin{bmatrix} 10 \\ 1 \end{bmatrix} \quad (5.240)$$

and the input cost weight is:

$$R_{\theta z}^a = 0.0001 \quad (5.241)$$

The process noise, $d_{\angle z}$, is specified to be white Gaussian noise with a magnitude of 0.2 and the measurement noise, $n_{\angle z}$, is white Gaussian noise with a magnitude of 2×10^{-4} .

The pitch system LQGI simulation is shown in Fig. 137.

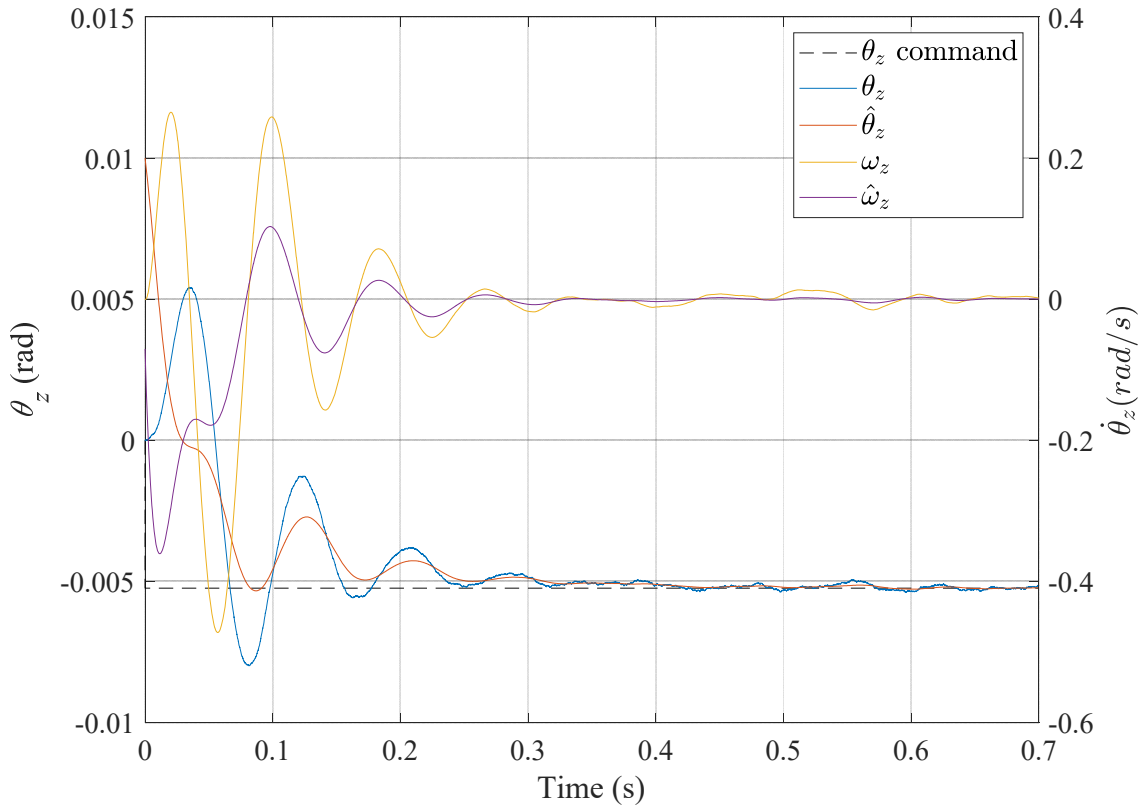


Fig. 137: Pitch dynamics LQGI simulation for initial conditions $(\theta_z, \hat{\theta}_z) = (0, 0.01)$ rad, $(\omega_z, \hat{\omega}_z) = (0, -0.7)$ rad/s, and $r_z = -0.00524$ rad, (parameters from Table 1, Table 6, Table 7, Table 14)

The pitch system, on average, settles in 0.33 seconds. This system recovers from the initial estimation error in roughly 0.06 seconds as well. The noise has a larger effect on velocity than position, and this noise is well tracked by the estimator. As such, the system damps the noise on position and the error caused by the velocity noise quite well, not varying by more than 2% after reaching the reference.

For the yaw system, the cost and covariance weights are defined by (5.233) - (5.235).

The process noise weighting matrix is:

$$G_{\angle y} = \begin{bmatrix} 10 \\ 1 \end{bmatrix} \quad (5.242)$$

and the input cost weight is:

$$R_{\theta_y}^a = 0.0001 \quad (5.243)$$

The process noise, $d_{\angle y}$, is specified to be white Gaussian noise with a magnitude of 0.2 and the measurement noise, $n_{\angle y}$, is white Gaussian noise with a magnitude of 2×10^{-4} .

The yaw system LQGI simulation is shown in Fig. 138.

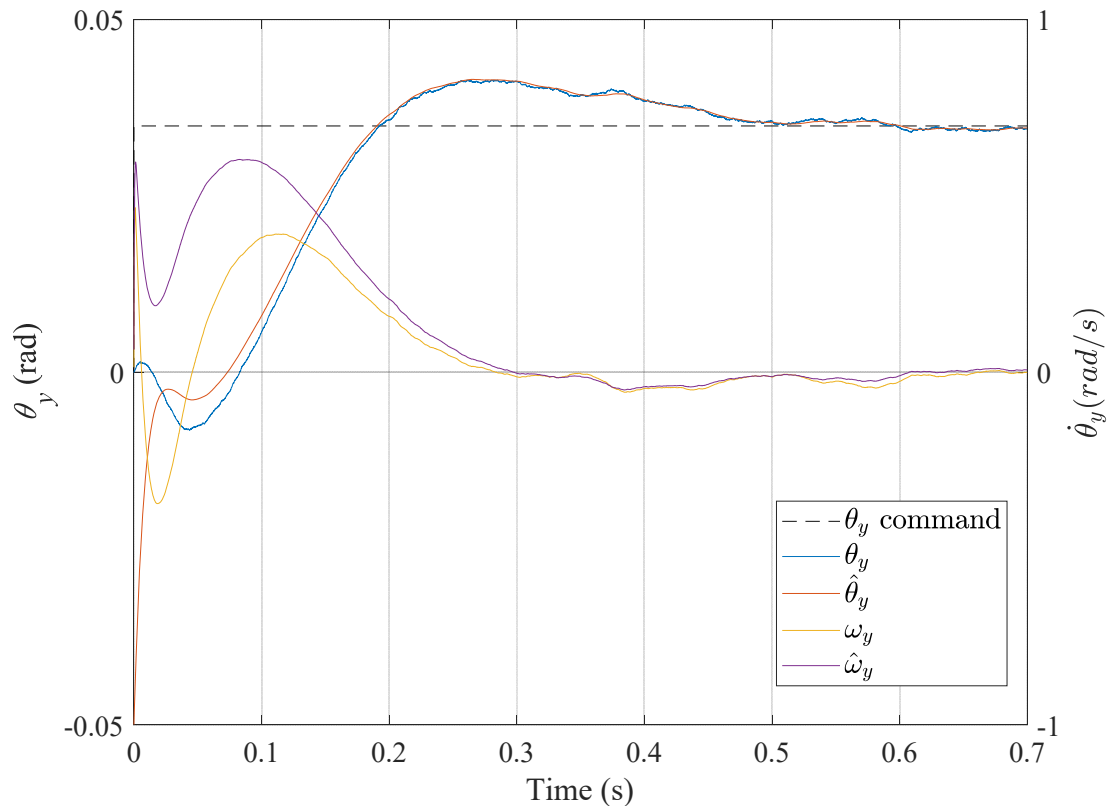


Fig. 138: Yaw dynamics LQGI simulation for initial conditions $(\theta_y, \hat{\theta}_y) = (0, -0.05)$ rad, $(\omega_y, \hat{\omega}_y) = (0, 0.05)$ rad/s, and $r_{\theta_y} = 0.0349$ rad, (parameters from Table 1, Table 6, Table 7, Table 14)

As yaw is not as mission critical as height, roll, and pitch, it is allowed to respond slower, settling in 0.59 seconds. This is a natural byproduct of the additional inertial in this axis, as well as the smaller stiffness magnitude and unstable damping term compared

to roll and pitch. As with the roll and pitch systems, the error between the estimated and plant states becomes negligible after 0.15 seconds, even with noise.

We can also verify the performance of the LQGI system by comparing it to the simpler observer system described in section 0. This comparison for the height system is shown in Fig. 139 and Fig. 140. The simulation parameters, including plant LQR weighting matrices, noise vectors, and reference command are identical to height simulation from Fig. 135. The poles of the observer system's estimator are the same as those from the simulation in section 5.4.3.1, defined by (5.139) and (5.140).

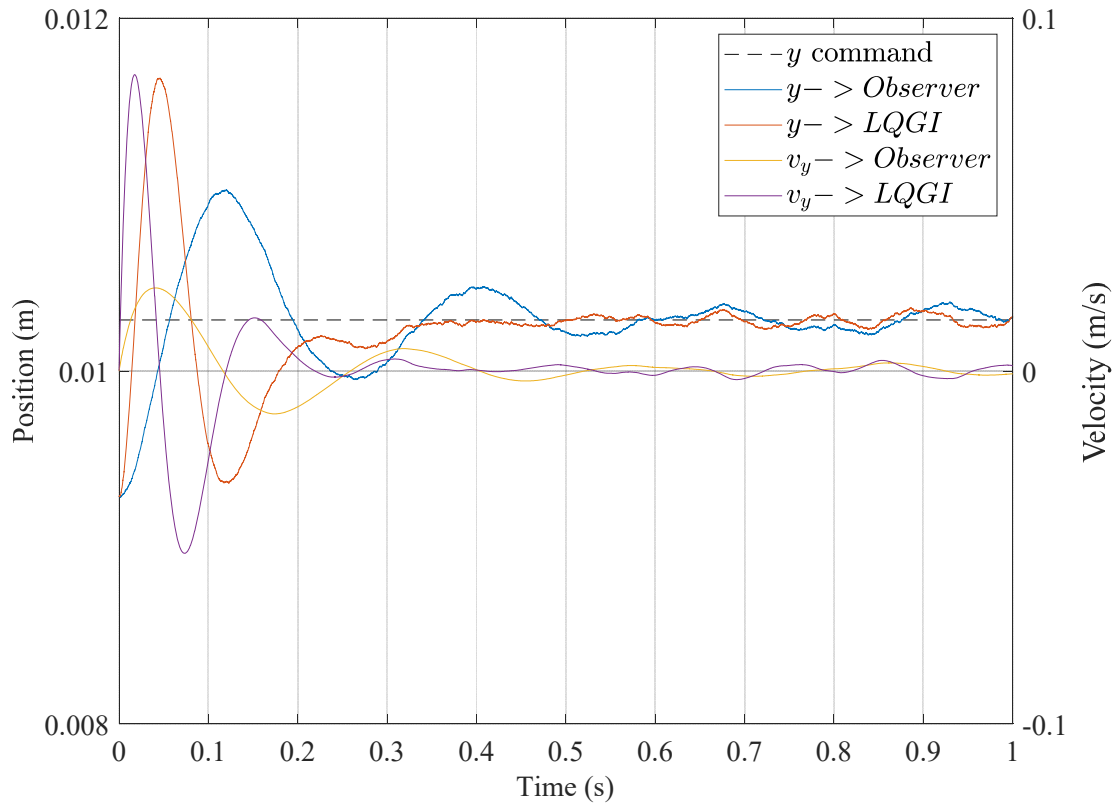


Fig. 139: Comparison of height dynamics using simple Observer control and LQGI (parameters from Table 1, Table 6, Table 7, Table 14)

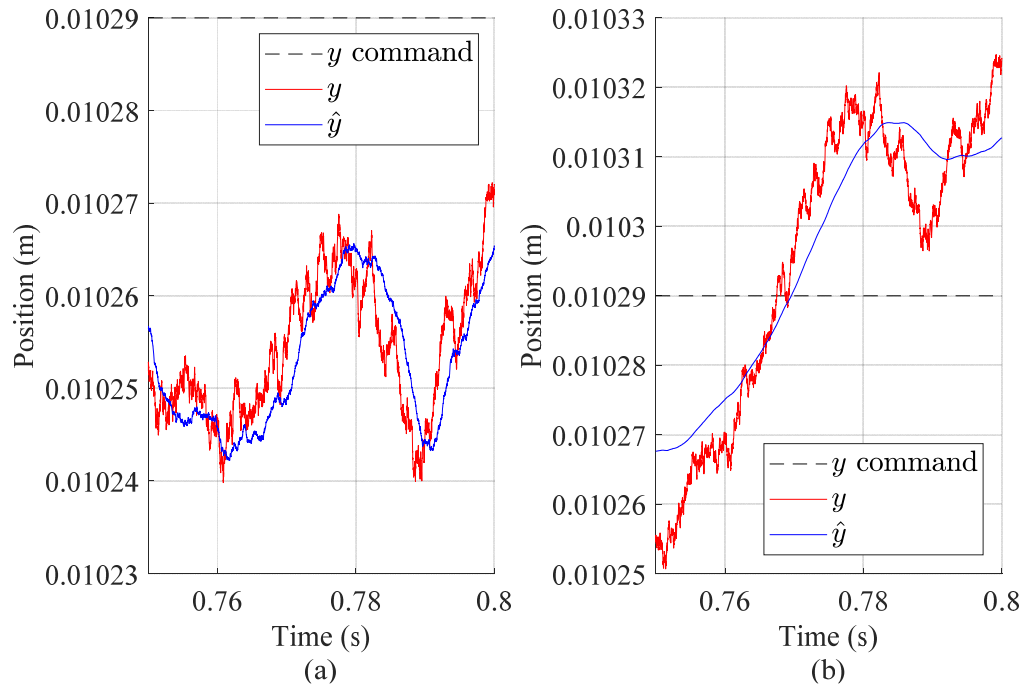


Fig. 140: Zoomed view of Observer vs. LQGI control of height system for (a) Observer, (b) LQGI

We can observe that the LQGI system settles close to the reference command, $r_y = 10.29$ mm, quicker than the simple observer system when it is subjected to noise (0.37 seconds for the LQGI system and 0.59 seconds for the simple observer system). The height state also exhibits less error due to noise than the previous model. Also note that in the zoomed-in plots of height, from Fig. 140, the LQGI system's estimator has been tuned to reject more high frequency noise than the simple observer.

Fig. 141 shows each rotors' rotational velocity during the simulations above. Fig. 142 show the torque and vertical force experienced by each rotor. We can see that a large initial rotational velocity is necessary to accomplish the goal of raising the vehicle by 1mm. To achieve the desired banking, each rotor has a unique steady-state value. It's interesting to

note that while noise is present and is actively damped by the controller, it is difficult to see the noise manifest in the rotor speeds, force, or torque plots.

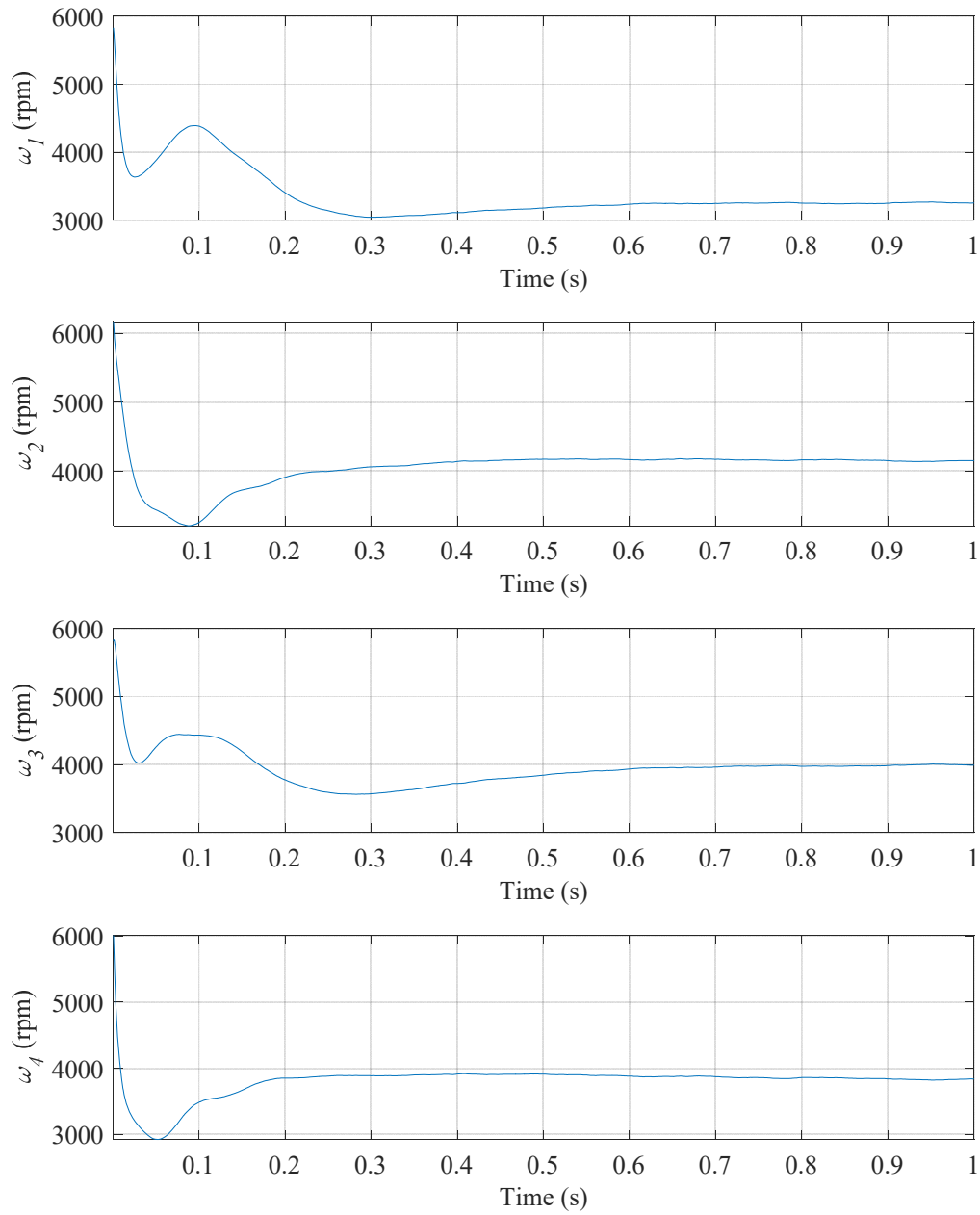


Fig. 141: Individual rotor rotational velocity during simulations from Fig. 135 to Fig. 138

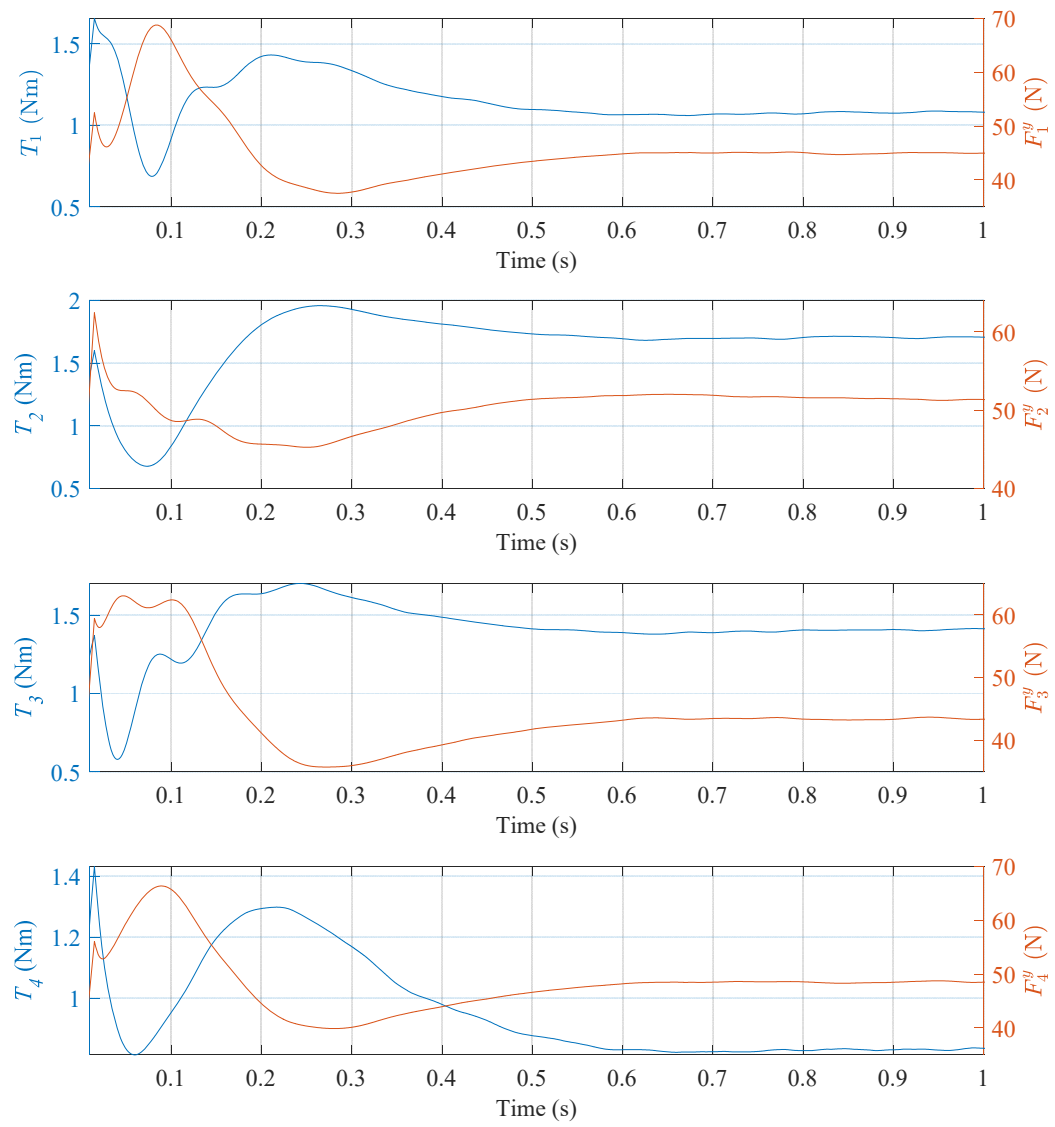


Fig. 142: Individual rotor torque and vertical force during simulations from Fig. 135 to Fig. 138

5.5.2 NONLINEAR QUADRATIC GAUSSIAN INTEGRAL CONTROL

Using the LQGI framework from section 5.5.1, we can create a Nonlinear Quadratic Gaussian Integral NQGI controller to more accurately model and control the system. In essence, the linear equations can be updated to reflect the actual system states as they change with time. The system can be changed from assuming a constant system matrix as in Fig. 134 to a more general representation that allows time-varying system parameters, represented by the general block diagram shown in Fig. 143.

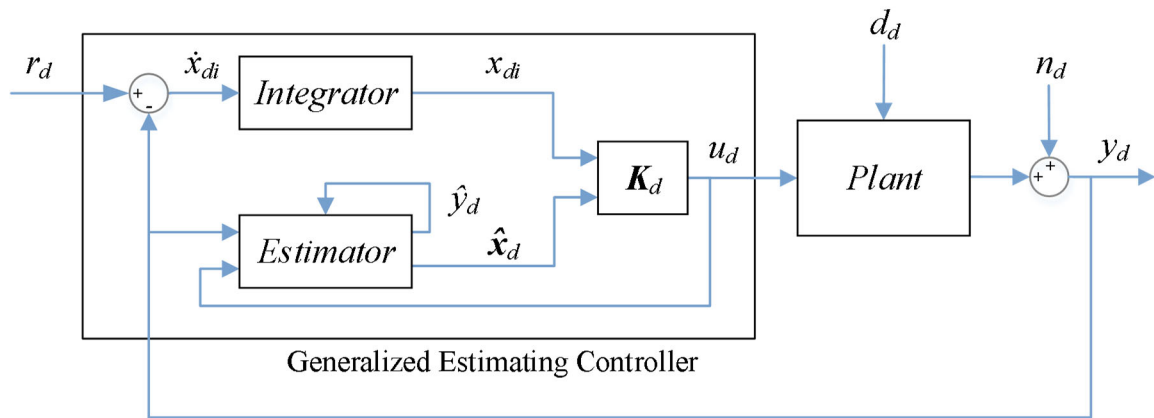


Fig. 143: Generalized nonlinear system model incorporating regulator and Kalman estimator

The nonlinear plant can be written as a general nonlinear function f_d [76]:

$$\dot{\mathbf{x}}_d(t) = f(\mathbf{x}_d(t), u_d(t)) + \mathbf{G}_d \mathbf{d}_d(t) \quad (5.244)$$

Inside the estimator shown in Fig. 135, the predicted state, $\hat{\mathbf{x}}_d$, is calculated using the corrected state, $\hat{\mathbf{x}}_d^c$, such that:

$$\hat{\mathbf{x}}_d^c(t) = \hat{\mathbf{x}}_d(t) + \mathbf{L}_d e_d(t) \quad (5.245)$$

The predicted state is

$$\dot{\hat{\mathbf{x}}}_d(t) = f(\mathbf{x}_d^c(t), u_d(t)) \quad (5.246)$$

Equations (5.244) and (5.246) can be expanded by rewriting the linear equations (5.213), (5.216), and (5.211) as time-variant to form nonlinear plant, estimator, and integrator state equations:

$$\dot{\mathbf{x}}_d(t) = \mathbf{A}_d(t)\mathbf{x}_d(t) + \mathbf{B}_d(t)K_{di}(t)x_{di}(t) - \mathbf{B}_d(t)\mathbf{K}_{dc}(t)\hat{\mathbf{x}}_d(t) + \mathbf{G}_d\mathbf{d}_d(t) \quad (5.247)$$

$$\begin{aligned} \dot{\hat{\mathbf{x}}}_d(t) = & \mathbf{L}_d(t)\mathbf{C}_d\mathbf{x}_d(t) + \mathbf{B}_d(t)K_{di}(t)x_{di}(t) \\ & + (\mathbf{A}_d(t) - \mathbf{B}_d(t)\mathbf{K}_{dc}(t) - \mathbf{L}_d(t)\mathbf{C}_d)\hat{\mathbf{x}}_d(t) + \mathbf{L}_d(t)\mathbf{n}_d(t) \end{aligned} \quad (5.248)$$

$$\dot{x}_{di}(t) = -\mathbf{C}_d\mathbf{x}_d(t) + r_d(t) - n_d(t) \quad (5.249)$$

Note that even though we wish to keep these equations as general as possible, the output equation is not going to change, and the noise distribution across the states will be constant, so both \mathbf{C}_d and \mathbf{G}_d are written as constants. With the decoupling blocks which allow us to represent the EDW vehicle as a set of LTI systems, the \mathbf{B}_d matrix will also be constant, but it is not written this way because it would very commonly change in other systems, or if it is desired to apply these methods to the non-decoupled system.

Modifying (5.212), the input is also re-written as a nonlinear equation:

$$u_d(t) = K_{di}(t)x_{di}(t) - \mathbf{K}_{dc}(t)\hat{\mathbf{x}}_d(t) \quad (5.250)$$

There are two pathways in which this type of system can be simulated numerically: by using the linear systems framework to create a piecewise linear system that is fine grained enough to closely approximate nonlinear behavior (ie. very small time stepping is required), or by directly solving the system's nonlinear differential equations, which can be accomplished by using either an Ordinary Differential Equation (ODE) solver, such as Matlab's ODE45.

For the first method, the set of equations described by (5.247) - (5.250) can be solved identically to LQGI systems described in the previous section by treating the system as an LTI system at each small time step. The A_d , B_d , and C_d matrices are recalculated at each chosen time interval (although for our systems, only A_d will change), and the system is simulated in continuous-time between each interval. The nonlinear system matrix is calculated from

$$A_d(t) = \left. \frac{\partial f_d(\mathbf{x}(t), u(t))}{\partial \mathbf{x}(t)} \right|_{\mathbf{x}(t) \rightarrow \hat{\mathbf{x}}_d^c(t), u(t) \rightarrow u_d(t)} \quad (5.251)$$

This method of simulation can perform well if the time step is kept small, and it provides the advantage of simplicity, since it uses a linear systems framework.

The second method is much more general as it does not use a linear or a state space representation, and requires less approximations and linearizations of the system. Instead, it solves the original differential equations governing the system, which for the 4-DOF EDW vehicle means solving for heave, roll, pitch, and yaw dynamics as a function of the force generated by each rotor:

$$\begin{aligned} \dot{v}_y \cong & [F_1^y(y_1, v_{y1}, \omega_{m1}) + F_2^y(y_2, v_{y2}, \omega_{m2}) \\ & + F_3^y(y_3, v_{y3}, \omega_{m3}) + F_4^y(y_4, v_{y4}, \omega_{m4})] \frac{1}{m} - g \end{aligned} \quad (3.57)$$

$$\begin{aligned} \dot{\omega}_x \cong & [F_3^y(y_2, v_{y2}, \omega_{m2}) + F_4^y(y_3, v_{y3}, \omega_{m3}) \\ & - F_1^y(y_4, v_{y4}, \omega_{m4}) - F_2^y(y_1, v_{y1}, \omega_{m1})] \frac{w}{I_{xx}} \end{aligned} \quad (3.58)$$

$$\begin{aligned}\dot{\omega}_y \cong & [F_2^x(y_3, v_{y3}, \omega_{m3}) - F_4^x(y_1, v_{y1}, \omega_{m1}) \\ & + F_1^x(y_2, v_{y2}, \omega_{m2}) - F_3^x(y_4, v_{y4}, \omega_{m4})] \frac{w}{I_{yy}}\end{aligned}\quad (3.59)$$

$$\begin{aligned}\dot{\omega}_z \cong & [F_2^y(y_2, v_{y2}, \omega_{m2}) + F_3^y(y_3, v_{y3}, \omega_{m3}) \\ & - F_1^y(y_1, v_{y1}, \omega_{m1}) - F_4^y(y_4, v_{y4}, \omega_{m4})] \frac{l}{I_{zz}} \\ & + [F_1^x(y_2, v_{y2}, \omega_{m2}) + F_4^x(y_3, v_{y3}, \omega_{m3}) \\ & + F_2^x(y_4, v_{y4}, \omega_{m4}) + F_3^x(y_1, v_{y1}, \omega_{m1})] \frac{d_s}{I_{zz}}\end{aligned}\quad (3.60)$$

The force components can be solved by the SOVP model, the results of which can be input into an ODE solver. Alternatively, the system can be discretized and programatically looped through the desired number of time steps, with the SOVP model updating the forces on each loop iteration. For the simulations performed in this chapter, this was the chosen method, and a First-Order Hold was used between each time interval. Since the system is not built from the existing linear framework discussed in previous sections, the extra step of building a “dummy” LQGI model is needed each time the controller gains are to be updated. This model is only used to calculate the gains that are subsequently fed into the nonlinear simulation’s controller and is not used for vehicle trajectory.

The updating of controller and estimator gains, however, should not happen at every time step. The result of such a simulation would be trivial, since it is not possible for a computer/controller to recalculate the system this rapidly during run-time. The controller gains K_{dc} and K_{di} in this section are calculated using LQR methods, and the Kalman filter gain, L_d , can be calculated using the auto-covariance of the predicted and corrected state

error. If the initial predicted state auto-covariance is an arbitrary value (ie. The system makes a guess), then each following iteration, the corrected state error auto-covariance, \mathbf{P}_d^c , can be calculated from

$$\mathbf{P}_d^c(t) = [\mathbf{I} - \mathbf{L}_d(t)\mathbf{C}(t)]\mathbf{P}_d^p(t) \quad (5.252)$$

and the auto-covariance of the predicted state, \mathbf{P}_d^p , is calculated by solving the differential equation (this can also be solved using the same ODE numerical solver):

$$\dot{\mathbf{P}}_p(t) = \mathbf{A}_d(t)\mathbf{P}_d^c(t)\mathbf{A}_d^T(t) + \mathbf{G}_d\mathbf{W}_d\mathbf{G}_d^T \quad (5.253)$$

The Kalman gain at time t is

$$\mathbf{L}_d(t) = \mathbf{P}_d^p(t)\mathbf{C}_d^T(t) \left[\mathbf{C}_d(t)\mathbf{P}_d^p(t)\mathbf{C}_d^T(t) + \mathbf{V}_d \right]^{-1} \quad (5.254)$$

While it would be ideal to recalculate the gains at every instant in time, practically, this is not possible. The SOVP calculation of damping and stiffness requires processor time. Using the equations from Chapter 2.2, a Dell T5500 computer with an Intel Xeon E5620 running at 2.40GHz can calculate the damping and stiffness terms required for the 2nd order LTI systems in an average of 0.47 seconds. Note that while this time could be reduced by sacrificing some accuracy for speed by calculating the damping and stiffness using only the dominant harmonics, and by using a computer with greater arithmetic performance, this number is a good baseline for simulating system performance.

To more realistically simulate an actual system, the controller's updating of the \mathbf{A}_d matrix and subsequent gains is only performed at reasonable time intervals that would be possible for a computer to achieve. Note that the plant can still be recalculated at each small time step for accuracy, but we will assume that the estimator and therefore controller

will only get this information at much more infrequent intervals. The pace at which the new information becomes available to the controller is based on the probability distribution histogram shown in Fig. 144, which was created by recording each SOVP calculation time for 5000 iterations on the E5620 machine.

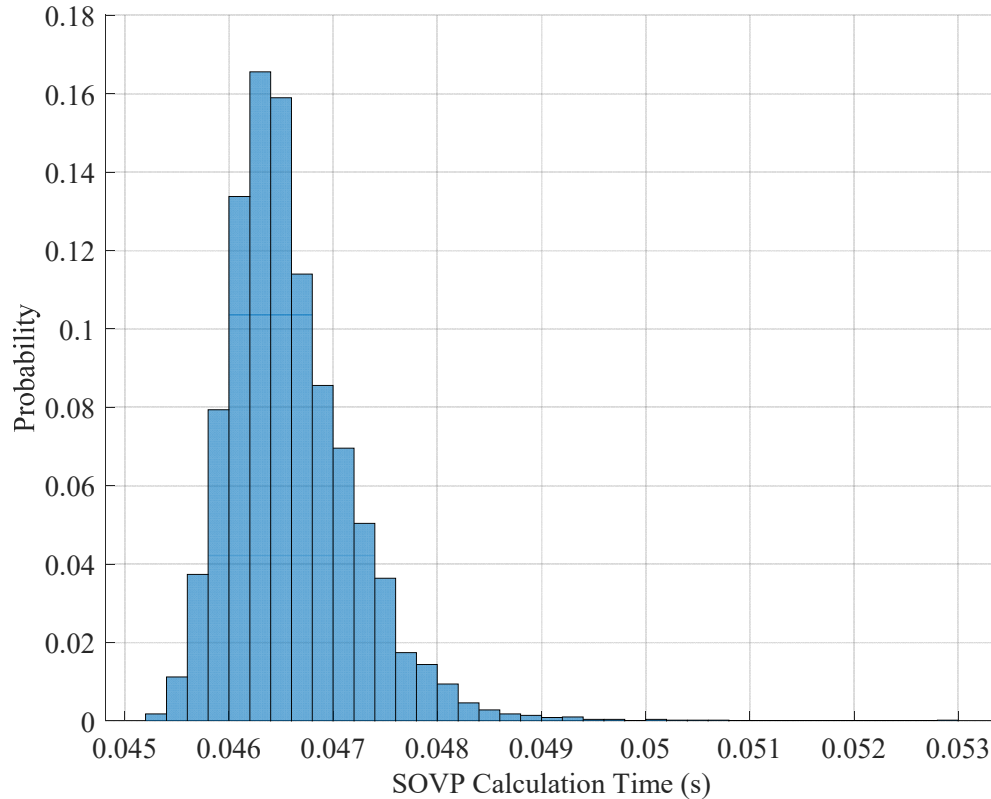


Fig. 144: Probability distribution of time require to calculate SOVP damping and stiffness terms for 2nd order LTI systems (rotor parameters from Table 1) using Intel E5620 running at 2.4GHz

The simulated system's parameters are described in Table 15. The system is assumed to start from rest (velocities are all zero). The simulation starts from a lower height and uses larger reference commands compared to previous sections to show that this control methodology is well suited to transient control. That is, when the operating point significantly changes, such as when banking heavily for a turn, accelerating towards a

cruising speed, or lifting off the track from a standstill, the NQGI model will provide better performance.

Table 15: Nonlinear radial EDW vehicle simulation parameters

| Parameter | Value | Unit |
|--|-------------------|-------------|
| Initial height, y_0 | 0.00529 (5.29) | m (mm) |
| Initial roll angle, θ_{x0} | 0 | rad |
| Initial pitch angle, θ_{z0} | 0 | rad |
| Initial yaw angle, θ_{y0} | 0 | rad |
| Initial height estimate, \hat{y}_0 | 0.00479 | m |
| Initial heave estimate, \hat{v}_0 | -0.1 | m/s |
| Initial roll estimate, $\hat{\theta}_x$ | 0.02 | rad |
| Initial roll velocity estimate, $\hat{\omega}_x$ | -0.01 | rad/s |
| Initial roll estimate, $\hat{\theta}_z$ | 0.01 | rad |
| Initial roll velocity estimate, $\hat{\omega}_z$ | -0.07 | rad/s |
| Initial roll estimate, $\hat{\theta}_y$ | -0.05 | rad |
| Initial roll velocity estimate, $\hat{\omega}_y$ | 0.05 | rad/s |
| Initial k_{yv} | -11645.68 | N/m |
| Initial d_{yv} | -10.81517 | $N/m/s$ |
| Initial k_{xx} | -3711.923 | N/m |
| Initial d_{xx} | 3.043214 | $N/m/s$ |
| Initial K_{yc} | [3647.5 85.556] | |
| Initial K_{yi} | -10000 | |
| Initial L_y | [105.39 553.12] | |
| Initial $K_{\theta xc}$ | [761.12 45.226] | |
| Initial $K_{\theta xi}$ | -10000 | |
| Initial $L_{\theta x}$ | [10093.75 941931] | |
| Initial $K_{\theta zc}$ | [816.06 46.566] | |
| Initial $K_{\theta zi}$ | -10000 | |
| Initial $L_{\theta z}$ | [385.68 24374.3] | |
| Initial $K_{\theta yc}$ | [209.78 51.260] | |
| Initial $K_{\theta yi}$ | -10000 | |
| Initial $L_{\theta y}$ | [381.32 22701.6] | |
| Height command, r_y | 0.01129 (11.29) | m (mm) |
| Roll angle command, $r_{\theta x}$ | 0.087267 (5) | rad (deg) |
| Pitch angle command, $r_{\theta z}$ | -0.069813 (-4) | rad (deg) |
| Yaw angle command, $r_{\theta y}$ | 0.12217 (7) | rad (deg) |

The autocovariance values used to calculate estimator gains for the simulation are tuned to achieve a smooth motion on the estimator position states which converge to the plant's states in less than 0.1 seconds:

$$\mathbf{W}_y = \mathbf{W}_{\angle x} = \mathbf{W}_{\angle z} = \mathbf{W}_{\angle y} = \begin{bmatrix} 30 & 0 \\ 0 & 10^7 \end{bmatrix} \quad (5.255)$$

$$V_y = V_{\angle x} = V_{\angle z} = V_{\angle y} = 0.01 \quad (5.256)$$

The LQR cost weights are tuned to avoid large velocities and inputs compared to previous simulations, since the reference commands are large and we wish the system to have smooth transient performance. The cost weights are defined as follows:

$$\mathbf{Q}_y^a = \mathbf{Q}_{\angle x}^a = \mathbf{Q}_{\angle z}^a = \mathbf{Q}_{\angle y}^a = \begin{bmatrix} 1 & 0 & 0 \\ 0 & 10 & 0 \\ 0 & 0 & 5 \times 10^5 \end{bmatrix} \quad (5.257)$$

$$R_y^a = R_{\angle x}^a = R_{\angle z}^a = R_{\angle y}^a = 0.001 \quad (5.258)$$

For comparison, an LQGI controller applied to a nonlinear system is modeled alongside the nonlinear system with a nonlinear controller. The LQGI-controlled model still uses an differential equation solver to simulate a real time-varying plant, but the controller will not receive any communication/updates from the plant. The controller for the LQGI system therefore is linear (the gains remain unchanged from $t = 0$). Since section 5.5.1 proved that a Kalman filter observer effectively controls the system subject to noise, we will omit noise from this simulation, knowing that this similar approach is also able to control a noisy system. This allows the performance of the NQGI and LQGI controller to be compared without introducing random variables.

The height system NQGI vs. LQGI system is shown in Fig. 145, and the variation in system gains, which will be shown as a percentage difference between the nonlinear and linear model, is shown in Fig. 146.

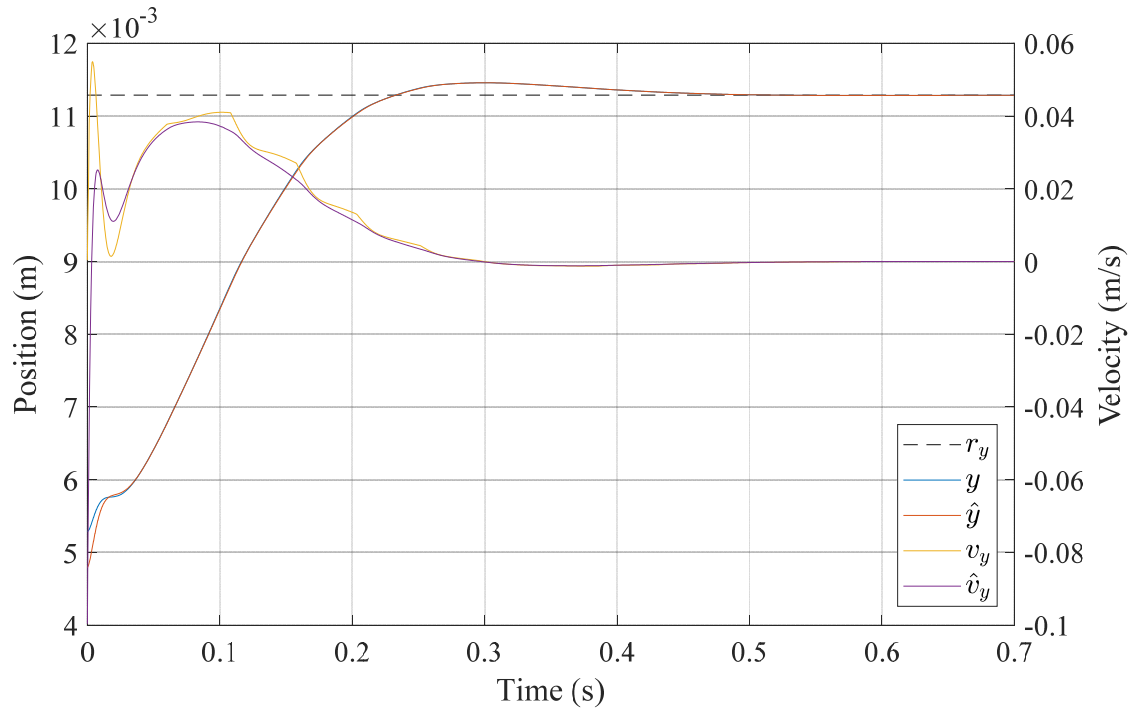


Fig. 145: NQGI vs. LQGI height dynamic system simulation (parameters from Table 1, and Table 15)

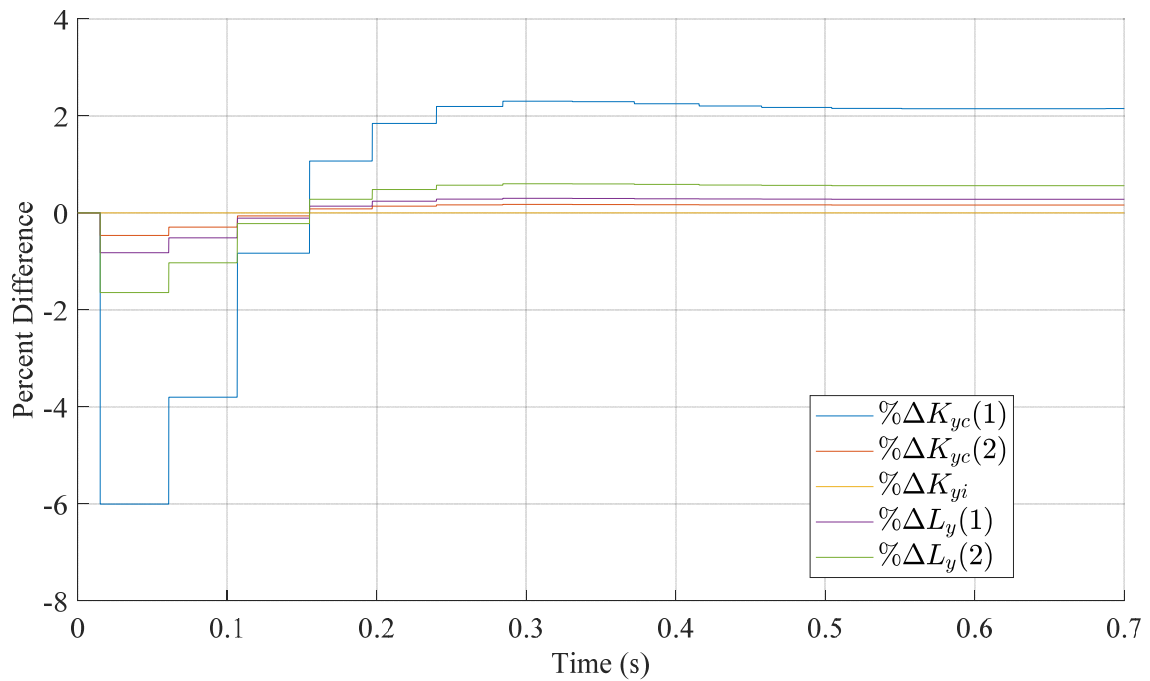


Fig. 146: NQGI gain variation for height dynamic system (parameters from Table 1, and Table 15)

The nonlinear controller settles to the reference command in 0.45 seconds. Despite the initial observer error, the height estimate converges in less than 0.04 seconds. The heave estimate roughly follows the plant, but exhibits some oscillatory motion when heave is transient. Observing at the gain variation plot in Fig. 146, the oscillatory motion has the same period as the gain steps, showing that the oscillation is due to gain steps.

Changes to the gains can be seen as the system transitions from one operating point to another, approximately following the shape of the system's height plot. The change in gains is not extremely large; the peak magnitude change of any gain is 6%. Nonetheless, the NQGI controller implements these updated gains for increased accuracy. Note that as the height approaches the reference command, the gain settles to a steady-state value. Hypothetically the system could revert to linear control (LQGI) once near steady-state is achieved (switching back to NQGI if the system leaves strays sufficiently from the operating point).

The roll system NQGI vs. LQGI system is shown in Fig. 147, and the variation in the system gains is shown in Fig. 148.

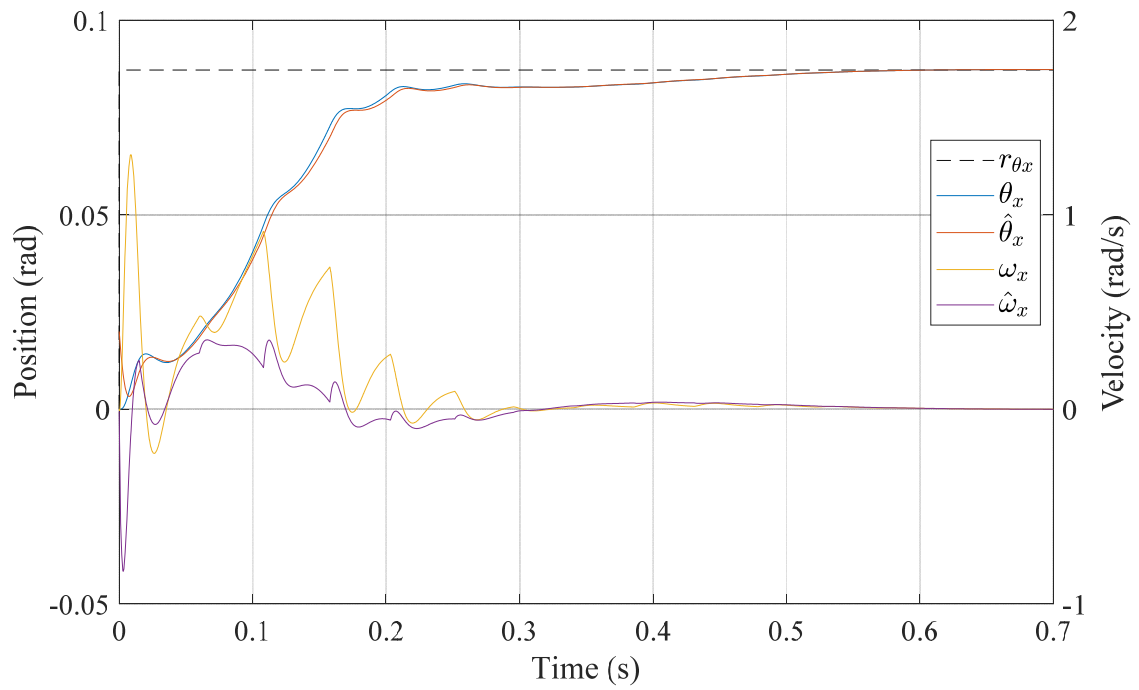


Fig. 147: NQGI vs. LQGI roll dynamic system simulation (parameters from Table 1, and Table 15)

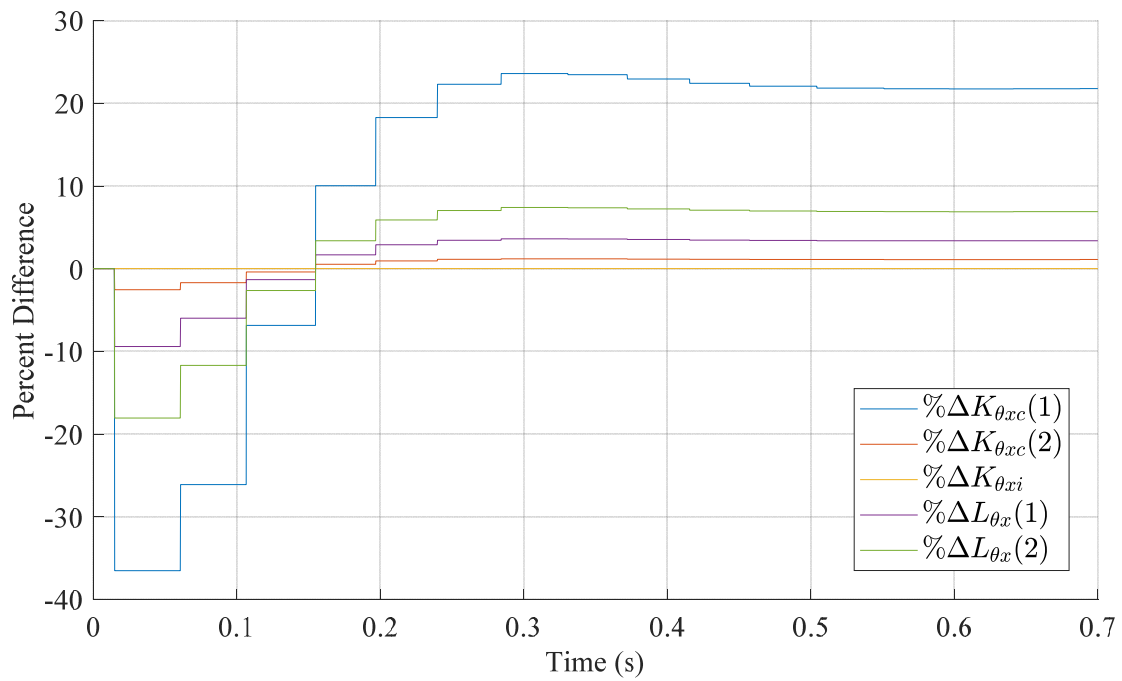


Fig. 148: NQGI gain variation for roll dynamic system (parameters from Table 1, and Table 15)

The nonlinear controller settles the roll angle in 0.52 seconds with no overshoot. The roll estimate quickly converges in less than 0.04 seconds, but lags behind the plant slightly during transition. Roll velocity exhibits some oscillatory motion due to the stepped change in the controller gains, and the velocity variations are large enough to cause small (sub 1mm) oscillations in height until steady-state is achieved.

The gain variation plots highlight the importance of periodically updating the controller with new SOVP damping and stiffness terms and recalculating the gains. The roll gain variations are significant at the start of the simulation when the system is undergoing large motions, again roughly following the shape of the height signal from Fig. 145 and also the shape of the height gain variations from Fig. 146. This is due to the stiffness and damping terms being very sensitive to height variation. Since the system undergoes a large change in height, all of the LQR gains will display the effect of this dominant parameter.

The pitch system NQGI vs. LQGI system is shown in Fig. 149, and the variation in the system gains is shown in Fig. 150.

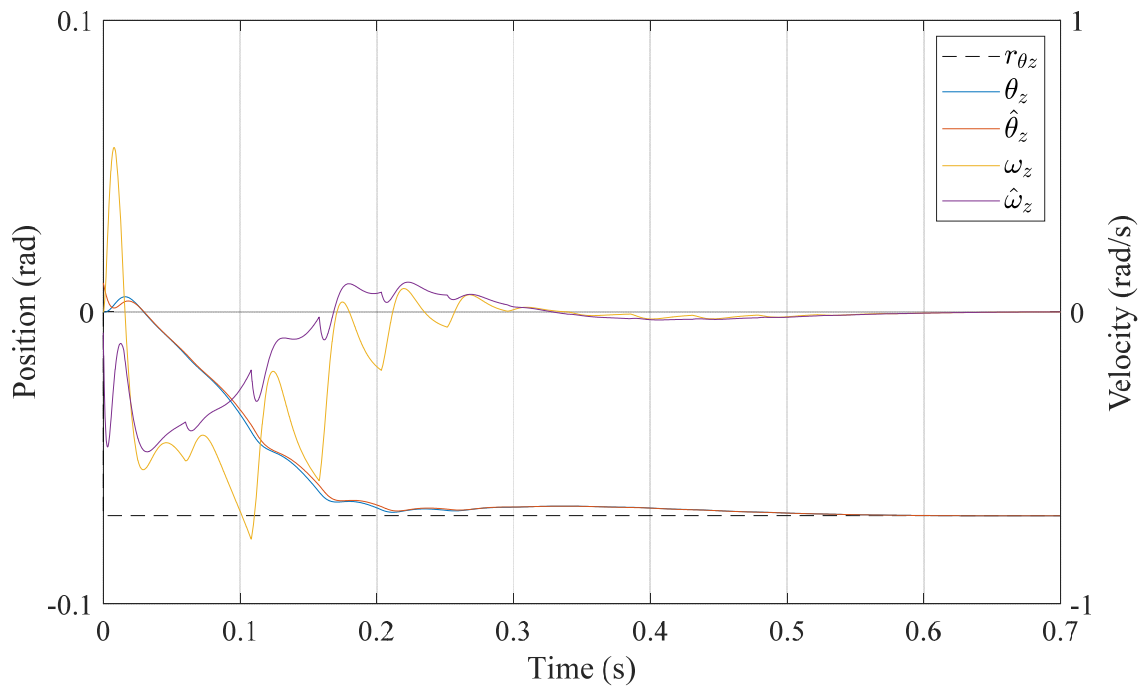


Fig. 149: NQGI vs. LQGI pitch dynamic system simulation (parameters from Table 1, and Table 15)

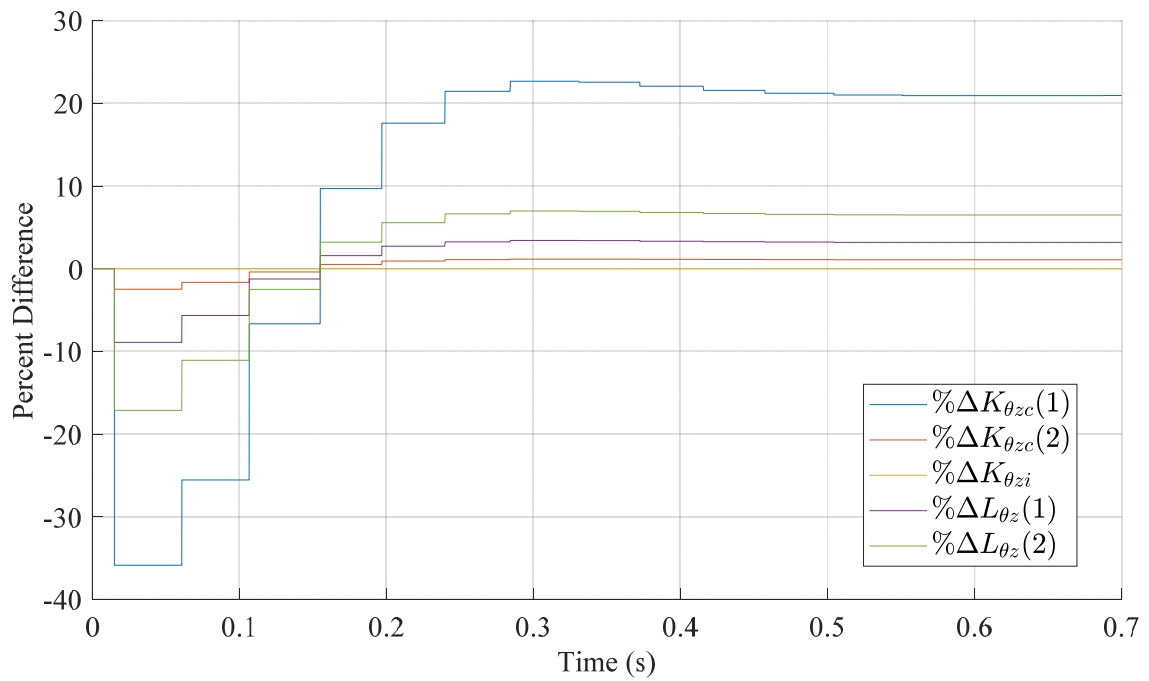


Fig. 150: NQGI gain variation for pitch dynamic system (parameters from Table 1, and Table 15)

Although it settles slightly faster at 0.47 seconds, the pitch NQGI system has very similar performance characteristics to the roll system, exhibiting an oscillatory behavior due to the gain steps. With the chosen cost function and autocovariances, the estimated angle velocity of these systems is not accurate during transition, although the controller is robust enough to stabilize the system anyway.

The gain variations shown in Fig. 150, similarly to the height and roll systems, display changes as the system transitions to a new operating point, and the shape of these changes roughly follows the height signal.

The yaw system NQGI vs. LQGI system is shown in Fig. 151, and the variation in the system gains is shown in Fig. 152.

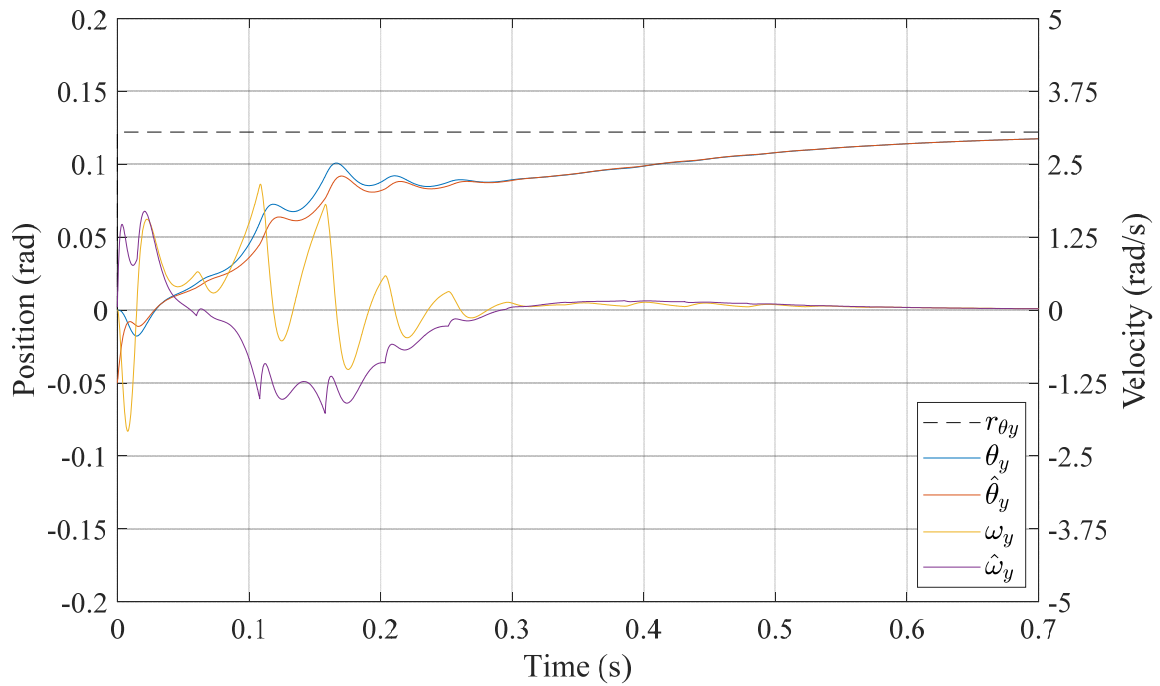


Fig. 151: NQGI vs. LQGI yaw dynamic system simulation (parameters from Table 1, and Table 15)

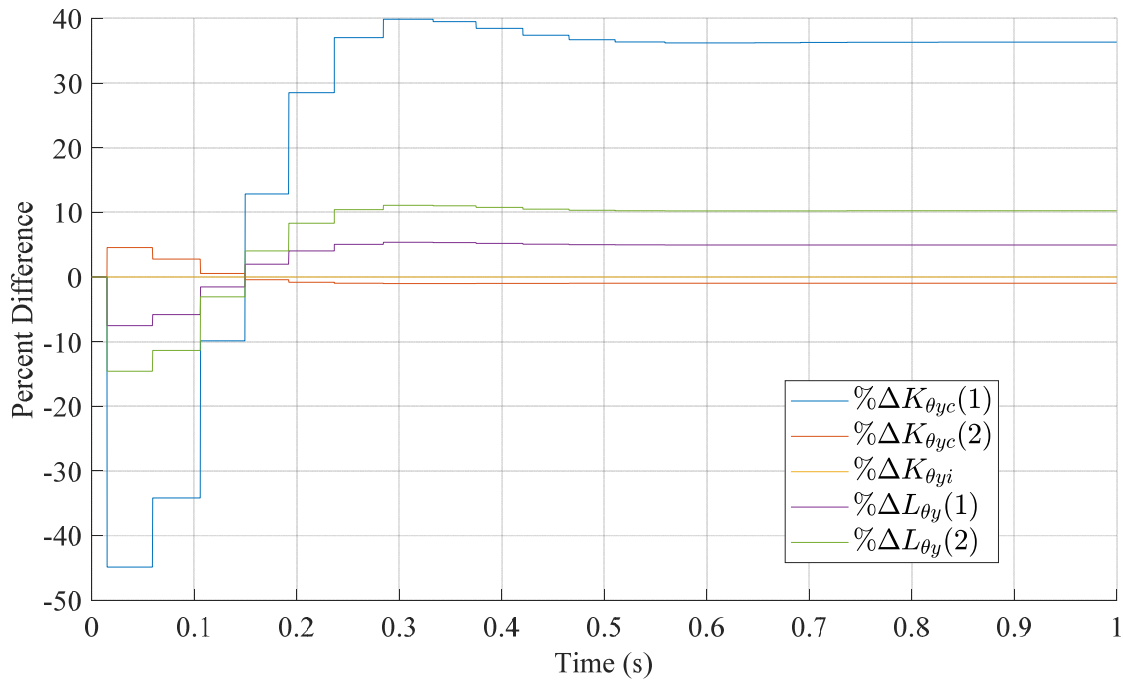


Fig. 152: NQGI gain variation for yaw dynamic system (parameters from Table 1, and Table 15)

The yaw position has a settling time of 0.84 seconds for using this nonlinear controller. During transition, the large step changes in gains drives large oscillations in yaw velocity and consequently in yaw position. The positional variations are significant enough to cause the estimator to have an error of up to 21%.

The gain variation plot shown in Fig. 152, despite having dynamics defined by different stiffness and damping terms than the height, roll, and pitch LTI systems, shows a familiar shape (to that of the height signal) and large variations while the system is transient.

Note that in the simulations above, the LQGI controller is robust enough to stabilize the system despite the large command, so linear control would also be appropriate for

rejecting small disturbances and noise if they move the system only slightly from its operating point. In addition, as suggested previously, for real-time control of a real system, any axis of motion that is currently relatively unvarying can have its control method switched to LQGI (disallow updates to SOVP model and gains) so that more processor time could be devoted to axes that are in flux, allowing them to update more quickly.

The individual rotor speeds and forces can also be plotted for the simulations shown in Fig. 145 - Fig. 152. The rotors' rotational velocities are shown in Fig. 153 and the torque and vertical forces are shown in Fig. 154. The rotor speeds change significantly throughout the simulation due to the more accurate model which factors in changes in the system plant as the vehicle moves. Rotor speeds, torque, and forces undergo higher frequency changes whenever the controller updates its SOVP values.

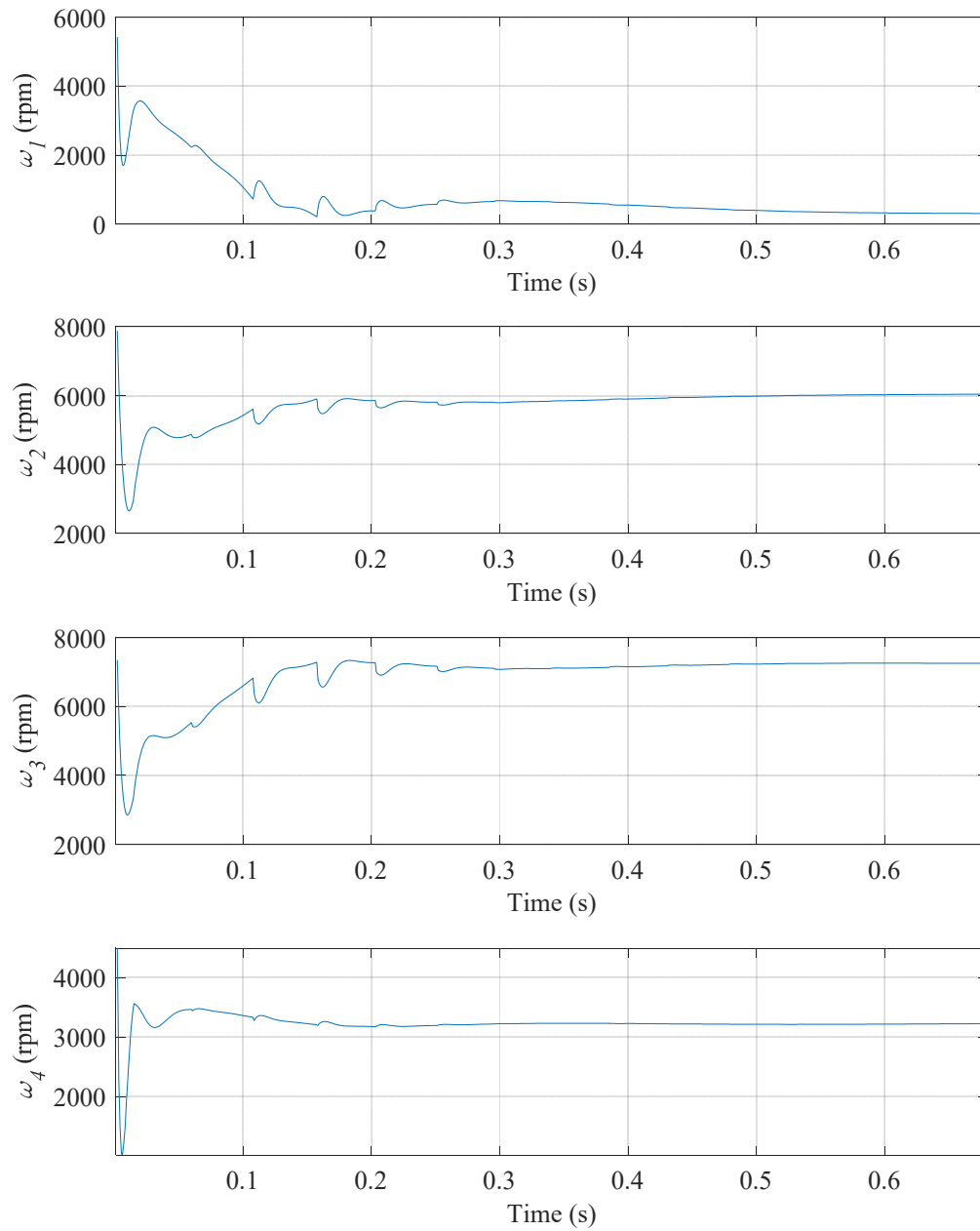


Fig. 153: Individual rotor rotational velocities for simulations from Fig. 145 - Fig. 152

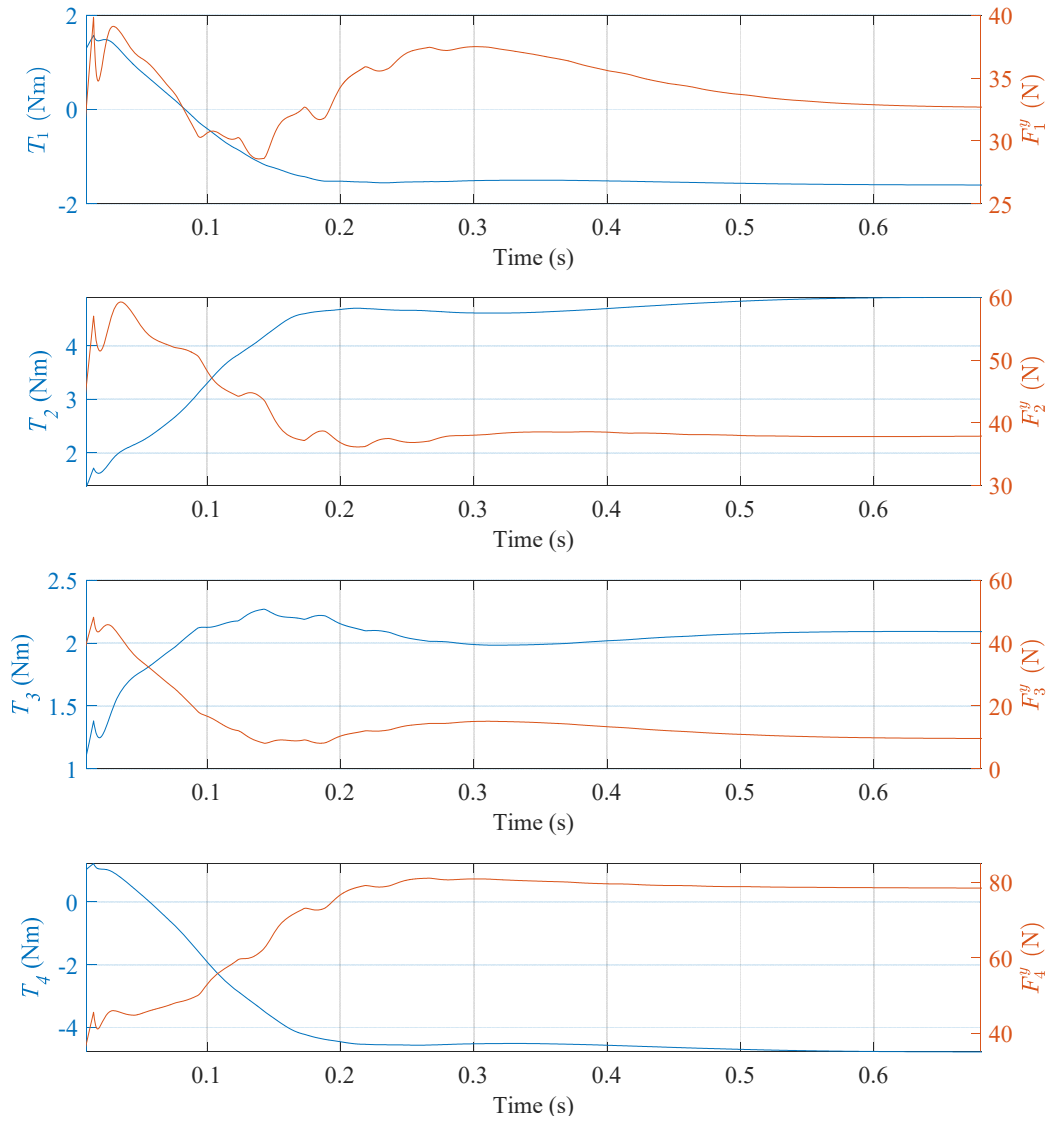


Fig. 154: Individual rotor torque and vertical force for simulations from Fig. 145 - Fig. 152

To further prove the value of a NQGI over a linear controller during transition, another simulation is performed, again using the parameters from Table 15, but this time using a different set of cost function weighting terms:

$$\mathbf{Q}_y^a = \begin{bmatrix} 0.1 & 0 & 0 \\ 0 & 70 & 0 \\ 0 & 0 & 1.1 \times 10^4 \end{bmatrix} \quad (5.259)$$

$$R_y^a = 0.001 \quad (5.260)$$

$$\mathbf{W}_y = \begin{bmatrix} 10 & 0 \\ 0 & 10^3 \end{bmatrix} \quad (5.261)$$

$$V_y = 0.01 \quad (5.262)$$

The cost terms are chosen to enforce additional cost on heave. Since this is simply an illustrative example concerning mainly the stability of the nonlinear vs. linear system, only the height system is be plotted. Comparison of heights for a NQGI and LQGI system are shown in Fig. 155 and the gain variations are shown in Fig. 156.

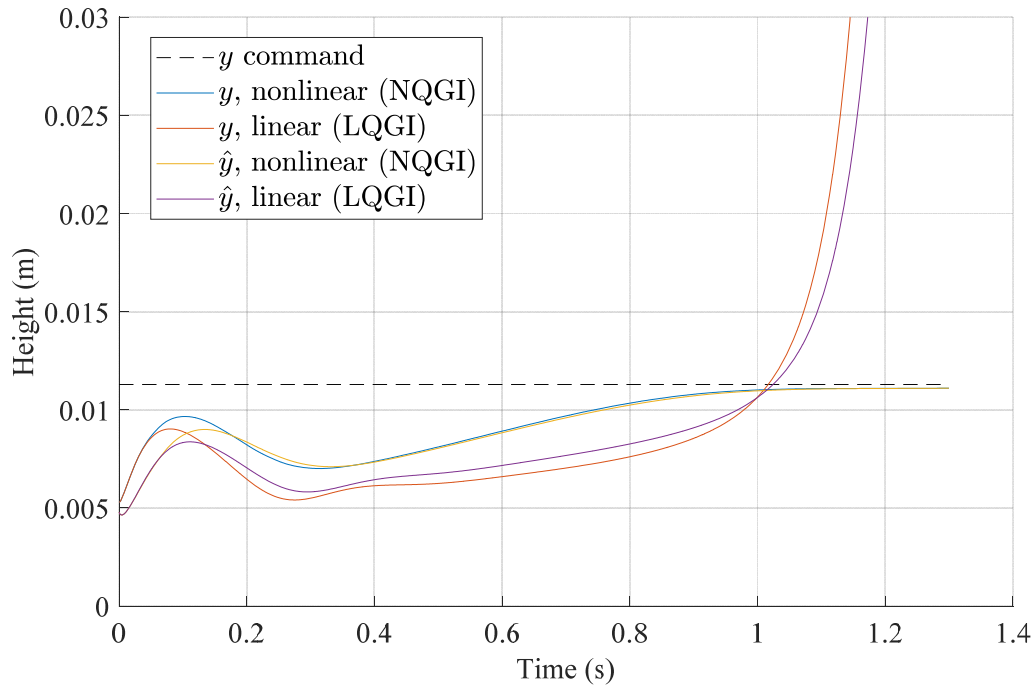


Fig. 155: Simulation comparing height system stability for NQGI and LQGI system (parameters from Table 1, and Table 15, using cost weights from (5.259) - (5.262))

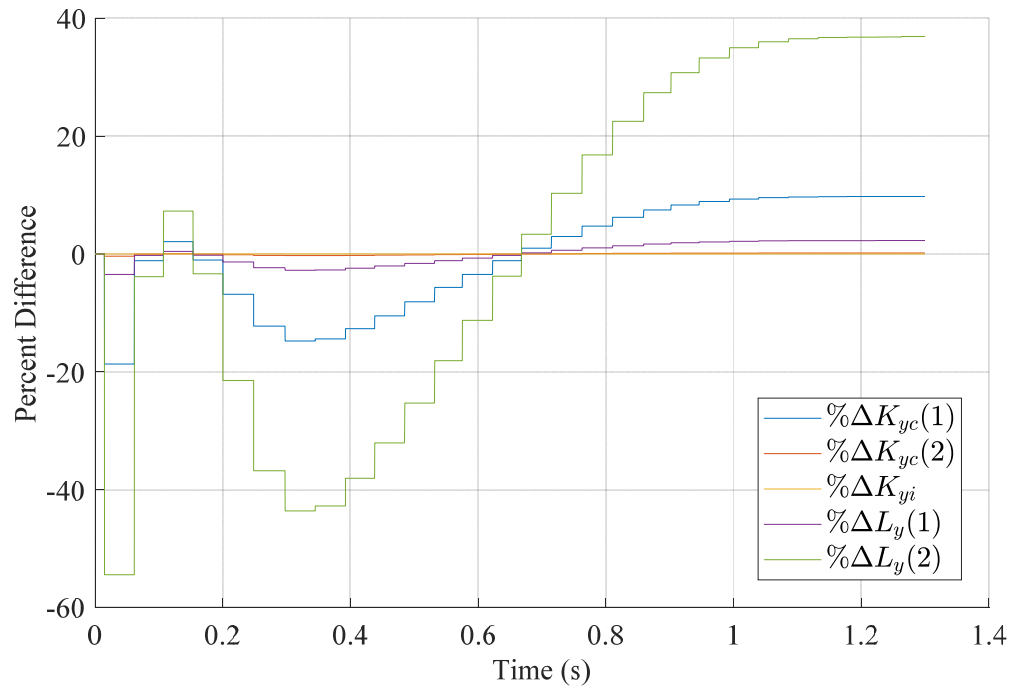


Fig. 156: Gain variation between stable NQGI and unstable LQGI height systems (parameters from Table 1, and Table 15, using cost weights from (5.259) - (5.262))

With more aggressive velocity cost, the LQGI system fails to stabilize the system. This is due to the time-varying plant undergoing enough change that the estimator is no longer able to predict the states. By contrast, the NQGI controller is able to stabilize the system because the estimator is updated with new plant parameters. The difference in gains further highlights the difference between the linear and nonlinear controller. It is the difference in these gains which is ultimately the difference between stability and instability.

5.6 CONCLUSION

In this chapter, using the LTI systems developed in Chapter CHAPTER 4:, a series of controllers of increasing complexity are presented. As the controller strategies become more complex, they offer increased robustness and the possibility of increased performance. Starting from a simple Linear Quadratic Regulator, an integrator was added to provide steady-state tracking. Realizing that direct measurement of all states may not be possible, the system was then augmented with an estimator which provides approximate state information. The estimator was then converted to a Kalman filter which excels at rejecting noise while providing an estimate of the plant. For an EDW system, the plant undergoes significant changes during run-time when changing operating points, such as accelerating to a different speed, lifting off the track, or banking\yawing for a turn. Since linear modeling is not appropriate for a system whose plant is time-varying, a Nonlinear Quadratic Gaussian Integral controller is created with a realistic updating schedule. Although the system is simulated in continuous time, the estimator and controller are updated discrete intervals based on how long it takes to calculate a new plant estimate. The NQGI controller is robust, even during transient periods, and is easily configurable to switch to linear control when the plant stays relatively constant.

CHAPTER 6: AXIAL ELECTRODYNAMIC WHEEL

This chapter explores the design and performance analysis of an axial EDW. The new rotor type is introduced in section 6.1, then, in 6.2, an axial rotor is simulated using FEA. Section 6.3 validates the source field model against previous researchers' models following a modification to the equations, while section 6.4 validates the field against FEA simulations. With the analytic field, section 6.5 applies the SOVP force model to the axial rotor, and section 6.6 compares the analytic and FEA models to an experimental prototype.

6.1 INTRODUCTION

An alternative to the radial EDW is the axial EDW, which orients a Halbach array radially in a disk, as shown in Fig. 157. The axial EDW is formed by rotating this rotor above a conductive track as shown in Fig. 158. This has the potential advantage of increased magnet mass usage, as more of the magnetic material is placed over the track in any given instant. However, the rotation of the axial EDW with a constant airgap will not create any thrust force. This chapter compares the SOVP model, FEA models, and an experimental prototype to both study the performance capabilities of the axial EDW, and to attempts to arrive at a computationally efficient analytical solution for the forces and torque generated from an axial EDW.

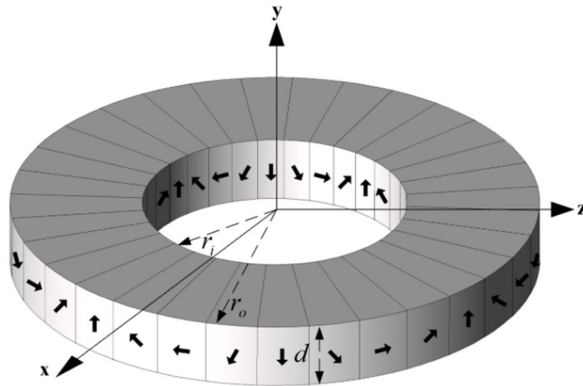


Fig. 157: An axial Halbach rotor, where r_i is the inner radius, r_o is the outer radius, d is the rotor thickness [71]

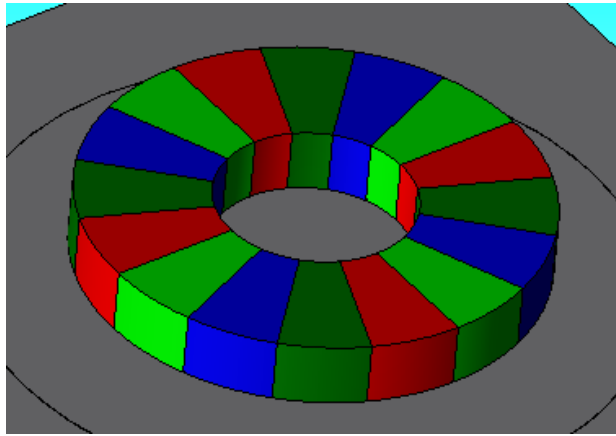


Fig. 158: Axial EDW FEA model (4 pole, 4 segment-per-pole)

6.2 FINITE ELEMENT ANALYSIS MODEL

In order to analyze the effectiveness and viability of this axial EDW, the field between the rotor and track surface must first be known. A finite element model was created using JMAG, as shown in Fig. 158. The simulations in this chapter are based on a prototype rotor with parameters defined in Table 16, and the coordinate axes are defined in Fig. 159.

Table 16: Standard axial Halbach rotor field simulation parameters

| Parameter | Value |
|----------------------|-------|
| r_o | 70 mm |
| r_i | 30 mm |
| r_c | 48 mm |
| rotor thickness, d | 20 mm |
| airgap, y | 10 mm |
| pole pairs, P | 4 |
| μ_r | 1.05 |

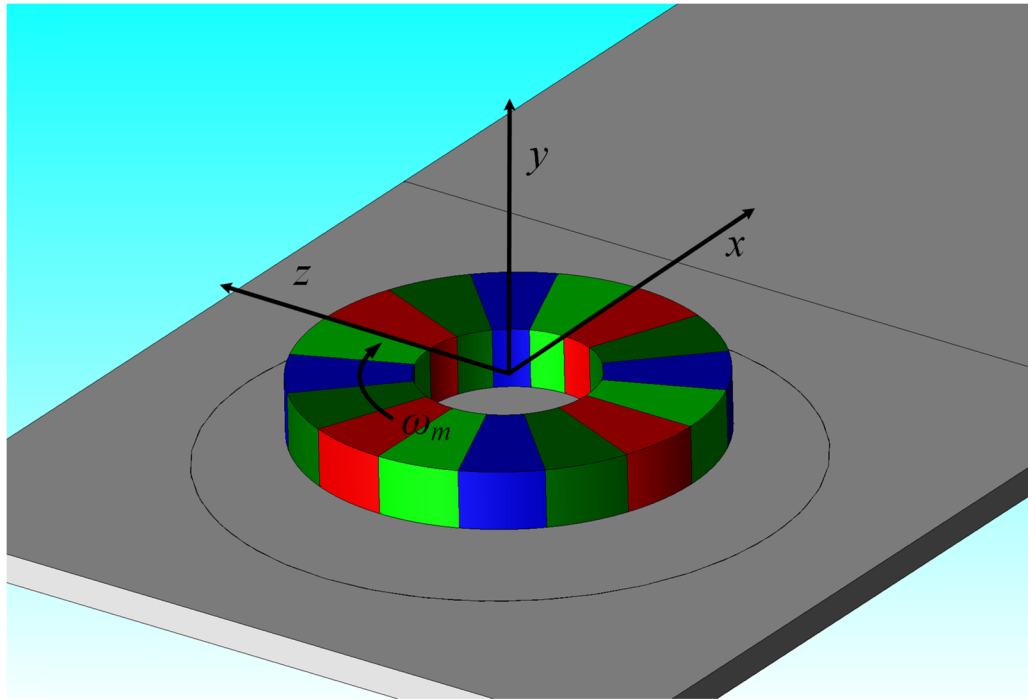


Fig. 159: Axial EDW Cartesian coordinate axis definitions

The y -axis field is of particular importance for calculating torque and forces produced by the axial EDW. The field at radius $r = 50\text{mm}$ on the track surface (10mm airgap) is shown in Fig. 160.

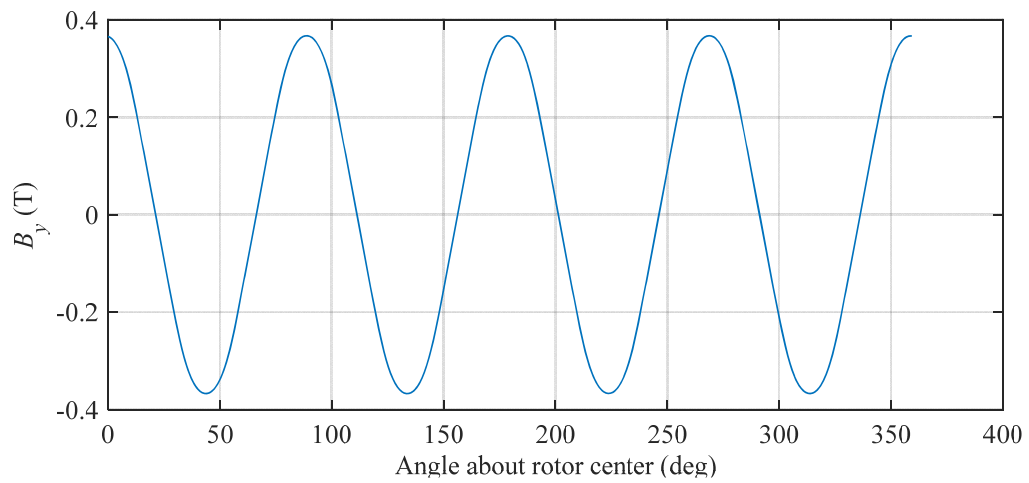


Fig. 160: Prototype axial EDW FEA calculated field at $r = 50\text{mm}$ and $y = 10\text{mm}$
(rotor parameters from Table 16)

6.3 ANALYTIC SOURCE FIELD VERIFICATION

The B_y field for an axial Halbach rotor was recently derived by Li [71]. The solution is expressed in a single integral form such that:

$$\begin{aligned}
 B_y^l(r, \theta, y) = & \frac{pM_f}{4\pi\mu_r} \cos(p\theta) \int_0^{2\pi} \cos(p\theta_d) [R_v(r, r_o, \theta_d, y, d_l) - R_v(r, r_i, \theta_d, y, d_l) \\
 & + R_v(r, r_i, \theta_d, y, 0) - R_v(r, r_o, \theta_d, y, 0)] d\theta_d \\
 & + \frac{M_f(y-d_l)}{4\pi} \cos(p\theta) \int_0^{2\pi} \cos(p\theta_d) \times \left[\frac{R_s(r, r_i, \theta_d, y, d_l) + R_s(r, r_o, \theta_d, y, d_l)}{-r^2 \sin^2(\theta_d) - (y-d_l)^2} \right] d\theta_d \\
 & - \frac{M_f y}{4\pi} \cos(p\theta) \int_0^{2\pi} \cos(p\theta_d) \left[\frac{R_s(r, r_i, \theta_d, y, 0) + R_s(r, r_o, \theta_d, y, 0)}{-r^2 \sin^2(\theta_d) - y^2} \right] d\theta_d
 \end{aligned} \tag{6.1}$$

where (r, θ, y) represents the cylindrical coordinates of the point where the field is being calculated, M_f is the fundamental of the magnetization vector, μ_r is the relative permeability, p is the number of pole pairs, θ_d is the rotation angle of the rotor, and

$$R_v(r, r_A, \theta_d, y, h_s) = \frac{r_A - r \cos(\theta_d)}{\sqrt{[r_A - r \cos(\theta_d)]^2}} \cdot \tanh^{-1} \left[\sqrt{\frac{C(r, r_A, \theta_d) + (y - h_s)^2}{[r_A - r \cos(\theta_d)]^2}} \right] \tag{6.2}$$

$$R_s(r, r_A, \theta_d, y, h_s) = \frac{r^2 + (y - h_s)^2 - r r_A \cos(\theta_d)}{R(r, r_A, \theta_d, y, h_s)} \tag{6.3}$$

where (r_A, θ_d, h_s) are the cylindrical coordinates of the point on the surface of the rotor, and

$$R(r, r_c, \phi, y, h_s) = \sqrt{C(r, r_c, \phi) + (y - h_s)^2}, \tag{6.4}$$

where ϕ is the rotational position of the rotor in the y-axis.

$$C(a, b, \phi) = a^2 + b^2 - 2ab \cos(\phi) \tag{6.5}$$

Note that (6.5) is simply the Law of Cosines. The integral in (6.1) can be solved numerically to arrive at an analytical solution for force. The implementation chosen for numerical integration was Simpson's Rule, which can be summarized by [79]:

$$\int_a^b f(x)dx = \frac{b-a}{3n} \left[f\left(a\right) + 4f\left(a + 1\left(\frac{b-a}{n}\right)\right) + 2f\left(a + 2\left(\frac{b-a}{n}\right)\right) + 4f\left(a + 3\left(\frac{b-a}{n}\right)\right) + 2f\left(a + 4\left(\frac{b-a}{n}\right)\right) + \dots + 4f\left(a + (n-1)\left(\frac{b-a}{n}\right)\right) + f\left(a + n\left(\frac{b-a}{n}\right)\right) \right] \quad (6.6)$$

where the continuous integral is divided into n equally spaced subdivisions. The accuracy of the integral's numerical solution is dependent on n , which is directly proportional to the solution's calculation time. For accuracy at the expense of computation time, n was chosen to be 3000. Using a Dell T5500 computer with an Intel Xeon E5620 running at 2.40GHz, the calculation time averages 0.0581 seconds.

Using the calculated field for the Halbach axial rotor with the parameters given in Table 16 is shown in Fig. 161. The field is rotated by $\pi/6$ to show that the field rotation is correctly modeled by equation (6.1). Fig. 162 shows the 3-D field using the polar equation (6.1) and parameters in Table 16.

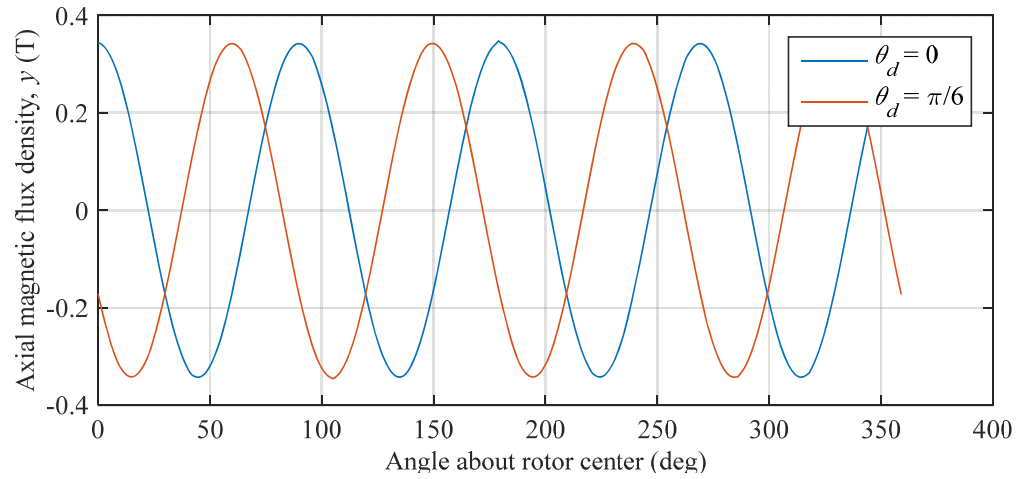


Fig. 161: Axial magnetic flux density simulation at a $r = 50\text{mm}$ when using (6.1) (rotor parameters from Table 16)

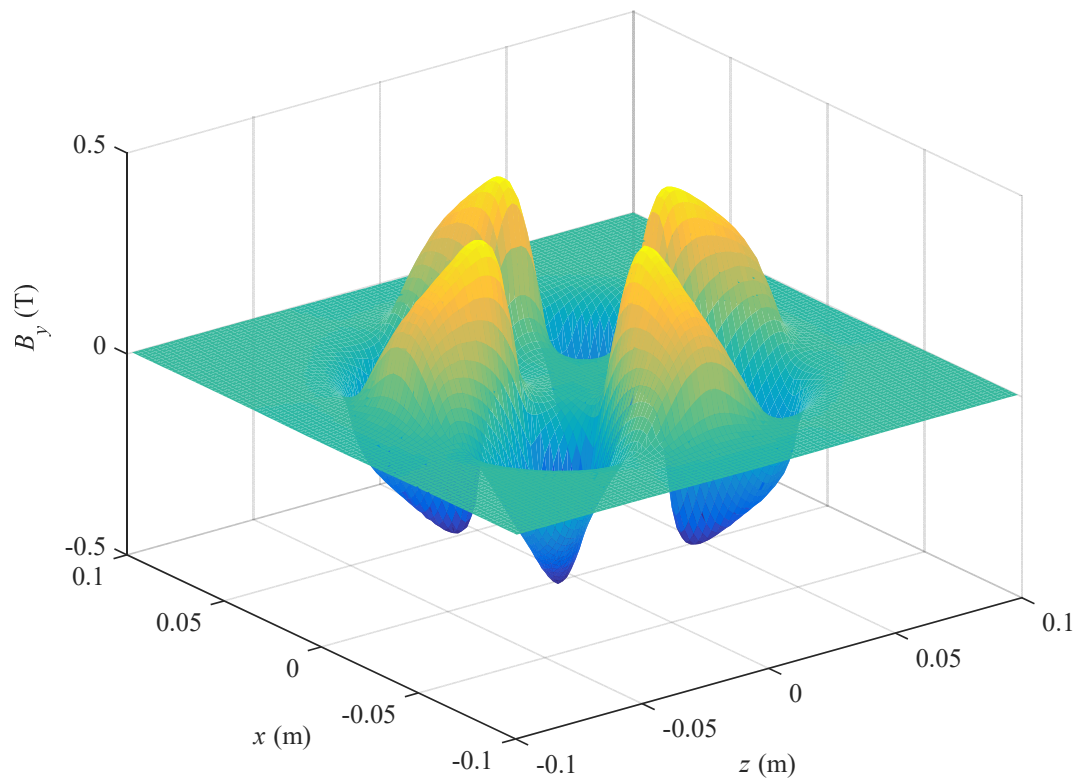


Fig. 162: 3-D axial magnetic flux density using equation (6.1) (rotor parameters from Table 16)

We would like to reformulate the equations to give an output in Cartesian form while being able to be rotated to provide an imaginary field component which is out of phase with the real field. This is needed because the SOVP model uses cartesian coordinates. The imaginary component arises from replacing the cosine term inside the integrals with an exponential term. The reformulated equations are:

$$\begin{aligned}
B_y^I(x, y, z) = & \\
& + \frac{p_I M_f}{4\pi\mu_r} \cos(p\theta) \int_0^{2\pi} e^{jp(\theta_d - \phi)} \left[R_v(x, y, z, r_o, \theta_d, d_I) - R_v(x, y, z, r_i, \theta_d, d_I) \right. \\
& \quad \left. + R_v(x, y, z, r_i, \theta_d, 0) - R_v(x, y, z, r_o, \theta_d, 0) \right] d\theta_d \quad (6.7) \\
& + \frac{M_f(y - d_I)}{4\pi} \cos(p\theta) \int_0^{2\pi} e^{jp(\theta_d - \phi)} \left[\frac{R_s(x, y, z, r_i, \theta_d, d_I) + R_s(x, y, z, r_o, \theta_d, d_I)}{-(x^2 + z^2) \sin^2(\theta_d) - (y - d_I)^2} \right] d\theta_d \\
& - \frac{M_f(y)}{4\pi} \cos(p\theta) \int_0^{2\pi} e^{jp(\theta_d - \phi)} \left[\frac{R_s(x, y, z, r_i, \theta_d, 0) + R_s(x, y, z, r_o, \theta_d, 0)}{-(x^2 + z^2) \sin^2(\theta_d) - (y)^2} \right] d\theta_d
\end{aligned}$$

Where ϕ is the additional rotation angle that the rotor has been moved to, and

$$\begin{aligned}
R_v(x, y, z, r_A, \theta_d, h_s) = & \frac{r_A - \sqrt{x^2 + z^2} \cos(\theta_d)}{\sqrt{\left[r_A - \sqrt{x^2 + z^2} \cos(\theta_d) \right]^2}} \\
& \cdot \tanh^{-1} \left[\frac{\sqrt{C(x, z, r_A, \theta_d) + (y - h_s)^2}}{\sqrt{\left[r_A - \sqrt{x^2 + z^2} \cos(\theta_d) \right]^2}} \right] \quad (6.8)
\end{aligned}$$

$$R_s(x, y, z, r_A, \theta_d, h_s) = \frac{x^2 + z^2 + (y - h_s)^2 - \sqrt{x^2 + z^2} r_A \cos(\theta_d)}{R(x, z, r_A, \theta_d, y, h_s)} \quad (6.9)$$

$$R(x, y, z, r_c, \theta_d, h_s) = \sqrt{x^2 + z^2 + r_c^2 - 2r_c^2 \sqrt{x^2 + z^2} \cos(\theta_d) + (y - h_s)^2} \quad (6.10)$$

$$C(x, z, r_A, \phi) = \sqrt{x^2 + z^2} + r^2 - 2\sqrt{x^2 + z^2} r_A \cos(\phi) \quad (6.11)$$

$$\theta = \tan^{-1}\left(\frac{z}{x}\right) \quad (6.12)$$

Equation (6.1) will be referred to as the polar equation while (6.7) will be referred to as the Cartesian or exponential equation. We can check that the real component of the field output is the same by plotting the field for the same rotor around a radius of 50mm from the centerline of the rotor, as shown in Fig. 163. The small non-sinusoidal irregularities are due to a coarse numerical integration. If calculation time is of no consequence, the integration can occur in smaller steps and the field result has fewer ripples. We can also check that the field is the same at other radii by taking a longitudinal (x -axis) transection of the field at a couple of z lines, $z = 0$ and $z = 30\text{mm}$, as shown in Fig. 164 and Fig. 165. Note that the field is negligible near the edge of the track, so an infinite track SOVP model is valid.

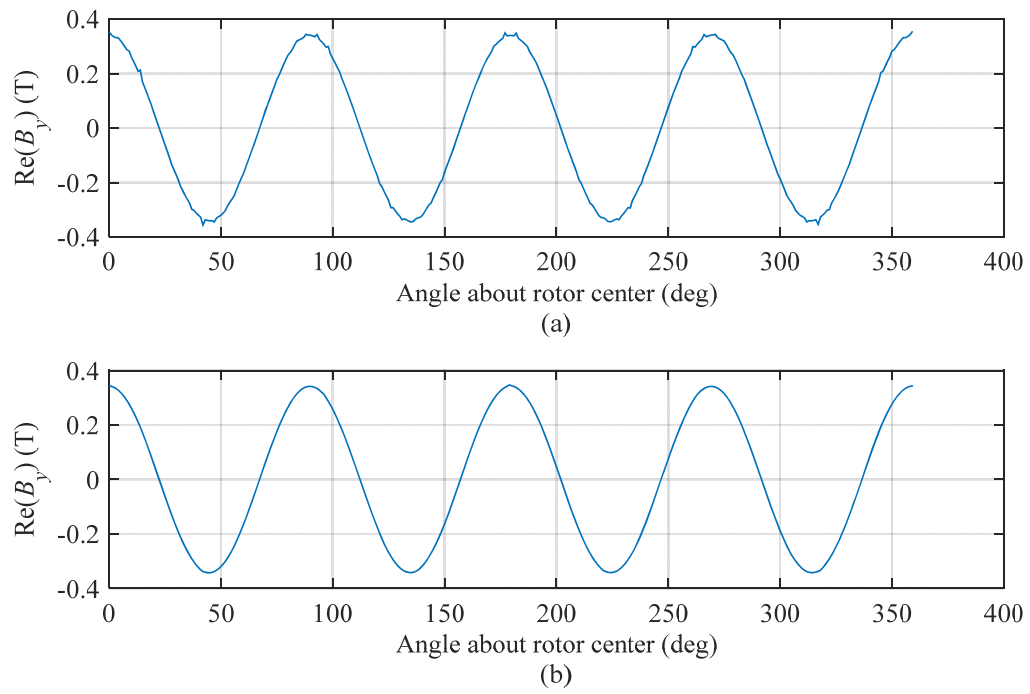


Fig. 163: (a) Real y field using polar equation (6.1) and Table 16 at $r = 50\text{mm}$ (b) Real y field using Cartesian equation (6.7) and Table 16 at $r = 50\text{mm}$ (rotor parameters from Table 16)

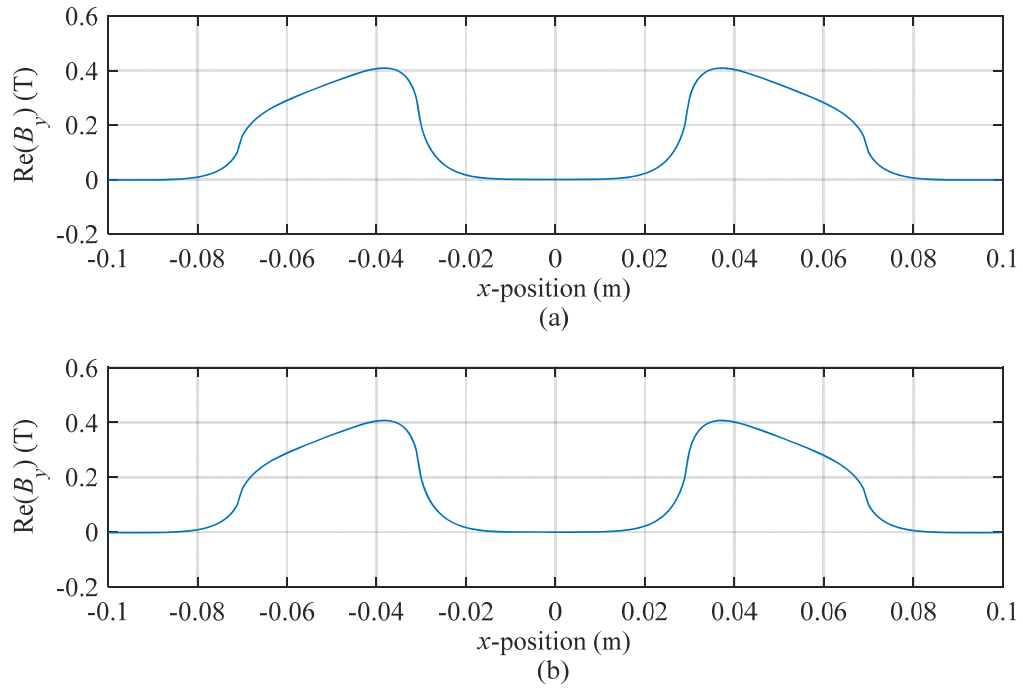


Fig. 164: (a) Real y field using polar equation (6.1) and Table 16 at $z = 0\text{mm}$ (b) Real y field using Cartesian equation (6.7) and Table 16 at $z = 0\text{mm}$ (rotor parameters from Table 16)

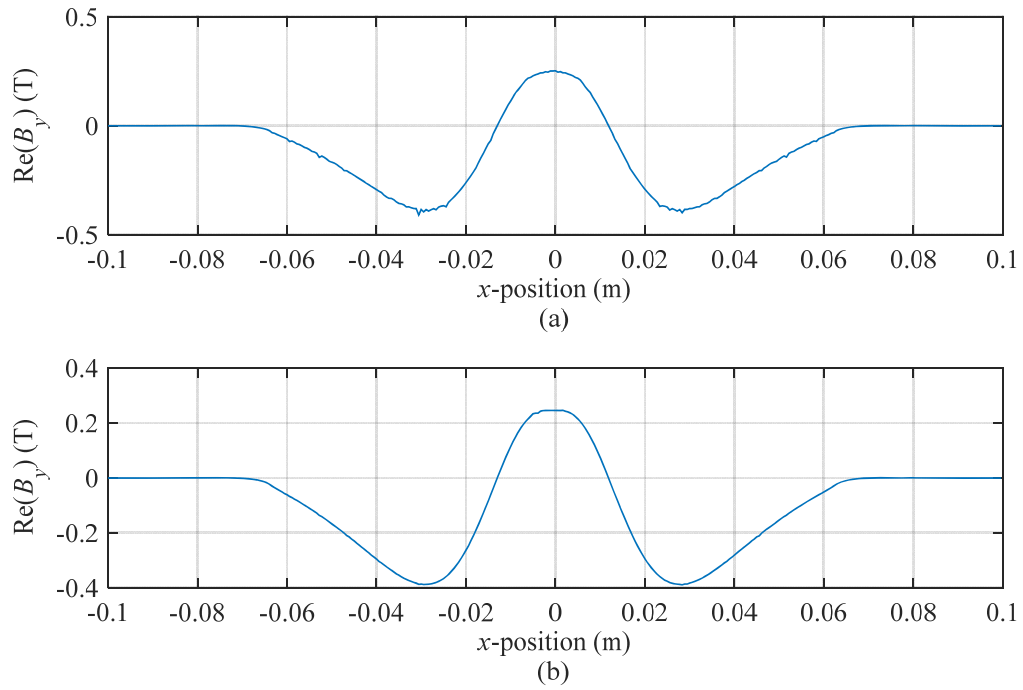


Fig. 165: (a) Real y field using polar equation (6.1) and Table 16 at $z = 30\text{mm}$ (b) Real y field using Cartesian equation (6.7) and Table 16 at $z = 30\text{mm}$ (rotor parameters from Table 16)

The Cartesian equation, (6.7), yields the same real field as the polar equation, (6.1). Whereas the polar equation simply yielded the real field, with the imaginary component being zero, the advantage of the Cartesian equation which will allow us to use an SOVP solution to calculate the eddy-current force stiffness and damping terms, is that it provides an imaginary field component, as shown in Fig. 166.

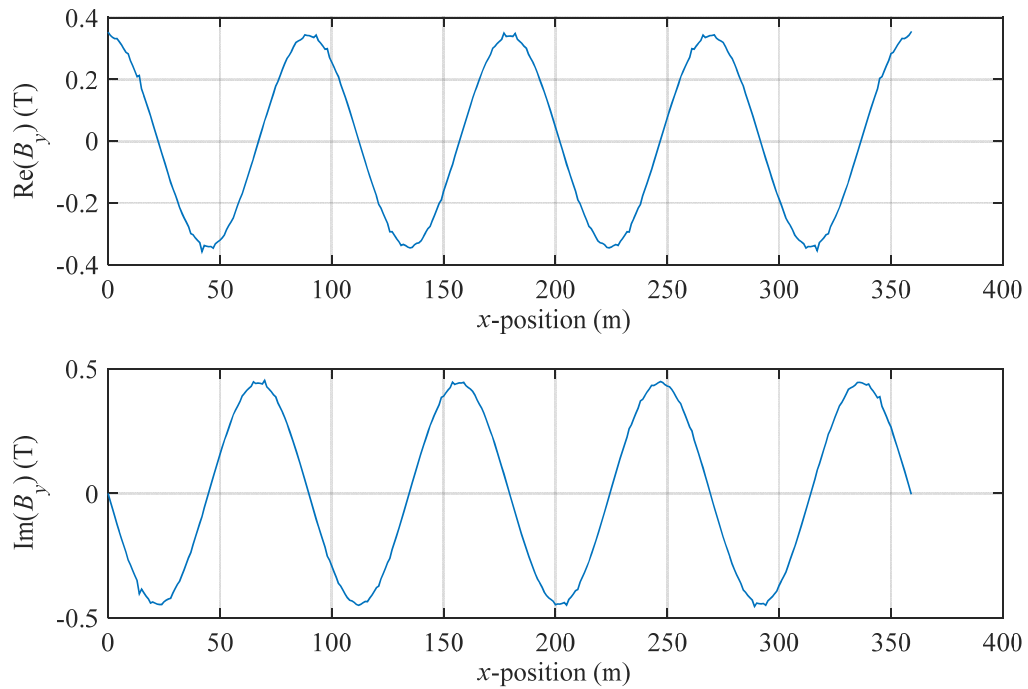


Fig. 166: Comparison of real and imaginary normal field from axial EDW rotor using (6.7) at $r = 50\text{mm}$ (rotor parameters from Table 16)

The axial EDW 3-D source field from equation (6.7) is shown in Fig. 167. The imaginary component is phase shifted from the real field.

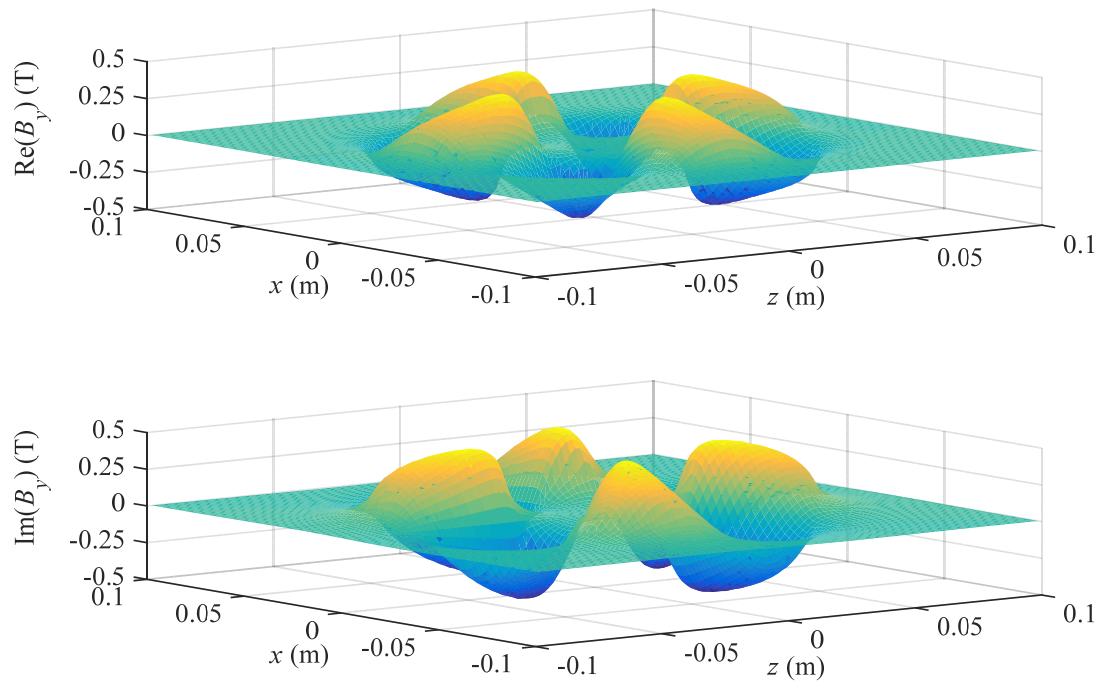


Fig. 167: Comparison of real and imaginary 3-D field using (6.7) (rotor parameters from Table 16)

6.4 VALIDATION OF ANALYTIC FIELD MODEL

Since it was required to modify the analytic field solution proposed by Li [71] and rewrite it in Matlab code, it must be verified that the new model implementation is correct. To do this, the analytic solution is compared to an FEA model.

6.4.1 VERIFICATION OF FIELD USING LI'S ROTOR DIMENSIONS

An axial Halbach rotor model was created in JMAG with the dimensions listed in Table 17. An analytic model with the same dimensions was also made to verify that the FEA and SOVP field results match sufficiently. The dimensions were chosen to compare to the matching field results shown by Li [71].

Table 17: Li's axial Halbach rotor dimensions

| Dimension | Value | Units |
|---|-----------|-------|
| Outer radius, r_o | 100 | mm |
| Inner radius, r_i | 90 | mm |
| Thickness, d | 10 | mm |
| Pole pairs | 4 | |
| Segments per pole | 8 | |
| Magnetization magnitude, M | 1.28 | A/m |
| Fundamental magnetization vector, M_f | $0.9745M$ | A/m |

Some selected field plots are shown below. Fig. 168 shows the field comparison at a radius of 90mm and airgap of 12mm, Fig. 169 shows the field comparison at a radius of 98mm and airgap of 8mm, Fig. 170 shows the field comparison at a radius of 94mm and airgap of 3mm, and Fig. 171 shows the field comparison at a radius of 96mm and airgap of 1mm. When the airgap is relatively large (e.g. 12mm), the fields match closely, but as the airgap becomes smaller, the segmentation causes the field to deviate from the ideal Halbach model due to higher order harmonics. To compare the models, we plot the

fundamental of the JMAG FEA results which more closely matches the ideal case that the analytic model calculates.

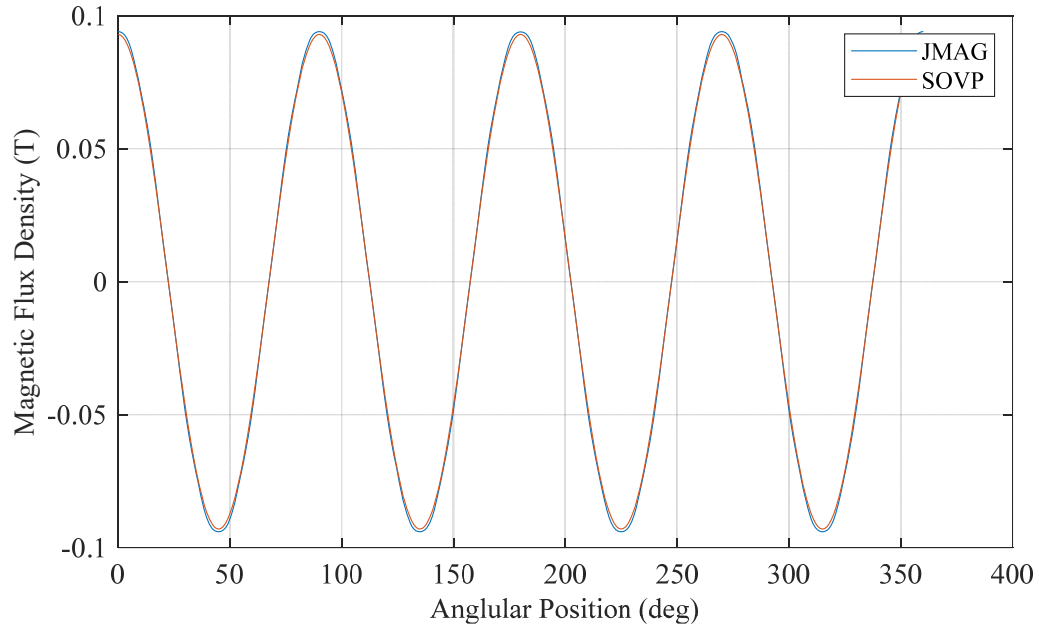


Fig. 168: Field comparison at $r = 90\text{mm}$, airgap $y = 12\text{mm}$, for Li's rotor defined by Table 17

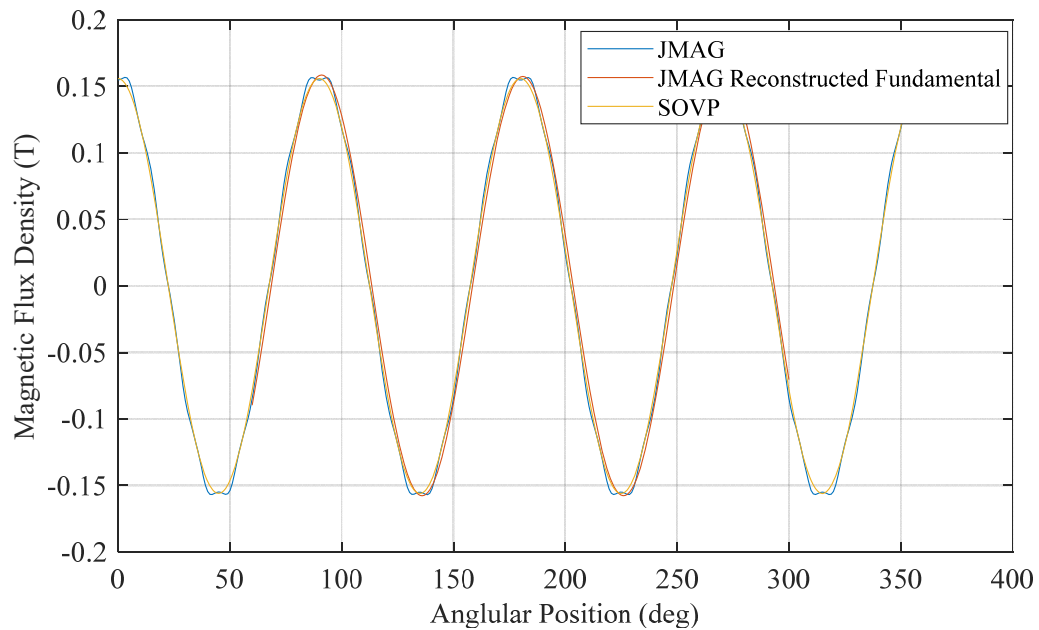


Fig. 169: Field comparison at $r = 98\text{mm}$, airgap $y = 8\text{mm}$, for Li's rotor defined by Table 17, including a reconstructed JMAG field using only the fundamental of the FFT

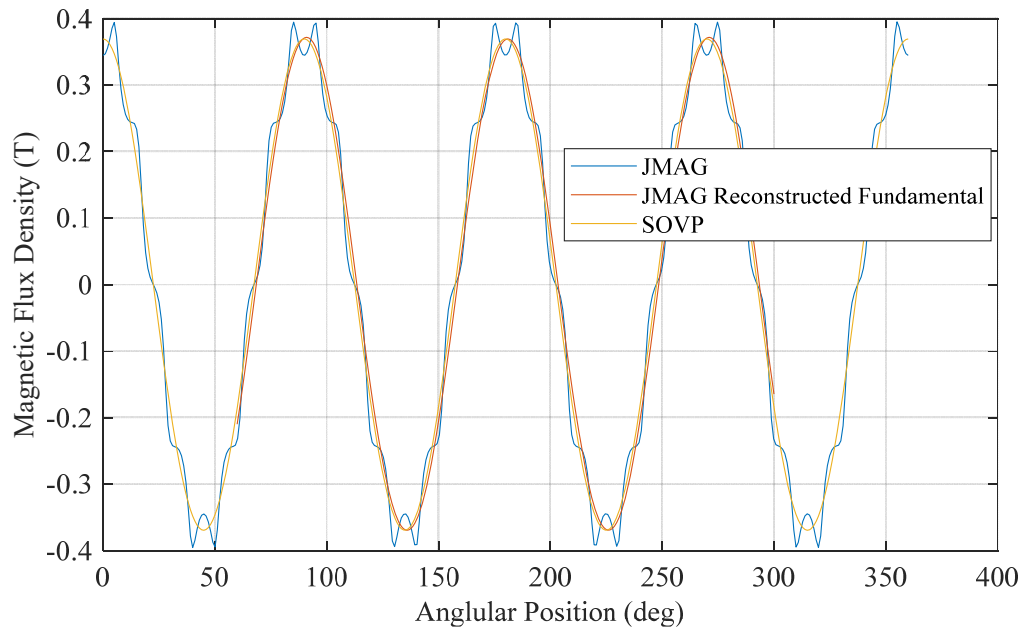


Fig. 170: Field comparison at $r = 94\text{mm}$, airgap $y = 3\text{mm}$, for Li's rotor defined by Table 17, including a reconstructed JMAG field using only the fundamental of the FFT

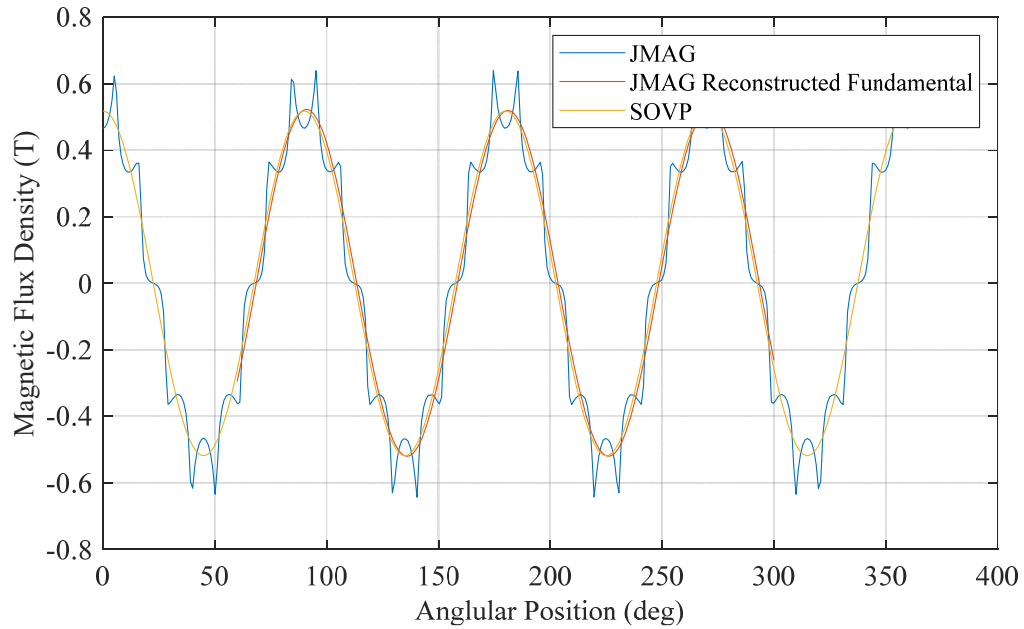


Fig. 171: Field comparison at $r = 96\text{mm}$, airgap $y = 1\text{mm}$, for Li's rotor defined by Table 17, including a reconstructed JMAG field using only the fundamental of the FFT

Table 18 shows the comparison of the FEA field generated using JMAG and the analytic field generated using the SOVP model. The table compares the peak field in each case as the radius and air gap vary. For the JMAG results, only the fundamental is considered, which is achieved in MATLAB by taking the Discrete Fourier Transform (DFT) of the field, isolating the fundamental (by eliminating the higher order components), and taking the inverse DFT of the resulting spectrum. This is consistent with the method used by Li.

Table 18: Comparison of FEA and analytic field results for Li's axial Halbach rotor

| Radius r (mm) | Air gap (mm) | Peak B_z (T), JMAG | Peak B_z (T), SOVP | Discrepancy (%) | Kang's Discrepancy (%) |
|--------------------|-----------------|-------------------------|-------------------------|--------------------|---------------------------|
| 92 | 1 | 0.4809 | 0.4816 | -0.15% | -1.47% |
| 94 | 1 | 0.5201 | 0.5193 | 0.15% | -1.50% |
| 96 | 1 | 0.5198 | 0.5179 | 0.37% | -1.36% |
| 98 | 1 | 0.4811 | 0.4776 | 0.73% | -1.01% |
| 92 | 3 | 0.3220 | 0.3214 | 0.19% | -1.06% |
| 94 | 3 | 0.3692 | 0.3691 | 0.03% | -1.29% |
| 96 | 3 | 0.3683 | 0.3673 | 0.27% | -1.17% |
| 98 | 3 | 0.3193 | 0.3162 | 0.97% | -0.73% |
| 92 | 12 | 0.1039 | 0.1032 | 0.67% | -0.28% |
| 94 | 12 | 0.1094 | 0.1085 | 0.82% | -0.36% |
| 96 | 12 | 0.1087 | 0.1077 | 0.92% | -0.35% |
| 98 | 12 | 0.1020 | 0.1008 | 1.18% | -0.14% |

The results have a maximum discrepancy of 1.18%, which is smaller than those published by Li. The FEA and analytic results co-validate each other with the closely matching results. Note that for computational convenience, the FEA model element size was set to 4mm and the air region was set to 2.5 times the model length with an element size of 8mm. Further improvements in accuracy would be possible with a finer model.

6.4.2 VALIDATION OF ANALYTIC FIELD SOLUTION FOR PROTOTYPE ROTOR

In the previous section, 6.4.1, the axial Halbach analytic model code (written in Matlab code) was verified to produce a result which matched an equivalent JMAG FEA model, thereby confirming that our models match Li's models. The section applies a similar process to validate that the analytic and FEA field match for the prototype rotor, first with 8 segments per pole, then with 4 segments per pole.

6.4.2.1 FIELD COMPARISON WITH 8 SEGMENTS PER POLE

An FEA and analytic model are built according to dimensions shown in Table 19. This rotor is designed with 8 segments per pole, since this is the configuration that Li and other researchers have typically chosen in the past [71]. This is a precursor to validating the field with 4 segments per pole, providing that matching results are obtained in this section.

Table 19: 8 Segment-per-pole prototype axial Halbach rotor dimensions

| Dimension | Value | Units |
|---|-----------|-------|
| Outer radius, r_o | 70 | mm |
| Inner radius, r_i | 30 | mm |
| Thickness, d | 20 | mm |
| Pole pairs | 4 | |
| Segments per pole | 8 | |
| Magnetization magnitude, M | 1.28 | A/m |
| Fundamental magnetization vector, M_f | $0.9745M$ | A/m |

A set of comparisons is shown in the plots below, which are chosen to show one at each radius (35mm, 50mm, and 65mm), and one at each arbitrary height (1mm, 3mm, and 12mm). Fig. 172, Fig. 173, and Fig. 174 show the field comparison at an airgap of 12mm

and radii of 35mm, 50mm, and 65mm, respectively. Fig. 175 and Fig. 176 show the field comparison at a radius of 50mm and airgaps of 3mm and 1mm, respectively. Similar to Li's rotor, when the airgap is relatively large (e.g. 12mm), the FEA field is approximately sinusoidal and closely matches the analytic field, but as the airgap becomes smaller, the non-ideal Halbach field shows higher order harmonics in the field due to magnet segmentation. The fundamental of the field is derived from the signal, which is then used to compare to the analytic field.

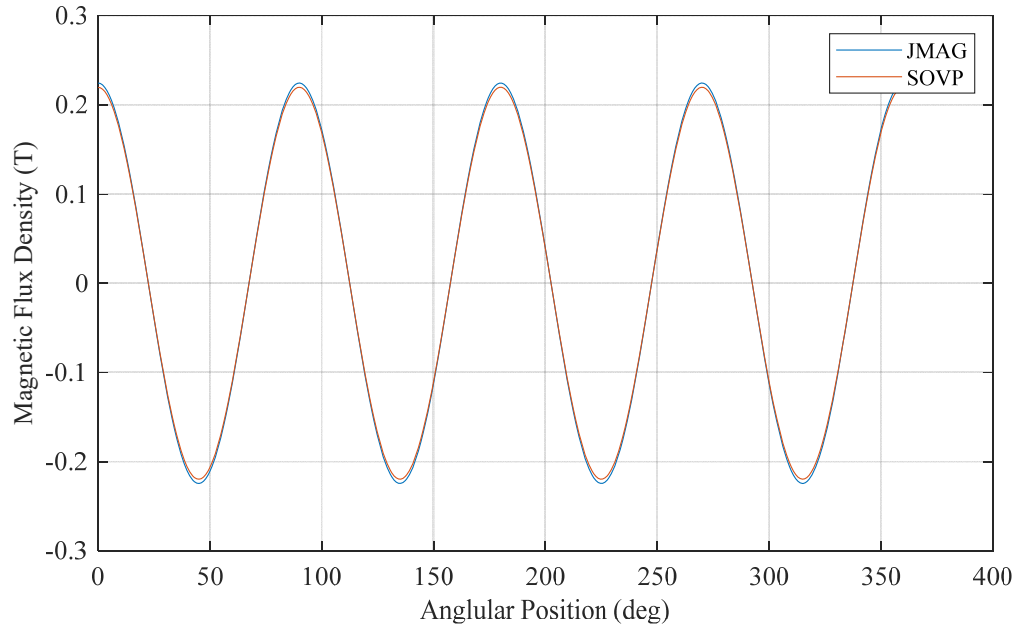


Fig. 172: Field comparison at $r = 35\text{mm}$, airgap $y = 12\text{mm}$, for prototype rotor defined by Table 19

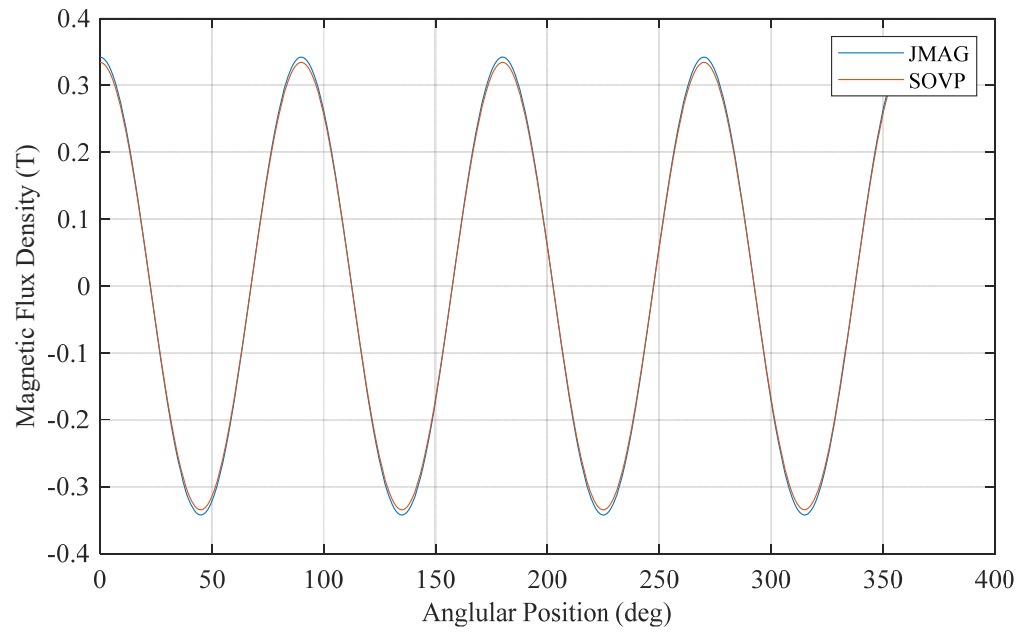


Fig. 173: Field comparison at $r = 50\text{mm}$, airgap $y = 12\text{mm}$, for prototype rotor defined by Table 19

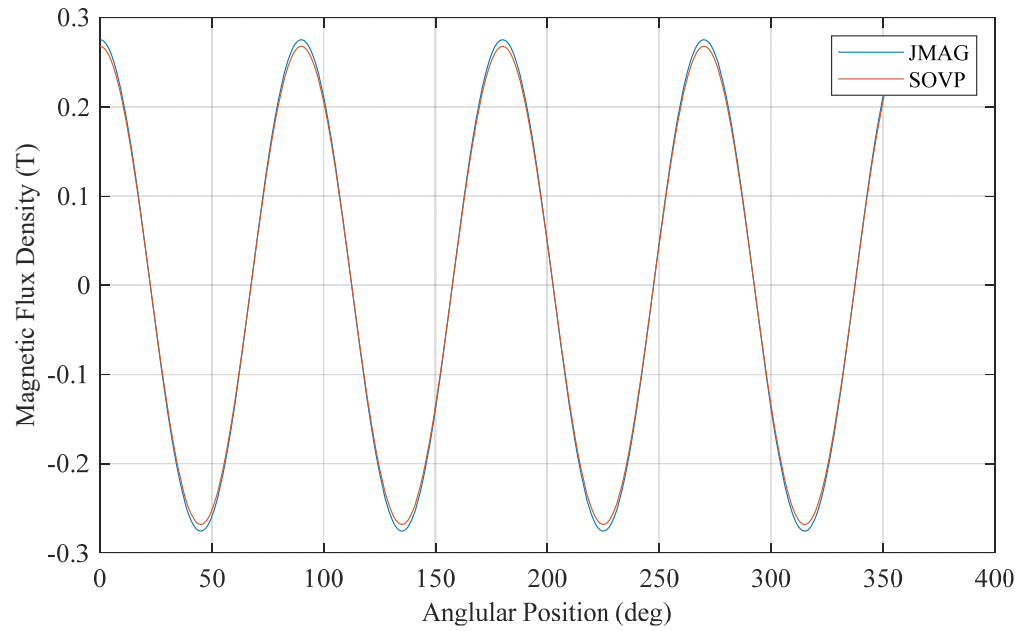


Fig. 174: Field comparison at $r = 65\text{mm}$, airgap $y = 12\text{mm}$, for prototype rotor defined by Table 19

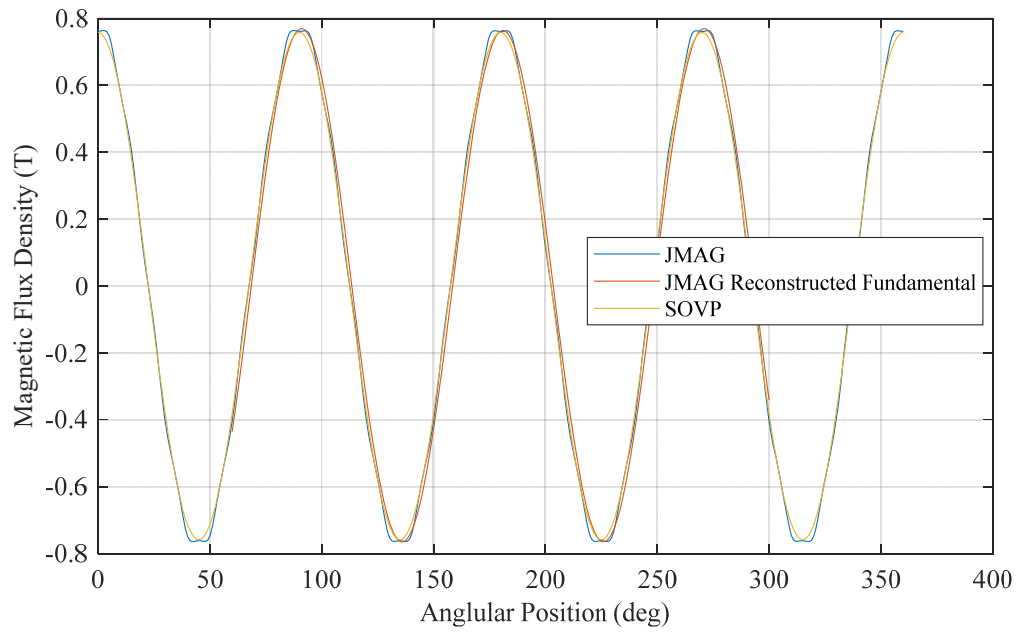


Fig. 175: Field comparison at $r = 50\text{mm}$, airgap $y = 3\text{mm}$, for prototype rotor defined by Table 19, including a reconstructed JMAG field using only the fundamental of the FFT

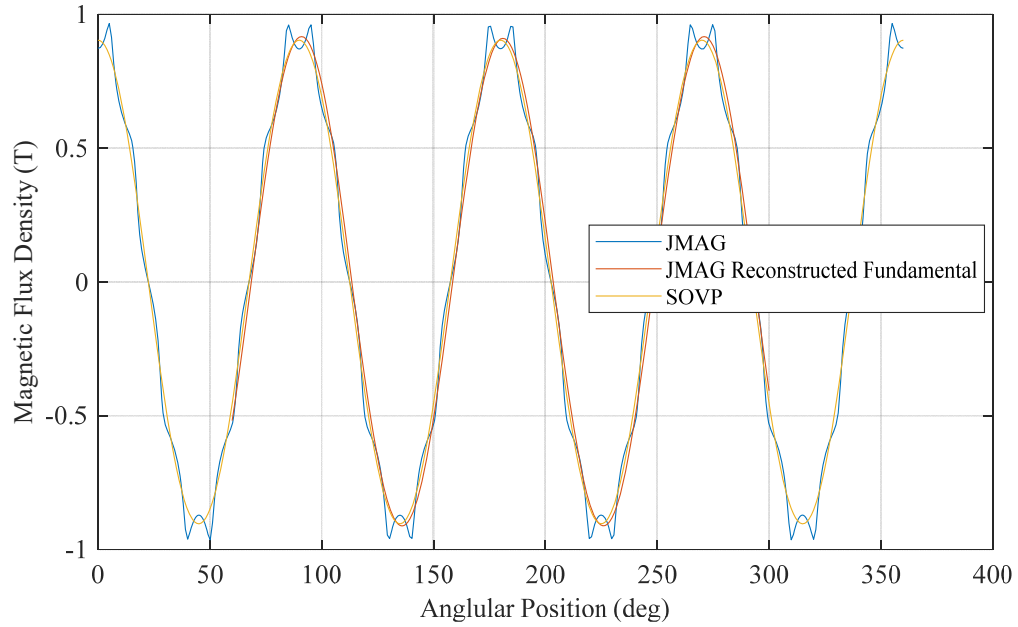


Fig. 176: Field comparison at $r = 50\text{mm}$, airgap $y = 1\text{mm}$, for prototype rotor defined by Table 19, including a reconstructed JMAG field using only the fundamental of the FFT

Table 20 compares the discrepancies between the FEA and analytic field peaks at various radii and heights. Since the fields (or fundamentals of the fields) are sinusoidal, comparing peaks is a reasonable way to approximate the degree to which the results are a match. As in Section 6.4.1, only the fundamental is considered for the FEA results in Table 20.

Table 20: Comparison of FEA and analytic field results
for 8-segment prototype axial Halbach rotor

| Radius r (mm) | Air gap (mm) | Peak B_z (T), JMAG | Peak B_z (T), SOVP | Discrepancy (%) |
|--------------------|-----------------|----------------------|----------------------|-----------------|
| 35 | 1 | 0.9057 | 0.8989 | 0.75% |
| 50 | 1 | 0.9104 | 0.9032 | 0.79% |
| 65 | 1 | 0.7904 | 0.7801 | 1.30% |
| 35 | 3 | 0.682 | 0.6771 | 0.72% |
| 50 | 3 | 0.7645 | 0.7578 | 0.88% |
| 65 | 3 | 0.6345 | 0.6262 | 1.31% |
| 35 | 12 | 0.2213 | 0.2196 | 0.77% |
| 50 | 12 | 0.3374 | 0.3343 | 0.92% |
| 65 | 12 | 0.2718 | 0.2679 | 1.43% |

The results have a maximum discrepancy of 1.43% and a mean discrepancy of 0.986%. Given the fact that these values are calculated using a real-world approach of practical computation times which may degrade accuracy slightly, this discrepancy is small enough to claim that the FEA and analytic models are a close match. The main FEA considerations that can reduce accuracy are the rotor element size of 2mm, air region element size of 3mm, and air region of 3 times the model length. Smaller element sizes and larger model length to reduce edge-effects would improve the models' performance. Some of the discrepancy can also be attributed to arithmetic rounding error and small offsets in the analytical code that are used to prevent division-by-zero errors during run-time.

6.4.2.2 MAGNETIZATION VECTOR CALCULATION OF 4 POLE PAIR AXIAL ROTOR

The 4-magnet per pole Halbach array is only an approximation of an ideal Halbach array. In order to model a rotor with 4 segments per pole, the magnetization vector must be calculated for this condition. According to Li, the magnetizing distribution of the magnets can be described by a Fourier series consisting of the axial and azimuthal components of the field [71]:

$$\mathbf{M} = M_y(\theta)\hat{\mathbf{y}} + M_\theta(\theta)\hat{\boldsymbol{\theta}} \quad (6.13)$$

where \mathbf{M} is the magnetization vector, M_y and M_θ are the axial and azimuthal components of the magnetization vector, and $\hat{\mathbf{y}}$ and $\hat{\boldsymbol{\theta}}$ are the unit vectors in the vertical and tangential angle directions. Substituting in the magnitude components into (6.13):

$$\mathbf{M} = \sum_{n=1}^{\infty} a_n \cos(np_l\theta)\hat{\mathbf{y}} \pm \sum_{n=1}^{\infty} b_n \sin(np_l\theta)\hat{\boldsymbol{\theta}} \quad (6.14)$$

where

$$a_n = \frac{4}{T} \int_0^{T/2} M_y(\theta) \cos(np_l\theta) d\theta \quad (6.15)$$

$$b_n = -\frac{4}{T} \int_0^{T/2} M_\theta(\theta) \sin(np_l\theta) d\theta \quad (6.16)$$

$$T = \frac{2\pi}{p_l} \quad (6.17)$$

where p_l is the number of pole pairs. The values of M_y and M_θ are plotted as functions of angular position in Fig. 177 and Fig. 178. Note that in these figures:

$$M = \frac{B_m}{\mu_o} \quad (6.18)$$

where M is the magnetization magnitude and B_m is the residual flux density of the magnet.

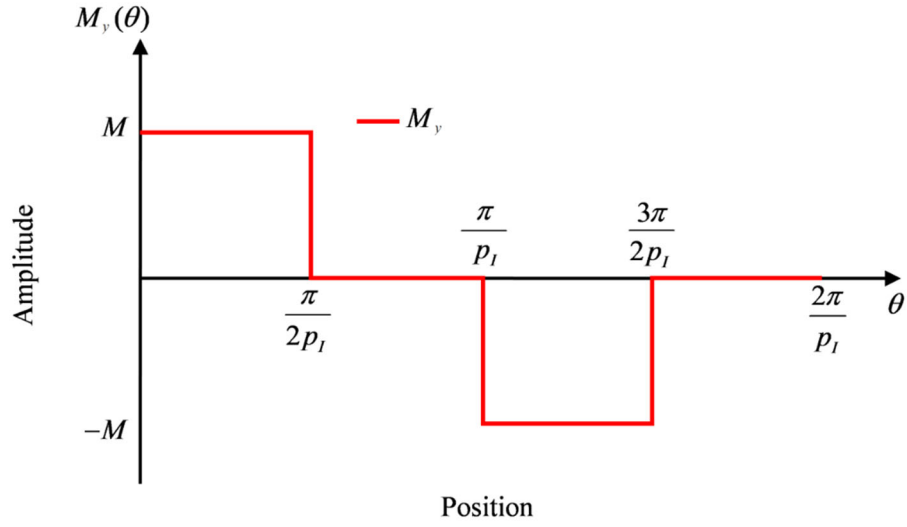


Fig. 177: Magnitude of M_y vs. angular position for 4 segment-per-pole rotor

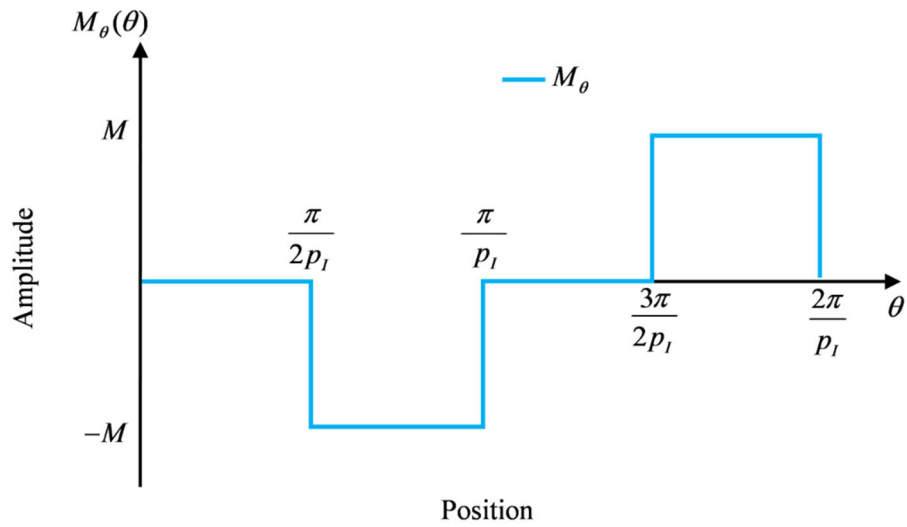


Fig. 178: Magnitude of M_θ vs. angular position for 4 segment-per-pole rotor

Using Fig. 177, equation (6.15) can be rewritten:

$$a_n = \frac{4}{T} \int_0^{\frac{\pi}{2p_l}} M \cos(np_l \theta) d\theta \quad (6.19)$$

Evaluating the integral in (6.19) yields:

$$a_n = \frac{4M \sin(np_l \theta)}{Tnp_l} \bigg|_{\theta=0}^{\theta=\frac{\pi}{2p_l}} \quad (6.20)$$

Substituting the pole pair number ($p_l = 4$), and further solving (6.20):

$$a_n = \frac{2M \sin\left(\frac{\pi n}{2}\right)}{\pi n} \quad (6.21)$$

Similarly, using Fig. 178, equation (6.16) can be rewritten:

$$b_n = -\frac{4}{T} \int_{\pi/2p_l}^{\pi/p_l} M \sin(np_l \theta) d\theta \quad (6.22)$$

Solving the integral in (6.22) and simplifying yields:

$$b_n = -\frac{2M}{\pi n} \left[\cos\left(\frac{\pi n}{2}\right) - \cos(\pi n) \right] \quad (6.23)$$

Substituting (6.21) and (6.23) into (6.14):

$$\begin{aligned} \mathbf{M} = & \sum_{n=1}^{\infty} \left[\frac{2M \sin\left(\frac{\pi n}{2}\right)}{\pi n} \cos(np_l \theta) \right] \hat{\mathbf{y}} \\ & - \sum_{n=1}^{\infty} \left[\frac{2M}{\pi n} \left[\cos\left(\frac{\pi n}{2}\right) - \cos(\pi n) \right] \sin(np_l \theta) \right] \hat{\mathbf{z}} \end{aligned} \quad (6.24)$$

When $n = 1$, then the absolute magnitude of the harmonics in (6.21) and (6.23) evaluate to:

$$|a_1| = |b_1| = \frac{2\sqrt{2}}{\pi} M \approx 0.9003M \quad (6.25)$$

If we consider only the fundamental harmonic (when $n = 1$), then (6.18) becomes:

$$M_f = c_{fn} M \quad (6.26)$$

where

$$c_{\hbar} = \frac{2\sqrt{2}}{\pi} \tag{6.27}$$

6.4.2.3 FIELD COMPARISON USING 4 SEGMENTS PER POLE

A prototype rotor with 4 magnet segments per pole is modeled both analytically and using JMAG for FEA comparison. Table 21 defines the rotor's physical parameters.

Table 21: 4 Segment-per-pole prototype axial Halbach rotor dimensions

| Dimension | Value | Units |
|---|-----------|-------|
| Outer radius, r_o | 70 | mm |
| Inner radius, r_i | 30 | mm |
| Thickness, d | 20 | mm |
| Pole pairs | 4 | |
| Segments per pole | 4 | |
| Magnetization magnitude, M | 1.42 | A/m |
| Fundamental magnetization vector, M_f | $0.9003M$ | A/m |

A selection of field comparisons at varying radial distance and airgap are plotted in the figures below. Similarly to the previous rotors studied, the FEA field at a relatively large airgap of $y = 12\text{mm}$ does not exhibit significant higher order harmonics, as shown in Fig. 179. It can thus be directly compared against the analytic field which only includes the fundamental component. The fields shown in Fig. 180 and Fig. 181, at airgaps of $y = 3\text{ mm}$ and $y = 1\text{ mm}$, respectively, can be compared to the analytic solution by examining their fundamental harmonic component. Table 22 compares the peak fields from both models at 3 different radii and 3 different airgaps, and shows that the models match reasonably well, with the largest discrepancy being 4% at a 12 mm airgap and a radii of 65mm. The table also shows that the models tend to agree with each other more as the measurement radii decreases.

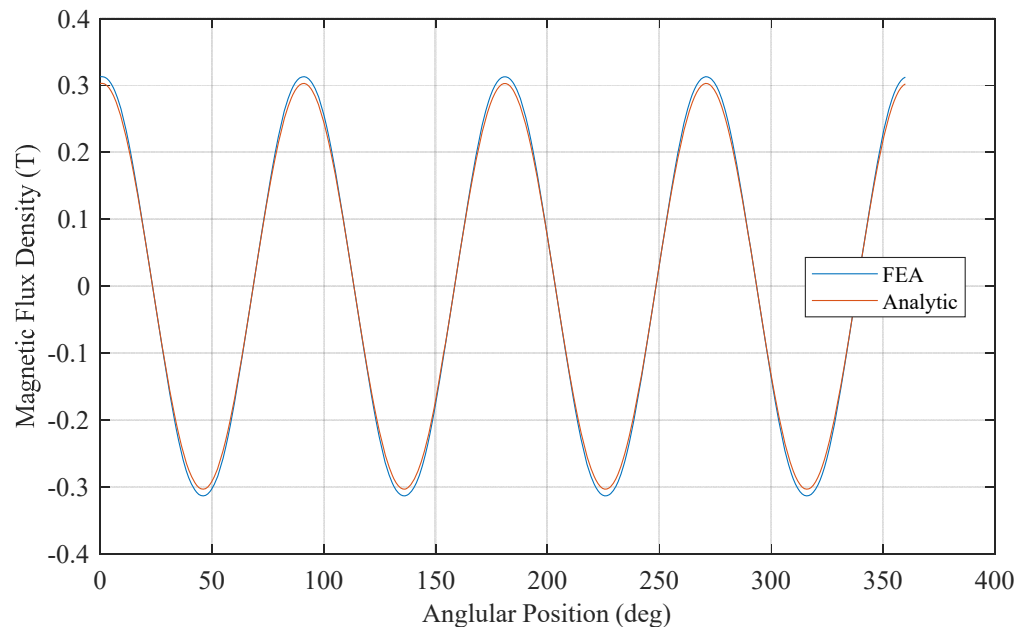


Fig. 179: Field comparison at $r = 50\text{mm}$, airgap $y = 12\text{mm}$, for 4-segment prototype rotor defined by Table 21

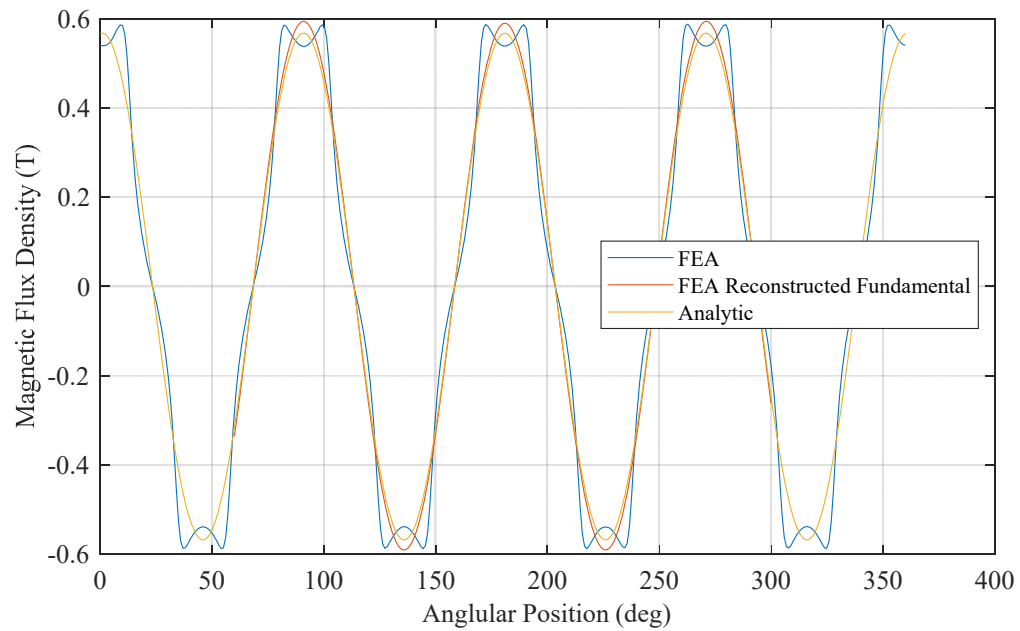


Fig. 180: Field comparison at $r = 65\text{mm}$, airgap $y = 3\text{mm}$, for 4-segment prototype rotor defined by Table 21, including a reconstructed FEA field using only the fundamental of the DFT

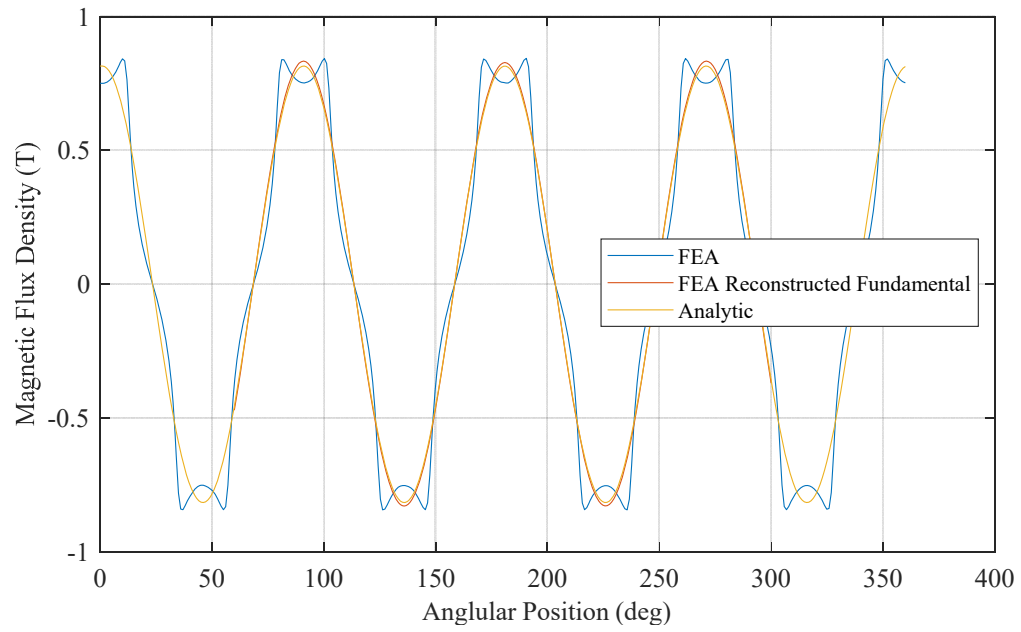


Fig. 181: Field comparison at $r = 35\text{mm}$, airgap $y = 1\text{mm}$, for 4-segment prototype rotor defined by Table 21, including a reconstructed FEA field using only the fundamental of the DFT

Table 22: Comparison of FEA and analytic field results for
4-segment prototype axial Halbach rotor

| Radius r (mm) | Air gap (mm) | Peak B_z (T), JMAG | Peak B_z (T), SOVP | Discrepancy (%) |
|--------------------|-----------------|----------------------|----------------------|-----------------|
| 35 | 1 | 0.8281 | 0.8145 | 1.64% |
| 50 | 1 | 0.837 | 0.8183 | 2.23% |
| 65 | 1 | 0.7341 | 0.7068 | 3.72% |
| 35 | 3 | 0.6225 | 0.6135 | 1.45% |
| 50 | 3 | 0.7021 | 0.6867 | 2.19% |
| 65 | 3 | 0.590 | 0.5674 | 3.83% |
| 35 | 12 | 0.2021 | 0.1989 | 1.58% |
| 50 | 12 | 0.3104 | 0.3029 | 2.42% |
| 65 | 12 | 0.2528 | 0.2427 | 4.00% |

6.5 AXIAL ELECTRODYNAMIC WHEEL SOVP MODEL

In this section, the SOVP model's force results are compared to the FEA model.

6.5.1 REVIEW OF PREVIOUS SOURCE FIELD

The SOVP model that was derived and used in chapters CHAPTER 2:-CHAPTER 4: was designed to be used with a radial EDW. The section of code that generates the source field was isolated in the SOVP model. For illustrative purposes, the source field calculated inside the SOVP function code is shown below in Fig. 182 for a radial Halbach rotor with 4 pole-pairs, with an outer radius of 26mm, rotor width of 52mm, track width (z-direction) of 77mm, track length (x- direction) of 160mm, and track thickness (y-direction of 10mm).

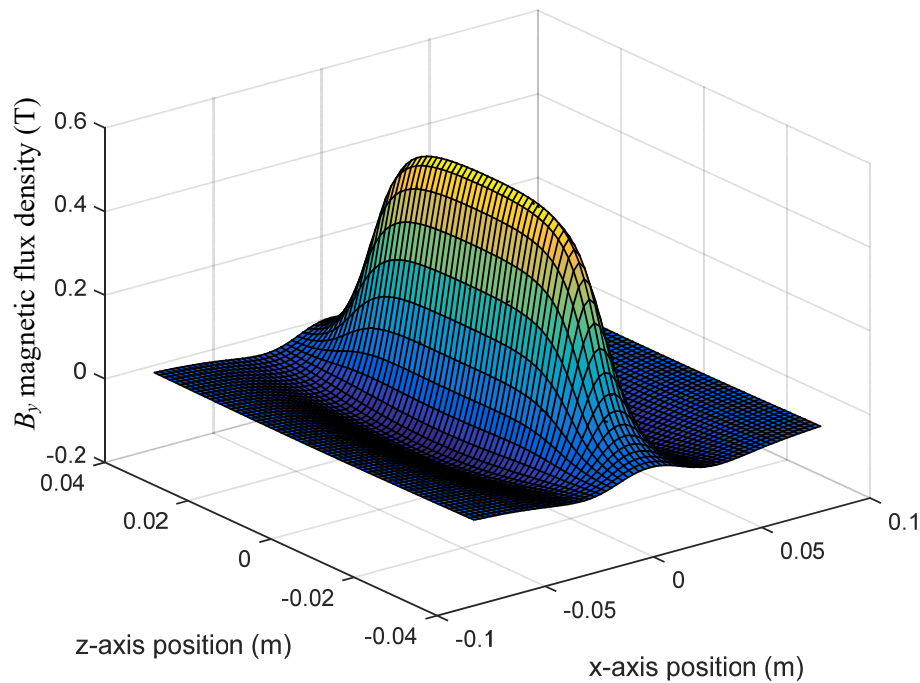


Fig. 182: Original y-axis source field from radial Halbach rotor used in SOVP model
(rotor parameters from Table 1 and above)

6.5.2 FORCE CALCULATION TIME

FEA methods are compute intensive, and each FEA data point took between 52 and 65 hours to calculate. It would therefore not be possible to calculate force or it's partial derivatives, stiffness and damping, during run-time with FEM, even with a powerful computer. The SOVP calculation, by comparison, took only 234.94 seconds which is largely dominated by the source field calculation (when the source field grid is 64×64 and the numerical integration from (6.7) has 3000 subdivisions using Simpson's Rule). Though much more efficient than FEM, this is still not suitable for run-time calculations for control purposes. If the field calculation was being used in a run-time situation, the time could be reduced by using a coarser grid or by reducing the integration subdivisions. Table 23 summarizes the inverse relationship between accuracy and computation time, where percent error is calculated to be the difference in y -force relative to the original parameters (64×64 grid and 3000 integration points), which provide the most accurate integral calculation. The comparison is made at $(x, y, z) = (0, 14.7\text{mm}, 0)$ and $(v_x, v_y, v_z, \omega_m) = (4 \text{ m/s}, 0, 0, 400 \text{ rpm})$. Note that calculation time can be greatly reduced to less than one second if the controller is sufficiently robust to perform well with force modeling error of 8.75%.

Table 23: Summary of axial Halbach field computation time vs. accuracy of field model

| Field Grid | Integration Subdivisions | Percent Error (%) | Calculation Time (s) |
|----------------|--------------------------|-------------------|----------------------|
| 64×64 | 3000 | N/A | 234.94 |
| 64×64 | 300 | 0.002 | 23.49 |
| 64×64 | 100 | 2.43 | 8.22 |
| 32×32 | 3000 | 2.19 | 59.05 |
| 32×32 | 300 | 2.20 | 6.154 |
| 32×32 | 100 | 4.56 | 2.26 |
| 16×16 | 3000 | 6.36 | 15.05 |
| 16×16 | 300 | 6.37 | 1.74 |
| 16×16 | 100 | 8.75 | 0.59 |

6.5.3 SOVP RESULTS

A 64×64 point field generated inside of the SOVP function code is shown in Fig.

183. The track dimensions are modified to 280mm by 280mm by 10mm.

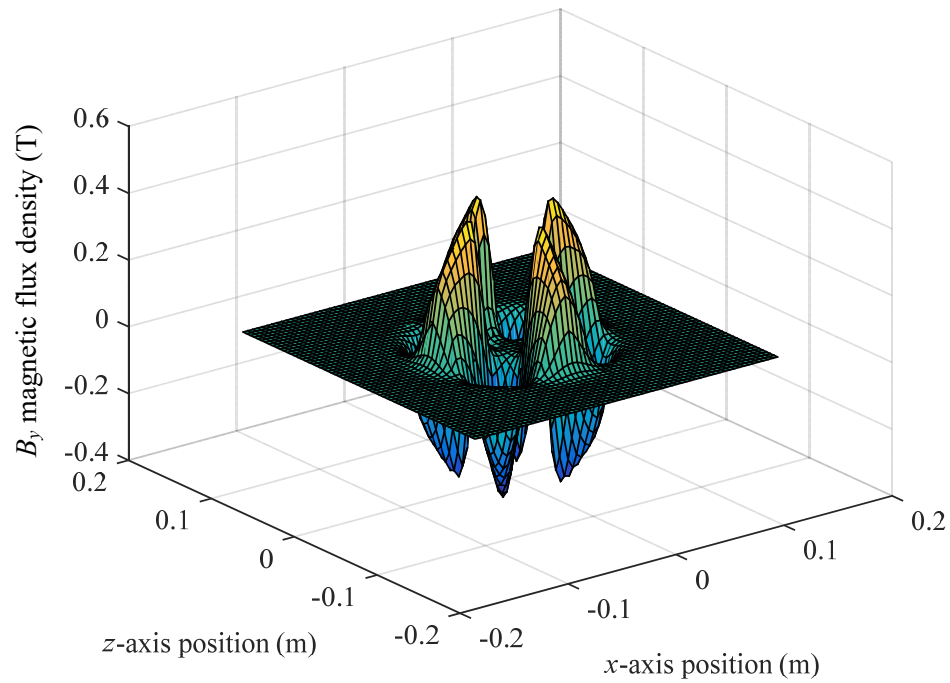


Fig. 183: Axial Halbach source field for use in SOVP model (rotor parameters from Table 16)

The source field data is then input into the SOVP model's force calculation block. These results were compared to an FEA model in which steady state values are obtained by simulating the rotor at each speed until the data settles to a constant plus some noise, which is filtered out. The rotor is simulated using the rotor parameters given in Table 16 and the track values given in Table 24. The rotor is held in the center of the track and rotational velocity is varied from $\omega_m = 0$ rad/s to $\omega_m = 150$ rad/s. Vertical force, F_y is shown in Fig. 184, rotor torque, and T_{em} is shown Fig. 185, and power loss, P_l , is shown in Fig. 186.

Table 24: Track parameters for axial EDW SOVP simulation

| Parameter | Value |
|------------------------|-------------------------|
| length, l | 105 mm |
| width, w | 105 mm |
| Thickness, d | 12.7 mm |
| conductivity, σ | 3.7665×10^{-7} |

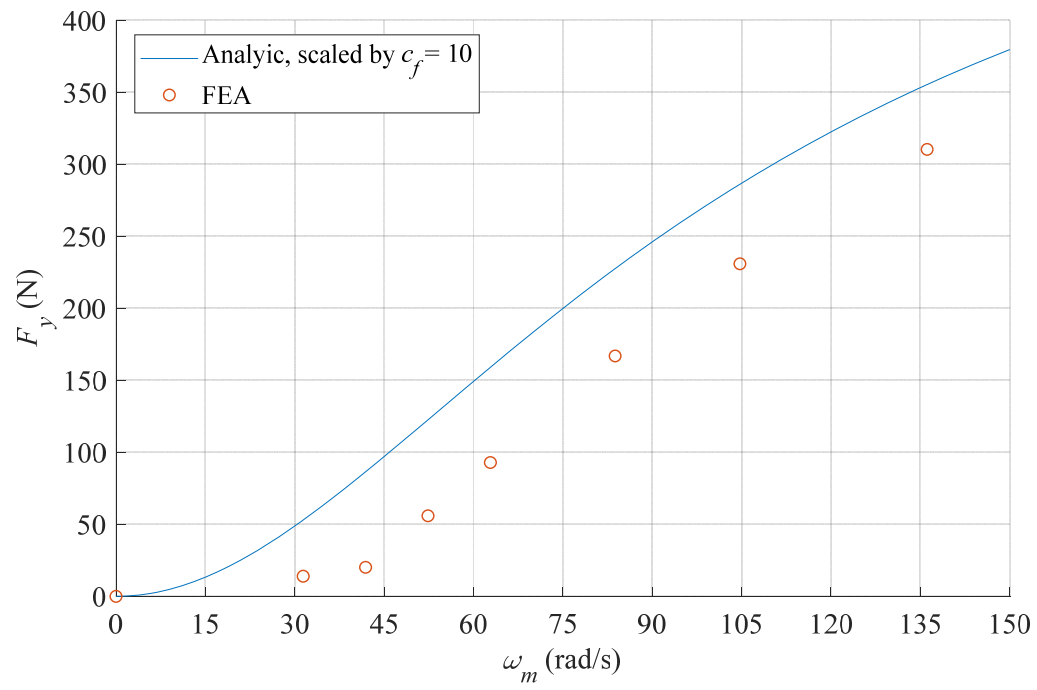


Fig. 184: Comparison of vertical force results from analytic solution and FEA when ω_m varies and $v_y = v_x = 0$

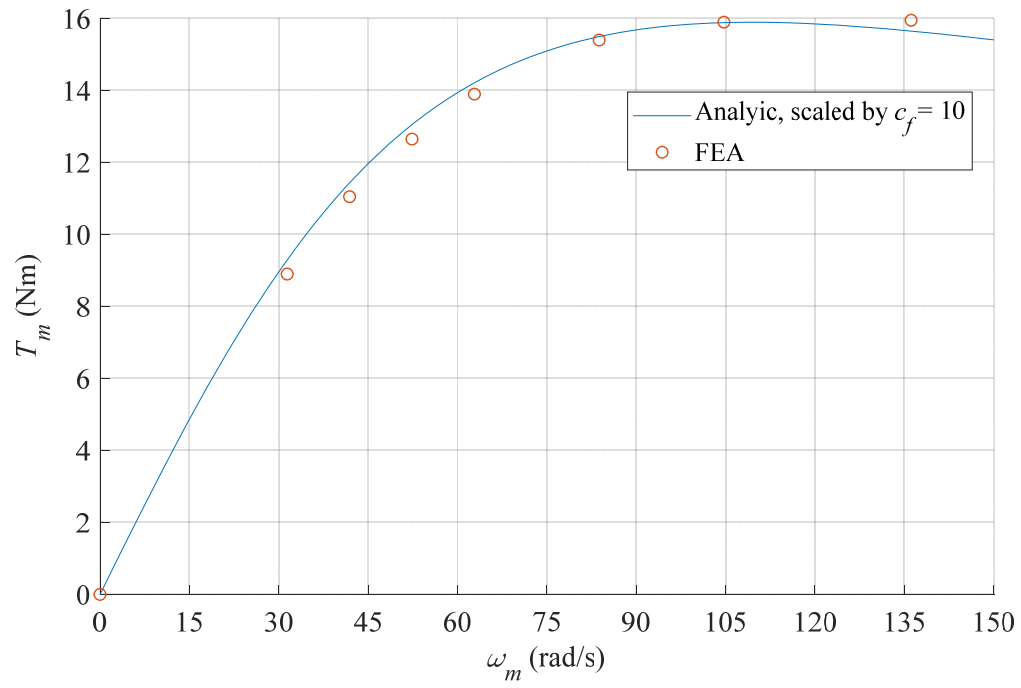


Fig. 185: Comparison of translational force results from analytic and FEA solution when ω_m varies and $v_y = v_x = 0$

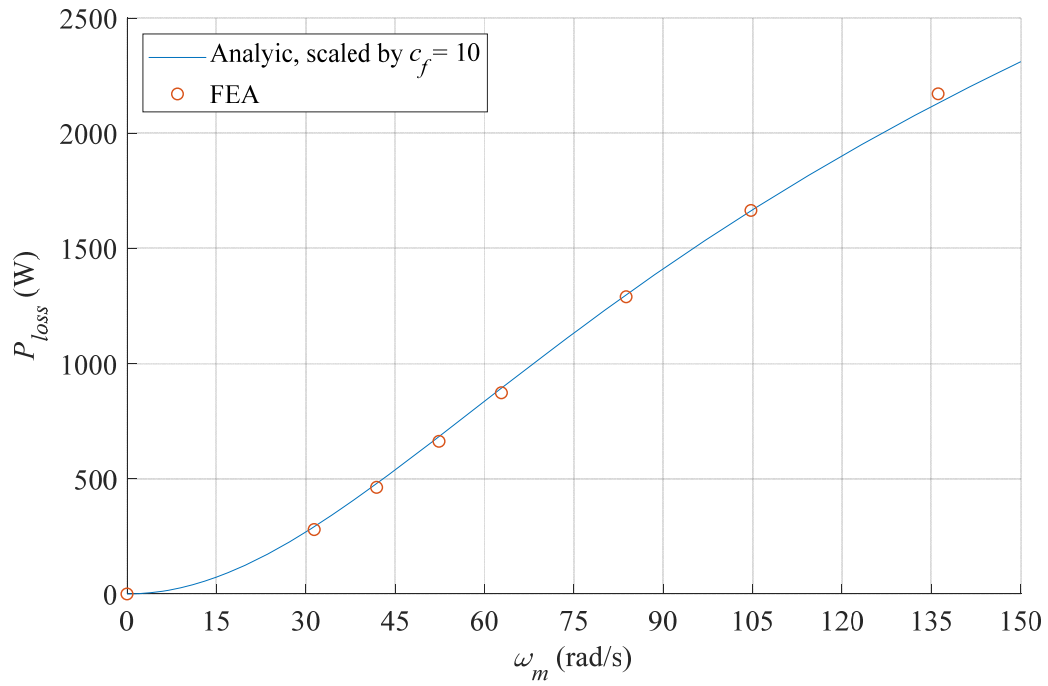


Fig. 186: Comparison of power loss results from analytic and FEA solution when ω_m varies and $v_y = v_x = 0$

Although the general shapes of the results show consistency between the SOVP solution and the FEA solution (as well as hypothesized expectations based on experience with the radial EDW), note that the analytic results are scaled by a constant c_f , which happens to be $c_f = 10$ for the lift force, torque, and power loss plots. When scaled, the torque and power loss results match quite well. The analytic solution for lift force, however, while predicting a similar behavior as the FEA solution, appears to show the force shifted left on the x -axis by approximately 20 rad/s.

Simulations were also performed for the case when the rotor is translated over the track with zero rotational velocity. The simulations were performed with parameters from Table 16, and results are summarized in Fig. 187, Fig. 188, and Fig. 189.

Table 16: Standard axial Halbach rotor field simulation parameters

| Parameter | Value |
|----------------------|----------|
| r_o | 70 mm |
| r_i | 30 mm |
| r_c | 48 mm |
| rotor thickness, d | 20 mm |
| airgap, y | 10 mm |
| pole pairs, P | 4 |
| M_f | 0.9745M |
| μ_r | 1.05 H/m |
| Magnet Grade | NMX-40CH |

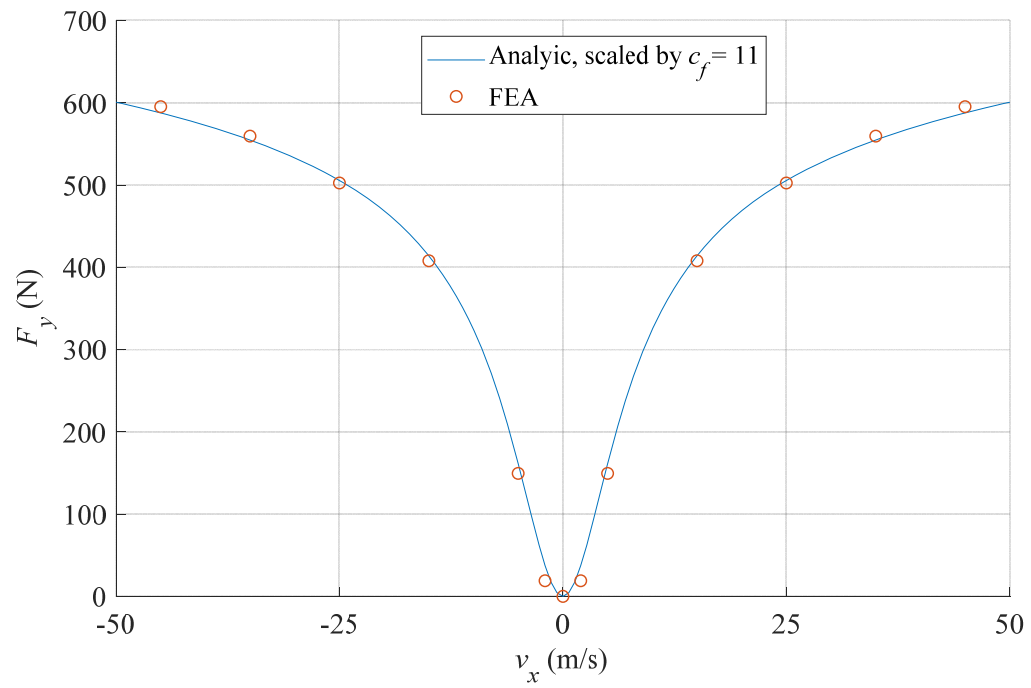


Fig. 187: Comparison of translationally induced lift force predicted by analytic and FEA models when v_x varies and $v_y = \omega_m = 0$

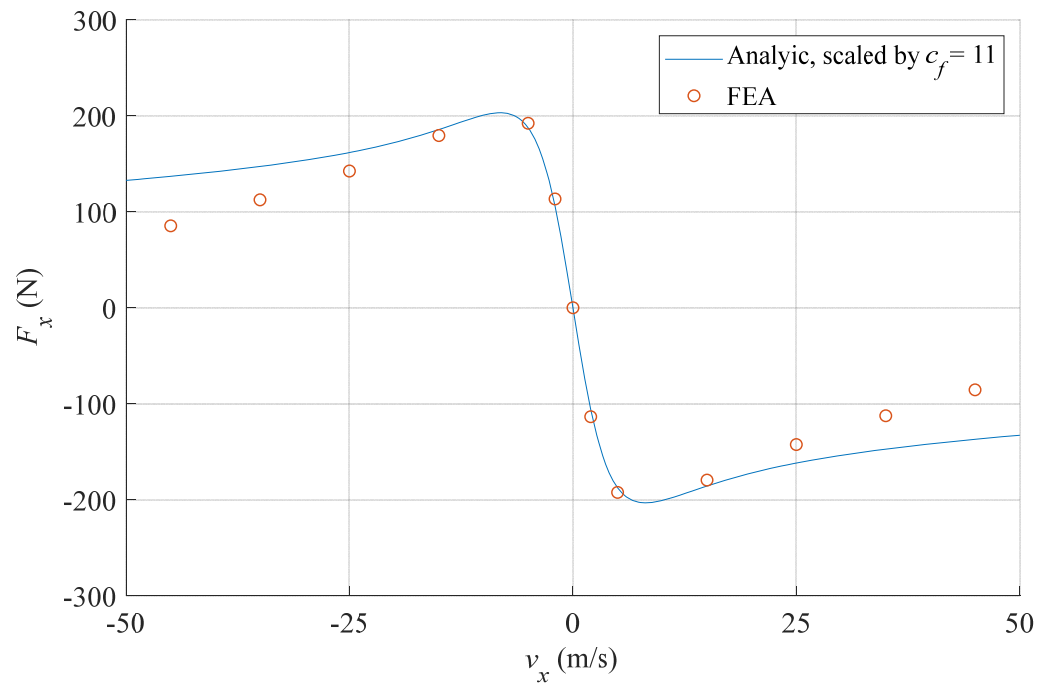


Fig. 188: Comparison of translationally induced thrust force predicted by analytic and FEA models when v_x varies and $v_y = \omega_m = 0$

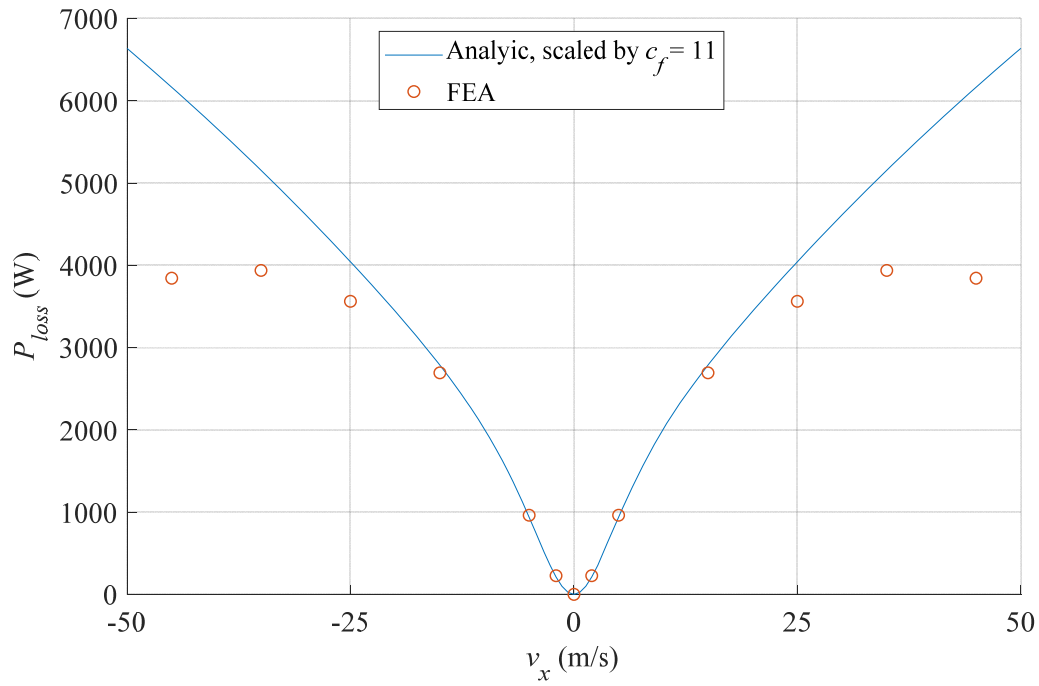


Fig. 189: Comparison of translationally induced power loss predicted by analytic and FEA models when v_x varies and $v_y = \omega_m = 0$

Unfortunately, the results still exhibit large discrepancies, necessitating a scaling coefficient of $c_f = 11$ for the lift force, thrust/braking force, and power loss, but once again the general behavior (ie. the shape of the plot) of both models match both each other and expectations based on our experience with the radial EDW. Note that while the lift force results show a good match throughout the chosen range of v_x , the thrust/braking force and power loss both match better near $v_x = 0$ and the discrepancy between the analytic and FEA models grows larger as translational speed is increased. More work is required to augment the derivation of the SOVP force model, as the suspected cause of the poor scaling with the FEA model is the manner in which the radial EDW's rotation is defined, whereby rotation is akin to translation in the x -axis due to the relationship between ω_m , v_x , and slip, s .

6.6 AXIAL ELECTRODYNAMIC WHEEL EXPERIMENTAL RESULTS

An experimental axial EDW with parameters defined by Table 25 was constructed using an aluminum housing with magnets glued in place. The rotor is designed to run on a test stand which measures torque and rotational velocity. If the torque matches the mathematical models, then it can be reasonably assumed that the other forces will also match.

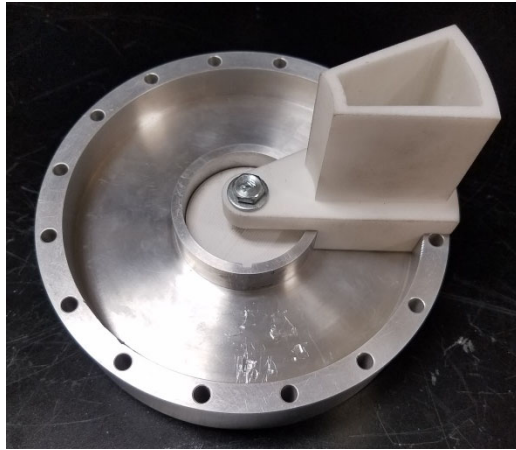
Table 25: Experimental axial Halbach rotor parameters

| Parameter | Value |
|----------------------|---------------|
| r_o | 70 mm |
| r_i | 30 mm |
| rotor thickness, d | 20 mm |
| pole pairs, P | 4 |
| Segments | 16 |
| Magnet grade | NMX-S45SH |
| Housing material | 6061 Aluminum |

Fig. 190 shows the rotor at various stages of assembly. In picture (a), the rotor housing is prepped to receive the first magnet. A Selective Laser Sintering (SLS) 3D printed fixture is used to ensure that the magnets are seated properly in the rotor housing. The partially assembled rotor with 2 magnets glued in place with Loctite 392 structural adhesive cured with Loctite 7387 activator is shown in picture (b), and a further assembled rotor with 10 magnets is shown in picture (c). The tight tolerances on the inner and outer radii of the magnets and rotor housing required the magnets to be pressed and impacted into place, causing some scratches and gouges which are evident in the photos. The assembly fixture was not stiff enough to hold the magnet tight against the adjacent magnet, so several additional clamps were needed to hold the magnet in place during curing, as shown in picture (d). The rotor with all magnets installed, as in picture (e), was only achievable by

grinding away 4.6% of the final magnet (by volume) on its' sides, due to the cumulative extra space between all other magnets. Picture (f) shows the completed axial rotor with the shaft spacer press fit and 1" aluminum shaft press fit and keyed into place.

Note that the aluminum housing was chosen for its mechanical properties and ready availability but it should be mentioned that a small error between the SOVP model and the experimental model is expected due to parasitic eddy currents. As the rotor rotates the conductive aluminum rotor housing experiences a time-varying magnetic field from the eddy currents induced in the track. This causes eddy currents to be induced in the rotor which can interact with the track and cause parasitic drag and other forces not accounted for by any previous models. To verify that the error would not markedly affect results, an FEA model was constructed to include the housing, and it was found that the effect on torque was minimal, with a discrepancy of less than 1%.



(a)



(b)



(c)



(d)



(e)



(f)

Fig. 190: Axial EDW at various stages of assembly (a) Bare rotor with assembly fixture bolted in place (b) Rotor during initial assembly with 2 magnets (c) Roughly half assembled rotor with assembly fixture prepped for 11th magnet (d) Clamping setup to ensure proper magnet placement (e) Rotor with all magnets installed (f) Complete rotor with shaft and shaft spacer

Once completed, the rotor is mounted to the bearing assembly which consists of two 316 stainless steel 1.5” thick endplates, each with a 1” bearing mounted at identical heights, and a square steel spacer to allow the endplates to be firmly bolted together. The rotor shaft is then inserted into the bearings such that the bearings provide both lateral and thrust support. The complete rotating assembly is shown in Fig. 191.

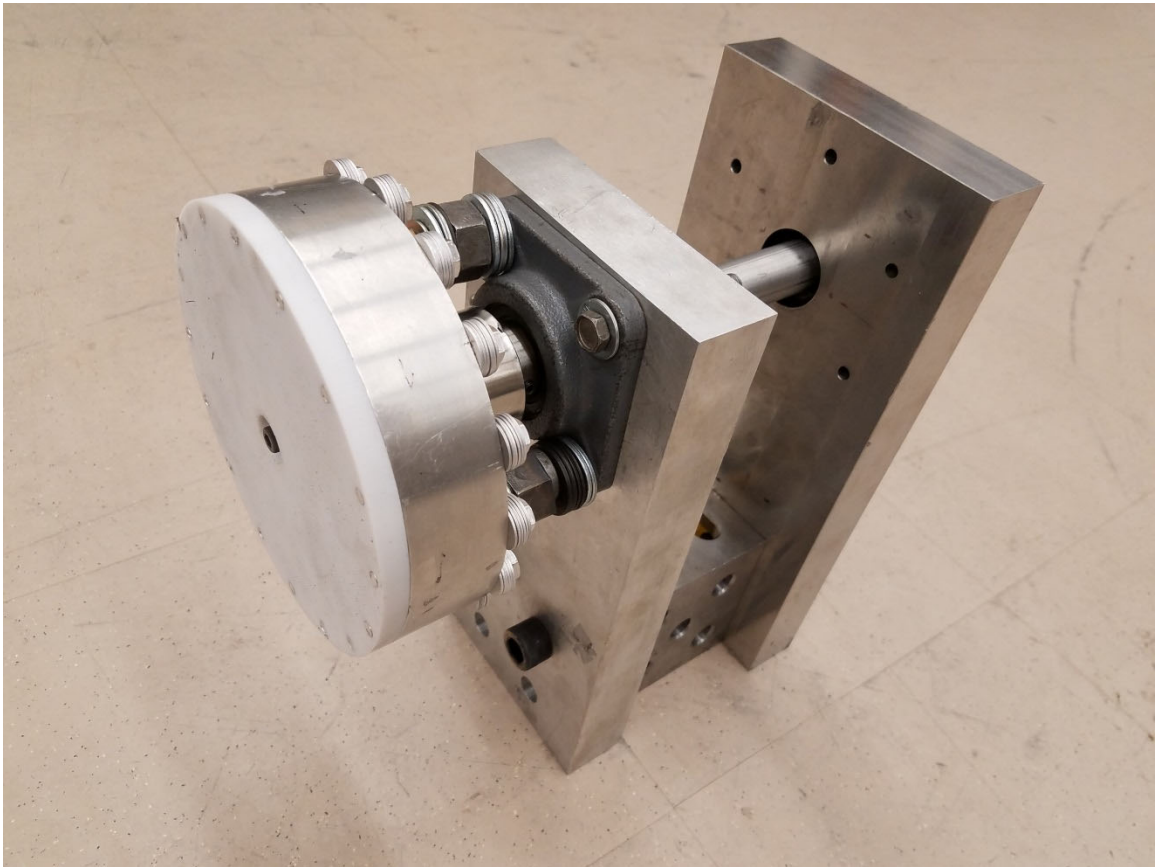


Fig. 191: Experimental axial EDW rotating assembly

Fig. 192 shows the prototype rotor mounted to the test bed. The rotor induced eddy currents in a 0.5” thick plate of 6061 aluminum which is wide and long enough to negate edge effects, according the analytic model. The rotor is driven by a Dayton 10hp, 4 pole induction motor through a Futek 605 torque transducer and encoder.

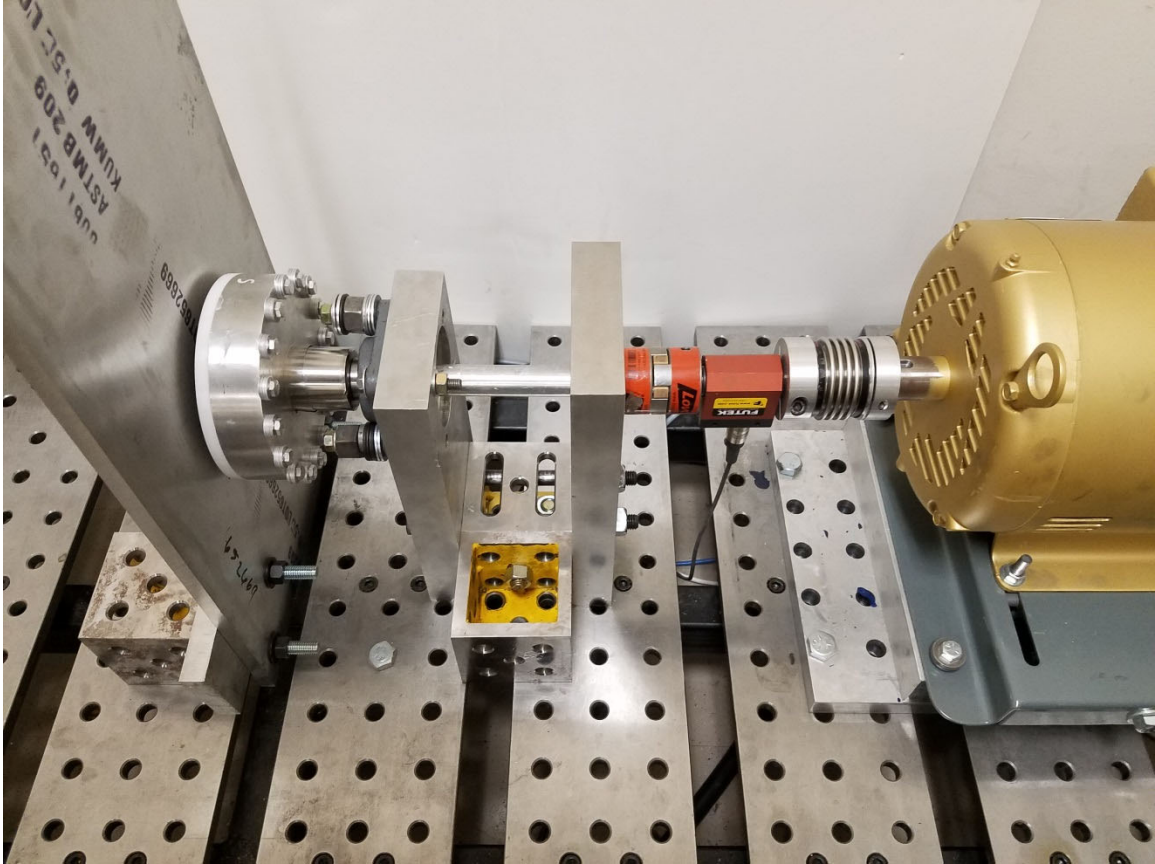


Fig. 192: Experimental axial EDW mounted to test bench

The field from the prototype rotor was measured at various radii with an airgap of 6.45mm, and the results are shown in Fig. 193. The field is sinusoidal, with the strongest measured field found at the center of the magnets, at radius 50mm. The measured field at $r = 32.94$ mm, $r = 50$ mm, and $r = 62.71$ mm is compared to the SOVP analytic model in Fig. 194, Fig. 195, and Fig. 196. Near the inner rotor radius, at $r = 32.94$ mm, the experimental and analytic field match very well, but in the center, at $r = 50$ mm, and near the outer radius, at $r = 62.71$ mm, the analytic predicts a field magnitude 11.3% larger and 9.6% larger, respectively. A larger analytic field, is expected, and can be attributed to the higher order harmonics that tend to flatten the peaks of the signal.

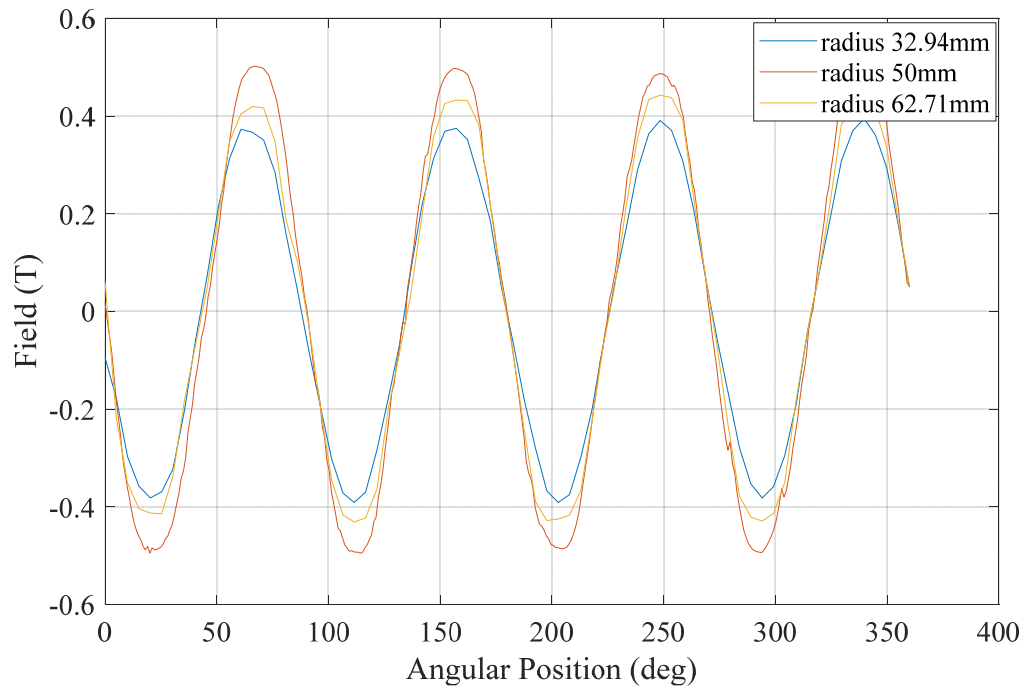


Fig. 193: Prototype axial EDW field measurements at airgap = 5.7mm (parameters from Table 25)

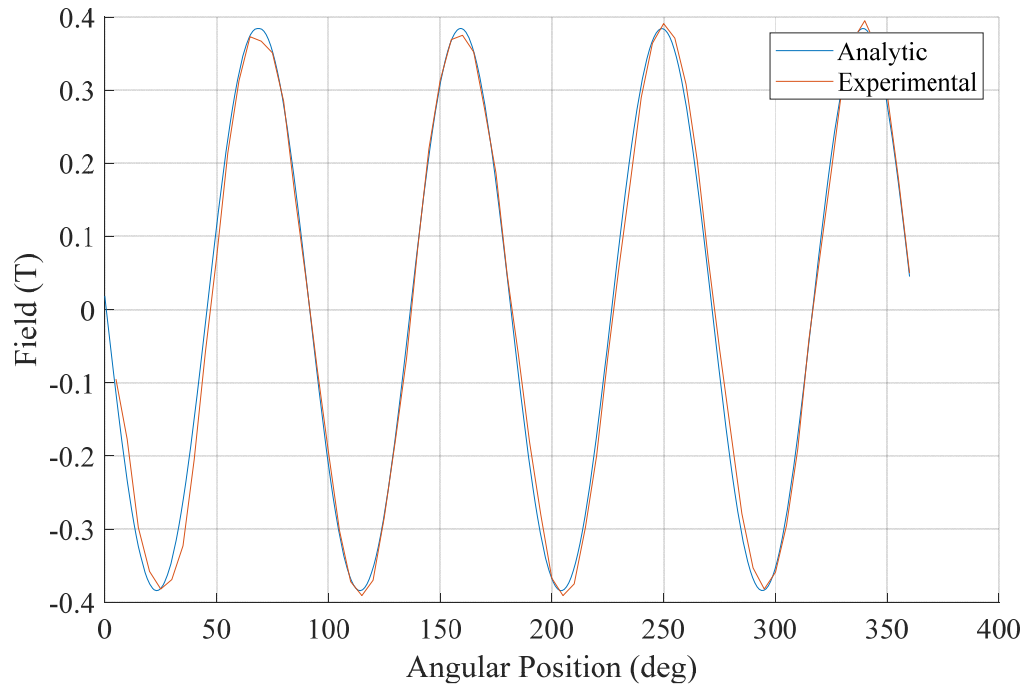


Fig. 194: Comparison of simulated analytic field and experimental field when $y = 5.7\text{mm}$ and $r = 32.94\text{mm}$, (parameters from Table 25)

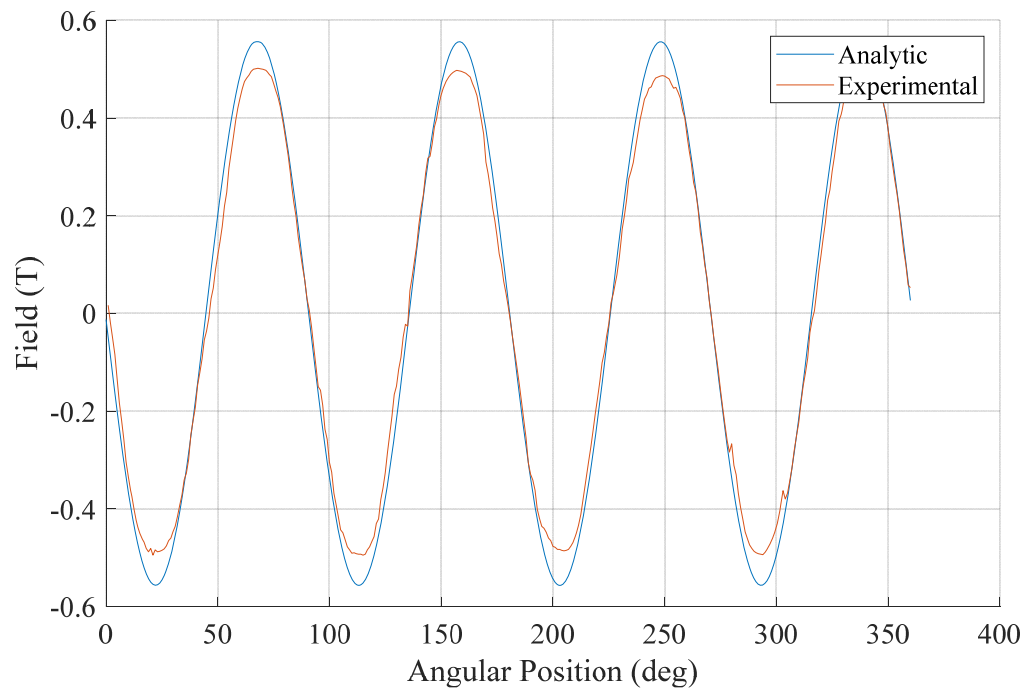


Fig. 195: Comparison of simulated analytic field and experimental field
when $y = 5.7\text{mm}$ and $r = 50\text{mm}$, (parameters from Table 25)

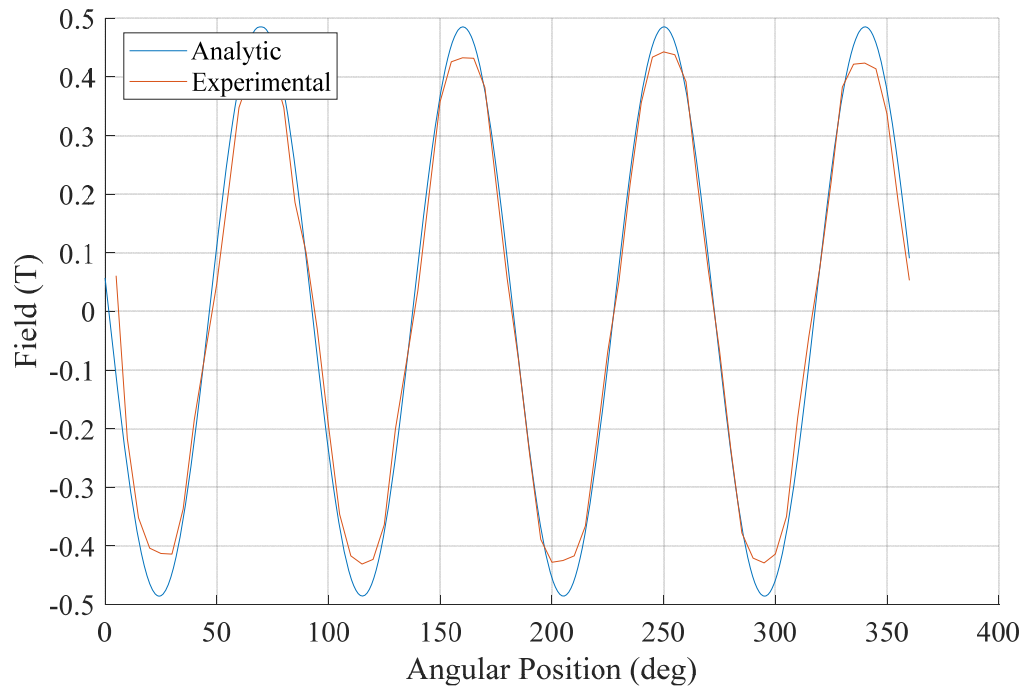


Fig. 196: Comparison of simulated analytic field and experimental field when $y = 5.7\text{mm}$ and $r = 62.71\text{mm}$, (parameters from Table 25)

Fig. 197 and Fig. 198 show the experimental, FEA calculated, and SOVP calculated torque results at airgaps of 14.7mm and 8.87mm, respectively. By full motor speed (1800 RPM), the experimental EDW has reached a plateau in which the smaller airgap produces a torque 2.49 times greater than the larger airgap. The SOVP and FEA models showed a similar behavior for small rotational velocities, but as the speed increased, the torque began to become smaller. Note that although the SOVP and FEA appear to agree with each other, the analytic results have been scaled by a scalar c_f , such that only the general behavior of the results are a direct match. Some sources of error in the experimental setup include frictional losses in the bearings and eddy current losses in the rotor housing that were not

properly accounted for by FEA analysis or the analytic model. This is likely why the experimental shows a higher torque with no peak before max speed.

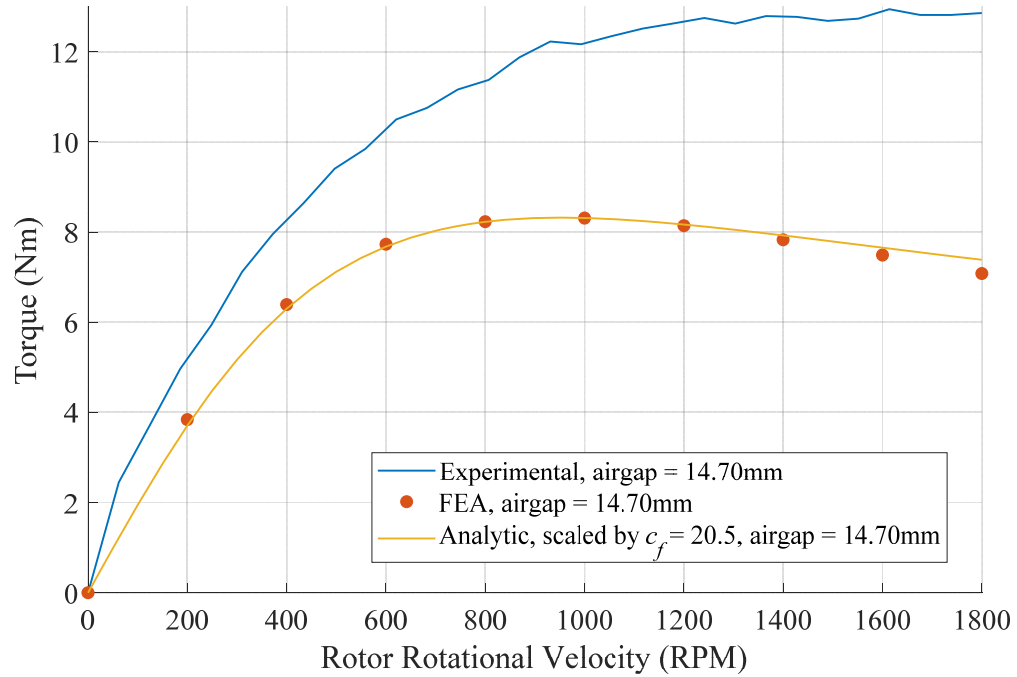


Fig. 197: Prototype axial EDW experimental torque results at airgap of $y = 14.7\text{mm}$ (parameters from Table 25)

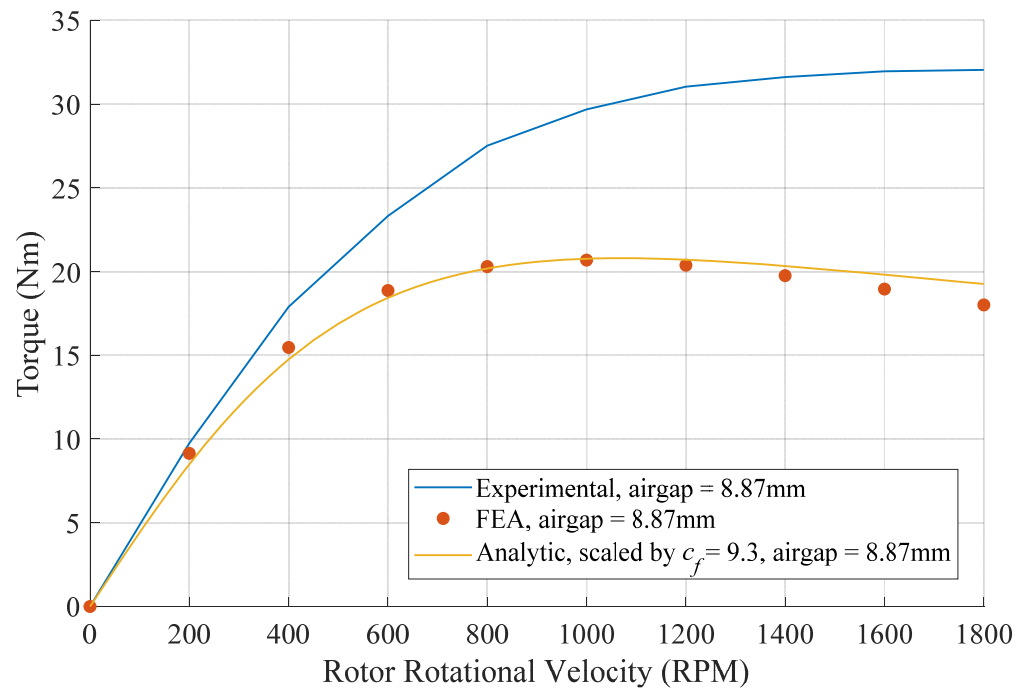


Fig. 198: Prototype axial EDW experimental torque results at airgap of $y = 8.87\text{mm}$
(parameters from Table 25)

6.7 CONCLUSION

An axial EDW topology is introduced in this chapter as an alternative to the radial EDW. The analytical field model is modified to allow Cartesian coordinates and an imaginary component. The analytical field solution is verified by comparison to an FEA model. The force, torque, and power loss calculated when the axial field is fed into the SOVP model does not currently agree with the FEA results or the available experimental results, but it appears to correctly predict the general expected trends. More work on the SOVP model is required to accurately simulate the EDW performance analytically. This will be required in order to explore more rotor geometries which have the greatest lift-to-power ratio.

CHAPTER 7: CONCLUSION AND FUTURE WORKS

7.1 INTRODUCTION

The goal of this research was to build an analytical EDW vehicle model to analyze the viability of such a system, and to explore a possible alternative to the radial EDW in an axial EDW. Section 7.2 serves as an overall conclusion to the research from earlier chapters. In section 7.3, the unique contributions that this research provides are discussed. Section 7.4 outlines the recommended direction for future research on the topic of EDW maglev.

7.2 RESEARCH CONCLUSION

In chapter CHAPTER 2:, the relevant damping and stiffness terms for a 4-DOF radial EDW vehicle were discussed. For the radial EDW vehicle, many of the damping and stiffness dynamics are inherently stable or are of no consequence to vehicle stability. For the damping and stiffness terms that do not contribute stability, their effect is often limited to one mode or axis. The summary tables at the end of chapter 2.3 serve as a guide for which terms are problematic, and when they manifest as such. Careful application of control and frequent updating of SOVP damping and stiffness terms is critical for the unstable terms.

In chapter CHAPTER 3:, the height, roll, pitch, and yaw equations are derived using a linearized approach based on terms from the SOVP model and in chapter CHAPTER 4:, these equations are wrapped into a single state-space system. Reasonable assumptions

were made to obtain a model that is both controllable and observable. Although the model is framed as linear, it is assumed to be piecewise linear in a later section. Also, if the damping and stiffness terms are thought of as functions, then the model becomes non-linear. Therefore, the model can be tailored to suit the desired level of refinement. The model was compared to an experimental setup, and the two had matching elements for long time constants (although their high frequency components did exhibit some differences). Unfortunately, more experimental testing was not possible due to an equipment change-of-custody.

Several types of controls of increasing complexity are discussed in chapter CHAPTER 5:, with the overarching intention of keeping the control methodology as simple as possible for the given situation rather than an unnecessary academic pursuit. For systems which remain close to desired operating point, simple linear control (with or without an observer depending on the available sensors) is preferred and functions well as shown in the simulations. When noise is introduced, LQGI control rejects noise and drives the EDW vehicle acceptably towards the desired reference. For systems which require large changes to the operating point or for controlling the vehicle while one or more of its damping and stiffness terms are in a highly unstable region, NGQI control is recommended. The piecewise linear observer/controller represents a very realistic control scenario since it is based on updating frequencies that match the SOVP calculation time.

A different wheel topology is explored in chapter CHAPTER 6:: the axial EDW. This arrangement of magnets directs a much larger percentage of the rotor's field into the track,

thereby increasing magnet utilization, which becomes an important consideration for cost and weight. It is thought that an axial EDW may offer increased efficiency when the pole pair count is kept low, but much more research is required. A field model developed by Li [71] was augmented to include an imaginary field component so that the SOVP model could be used to calculate the forces developed by the rotor. The SOVP model was accompanied by an FEA model as well, and an experimental prototype was built and tested on a rotational testbed. The results of the three models did not agree, but it is suspected that future work could solve this issue by redefining the axial motion in the SOVP model.

7.3 RESEARCH CONTRIBUTIONS

This section highlights several key features of this research project which have expanded our knowledge base of EDW maglev.

7.3.1 MAJOR CONTRIBUTIONS

1. For the radial EDW topology, the SOVP damping and stiffness terms were analyzed from a vehicle dynamics perspective, and important or problematic terms were identified and their potential deleterious effects were categorized. This has value to future vehicle and track design, so that special considerations could be made to allow those modes to be more responsive to control efforts. This information can also help tune a real-time controller with finite computational power so that it updates suspected unstable terms before the stable terms.

2. A 4-rotor EDW vehicle model using the SOVP force/torque model to calculate the damping and stiffness terms of the EDW as it rotates and translates above a conductive aluminum track was created which was simulated using Matlab. Using the analytic solution for damping and stiffness values allows the terms to be updated at a rate greater than 20Hz (less 50ms is typically required for the SOVP calculation, see Fig. 144). This model was compared to an experimental prototype (although there was limited access to equipment for extensive testing).
3. Controls were applied to a radial EDW maglev vehicle model. Despite the fact that some believe an EDW design is a poor candidate for maglev vehicles due to inherently difficult control paired with inherent instability, satisfactory control was achieved even with more rudimentary linear methods. The reason this is possible (and novel) is because of the use of an analytical force model (SOVP), which allows the very complicated, nuanced, and nonlinear EDW dynamics to be expressed as a linear approximation which remains accurate for small-order deviations from the calculation point (often referred to as “operating point” in earlier chapters).
4. By demonstrating that the piecewise linear NQGI controller is effective for a system which undergoes a large change in operating parameters (noting that plant was simulated nonlinearly and pseudo-continuously, and the controller was given realistic refresh rates), a major hurdle in the viability of EDW maglev vehicles has been mitigated considerably.

7.3.2 MINOR TECHNICAL CONTRIBUTIONS

1. An FEA model of the radial EDW was created using JMAG. To the author's knowledge, this is the first independent validation of the radial EDW SOVP model.
2. The radial SOVP model implementation in Matlab code was re-written and re-organized to be portable and customizable, with more user defined parameters to suit a wider variety of possible geometries. It has no function or toolbox dependencies.
3. Li's field model [71] was re-written in code (Matlab) and augmented to include an imaginary component for input into a modified version of the SOVP force model code.
4. An FEA model of the axial EDW was created, and its field validated against Li's field model [71]
5. An axial EDW prototype was designed and constructed, and torque was measured as it was rotated over a conductive aluminum sheet.

7.4 FUTURE WORK

The following objectives for future work have been identified:

1. With the experimental 4-rotor radial EDW vehicle setup currently residing at Portland State University, future work should be conducted to collect more experimental results to validate both the 4-DOF vehicle model from chapter CHAPTER 4:, as well as the controller simulations in chapter CHAPTER 5:. Further work could also expand the model to 6-DOF.

2. In order to obtain a computationally efficient solution for the forces from an axial EDW, an SOVP model will need to be derived using a different rotational axis (about the y axis).
3. Further experimental results using the axial EDW would enable proper validation of an axial SOVP model. A more complex setup which is able to measure lift and lateral force would be ideal.
4. Providing that satisfactory efficiency results are obtained with an axial EDW, it may be worthwhile to model and/or experimentally evaluate the forces when the EDW is tilted off-axis. A tilting mechanism would allow thrust, braking, and lateral forces to be achieved by an axial EDW.

CHAPTER 8: REFERENCES

- [1] "2014 World Population Data Sheet", U.S. Agency of International Development, PRB.
- [2] "World economic outlook (WEO), april 2015 - chapter 1: Recent developments and prospects," IMF, 2015.
- [3] International Energy Outlook 2016. (2016). U.S. Energy Information Administration.
- [4] U. Canon, "Boeing's 'more electric' 787 Dreamliner spurs engine evolution," in *Automation and Motion Control*, Design News, June 4, 2007.
- [5] B. Vlasic, "Honda stays true to efficient driving," in *Business Day*, The New York Times, Aug. 26, 2008.
- [6] "U.S. Passenger-Miles (xlsx)". *U.S. Dept. of Transportation*, 2014.
- [7] Revenue Passenger-miles. (2017, May 1). *U.S. Dept. of Transportation*, 2017.
- [8] Post, R. and Ryutov, D. (2000). The Inductrack Approach to Magnetic Levitation. In: MAGLEV 2000 The 16th International Conference on Magnetically Levitated Systems and Linear Drives.
- [9] "High-Tech for 'Flying on the Ground'," *Transrapid International*.
- [10] R. F. Post and D. D. Ryutov, "The Inductrack: A simpler approach to magnetic levitation," *IEEE Transactions on Applied Superconductivity*, vol. 10, no. 1, pp. 901–904, Mar. 2000.
- [11] W. Ko, C. Ham, J. Hong, and J. Choi, "Dynamics and controls of a Maglev vehicle," *2009 IEEE International Symposium on Industrial Electronics*, Jul. 2009.
- [12] K. R. Davey, "Electrodynamic Maglev coil design and analysis," *IEEE Transactions on Magnetics*, vol. 33, no. 5, pp. 4227–4229, 1997.
- [13] J. de Boeij, M. Steinbuch, and H. Gutierrez, "Modelling the electromechanical interactions in a null-flux EDS maglev system," *2004 12th Symposium on Electromagnetic Launch Technology, 2004.*, 2004.
- [14] J. de Boeij, M. Steinbuch, and H. M. Gutierrez, "Mathematical model of the 5-DOF sled dynamics of an electrodynamic maglev system with a passive sled," *IEEE Transactions on Magnetics*, vol. 41, no. 1, pp. 460–465, Jan. 2005.
- [15] J. Boeij, M. Steinbuch, and H. Gutierrez, "Real-time control of the 3-DOF Sled dynamics of a null-flux Maglev system with a passive Sled," *2006 IEEE International Symposium on Industrial Electronics*, Jul. 2006.
- [16] Chen, Y., Zhang, W., Bird, J. Z., Paul, S., & Zhang, K. (2015). A 3-D Analytic-Based Model of a Null-Flux Halbach Array Electrodynamic Suspension Device. *IEEE Transactions on Magnetics*, 51(11), 1–5. <https://doi.org/10.1109/tmag.2015.2444331>
- [17] J. Du and H. Ohsaki, "Numerical Analysis of Eddy Current in the EMS-Maglev System," *ICEMS2003 proceedings of the sixth international conference on electrical machines and systems: November 9-11, 2003, Beijing, china*, Jan. 2003.

- [18] L. Songqi, Z. Kunlun, L. Guoqing, and G. Wei, "EMS maglev vehicles model reference adaptive control," *34th Chinese Control Conference (CCC)*, Jul. 2015.
- [19] C. Dumont, V. Kluyskens, and B. Dehez, "Null-flux radial Electrodynamic bearing," *IEEE Transactions on Magnetics*, vol. 50, no. 10, pp. 1–12, Oct. 2014.
- [20] J. L. He, D. M. Rote, and H. T. Coffey, "Study of Japanese electrodynamic-suspension maglev systems. Argonne National Laboratory, IL (United States), Apr. 1, 1994. [Online]. Available: <http://www.osti.gov/scitech/servlets/purl/10150166>. Accessed: Oct. 6, 2016.
- [21] J. Bird and T. A. Lipo, "Characteristics of an electrodynamic wheel using a 2-D steady-state model," *IEEE Transactions on Magnetics*, vol. 43, pp. 3395–3405, Aug. 2007. DOI: <http://dx.doi.org/10.1109/TMAG.2007.900572>
- [22] J. Bird and T. A. Lipo, "Calculating the forces created by an electrodynamic wheel using a 2D steady-state finite element model," *IEEE Trans. Magn.*, 2006.
- [23] J. Powell and G. Danby, "Energy Efficiency and Economics of Maglev Transport," in *Advanced Energy Conference*, Long Island, NY, 2008.
- [24] L. Kang and J. Bird, "A 3-D Analytical Model of a Halbach Axial Magnetic Coupling"
- [25] Iwamoto, M., T. Yamada, and E. Ohno, "Magnetic damping force in electrodynamically suspended trains," *IEEE Transactions on Magnetics*, Vol. 10, No. 3, 458–461, 1974
- [26] Moon, F. C., *Superconducting Levitation: Applications to Bearings and Magnetic Transportation*, WILEY-VCH Verlag GmbH & Co. KGaA, 2004.
- [27] Zhu, S., Y. Cai, D. M. Rote, and S. S. Chen, "Magnetic damping for maglev," ANL/ET/CP-82419, CONF-9411194–2, Energy Technology Division, Argonne National Laboratory, 1995.
- [28] Zhu, S., Y. Cai, D. M. Rote, and S. S. Chen, "Magnetic damping for maglev," *Shock and Vibration*, Vol. 5, 119–128, 1998.
- [29] Davis, L. C. and D. F. Wilkie, "Analysis of motion of magnetic levitation systems: Implications for high-speed vehicles," *Jour. of Appl. Phys.*, Vol. 42, No. 12, 4779–4793, Nov. 1971.
- [30] Paudel, N. (2012). *Dynamic Suspension Modeling of an Eddy-Current Device: An Application To Maglev*. Ph.D. The University of North Carolina at Charlotte.
- [31] Paul, S. (2013). *Three-Dimensional Steady State and Transient Eddy Current Modeling*. Ph.D. The University of North Carolina at Charlotte.
- [32] S. Paul, W. Bomela, N. Paudel, and J. Z. Bird, "3-D eddy current torque modeling," *IEEE Trans. Magn.*, vol. 50, no. 2, pp. 905–908, Feb. 2014.
- [33] S. Paul, D. Bobba, N. Paudel, and J. Z. Bird, "Source field modeling in air using magnetic charge sheets," *IEEE Trans. Mag.*, vol. 48, no. 11, pp. 3879–3882, Nov. 2012.
- [34] J. Bird and T. A. Lipo, "Modeling the 3-D rotational and translational motion of a Halbach rotor above a split-sheet guideway," *IEEE Transactions on Magnetics*, Vol. 45, pp. 3233–3242, Sept. 2009. DOI: <http://dx.doi.org/10.1109/TMAG.2009.2021160>

- [35] S. Paul, J. Wright, and J. Z. Bird, "3-D Steady-State Eddy-Current Damping and Stiffness Terms for a Finite Thickness Conductive Plate," *IEEE Transactions on Magnetics*, Vol. 50, Article #: 6301404, Nov., 2014. DOI: <http://dx.doi.org/10.1109/TMAG.2014.2327097>
- [36] Napolitano, M. (2012). *Aircraft dynamics*. Hoboken, NJ: J. Wiley.
- [37] Ko, W. (2007). *Modelling and Analysis of the EDW Maglev System with the Halbach Magnet Array*. Ph.D. The University of Central Florida.
- [38] Chen, S. (1993). *On the Unsteady-Motion Theory of Magnetic Forces for Maglev*. Argonne National Laboratory.
- [39] Q. Han, C. Ham and R. Phillips, "Four- and eight-piece Halbach array analysis and geometry optimisation for maglev," in *IEE Proceedings - Electric Power Applications*, vol. 152, no. 3, pp. 535-542, 6 May 2005. doi: 10.1049/ip-epa:20045059
- [40] Han, Q. (2000). *Analysis and Modeling of the EDS Maglev System Basic on the Halbach Permanent Magnet Array*. Ph.D. The University of Central Florida
- [41] Borowy, Bogdan & Kang, Keunmo. (2017). *Modeling of the General Atomics Urban Maglev: System Identification Approach*.
- [42] Haus, Hermann A., and James R. Melcher. *Electromagnetic Fields and Energy*. Englewood Cliffs, NJ: Prentice-Hall, 1989. ISBN: 9780132490207.
- [43] Hamid Yaghoubi, Nariman Barazi and Mohammad Reza Aoliaei (2012). *Maglev, Infrastructure Design, Signalling and Security in Railway*, Dr. Xavier Perpinya (Ed.), ISBN: 978-953-51-0448-3
- [44] "Hover Engine HE3.0 Datasheet," Revision 2, Arx Pax Labs, Inc., March 3, 2016.
- [45] Kim, N. and Ge, L. (2012). Dynamic modeling of electromagnetic suspension system. *Journal of Vibration and Control*, 19(5), pp.729-741.
- [46] Sepe, R., Bastien, S., Steyerl, A. and Borowy, B. (2010). Robust absolute position sensing for MagLev. 2010 IEEE Energy Conversion Congress and Exposition.
- [47] Gurol, H. (2009). General Atomics Linear Motor Applications: Moving Towards Deployment. *Proceedings of the IEEE*, 97(11), pp.1864-1871.
- [48] Jeong, J., Ha, C., Lim, J. and Choi, J. (2017). Analysis and Control of Electromagnetic Coupling Effect of Levitation and Guidance Systems for Semi-High-Speed Maglev Train Considering Current Direction. *IEEE Transactions on Magnetics*, 53(6), pp.1-4.
- [49] International Energy Agency (2017). *Global EV Outlook 2017*. International Energy Agency.
- [50] Kossowsky, R. (1999). *Physics and materials science of vortex states, flux pinning and dynamics*. Dordrecht: Kluwer Academic Publishers.
- [51] Fujii, N., O. Ogawa, and T. Matsumoto, *Revolving Magnet Wheels with Permanent Magnets*. *Electrical Engineering in Japan*, 1996. 116(1): p. 106-117.
- [52] Fujii, N., G. Hayashi, and Y. Sakamoto, *Characteristics of magnetic lift, propulsion and guidance by using magnet wheels with rotating permanent magnets*. *Industry Applications Conference*, 2000: p. 257-262.

- [53] Fujii, N., Naotsuka, K., Ogawa, K. and Matsumoto, T. (n.d.). Basic characteristics of magnet wheels with rotating permanent magnets. Proceedings of 1994 IEEE Industry Applications Society Annual Meeting.
- [54] O. D. Jefimenko, Electricity and Magnetism. New York, NY, USA: Meredith, 1966.
- [55] Hyung-Woo Lee, Ki-Chan Kim, & Ju Lee. (2006). Review of maglev train technologies. IEEE Transactions on Magnetics, 42(7), 1917–1925. <https://doi.org/10.1109/tmag.2006.875842>
- [56] Rawlings, J. & Mayne, D. (2009). Model predictive control : theory and design. Madison, Wis: Nob Hill Pub.
- [57] Papalambros, P. & Wilde, D. (2000). Principles of optimal design : modeling and computation. Cambridge New York: Cambridge University Press.
- [58] Kirk, D. (1970). *Optimal control theory; an introduction*. Englewood Cliffs, N.J: Prentice-Hall.
- [59] Periyasamy, D., & Nisha, M. G. (2017). Model predictive control of maglev system. In 2017 International Conference on Innovations in Green Energy and Healthcare Technologies (IGEHT). IEEE. <https://doi.org/10.1109/igeht.2017.8094050>
- [60] Spurgeon, S. (2014). Sliding mode control: a tutorial. In 2014 European Control Conference (ECC). IEEE. <https://doi.org/10.1109/ecc.2014.6862622>
- [61] Fliess, M., Lévine, J., Martin, P., & Rouchon, P. (1995). Flatness and defect of non-linear systems: introductory theory and examples. International Journal of Control, 61(6), 1327–1361. <https://doi.org/10.1080/00207179508921959>
- [62] Beltran-Carbajal, F., Valderrabano-Gonzalez, A., Rosas-Caro, J. C., & Favela-Contreras, A. (2015). Output feedback control of a mechanical system using magnetic levitation. ISA Transactions, 57, 352–359. <https://doi.org/10.1016/j.isatra.2015.01.012>
- [63] Didam, M. E., Agee, J. T., Jimoh, A. A., & Tlale, N. (2012). Nonlinear control of a single-link flexible joint manipulator using differential flatness. In 2012 5th Robotics and Mechatronics Conference of South Africa. IEEE. <https://doi.org/10.1109/robomech.2012.6558453>
- [64] El Hajjaji, A., & Ouladsine, M. (2001). Modeling and nonlinear control of magnetic levitation systems. IEEE Transactions on Industrial Electronics, 48(4), 831–838. <https://doi.org/10.1109/41.937416>
- [65] Khalil, H. K. (2001). Nonlinear Control (3rd ed.). Boston, MA: Pearson.
- [66] Bächle, T., Hentzelt, S., & Graichen, K. (2013). Nonlinear model predictive control of a magnetic levitation system. Control Engineering Practice, 21(9), 1250–1258. <https://doi.org/10.1016/j.conengprac.2013.04.009>
- [67] Periyasamy, D., & Nisha, M. G. (2017). Model predictive control of maglev system. In 2017 International Conference on Innovations in Green Energy and Healthcare Technologies (IGEHT). IEEE. <https://doi.org/10.1109/igeht.2017.8094050>
- [68] Qin, Y., Peng, H., Zhou, F., Zeng, X., & Wu, J. (2015). Nonlinear modeling and control approach to magnetic levitation ball system using functional weight RBF network-based state-dependent ARX model. Journal of the Franklin Institute, 352(10), 4309–4338. <https://doi.org/10.1016/j.jfranklin.2015.06.014>

- [69] E. P. Furlani, *Permanent Magnet and Electromechanical Devices Materials, Analysis, and Applications*. San Diego, CA, USA: Academic, 2001.
- [70] F. C. Moon, *Superconducting Levitation: Applications to Bearings and Magnetic Transportation*. New York, NY, USA: Wiley, 2004.
- [71] Li, K (2018). An Investigation Into the Torque Capabilities of High Gear Ratio Magnetic Gearboxes. Ph.D. The University of North Carolina at Charlotte.
- [72] Pradhan, S. K., & Subudhi, B. (2016). Nonlinear Control of a Magnetic Levitation System Using a New Input-Output Feedback Linearization. *IFAC-PapersOnLine*, 49(1), 332–336. <https://doi.org/10.1016/j.ifacol.2016.03.075>
- [73] Fastenal. (2005, September 13). Technical Reference Guide. Retrieved from <https://www.fastenal.com/content/documents/FastenalTechnicalReferenceGuide.pdf>
- [74] Scorpion SII-4035-250KV Specifications. (n.d.). Retrieved from https://www.scorpionsystem.com/catalog/aeroplane/motors_1/sii-40/SII-4035-250/
- [75] Åström, K. J., & Murray, R. M. (2011). *Feedback systems: An introduction for scientists and engineers*. Princeton: Princeton University Press. ISBN 978-0-691-13576-2
- [76] Naidu, D. S. (2003). *Optimal control systems*. Boca Raton, FL: CRC Press. ISBN 0-8493-0892-5
- [77] Ogata, K. (2010). *Modern control engineering*. Upper Saddle River, NJ: Prentice-Hall/Pearson. ISBN 978-0-13-615673-4
- [78] Georgiou, T. T., & Lindquist, A. (2013). The Separation Principle in Stochastic Control, Redux. *IEEE Transactions on Automatic Control*, 58(10), 2481–2494. <https://doi.org/10.1109/tac.2013.2259207>
- [79] Burden, Richard L.; Faires, J. Douglas (2000). *Numerical Analysis* (7th ed.). Brooks/Cole. ISBN 0-534-38216-9.
- [80] Teschl, G. (2012). *Ordinary differential equations and dynamical systems*. Providence, RI: American Mathematical Society. ISBN 978-0-8218-8328-0
- [81] Groves, K., & Serrani, A. (2004). Modeling and Nonlinear Control of a Single-link Flexible Joint Manipulator.